Deployment and Capture Dynamics of Tether-Nets for Active Space Debris Removal

Eleonora M. Botta

The Department of Mechanical Engineering
McGill University, Montreal.

November 2017

A thesis submitted to McGill University in partial fulfilment of the requirements of the degree of Doctor of Philosophy.

Abstract

For containing the growth of space debris, which jeopardizes operation of spacecraft, the active removal of large and massive derelict satellites and launcher upper stages is needed. A promising technology for this endeavor is the use of tether-nets. In this concept, a tether-net is thrown from a chaser spacecraft in the proximity of a target debris towards this target; the net entangles the target or closes around it, and the tether connecting the net to the chaser provides a link to tug debris to its disposal orbit.

The aim of this research is to gain insight into the dynamics of tether-nets in space: the focus is on the deployment and capture phases of the mission. This is done primarily through numerical simulation, with tools expressly developed in MATLAB and in Vortex Dynamics. The latter simulation tool is representative of the main components of the system, flexible, and computationally efficient.

The first part of this study is dedicated to the deployment phase. A standard lumped-parameter model of the net is introduced and its implementation in the two simulators is verified. Results of deployment simulations reveal a snapping behavior of tension. The effect of taking into account the bending stiffness of the threads of the net on the deployment dynamics is analyzed, thanks to the implementation of an augmented lumped-parameter model. Further, analytical derivations based on work-energy and linear momentum principles allow to identify bounds for centroidal velocities during deployment and key parameters leading this dynamics; a sensitivity study shows that more lasting deployment and safer capture can be obtained by employing moderately heavy corner masses, moderate shooting angles, and low shooting velocities. The effect of tensioning of the main tether on the quality of deployment is also investigated.

The second part of this work deals with the dynamics of net-based capture of space debris. Continuous compliant models for the normal contact force and micro-slip models for friction are used to represent contacts; the effect of contact modeling choices is evaluated in a simple capture scenario. Analysis of the effect of representing the bending stiffness of the threads of the net on capture shows that, notwithstanding visible differences in the dynamics, the success of capture remains similar. It is ascertained that capture of realistic tumbling debris is robust to multiple non-nominal deployment conditions; however, the need to include a closing mechanism is recognized. The working principle of a possible closing mechanism based on spooling-in of the main tether is verified through modeling and simulation, following analysis of the effect of tether tensioning on capture dynamics. Simulations with simple closing mechanisms, independent of the spooling of the main tether, help identify safer scenarios for capture. Modification of the net model allows to overcome limitations of the lumped-parameter model and to detect collisions with thin elements, such as solar arrays. Finally, it is suggested that tether-nets could be used to capture small asteroids.

Résumé

Pour contenir la croissance des débris spatiaux, qui met en péril le fonctionnement des satellites, il est nécessaire d'éliminer activement les plus gros et massifs satellites abandonnés et les étages supérieures des lanceurs. Une technologie prometteuse pour cette entreprise est l'utilisation de filets. Dans ce concept, un filet est jeté à partir d'un satellite à proximité d'une cible vers cette cible; le filet attrape la cible, et l'attache reliant le filet au satellite fournit une connexion pour transporter le débris à son orbite d'élimination.

L'objectif de cette recherche est de mieux comprendre la dynamique des filets dans l'espace: l'accent est mis sur les phases de déploiement et de capture. Ceci se fait principalement par la simulation numérique, avec des outils expressément développés dans MATLAB et dans Vortex Dynamics. Ce dernier outil de simulation est représentatif des composants principaux du système, flexible et efficace en termes de calcul.

La première partie de cette étude est consacrée à la phase de déploiement. Un modèle standard à paramètres localisés est introduit pour le filet et sa mise en œuvre dans les deux simulateurs est vérifiée. Les résultats des simulations de déploiement révèlent des tensions instantanées dans les fils. L'effet de la prise en compte de la rigidité en flexion des fils sur la dynamique de déploiement est analysé grâce à la mise en place d'un modèle à paramètres localisés augmenté. De plus, des dérivations analytiques basées sur le principe du travail et de l'énergie et sur le principe du moment linéaire permettent d'identifier des limites pour les vitesses des centres de masse pendant le déploiement et les paramètres clés qui influencent cette dynamique. Une étude de sensibilité montre qu'un déploiement plus durable et une capture plus sécuritaire peuvent être obtenus en utilisant des poids modérément lourds, des angles d'éjection modérés et des vitesses de tir faibles. L'effet de la tension de l'attache principale sur la qualité du déploiement est également étudié.

La deuxième partie de ce travail traite de la dynamique de la capture de débris spatiaux avec un filet. Les contacts sont représentés avec des modèles continus pour la force de contact normale et des modèles "stick-slip" pour le frottement; l'effet des choix de modélisation des contacts est évalué dans un scénario de capture simple. L'analyse de l'effet de représentation de la rigidité de flexion des fils lors de la capture montre que, malgré des différences, le succès de la capture reste similaire. Il est constaté que la capture de débris vraisamblables et qui tournent est robuste à de multiples conditions de déploiement non nominales. Cependant, la nécessité d'inclure un mécanisme de fermeture est reconnue. Le principe de fonctionnement d'un possible mécanisme de fermeture basé sur le contrôle de l'attache principale est vérifié à travers la modélisation et la simulation de celui-ci, après avoir analysé l'effet de la tension sur la dynamique de capture. Des simulations avec des mécanismes de fermeture simples, indépendants du contrôle de l'attache principale, permettent d'identifier des scénarios sécuritaires pour la capture. La modification du modèle du filet permet de surmonter les limites du modèle standard à paramètres localisés et de détecter les collisions avec des éléments minces, tels que les panneaux solaires. Enfin, il est suggéré que des filets pourraient être utilisés aussi pour capturer de petits astéroïdes.

A Nonno Francesco,
per la sua precisione,
i suoi racconti,
e i suoi disegni tecnici.

To Grandfather Francesco,
for his precision,
his tales,
and his technical drawings.

Acknowledgements

A lot of people have contributed to the success of this Ph.D. research: many pages would be needed to thank everyone properly, but I hope I can summarize my gratitude in a few lines.

First of all, I am deeply grateful to Professor Sharf and Professor Misra, who were the best supervisors I could have wished for and who made this research possible in every way. They have taught me how to do proper research, while understanding my limits and pushing me to overcome them little by little. I am grateful for their availability all along this Ph.D., even during their sabbaticals. I appreciate immensely the freedom they gave me to stay next to family for weeks at times, and the possibilities to attend conferences and to gain experience in teaching. It is thanks to their example that I am considering a career in academia. Similarly, I would like to thank all the faculty members whom I collaborated with in the Mechanical Engineering Department at McGill, as well as GAMES: I have enjoyed the diverse, welcoming, and accessible environment, and I cannot believe how much I learned at McGill.

I would like to acknowledge funding received to support this research, in particular the McGill Engineering Doctoral Award, the Werner Graupe International Fellowship in Engineering, and the Zonta International Amelia Earhart Fellowship. For allowing the use of Vortex Dynamics during this study, I would like to thank CM Labs Simulations Inc.; in particular I want to thank Marek Teichmann for proposing the Engage Grant collaboration that led to the work based on Vortex Dynamics. My thanks go also to the support staff at CM Labs, who answered my many questions with competence and much patience. For sharing their knowledge on Vortex, I am grateful to Andreas Enzenhöfer, Albert Peiret, and Sheldon Andrews. Finally, I would like to thank the examiners and the members of the committee for accepting to review this work.

This Thesis would not exist if it weren't for Filippo, who brought me to Montreal in the first place. I am grateful for sharing every success and difficulty of our Ph.D. years and for him being family away from family; among many reasons, I want to thank him for helping me balance work and life, for protecting me during all the "scary" flights we took, and – last but not least – baking the best pizza in Montreal for the last four years.

My thought, of course, goes to my parents, who haven't been afraid of letting me follow my path to the other side of the ocean. They have made me love math and engineering growing up, they have set an example of hard work, and they have encouraged me to give my best in every situation. Even now, they continue to amaze me with their decisions to attend university and take on new jobs in different cities. I am thankful to my little (but huge) brother, who has found his place next to family (at least for now) and is able to

lighten the atmosphere in many situations. To all of them, and to Valeria, thanks for the wonderful holiday in Canada and in the US, and for being there as much as possible when I went home. I wish to thank all my friends and the rest of my family for the precious time spent together in Italy: especially, Alida, Lella, Giulia, all my cousins, aunts and uncles, as well as Filippo's family (especially Lulu, Lollo, Bea, and Enrico, for it is lovely to be "the uncles from Canada"). It is hard to be far away, but it fills my heart to find unchanged relationships with each and everyone of them again and again. To those who can't be there anymore, I am thankful for the many good memories.

Many thanks to Eleonora, Dea, and Evelina for the long talks (of course many of which Ph.D.-related) we have shared; we all are grateful to the Faculty of Engineering for organizing the MEDA event where we met: it turns out that being a girl in Engineering helps to meet new lifelong friends! With them, I would like to thank the community of Italian and non-Italian expats and the adopted Canadians for the uncountable dinners and the many Easters that brought us all closer to home: Agustin, Liam, Sibylle, Margherita, Alice, Alessandro, Matteo, Valentina, Davide, Marie, Jihad, Virginia, and many more. The cold winter days at McGill would have been incredibly much longer without the lunch crew, evolving in the years: Eleonora, Pamela, Leila, Gitsuzo, Albert, Giovanni, Prabakaran, Isabelle, Farnood, Andreas, and others.

Finally, I am extremely thankful to whoever invented volleyball, and to my team at Everton: everyone can testify that training there made me much much happier, and competing with them at Coupe du Quebec was a great experience (too bad we did not get to play against McGill). At Everton, I have found a coach that made me a better player (which is the last thing I would have expected coming to Canada) and many friends from all over the world that shared my passion; in particular I would like to thank Kate, who is the best warm-up mate and is cheering for us to stay forever and ever in Montreal.

Claims of originality

The main contributions of this Thesis are the implementation of a flexible simulator for the deployment and capture phases of a tether-net ADR mission in Vortex Dynamics, and the achievement of novel insight into the dynamics of deployment and capture phases. Original contributions to knowledge are:

- Simulation results of capture of multiple debris, such as launcher upper stages and Envisat, with a system including chaser, main tether, winch, net, and closing mechanisms. Novel features of the implemented simulator are a lumped parameter model of the net augmented with bending stiffness, the capability to reproduce the winching of the main tether, the possibility to include a tether-actuated closing mechanism, and a model for the net based on series of slender rigid bodies and prismatic constraints.
- Novel insight into the dynamics of deployment of tether-nets in space. Expressions for the centroidal velocities at several milestones in the deployment process and their limits are obtained through a novel analytical study; the key parameters that govern the deployment dynamics are formally determined. The effect of tensioning of the main tether on deployment dynamics is also investigated.
- Novel insight into the dynamics of net-based capture of debris in space. The robustness of net-based capture is analyzed, safe scenarios for the capture of rotating debris are identified, and the possibility to modify the capture dynamics through tensioning of the main tether is investigated.
- Evaluation of the effect of modeling choices on the dynamics of the system and on simulation performance. Non-linear continuous compliant models for the normal contact force and micro-slip models for the friction force are integrated in modeling of net-based capture of debris; novel results demonstrating the effect of contact force modeling choices on capture dynamics are presented. Evaluation of the effect of the bending stiffness of the threads of the net during deployment and capture dynamics is also provided.

The simulators, numerical results, graphs, illustrations, and text presented in this Thesis were created by Eleonora Botta. The models and the results were discussed with Inna Sharf and Arun Misra, who also edited the text and provided continuous guidance and suggestions. The idea of the analytical study on deployment dynamics of Section 3.2 and the preliminary derivations belong to Inna Sharf. Marek Teichmann provided the initial simulator in Vortex Dynamics, that included a simple net modeled with the standard lumped-parameter approach; he also provided the dynamical model of the target described in Section 4.6.1. Andreas Enzenhöfer provided code for handling graphics in Vortex Dynamics. Benjamin Thomsen, supervised by Inna Sharf, developed the experimental

setup and carried out the experiments described in Section 2.4.4.3; he also obtained the data from the recordings of the experiments that were used in the figures in that Section.

Large parts of this Thesis have appeared in the following publications:

E.M. Botta, I. Sharf, and A.K. Misra. Energy and Momentum Analysis of the Deployment Dynamics of Nets in Space. *Acta Astronautica*. 140:554-564, 2017. DOI : 10.1016/j.actaastro.2017.09.003. Published online: September 2017.

E.M. Botta, I. Sharf, and A.K. Misra. Contact Dynamics Modeling and Simulation of Tether Nets for Space-Debris Capture. *Journal of Guidance, Control, and Dynamics*. 40(1):110-123, 2017. DOI:10.2514/1.G000677.

E.M. Botta, I. Sharf, M. Teichmann, and A.K. Misra. On the Simulation of Tether-Nets for Space Debris Capture with Vortex Dynamics. *Acta Astronautica*. 123:91-102, 2016. DOI:10.1016/j.actaastro.2016.02.012.

E.M. Botta, I. Sharf, and A.K. Misra. Simulation of Tether-Nets for Capture of Space Debris and Small Asteroids. In *1st IAA Conference on Space Situational Awareness (ICSSA)*, Orlando, FL, November 2017.

E.M. Botta, I. Sharf, and A.K. Misra. Tether-Nets for Active Space Debris Removal: Effect of the Tether on Deployment and Capture Dynamics. In *27th AAS/AIAA Space Flight Mechanics Meeting*, San Antonio, TX, February 2017. AAS 17-387.

E.M. Botta, I. Sharf, and A.K. Misra. Energy and Momentum Considerations in the Deployment Dynamics of Nets for Active Space Debris Removal. In *67th International Astronautical Congress*, Guadalajara, Mexico, September 2016. IAC-16-A6.5.6.

E.M. Botta, I. Sharf, and A.K. Misra. Evaluation of Net Capture of Space Debris in Multiple Mission Scenarios. In *26th AAS/AIAA Space Flight Mechanics Meeting*, Napa, CA, February 2016. AAS 16-254.

E.M. Botta, I. Sharf, M. Teichmann, and A.K. Misra. On the Simulation of Tether-Nets for Space Debris Capture with Vortex Dynamics. In *66th International Astronautical Congress*, Jerusalem, Israel, October 2015. IAC-15-A6.5.6.

E.M. Botta, I. Sharf, and A.K. Misra. On the Modeling and Simulation of Tether-Nets for Space Debris Capture. In *25th AAS/AIAA Space Flight Mechanics Meeting*, Williamsburg, VA, January 2015. AAS 15-260.

Notation

Abbreviations

ADR	Active Debris Removal
ANCF	Absolute Nodal Coordinates Formulation
API	Application Programming Interface
DOF	Degree of Freedom
ESA	European Space Agency
GUI	Graphical User Interface
IOD	In-Orbit Demonstration
LCP	Linear Complementarity Problem
LEO	Low Earth Orbit
ODE	Ordinary Differential Equation
QP	Quadratic Programming
RMSE	Root-Mean-Square Error
TSS	Tethered Satellite System

Symbols

A	Net mouth area.
A_k	Cross-sectional area of k-th thread.
$\mathbf{B}$	Damping coefficients matrix.
E	Young's modulus.
$\mathbf{F}_{ext}$	External force.
$\mathbf{F}_n$	Normal contact force.
$\mathbf{F}_t$	Friction force.
$\mathbf{G}$	Constraint Jacobian.
G	Shear modulus.
I	Area moment of inertia about the in-plane axis of the circular section of a thread.

$\mathbf{I}$	Moments of inertia matrix.
$\mathbf{K}$	Stiffness matrix.
L	Length.
$\mathbf{M}$	Mass matrix.
M	Total mass.
N	Total number of nodes of the net system.
N_s	Number of nodes on a side of the net.
N_T	Number of threads in the net, including the corner threads.
R	Radius of a rigid body.
$\mathbf{T}$	Tension force.
T	Kinetic energy.
V	Potential energy.
W	Work.
$\mathbf{a}$	Absolute acceleration.
$\mathbf{c}$	Coriolis and centrifugal forces.
c_{br}	Bristle damping coefficient.
c_c	Linear contact damping coefficient.
c_k	Damping coefficient of k-th thread.
d_{ch}	Initial distance between net and chaser.
$\mathbf{e}$	Axial direction of a thread.
$\mathbf{f}$	Array of external forces.
$\hat{\mathbf{i}}, \hat{\mathbf{j}}, \hat{\mathbf{k}}$	Inertial reference frame.
$\hat{\mathbf{i}}_\mathbf{b}, \hat{\mathbf{j}}_\mathbf{b}, \hat{\mathbf{k}}_\mathbf{b}$	Body-fixed reference frame.
k_{br}	Bristle stiffness coefficient.
k_c	Contact stiffness coefficient.
k_k	Stiffness coefficient of k-th thread.
l	Current length of a thread.
l_0	Undeformed length of a thread.
m	Mass of elements in the system.
n_{sec}	Number of sections (i.e., rigid bodies) in a cable.
n_t	Number of tethers in the system.
$\mathbf{p}$	Linear momentum.
$\mathbf{q}$	Generalized coordinates.
$\mathbf{r}$	Position in inertial reference frame.
r	Cross-sectional radius of a thread.
t	Time.
t_f	Simulation time.
v_d	Threshold magnitude of relative velocity for sticking-slipping transition.
v_e	Magnitude of ejection velocity.

$\mathbf{v}$	Absolute velocity vector.
$\mathbf{v}_t$	Vector of relative tangential velocity between two contact bodies.
x, y, z	Coordinates in the inertial reference frame.
α_c	Coefficient in relation between restitution coefficient and initial contact velocity.
α_{net}	Initial stowing ratio.
β	Packing coefficient, defining how packed fibers are in a thread.
δ	Contact penetration.
Δt	Simulation time step.
ϵ	Integration tolerance.
ε	Energy term.
θ	Shooting angle.
$\boldsymbol{\lambda}$	Array of Lagrange multipliers.
λ	Non-linear contact damping coefficient.
μ_k	Kinetic friction coefficient.
μ_s	Static friction coefficient.
ν	Poisson's ratio.
ξ	Damping ratio.
ρ	Density.
$\dot{\rho}$	Velocity relative to the center of mass.
$\mathbf{\Phi}$	Array of constraints.
ω_{n1}	First natural frequency.
$\boldsymbol{\omega}$	Angular velocity vector.
$(\cdot)_{CM}$	Of a corner mass.
$(\cdot)_{CT}$	Of a corner thread.
$(\cdot)_T$	Of the target.
$(\cdot)_a$	Axial.
$(\cdot)_{al}$	Aluminum.
$(\cdot)_b$	Bending.
$(\cdot)_{ch}$	Of the chaser.
$(\cdot)_{knot}$	Of a physical knot of the net.
$(\cdot)_f$	Of a fiber.
$(\cdot)_{net}$	Of the net.
$(\cdot)_t$	Of the main tether.
$(\cdot)_w$	Of the winch.
$\|\| \cdot \|\|$	Euclidean norm.
$\lfloor \cdot \rfloor$	Floor function.
$\dot{(\cdot)}$	Time derivative.
$\hat{(\cdot)}$	Unit vector.

Contents

Part I

Introduction

Chapter 1

Introduction

1.1 Background and motivation

A large part of the world population has recently gotten used to technological achievements relying on operation of satellites, such as continuous worldwide telecommunications and the monitoring of weather. Although the presence of these technologies is often taken for granted, operation of spacecraft in the most useful and populated Earth's orbits is jeopardized by space debris. Space debris, that indicates all non-functional objects in orbit around the Earth, is nowadays a threat widely recognized by the scientific community, and collisions have been identified as the leading cause of the increase in the number of space debris in orbit [1]. Impacts between satellites or their components are not as unlikely as one would expect. In fact, the orbits that are actually interesting from the scientific and commercial points of view are limited and concentrated in quite restricted altitude bands; moreover, these orbits often intersect, which creates the conditions for energetic collisions, especially in Low-Earth Orbits (LEOs). A notorious accident happened in 2009, when two intact satellites, Cosmos 2251 (which was inactive) and Iridium 33 (fully operational), crashed, generating thousands of pieces of debris.

Since research has shown that the risk of accidental collisions can be reduced by actively removing a few massive objects per year [2], Active Debris Removal (ADR) is being advocated and studied by several researchers. In order to address the root of the long-term problem, ADR missions should be directed to the disposal of massive objects characterized by high collision probabilities, which embed the potential for the most catastrophic impacts [2, 3]. Existing research has pointed out that the priority high-risk objects in LEO are Envisat (a large ESA-owned satellite for Earth observation, inactive since 2012), as well as multiple stages 2 of Zenit-2 rockets [4]. The sooner ADR missions are performed, the more effective they will be, as long as the technologies are mature [2]. Therefore,

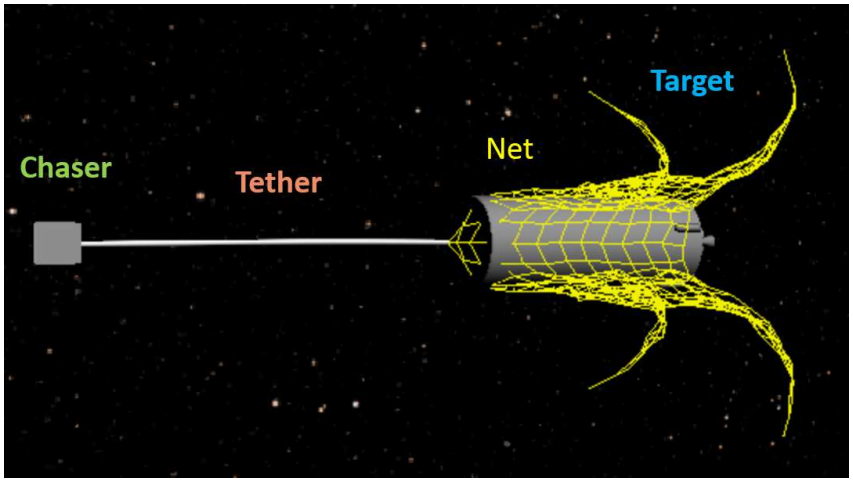

FIGURE 1.1: Illustration of tether-net ADR concept.

multiple methods to actively remove debris have been proposed in the last few years: some of them require establishing a link with the debris, through capture by means of robotic arms [5–7], tether-nets [8–11], or harpoons [12]; some others rely on contactless methods, such as lasers [13] or ion beams [14]. For a comparison of the different methods, the interested reader could refer to the review by Shan et al. [15]. A versatile solution is to employ a servicing spacecraft (called *chaser*) with maneuvering capabilities, that can transfer the *target* to disposal orbit and repeat the process many times. The main difficulties in this case consist in achieving a link with a non-collaborative tumbling target and in controlling the resulting system, composed of chaser, target and capture device.

A promising technology to collect large non-operational spacecraft is tether-nets, flexible devices that are thrown from a chaser towards a target debris, entangle it or close around it, and provide a link to tug it to a disposal orbit. An illustration of the concept is provided in Figure 1.1. This type of capturing device is lightweight and not bulky; compared to the more traditional robotic arms, it is more versatile with respect to the debris' configuration and its tumbling or spinning state, and allows the chaser spacecraft to stay at a safe distance. Comparatively less information on the object to be captured is needed with respect to robotic capture: its mass, size, and rotation axis need to be known, but not its exact inertia properties and rotation rates. The price to pay, in addition to the lower technological readiness of the system, are the non-repeatability of the capture (i.e., the fact that a net can be ejected only once) and risks associated with the possibility to generate more, smaller pieces of debris by rupture of elements such as antennas or solar arrays. Also, the structural flexibility of the net and the complex contact dynamics entail a more complicated dynamical system and require high modeling, simulation and experimentation efforts. Before employing tether-net devices in ADR missions, it is therefore necessary to accurately simulate the dynamics of deployment and capture, in order to gain understanding and insights into the dynamics and control of this complex system in space: this is the topic of the present Thesis.

Deployment and capture dynamics are highly non-linear, due to the inability of the material of the net to withstand compression, the inherently non-linear contact dynamics, the large deformations of the net, and the snapping tensions in the threads. This, together with the complex geometry of the system, entails important modeling issues and high computational cost for deployment dynamics simulation. Particularly complicated is simulation of capture dynamics: collision detection is hard because the target is tumbling and the dimensions of the threads of the net are small; moreover, many points of contact exist simultaneously between net and debris, as well as among different parts of the net; also, contacts can be both sustained and intermittent. Additional issues arise when the reeling of a tether has to be modeled and simulated.

At the time of writing, tether-net capture of debris has never been performed on orbit and, to the author's knowledge, the preferred nominal mission scenario has not been identified. Although some works on the simulation of net-based devices for ADR existed previous to this Ph.D. research, multiple issues remained outstanding. For example, a debate existed on whether the bending stiffness of the threads of the net needed to be modeled, representation of contact dynamics between net and debris was very limited, and the effect of tensioning of the main tether was not evaluated. Many developments occurred concurrently during this Ph.D. research and are reviewed in Section 1.2. Then, the remainder of this Chapter will outline the objectives of this Thesis and the methods put in place to achieve them.

1.2 Literature review

Although much work exists on the dynamics of Tethered Satellite Systems (TSSs), consisting of two satellites connected by a rigid or flexible tether (a concept that has already been employed in space missions), the use of nets has only recently been advocated. Interest in net-based systems to capture space debris is relatively recent and much of the research is being carried out through the support of the European Space Agency (ESA), with the aim of deorbiting the defunct Envisat satellite. The aim of this Section is to describe the state of the art on tether-nets for ADR, including both works existing before this Ph.D. research and developed concurrently. The design of tether-nets for ADR is discussed in Section 1.2.1; simulation of deployment, capture, and post-capture dynamics is the subject of Section 1.2.2; experimentation and demonstration activities are presented in Section 1.2.3. Although the post-capture phase is not simulated in this Thesis, it is important for the success of net-based ADR; this is why a short discussion of related literature is included.

1.2.1 Design of tether-nets for ADR

Although Carroll explored the possibility of capturing space debris by means of thrown-webs and spin-stabilized nets [16], the pioneer work to give credit to tether-net systems to capture and dispose of uncooperative objects was the preliminary study ROGER by Bischof et al. in 2004 [8]. Preliminary system design activities were later performed within ESA's e.Deorbit study [11, 17], as well as by other research groups [18–20]. The envisaged system consists of a small chaser spacecraft that rendez-vous with its debris target through a series of approach and inspection maneuvers; the foreseen distance from the chaser to the target is between 10 and 50 m. From that position, a net would be pulled out of a canister on the chaser by several corner masses, which are ejected towards the debris by a dedicated mechanism. After the envelopment and capture of the target, the chaser can pull it to its disposal orbit by means of a connecting tether and thrusters.

Different net geometries have been proposed, among which are planar [8], pyramidal [19], conical [18], and hemispherical [20]. With the aim of deorbiting large debris, such as the Envisat spacecraft, a 10×10 to 20×20 m^2 plane square net with a mesh length of 20–25 cm was recommended [8]. Zhai and Zhang speculated on a conical net with a diameter and height of 10 m [18]. The number of foreseen corner masses is usually 4 for planar nets [8], and 4 to 8 for 3D nets [21].

In order to contain the target after capture, a closing mechanism might need to be provided in the tether-net system, so that the perimeter of the net is maintained closed during tugging. The first mechanism to be proposed consisted in adding a "cinch cord" along each edge of the net and reeling these cords in by spring-loaded reels placed in the corner masses [10, 11, 19, 22]. A variation of this mechanism was proposed by Zhai and Zhang [18]: tension links between the perimeter of the net and each corner mass were added, so that onset of tension in those links after capture of debris causes them to break and makes the perimeter close. Recently, Sharf and al. [23] have proposed to exploit the tether linking the net to the chaser, by extending it from the center of the net to the net perimeter and by tensioning it in order to maintain closure.

Variations to the tether-net concept have been suggested in recent times. O'Connor and Hayden have hypothesized that a net might be deployed and kept open by inflating a tube attached around its mouth, as well as some spurs [24]. They also proposed a closing mechanism making use of the linking tether to close the mouth section of the net, similarly to what was proposed by Sharf et al. [23]. Other researchers have suggested the use of maneuverable space net systems, in which deployment would be achieved thanks to the autonomous control of several maneuverable units each holding a corner of the net, and - in some cases - its vertex [25, 26]; this would avoid the need to link the chaser to the net with a tether. In the rest of this Thesis, the discussion is limited to the ADR concept in

which a net is deployed by ejecting several corner masses from the chaser, to which the net remains attached thanks to a tether.

1.2.2 Simulation of the dynamics of tether-nets for ADR

With the objective of determining the feasibility of and gaining insight into net-based debris capture and removal, a few simulators for the deployment of nets in space, capture, de-tumbling, and tug of debris to its disposal orbit have been implemented recently. Preliminary simulations of capture were executed at the ESA with the 3D modeling environment Blender, and Bullet physics engine [10]. Another ESA-funded activity carried out at Politecnico di Milano resulted in a MATLAB simulator considering all the phases of a net-based ADR mission [9, 19, 21, 27]. These two research activities have been merged, with the participation of some European industries: a hybrid simulator has been assembled [28]. Concurrently, another collaboration with the ESA resulted in the creation of a simulator for deployment and capture by Golebiowski et al. [29, 30]. Independent simulation works on deployment were performed both before and during this research by Chen and Yang [31], Liu et al. [32, 33], and Shan et al. [34].

1.2.2.1 Deployment

In recent years, a number of numerical studies of the deployment dynamics of tether-nets in space have been performed by different research groups. The shared objective of these research efforts is to gain insight into the deployment process in microgravity and vacuum conditions, as it needs to be fully understood before these systems can be used in actual missions.

In the vast majority of the studies dedicated to the deployment dynamics of nets in space, the net is modeled with the standard lumped-parameter approach [9, 10, 19, 21, 31, 32, 34]: the mass is lumped at the nodes of the net, which are interconnected by massless springs and dashpots that represent the stiffness and damping properties of the threads. Some other simulators were based on an Absolute Nodal Coordinates Formulation (ANCF) [33, 34], which allows to describe the flexibility between two nodes of the net by using information only on the absolute positions of the two nodes and their gradients. Very recently, Shan et al. [34] have found good agreement in results of deployment simulations with the standard lumped-parameter method and with a model based on an ANCF cable element considering only the deformation along the longitudinal direction (which was developed by Gerstmayr and Shabana [35]); this confirms that, in the absence of bending stiffness, representation of the shape of the threads of the net during deployment is not necessary. A model based on Cosserat rods was implemented by Golebiowski et al., who

therefore considered bending stiffness of the threads of the net [29, 30]. In the literature, however, no quantitative evaluation of reasons to represent or neglect the bending stiffness of the threads of the net was found.

For characterizing the net deployment, several authors have proposed performance criteria and have analyzed, by means of simulations, how the net geometry, its mass properties, and the deployment initial conditions influence the dynamics. Bombelli aimed at achieving a deployment that maximizes the volume of a 3D net, to ease the capture process [19]. The effectiveness of the deployment of a planar net was first analyzed by Chen and Yang [31] and Liu et al. [32], and sensitivity analyses were performed by Salvi [21] and Shan et al. [34], in the absence of a tether linking the chaser and the net. The effect of tensioning of the tether on deployment dynamics was not considered in the literature.

1.2.2.2 Capture

Simulation of net-based capture is considerably more complicated than simulation of deployment, because the representation of collisions between the net and a piece of debris, as well as among the threads of the net, is a complex and computationally expensive problem. Before this research work, the study of contact dynamics in the simulation of tether-net capture was very limited: only two groups had tackled the problem of capture, and they had done so to a very limited extent. Advancements have occurred in the years of this research, but the number of studies on the subject remains small.

In work by Wormnes et al., contact is dealt with by imposing linearized velocity constraints for non-penetration, and by evaluating the friction force as independent of the normal force [10]: even though this approach is computationally affordable, it comes at a cost of lower physical relevance. With this model, the authors simulated capture of different large debris for various relative attitudes, positions, velocities, and for multiple net materials, with and without closing mechanisms: the modeled closing mechanism consisted of additional threads among the corner masses [10].

A similar closing mechanism was used by Bombelli [19] and Benvenuto et al. [27, 36, 37]. For simulating capture dynamics, Bombelli assumed inelastic collisions between the net and the target: a node impacting the target acquired the same motion as the center of mass of the debris [19]. Benvenuto et al. chose a compliant approach, based on a linear normal contact force model and Coulomb's friction force [27, 36]. In the wake of work performed within this Thesis, Benvenuto et al. improved the contact modeling in their simulator by using a non-linear continuous compliant model and a regularized version of Coulomb's friction model [37]. Collision detection in the latest version of their simulator was performed exploiting Bullet physics engine and allowed simulation of capture of a mock-up of Envisat [38].

Recently, Golebiowski et al. have assembled another simulator for capture, that also makes use of collision detection capabilities of Bullet physics engine, of an impulsive model for the normal contact force, and of Coulomb's law for friction [30]. Simulations of capture of a mock-up of Envisat were presented [30].

Zhai at al. investigated a different issue related to capture with tether-nets, i.e., the effect of orbital dynamics on the precision of capture [39]: they simplified the problem by modeling both the net and the target as point masses and by assuming that they should be in the same position at capture. Mankala and Agrawal focused on the effect on the tether of impact between a net (or harpoon) and the target [40]; however, once again, the net (or harpoon) was modeled as a point mass.

1.2.2.3 Post-capture: de-tumbling and removal

The dynamics of TSS (consisting of two point masses or rigid bodies connected by a tether and traveling in different orbits in space) has been extensively studied since the 1960s. Surveys of the scientific work in this area are found in [41] and [42]; recent developments are treated in [43] and [44].

In the framework of ADR, tethers can provide a link between the chaser spacecraft and the target debris, once the debris has been captured, for example, by means of a net or of a harpoon. Previous works on mechanical tethers have dealt primarily with the disposal phase of the mission, analyzing the dynamics of the system composed of chaser, tether, and debris during the tug. Among others, the dynamics of tug of a large space debris with a tether was studied by Aslanov and Yudintsev [45, 46], who demonstrated that safe transportation of debris can be achieved through tether tensioning and chaser-tether-target alignment; Aslanov recently explored the chaotic behaviour of such a system during tow [47]. Jasper and Shaub analyzed discrete input-shaping techniques for modulating the de-orbit burn and reducing the risk of collisions between chaser and target [48], while Sabatini et al. challenged the effectiveness of input shaping when the tether is initially slack and proposed different solutions to eliminate this problematic condition [49]. Linskens and Mooij used a sliding-mode controller to stabilize the chaser-tether-target system in the presence of perturbations [50]. Cleary and O'Connor proposed using wave-based control as a robust and generic method for maneuvering the chaser while maintaining control of the target at the end of the tether [51]; the same control was employed by Bellanca et al. [52]. Among the works on tether-nets, several have also dealt with the removal phase to some extent [10, 27, 37].

Recently, the de-tumbling of space debris, which is one of the salient issues of ADR, has also been tackled. O'Connor and Hayden have shown that wave-based control can

de-tumble the target while allowing to maneuver the entire system [24]. Hovell and Ulrich have advocated that attitude stabilization of captured debris can be achieved using multiple tethers [53]. The same concept has been investigated by Benvenuto et al. [54] and Qi et al. [55].

1.2.3 Experimental studies and demonstration missions

On-ground tests were performed by Lavagna et al. [9, 22] and Sharf et al. [23] both as demonstration tools and to validate their simulators. Parabolic flight experiments of capture of a satellite mock-up by means of a net have also been carried out recently as part of efforts to validate simulators of the deployment and capture phases of tether-net ADR by Golebiowski et al. [30] and Medina et al. [38]. Further parabolic flight experiments targeted validation of tether control strategies during the removal phase [52].

However, the environment in space remains different from the conditions experienced on-board parabolic flights; therefore, In-Orbit Demonstration (IOD) missions are necessary. Design activities in this direction have been performed by Forshaw et al. [56] and Pirat et al. [57]. With the aim of containing the cost and risks associated with these IOD missions, the idea of both groups is to employ controlled cubesats both as chaser and target: the net would be stored in the chaser cubesat; once the target cubesat is released, the net would be shot towards it [56, 57].

1.3 Objectives and methodology

The overarching objectives of this Thesis are:

1. to simulate the full scenario of tether-net capture of realistic space debris;
2. to gain insight into the dynamics of deployment of tether-nets in space;
3. to gain insight into the dynamics of net-based capture of debris in space;
4. to evaluate the effect of modeling choices on the dynamics of the system and on simulation performance.

The objectives of this Thesis are met primarily through numerical simulation, but some analytical derivations are also employed. A MATLAB-based and a Vortex-Dynamics[1]-based simulators were implemented and have different but also overlapping capabilities (see Figure 1.2). The MATLAB-based simulator was created from scratch, therefore the

[1]Vortex Dynamics is marketed by the company CM Labs Simulations Inc. The simulator implemented for this research is based on an *Essentials* free edition, that is available for research purposes. www.cm-labs.com/vortex-studio/vortex-studio-essentials.

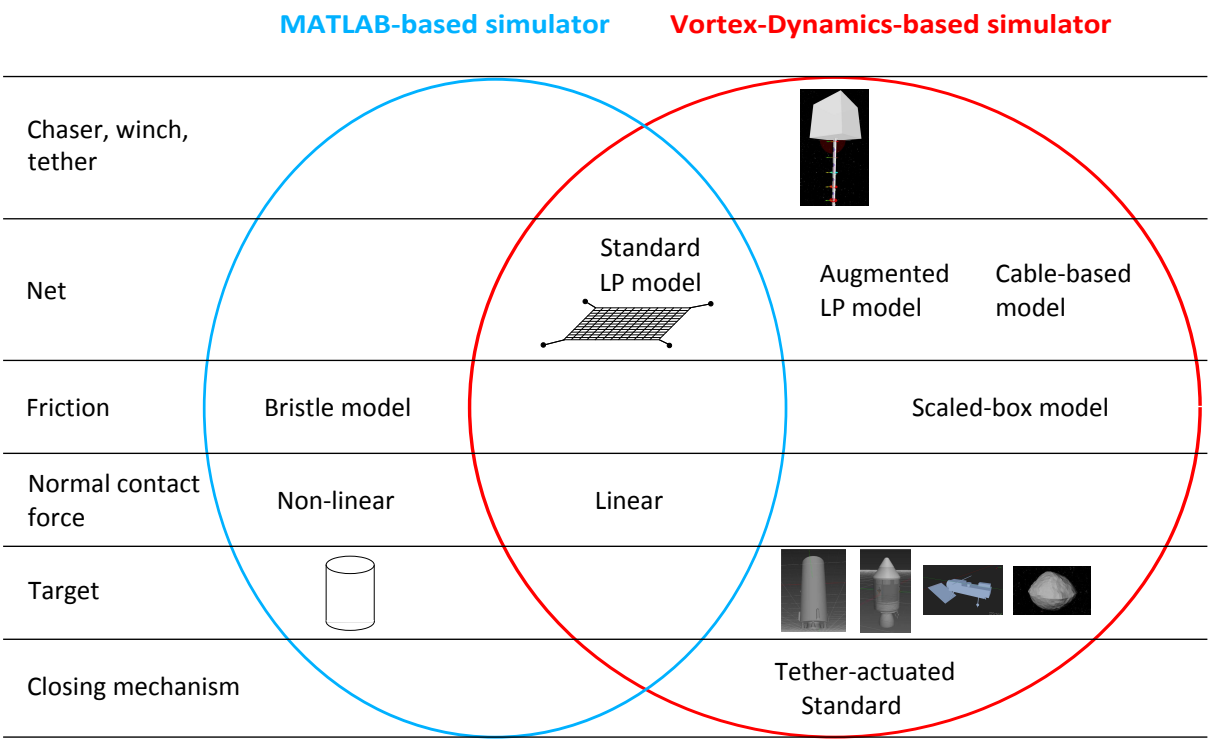

FIGURE 1.2: Capabilities of MATLAB- and Vortex-Dynamics-based simulators.

model of the net and of contact dynamics could be implemented ensuring that every detail is represented as desired; however, MATLAB is not optimized for such complex simulations, involving many bodies and collisions. This is why another simulator was implemented in Vortex Dynamics, a powerful multibody dynamics simulation platform designed for real-time simulation of complex systems, and providing built-in graphical visualization. Before this work, Vortex Dynamics had never been employed to model tether-nets, and using it was not straightforward; in fact, with Vortex Dynamics being a commercial tool, some details of the modeling and implementation are undisclosed, and therefore creation of benchmark tests (e.g., on the dynamics of contacts and of cables) was necessary. As a result of the modeling, implementation, and validation efforts performed for this Thesis, the Vortex-Dynamics-based simulator is representative of the whole system (see Figure 1.2).

The architecture of the simulator in Vortex Dynamics is shown schematically in Figure 1.3. Input text files are employed to let the user define the simulation parameters. Also, geometric and inertial properties of different target objects are defined off-line using the Graphical User Interface (GUI) of Vortex Editor. At the beginning of the simulation, the input parameters are read, and the desired target object is loaded and given the initial conditions specified in the input files. The rest of the components of the system (chaser, winch, tether, net, corner masses, closing mechanism) as well as the contact dynamics parameters are defined programmatically in a C++ Application Programming Interface (API) and according to the input simulation parameters. The dynamics equations are

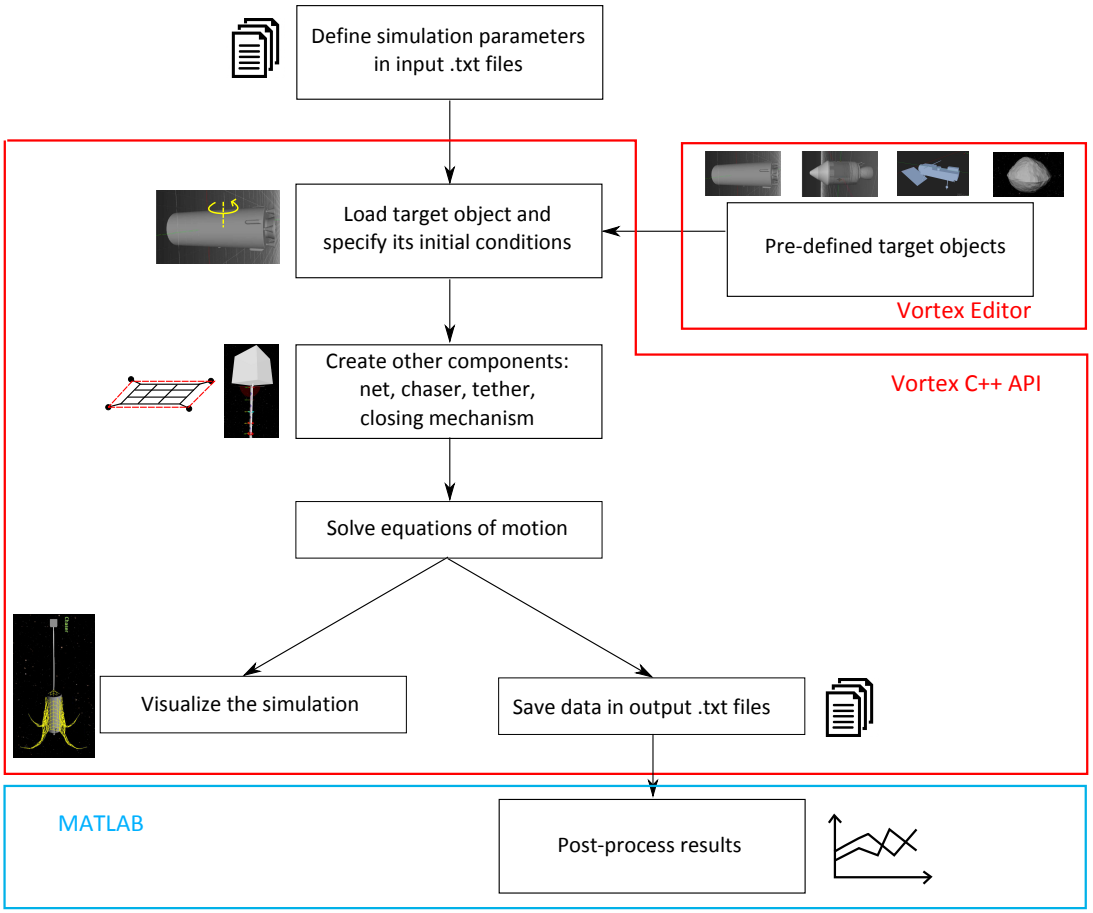

FIGURE 1.3: Architecture of Vortex-Dynamics-based simulator.

then integrated from the initial conditions, and the simulation can be visualized at run-time thanks to a graphics module. At the same time, data on the simulation (e.g., positions and velocities of all the nodes of the net) are saved in output text files for post-processing the results; the post-processing of results in this Thesis was performed using MATLAB.

The modular architecture of the C++ implementation of the Vortex-Dynamics-based simulator grants the user the flexibility to define differently scaled nets with a square mesh of any size, with or without corner masses, subject to diverse initial conditions and gravitational fields. Different models of the net (with and without representation of the bending stiffness of the threads) are also available in the implemented simulator. The user can decide whether to include in the simulation a chaser and a tether (with or without winch) and prescribe controls for the winching of the tether. The presence, type, and tumbling motion of the target can also be specified. The possibility to perform sensitivity studies on the dynamics of such a complicated system is enabled by the computational efficiency of the multibody simulation tool.

The objectives of this Thesis and the methods employed to achieve them are described in Table 1.1; references to the Sections addressing each objective are also provided. From

Objectives		MATLAB-based simulator	Vortex-Dynamics-based simulator	Analytical derivations
1.	**Simulate the full scenario of tether-net capture of realistic space debris.**			
	Model the net.	Chapter 2		
	Model chaser, main tether, and winch.		Section 3.4.1	
	Model contact dynamics.	Section 4.3	Section 4.5	
	Model targets.		Sections 4.6.1, 5.1.1, 5.4.1, 5.5	
	Model closing mechanisms.		Sections 5.2.1, 5.3.1	
	Simulate capture of realistic debris.		Chapter 5	
2.	**Gain insight into the dynamics of deployment of tether-nets in space.**			
	Understand the mechanisms of deployment.	Section 2.4.3		Section 3.2
	Understand the effect of giving initial velocity to the whole net.	Section 3.3.1		
	Identify key parameters leading the deployment dynamics.		Section 3.3.2	Section 3.2
	Understand the effect of tension in the main tether on deployment dynamics.	Section 3.4		
3.	**Gain insight into the dynamics of net-based capture of debris in space.**			
	Verify the robustness of net-based capture.		Section 4.7	
	Analyze the effect of tension in the tether on the capture dynamics.		Section 5.1	
	Study capture of realistic debris with different closing mechanisms.		Sections 5.2, 5.3.2	
	Identify preferred scenarios for capture.		Section 5.3.3	
4.	**Evaluate the effect of modeling choices on the dynamics.**			
	Analyze the effect of modeling the bending stiffness of the net threads on deployment dynamics.		Section 3.1	
	Analyze the effect of modeling the bending stiffness of the net threads on capture dynamics.		Section 4.6	
	Analyze the effect of contact dynamics modeling on capture dynamics.	Section 4.4		
	Analyze the limitations of the lumped-parameter modeling of the net.		Section 5.4	

TABLE 1.1: Objectives of this Thesis and methods employed to achieve them.

this table, it is clear that most of the objectives are met with the Vortex-Dynamics-based simulator, that is representative of the main components of the system, flexible, and efficient; however, the MATLAB-based simulator is useful for some of the studies, in addition to allowing validation the Vortex-Dynamics-based simulator. Mathematical analysis is employed to understand the mechanisms of deployment and to identify key parameters affecting the deployment dynamics.

1.4 Outline of the Thesis

This Thesis is organized in four parts: Introduction (Part I), Deployment dynamics (Part II), Capture dynamics (Part III), and Conclusions (Part IV).

In Part I, which is brought to a conclusion by this Section, the space debris problem, the use of tether-nets as an ADR solution, and its challenges were introduced. The literature on the design, simulation, and experimentation of tether-nets for ADR was reviewed. Finally, the objectives of this Thesis and the methodology employed to achieve them were described.

Part II deals with the deployment dynamics of nets in space. In Chapter 2, the modeling approach and the numerical simulators for the deployment dynamics are presented. The results of deployment simulations are shown, and the simulators are cross-verified and validated against experiments. Chapter 3 proposes analyses of several aspects linked to the deployment of nets in space: the effect of representing the bending stiffness of the threads of the net, the identification of key parameters that lead the deployment dynamics, and the effect of the tensioning of the main tether on the deployment dynamics.

The topic of Part III is the dynamics of net-based space debris capture. A large part of Chapter 4 is dedicated to the modeling of contact dynamics in such a complex scenario, and to the effect of the contact modeling choices on the simulation of capture dynamics. The issues of the effect of bending stiffness on the capture dynamics and of the robustness of net based capture are also investigated, and the need for a closing mechanism is observed. In Chapter 5, a closing mechanism based on tensioning of the main tether is proposed, and simulation of capture of realistic space debris with the tether-net system is shown. An alternative closing solution, independent of the winching of the main tether, is modeled and allows to identify preferred scenarios for capture. Limitations of the lumped-parameter model for the net are also recognized, and a cable-based model is proposed to overcome them. Finally, the possibility to simulate capture of different targets, including small asteroids, is also demonstrated.

Part IV, composed of Chapter 6 only, offers a discussion of the achievements of this dissertation research and suggestions for future activities.

Part II

Deployment dynamics

Chapter 2

Deployment dynamics modeling and simulation

The success of net-based capture of space debris depends on the correct deployment of the net in space. This Chapter presents the modeling of the net system and the numerical simulation of its deployment dynamics. The modeling approach is explained in Sections 2.1 and 2.2, and criteria to describe the quality of deployment are identified in Section 2.3. Section 2.4 deals with the simulation of deployment: the numerical tools at hand are presented and verified, and the results of a deployment simulation are discussed.

2.1 Modeling of the net

2.1.1 Net geometry and configuration

The net usually envisaged for capturing large space debris, such as Envisat, is planar, with four corner masses attached to the corners via four corner threads. Its side length is denoted by L_{net} and its undeformed mesh length by $l_{net,0}$. An illustration of the geometry of the net is provided in Figure 2.1 for $N_s = 6$, where N_s is the number of nodes on a side of the net. Paramount to the simulation of the dynamics of the net is the representation of its geometry in the software environment. The nodes and threads of the net are numbered and a connectivity table is created in an automated way for a square net of any size with any square mesh and with four corner masses.

Nodes such as 37, 38, 39, 40 in Figure 2.1 are called *corner masses* and threads such as 61, 62, 63, 64 in Figure 2.1 are called *corner threads*. The *net proper* is also defined as the set of N_s^2 nodes of the net, corner masses excluded; this definition will be used extensively in Section 3.2. The net proper is delimited by the square perimeter of the net, called

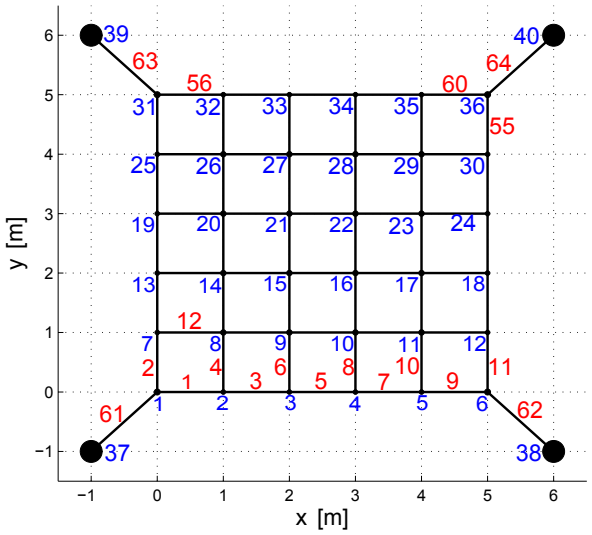

FIGURE 2.1: Net configuration for $N_s = 6$, with nodes and threads numbering.

mouth section. The total number of nodes, including the corner masses, is $N = N_s^2 + 4$. The number of internal threads of the net is $2N_s(N_s-1)$ and the total number of threads, including the corner threads, is $N_T = 2N_s(N_s - 1) + 4$. In the example in Figure 2.1, $N_s^2 = 36$, $N = 40$, and $N_T = 64$.

In the automated creation of the connectivity table, a link is added and numbered with sequential k when, for all $i = 1, ..., N_s^2$ and for all $j = i+1, ..., N_s^2$, the following conditions are verified:

$$(j = i + 1 \wedge i \bmod N_s \neq 0) \vee (j = i + N_s) \tag{2.1}$$

Once all the inner threads are defined the four corner threads are appended to the table. As an example and as reference for understanding the results in the rest of this Thesis, part of the connectivity table for the net in Figure 2.1 is reported in Table 2.1.

Link k	1	2	3	4	5	...	60	61	62	63	64
Node i	1	1	2	2	3	...	35	1	6	31	36
Node j	2	7	3	8	4	...	36	37	38	39	40

TABLE 2.1: Part of connectivity table for net in Figure 2.1.

2.1.2 Standard lumped-parameter model

One of the ways to model the net and account for its flexibility and elasticity is to take a lumped-parameter approach, which offers a good compromise between accuracy and computational efficiency. Much work on the application of this modeling technique to

flexible nets was carried out for fishing nets [58, 59]. Although the loads acting on an object immersed in water are obviously different from those acting on a body in space, the models developed for inertia and stiffness properties of nets remain applicable in either case. The lumped-parameter model has been extensively used in the simulation of the dynamics of nets, because of its simplicity of implementation. In this model the physical knots of the net and the four corner masses are represented by point masses, and the threads are represented by massless springs and dampers in parallel; standard lumped-parameter models consider only stiffness and damping properties in the direction of the axis of each thread.

The mass lumped in the i-th node is:

$$m_i = \begin{cases} \sum_{k \in K_i} m_k/2 + m_{knot} & \text{if} \quad i = 1, ..., N_s^2 \\ \sum_{k \in K_i} m_k/2 + m_{CM} & \text{if} \quad i = N_s^2 + 1, ..., N_s^2 + 4 \end{cases} \tag{2.2}$$

In equation (2.2), $m_k = \rho_{net} \pi r_k^2 l_{k,0}$ is the mass of each of the threads adjacent to the i-th node (said to belong to the set K_i), with ρ_{net} the net material density, r_k the k-th thread's radius, and $l_{k,0}$ its unstretched length; in general the radius and the length of the threads of the net proper r_{net} and $l_{net,0}$ are different from those of the corner threads r_{CT} and $l_{CT,0}$. The mass of the corner mass attached to each corner thread is indicated with m_{CM}; the mass of a physical knot of the net is $m_{knot} = \rho_{net} \pi r_{net}^2 l_{knot}$, with l_{knot} the length of thread that creates a physical knot in the net. It may be noted that the different sizes of the nodes in Figure 2.1 are indicative of the different node masses.

The stiffness properties of the net are modeled by representing each physical thread of the net with a massless spring; the energy dissipation is modeled by introducing a dashpot in parallel to each spring. However, the nature of the material of the net (unable to withstand compression) suggests that a force within a thread should exist only when that thread is elongated and in tension. Therefore, the tension in each thread $\mathbf{T}_k$ for $k = 1, ..., N_T$ is defined using a non-linearization of the well-known Kelvin-Voigt model:

$$\mathbf{T}_k = \begin{cases} T_k \mathbf{e}_k & \text{if } (l_k > l_{k,0}) \wedge (T_k > 0) \\ \mathbf{0} & \text{if } (l_k \leq l_{k,0}) \vee (T_k \leq 0) \end{cases} \tag{2.3}$$

where $T_k = k_{a,k}(l_k - l_{k,0}) + c_{a,k} v_{r,k}$, with $k_{a,k} = (E_{net} \pi r_k^2)/l_{k,0}$ and $c_{a,k} = 2\xi_a k_{a,k}/\omega_{n1,a}$ the stiffness and damping coefficients[1]. In these expressions, the Young's modulus of the net material is indicated with E_{net}, ξ_a is the chosen damping ratio, and $\omega_{n1,a}$ is the first natural frequency of the net. The axial unit vector of the k-th thread $\mathbf{e}_k$, its length l_k,

[1] In absence of precise knowledge of the dissipation properties of the threads of the net, a linear model is used to approximate the dissipation through friction among the fibers composing each thread.

and the projection of the relative velocity of the thread end nodes in the thread axial direction $v_{r,k}$ depend on the current configuration of the net and can be found as:

$$\mathbf{e}_k = (\mathbf{r}_j - \mathbf{r}_i)/||\mathbf{r}_j - \mathbf{r}_i|| \tag{2.4}$$

$$l_k = ||\mathbf{r}_j - \mathbf{r}_i|| \tag{2.5}$$

$$v_{r,k} = (\mathbf{v}_j - \mathbf{v}_i) \cdot \mathbf{e}_k \tag{2.6}$$

where $\mathbf{r}$ and $\mathbf{v}$ indicate the inertial position and velocity of nodes at time t, and the i-th and j-th indexes for the k-th thread are defined in the connectivity table (such as Table 2.1). In Figure 2.1, the inertial reference frame used in the simulations is shown: in the derivation of the equations of motion, it is assumed that the local orbital reference frame is the inertial reference frame.

2.2 Equations of motion and initial conditions

The equations of motion of the system are obtained by writing Newton's second law for each of the N lumped masses, subject to external forces and tensions of the threads. For the i-th lumped mass, for $i = 1, ..., N$:

$$m_i \mathbf{a}_i = \sum_{k \in K_i} (\pm \mathbf{T}_k) + \sum_{s=1}^{S_i} \mathbf{F}_{ext,s} \tag{2.7}$$

where $\mathbf{a}_i$ is the absolute acceleration of the i-th node, $\mathbf{T}_k$ is each of the tension forces in the threads adjacent to the i-th node (belonging to the set K_i), and $\mathbf{F}_{ext,s}$ is each of the S_i external forces on the i-th mass.

External forces might include gravitational forces, when present, applied forces (for example as produced by a closing mechanism), and contact forces. In this Thesis, the only forces external to the net that were considered are contact forces, closing forces, and forces due to attachments to the main tether; no environmental forces were included, which is justified by their small effect during the short deployment and capture phases. In equation (2.7), it should also be noted that the tension in the k-th thread is defined as acting in the direction of the k-th thread $\mathbf{e}_k$, i.e., from the i-th to the j-th node in the connectivity table as per equation (2.3), so it is taken with a positive sign in equation (2.7) for node i; the corresponding tension on the j-th mass will be taken with a negative sign in the j-th equation.

In the considered deployment scenario, the net is in a stowed configuration before ejection: this is represented by setting initial conditions to the nodes such that the net is stowed in a square of side length $\alpha_{net} L_{net}$ in the inertial x-y plane indicated in Figure 2.1, with

$0 < \alpha_{net} \leq 1$ the stowing ratio (e.g., the nodes of the net proper are placed at a relative distance of $\alpha_{net} l_{net,0}$). Although this choice of initial conditions does not represent a realistic folding pattern, it allows to have some deployment dynamics so that the debris can be captured.

The net is then deployed with the initial velocities defined in the inertial reference frame as follows:

$$\begin{aligned}
\mathbf{v}_{j,0} &= [\ 0 \quad 0 \quad -v_{e,net}\ ]^T \qquad j = 1, ..., N_s^2 \\
\mathbf{v}_{N_s^2+1,0} &= [\ -v_{x,0} \quad -v_{y,0} \quad -v_{z,0}\ ]^T \\
\mathbf{v}_{N_s^2+2,0} &= [\ v_{x,0} \quad -v_{y,0} \quad -v_{z,0}\ ]^T \\
\mathbf{v}_{N_s^2+3,0} &= [\ -v_{x,0} \quad v_{y,0} \quad -v_{z,0}\ ]^T \\
\mathbf{v}_{N_s^2+4,0} &= [\ v_{x,0} \quad v_{y,0} \quad -v_{z,0}\ ]^T
\end{aligned} \tag{2.8}$$

where the x- and y-axes are directed as shown in Figure 2.1, and the z-axis completes the right-handed orthogonal triad. In this Thesis, $v_{x,0} = v_{y,0}$ is chosen for maintaining central symmetry during the deployment (for ADR mission purposes); as a result, the center of mass of the net will always have a velocity in the direction of the central axis of symmetry, herein called *direction of deployment*, parallel to the z-axis. The components of the initial velocity vectors are computed as $v_{x,0} = v_{y,0} = v_e \sin\theta/\sqrt{2}$ and $v_{z,0} = v_e \cos\theta$, θ being the *shooting angle*, i.e. the angle between the initial velocity vector and the direction of deployment, and v_e the magnitude of the ejection velocity of the corner masses. The magnitude of the ejection velocity of the net proper is indicated with $v_{e,net}$.

2.3 Criteria for quality of deployment

Before presenting the results of numerical simulations, some criteria to describe the quality of the deployment of a net are defined: these criteria will be used in the discussion of the results. Also, when comparing the dynamics of nets during the deployment phase, several shape-related quantities will be used. In fact, due to the high number of nodes comprising the nets, comparison of positions and velocities of individual nodes or of tensions in individual threads is not meaningful, and aggregate measures to describe the overall dynamics of the net have to be established. Multiple options were identified, among which are:

(i) *Shape of the mouth section*: the shape of the polygon created by projecting the nodes of the mouth section of the net on the x-y plane.

(ii) *Mouth area*: the area of this polygon.

(iii) *Net height*: the difference between the z-coordinate of the innermost node of the net (or the average of the z-coordinates of the four innermost nodes of the net if

N_s is even) and the average z-coordinate of the four corner nodes of the net:

$$h(t) = \left| z_i(t) - \frac{1}{4}\left[z_p(t) + z_q(t) + z_r(t) + z_s(t)\right] \right| \tag{2.9}$$

with

$$z_i(t) = \begin{cases} z_c(t) & \text{if } N_s \text{ is odd} \\ \frac{1}{4}\left[z_d(t) + z_e(t) + z_c(t) + z_f(t)\right] & \text{if } N_s \text{ is even} \end{cases} \tag{2.10}$$

and where the indexes are $p = 1$, $q = N_s$, $r = N_s^2 - N_s + 1$, $s = N_s^2$, $c = N_s(N_s+1)/2$, $d = N_s(N_s-1)/2$, $e = d+1$, $f = c+1$.

Quality criteria for the deployment are defined considering that the aim of the deployment phase is to have a net opened in such a way that capture can happen successfully. As one can imagine, this is easiest if deployment is as good as possible and lasts for a sufficient amount of time. Also important for the safety of the mission is that capture happens sufficiently far from the chaser spacecraft. As a result of the previous considerations, the following criteria for the quality of deployment are used in this Thesis:

(i) *Maximum achievable deployment* with respect to the nominal mouth area: the specific measure employed in this study is A_{max}/L_{net}^2, i.e., the maximum ratio between the mouth area achieved during deployment and the nominal mouth area (that is the surface of the net in a flat, fully deployed configuration).

(ii) *Distance traveled* by the net when the maximum deployment is achieved: the measure employed in this Thesis is the distance traveled by the center of mass of the net proper when the maximum mouth area is reached.

(iii) *Effective period*, i.e., the period for which the net remains sufficiently open for successful capture. The exact measure used here is the time for which the mouth area is larger than 80% of its nominal value, i.e., $A > 0.8L_{net}^2$.

Finally, to achieve quantitative evaluation of the discrepancy between two large sets of data generated during simulations of net deployment, the Root-Mean-Square Error (RMSE) between positions and velocities of identical nodes will be used. A representative quantity of the positional accuracy is the RMSE between identical nodes positions[2]. For the position of the j-th node, for example, the accuracy measure is computed as:

$$RMSE_{j,pos} = \left\{ \frac{1}{n_t} \sum_{k=1}^{n_t} \left[\left(x_{j,A}^{(k)} - x_{j,B}^{(k)}\right)^2 + \left(y_{j,A}^{(k)} - y_{j,B}^{(k)}\right)^2 + \left(z_{j,A}^{(k)} - z_{j,B}^{(k)}\right)^2 \right] \right\}^{\frac{1}{2}} \tag{2.11}$$

[2]This a 3D extension of what is also used as US National Standard for Spatial Data Accuracy. Subcommittee for Base Cartographic Data, Federal Geographic Data Committee, *Geospatial Positioning Accuracy Standards - Part 3: National Standard for Spatial Data Accuracy*, 1998.

In this expression, n_t is the number of time steps, apex (k) indicates the k-th time step, and A and B refer to two data sets. An analogous quantity, called $RMSE_{j,vel}$, is computed for evaluating the accuracy at the velocity level for the j-th node; equation (2.11) applies when x, y, z are substituted with v_x, v_y, v_z. The variation along time of the position and velocity RMSEs, averaged over the N nodes, is also of interest. At the position level, this quantity at time t is computed as:

$$RMSE_{pos}(t) = \left\{ \frac{1}{N} \sum_{j=1}^{N} \left[\Big(x_{j,A}(t) - x_{j,B}(t) \Big)^2 + \right. \right. \\ \left. \left. + \Big(y_{j,A}(t) - y_{j,B}(t) \Big)^2 + \Big(z_{j,A}(t) - z_{j,B}(t) \Big)^2 \right] \right\}^{\frac{1}{2}} \tag{2.12}$$

2.4 Numerical simulators for the net deployment dynamics

The model for the net presented in Section 2.1 was implemented in two simulators, the first based on MATLAB, and the second based on Vortex Dynamics, whose main characteristics were introduced in Section 1.3. The rest of this Chapter delivers some more information on the implementation of the standard lumped-parameter model in the two simulators, shows the results of a deployment simulation, and presents the verification and validation activities performed on the simulators.

2.4.1 MATLAB simulator

For simulation purposes, the set of N vectorial Ordinary Differential Equations (ODEs) described by equation (2.7) is transformed into state-space form and solved numerically for the positions and velocities of the nodes. Let us call $\mathbf{r} \in \mathbb{R}^{3N}$ and $\mathbf{v} \in \mathbb{R}^{3N}$ the arrays of the position and velocities vectors of the nodes of the net and corner masses:

$$\mathbf{r} = \begin{bmatrix} \mathbf{r}_1^T & \dots & \mathbf{r}_N^T \end{bmatrix}^T \tag{2.13}$$

$$\mathbf{v} = \begin{bmatrix} \mathbf{v}_1^T & \dots & \mathbf{v}_N^T \end{bmatrix}^T \tag{2.14}$$

Then, the state vector $\mathbf{s} \in \mathbb{R}^{6N}$ is $\mathbf{s} = \begin{bmatrix} \mathbf{r}^T & \mathbf{v}^T \end{bmatrix}^T$, and its derivative is:

$$\dot{\mathbf{s}} = \begin{bmatrix} \mathbf{v} \\ \mathbf{M}^{-1}(\mathbf{T} + \mathbf{F}_{ext}) \end{bmatrix} \tag{2.15}$$

where $\mathbf{M}$ is the mass matrix of the system ($\dim[\mathbf{M}] = 3N \times 3N$), $\mathbf{T} \in \mathbb{R}^{3N}$ is the array of tension force resultants, and $\mathbf{F}_{ext} \in \mathbb{R}^{3N}$ is the array of external force resultants:

$$\mathbf{M} = \begin{bmatrix} m_1\mathbf{1} & \dots & \mathbf{0} \\ \vdots & \ddots & \vdots \\ \mathbf{0} & \dots & m_N\mathbf{1} \end{bmatrix} \tag{2.16}$$

$$\mathbf{T} = \begin{bmatrix} \mathbf{T}_1^T & \dots & \mathbf{T}_N^T \end{bmatrix}^T = \begin{bmatrix} \sum_{k\in K_1} (\pm\mathbf{T}_k)^T & \dots & \sum_{k\in K_N} (\pm\mathbf{T}_k)^T \end{bmatrix}^T \tag{2.17}$$

$$\mathbf{F}_{ext} = \begin{bmatrix} \mathbf{F}_{ext,1}^T & \dots & \mathbf{F}_{ext,N}^T \end{bmatrix}^T = \begin{bmatrix} \sum_{s=1}^{S_1} \mathbf{F}_{ext,s}^T & \dots & \sum_{s=1}^{S_N} \mathbf{F}_{ext,s}^T \end{bmatrix}^T \tag{2.18}$$

In these expressions, $\mathbf{1}$ is the 3×3 identity matrix, $\mathbf{0}$ is a 3×3 matrix of zeros, m_i for $i = 1, ..., N$ is found as per equation (2.2), $\mathbf{T}_k$ is found as per equation (2.3), and K_i and S_i for $i = 1, ..., N$ were defined for equation (2.7). In MATLAB, numerical integration is performed by exploiting the software's built-in Runge-Kutta ODE integration schemes.

2.4.2 Vortex Dynamics simulator

Since Vortex Dynamics is a commercial multibody dynamics simulation tool, the system is modeled by specifying rigid bodies, called *parts*, and linking them with kinematic constraints. A lumped-parameter model of the net under study was assembled in Vortex Dynamics by approximating the nodes of the net and the four corner masses with small spherical parts and by modeling the threads by means of position-based constraints (called *distance joints*) that force the attachment points of two parts to be within a given distance. The radius of each spherical rigid body is estimated knowing the mass of the corresponding node and its density (ρ_{net} for the net and ρ_{CM} for the corner masses). Visualization of the model implemented in Vortex Dynamics is provided by Figure 2.2: both the inertia properties and the constraints are shown for a net with the same configuration as in Figure 2.1.

In Vortex Dynamics, stiffness between two parts in a certain direction can be modeled by linking the two parts with a joint characterized by a constraint equation in that direction, and by relaxing that constraint. In order to model the tension in the threads, the attachment points of the *distance constraints* are set at the centers of mass of the adjacent nodes and each constraint in the direction of the thread is relaxed with a stiffness and a damping parameter. Thus, the distance between the attachment points is allowed to be slightly higher than the set distance, and when this happens, a force arises from these two contributions: the force is defined as the sum of the forces due to a linear elastic spring and to a viscous damper. In this way, a force in the p-th thread exists only when

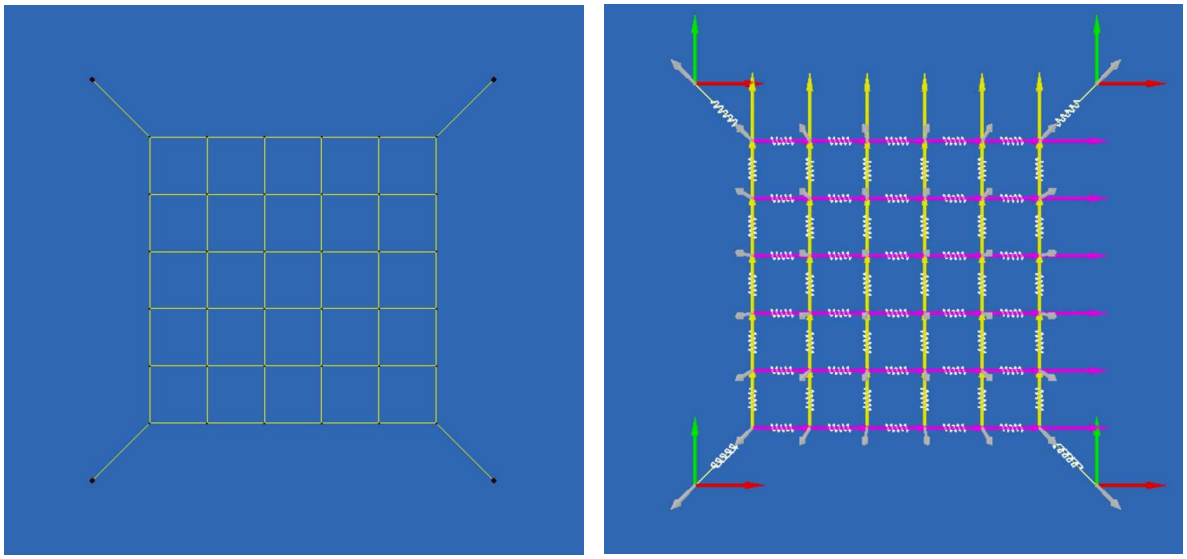

(a) (b)

FIGURE 2.2: Visualization of the model of the net in Vortex Dynamics: a) Inertia (black). b) Constraints.

that thread is elongated, which is consistent with the nature of the net material, unable to withstand compression. The expression for the tension in a thread is as follows:

$$\mathbf{T}_k = \begin{cases} T_k \mathbf{e}_k & \text{if } (l_k > l_{k,0}) \\ \mathbf{0} & \text{if } (l_k \leq l_{k,0}) \end{cases} \tag{2.19}$$

The nature of Vortex Dynamics causes the two simulators to have some discrepancies:

1. The nodes are implemented as particles in the MATLAB-based simulator and as small rigid bodies (i.e., with non-zero moments of inertia) in the Vortex-Dynamics-based simulator.
2. A condition on the tension in the threads being positive is included in the MATLAB-based simulator, but not in the Vortex-Dynamics-based simulator.

The effect of these discrepancies was investigated and both models appeared to be similarly representative, as will be shown in Section 2.4.4.2.

Vortex Dynamics physics engine is based on an augmented Lagrangian formulation. The well-known Lagrangian function is defined as $\mathcal{L}(\mathbf{q}, \dot{\mathbf{q}}) = T(\mathbf{q}, \dot{\mathbf{q}}) - V(\mathbf{q})$, with T the kinetic energy of the system, V the potential energy of the system, $\mathbf{q}$ the generalized coordinates, and $\dot{\mathbf{q}}$ the generalized velocities. The equations of motion of a system with applied forces $\mathbf{f}$ can be written in terms of the Lagrangian function as:

$$\frac{d}{dt}\frac{\partial \mathcal{L}}{\partial \dot{\mathbf{q}}} - \frac{\partial \mathcal{L}}{\partial \mathbf{q}} = \mathbf{f} \tag{2.20}$$

This formulation is augmented with kinematic constraints, that can be mathematically represented as an array function of the generalized coordinates: $\mathbf{\Phi}(\mathbf{q}) = \mathbf{0}$. The equations of motion and constraints are formulated in the following differential-algebraic system:

$$\begin{aligned} \mathbf{M}\dot{\mathbf{v}} + \mathbf{c} - \mathbf{G}^T\boldsymbol{\lambda} &= \mathbf{f} \\ \mathbf{\Phi}(\mathbf{q}) &= \mathbf{0} \end{aligned} \tag{2.21}$$

Here, $\mathbf{M}$ is the mass matrix of the system, $\mathbf{v}$ is the array of velocities of the rigid bodies – related to $\dot{\mathbf{q}}$ as $\dot{\mathbf{q}} = \mathbf{\Gamma}(\mathbf{q})\mathbf{v}$ –, $\mathbf{G}$ is the Jacobian of the constraints, such that $\dot{\mathbf{\Phi}} = \mathbf{G}\mathbf{v}$, $\boldsymbol{\lambda}$ is the vector of Lagrange multipliers, and $\mathbf{c}$ collects the nonlinear inertial terms.

In a regularized formulation (to allow for elongation in the threads, as shown before) a certain compliance is introduced in the kinematic constraints and a potential function can be defined: $V(\mathbf{q}) = \frac{1}{2}\Phi^T(\mathbf{q})\mathbf{K}\Phi(\mathbf{q})$, with $\mathbf{K}$ the stiffness matrix. A Rayleigh damping function can be used to model the dissipation occurring in the joints; this function reads $R(\mathbf{q}, \mathbf{v}) = \frac{1}{2}\mathbf{v}^T\mathbf{G}^T\mathbf{B}\mathbf{G}\mathbf{v}$, with $\mathbf{B}$ the damping coefficients matrix. The constraint forces can be defined as:

$$\boldsymbol{\lambda} = -\mathbf{K}\mathbf{\Phi} - \mathbf{B}\mathbf{G}\mathbf{v} \tag{2.22}$$

and the constraint equation $\mathbf{\Phi}(\mathbf{q}) = \mathbf{0}$ in (2.21) (which is no longer satisfied due to the regularization) is substituted by equation (2.22). At every time step in the simulation, the constraint Jacobian is calculated from the kinematic constraints, and equations are generated. With Euler's stepping method and h the time step, the discretized equations can be written as:

$$\begin{bmatrix} \mathbf{1} & -h\mathbf{\Gamma} & \mathbf{0} \\ \mathbf{0} & \mathbf{M} & -\mathbf{G}^T \\ \mathbf{0} & \mathbf{G} & \tilde{\mathbf{C}}_\Phi \end{bmatrix} \begin{bmatrix} \mathbf{q}_{n+1} \\ \mathbf{v}_{n+1} \\ h\boldsymbol{\lambda}_{n+1} \end{bmatrix} + \begin{bmatrix} -\mathbf{q}_n \\ -h\mathbf{M}\mathbf{v}_n - h(\mathbf{f} - \mathbf{c}) \\ \tilde{\mathbf{B}}_\Phi\mathbf{\Phi}_n \end{bmatrix} = \begin{bmatrix} \mathbf{0} \\ \mathbf{0} \\ \mathbf{0} \end{bmatrix} \tag{2.23}$$

where it can be demonstrated that $\tilde{\mathbf{C}}_\Phi = \text{diag}\{h^{-2}(1 + c_k/(hk_k))^{-1}/k_k\}$ and $\tilde{\mathbf{B}}_\Phi = \text{diag}\{h^{-1}(1 + c_k/(hk_k))^{-1}\}$. The forces necessary to satisfy the kinematic constraints, as well as the velocities and positions of all the bodies are computed at every time step. For further details on this formulation, the reader is referred to the paper by Lacoursière [60].

2.4.3 Results of a deployment simulation

With the simulation tools presented, numerical simulations have been performed for the net dynamics in various gravity conditions, subject to diverse initial conditions, and for differently scaled net geometries. The simulation tools proved able to deal with disparate dynamic scenarios, among which are free-fall, rotation of the net, fall with forces applied

Net and corner masses					
L_{net} (m)	$l_{net,0}$ (m)	r_{net} (m)	ρ_{net} (kg/m^3)	E_{net} (GPa)	ξ_a (-)
5	1	0.001	1390	70	0.106
l_{knot} (m)	$l_{CT,0}$ (m)	r_{CT} (m)	ρ_{CM} (kg/m^3)	m_{CM} (kg)	
0	1.4142	0.002	2700	0.5	
Initial conditions				**Simulation data**	
$v_{e,net}$	v_e (m/s)	θ (°)	α_{net} (-)	t_f (s)	ϵ (-)
0	2.5	36.87	0.25	6	10^{-6}

TABLE 2.2: Data for the simulation of a net deployment in space.

to the corner nodes, deployment, simple impact conditions, and capture of debris. In this Section we present the results of the deployment of a basic net in the 0g environment of space as obtained with the MATLAB-based simulator; the data for the simulation are given in Table 2.2[3]. The corner masses are assumed to be made of aluminum and the net material is assumed to be Technora, a polyaramid fiber (the axial damping ratio ξ_a for this fiber was estimated from tests in reference [21]). Although the geometry of this net is not realistic for ADR purposes, the reduced size of the problem allows to gain some initial insight into the deployment process; concurrently, it permits to refer to Figure 2.1 for the numbering of nodes and threads.

The dynamics of deployment was simulated for $t_f = 6$ s at a tolerance of $\epsilon = 10^{-6}$ and integration took around 3 min with an Intel®Core™ i7-4712HQ CPU @ 2.30 GHz processor. Several snapshots of the net during its deployment are included in Figure 2.3, starting with the stowed initial configuration at $t = 0.0$ s to the fully deployed configuration at $t = 3$ s. As time passes, the outer threads start elongating (see $t = 1.0$ s), followed by innermost threads (see $t = 2.0$ s); after 3 s, the net starts closing again. The configuration of the net remains symmetric at all times: this is expected, since the initial conditions, the applied loads, as well as the geometry and physical properties of the net are symmetric.

In Figure 2.4, the x- and z-coordinates of a subset of nodes are shown, to confirm that the symmetry among some groups of nodes is indeed preserved, other than for the accumulation of numerical error towards the end of the simulation period. The symmetry of the considered groups of nodes, whose indexes are in the legend, can be verified in Figure 2.1. The y-coordinates of nodes are not reported in this document for the sake of conciseness, but exhibit a behavior analogous to that of x-coordinates.

Figure 2.5 displays the magnitude of the force due to tension within the threads of the net on nodes 37, 1, 8 and 15, which lie on a diagonal of the net, as a function of time.

[3]Note that the chosen shooting angle corresponds to the following components of initial velocity: $v_{x,0} = v_{y,0} = 1$ m/s, $v_{z,0} = 2$ m/s (see definitions in equation (2.8)).

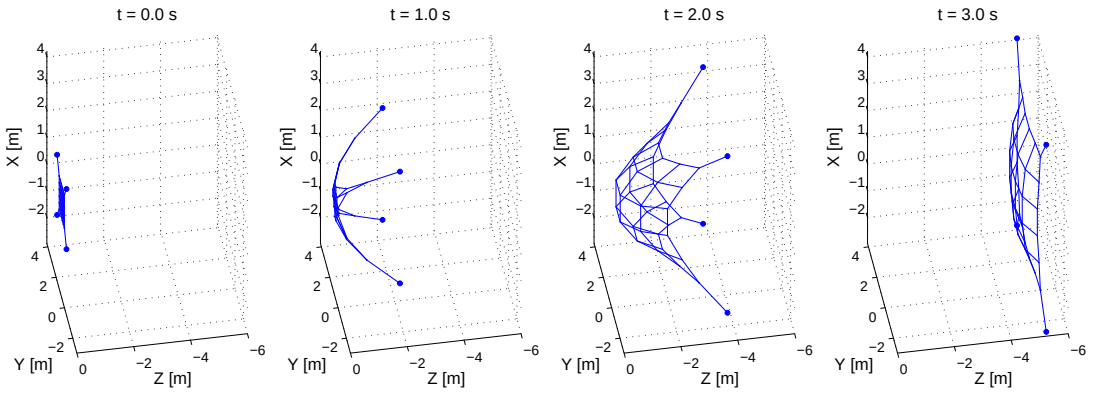

FIGURE 2.3: Deployment sequence.

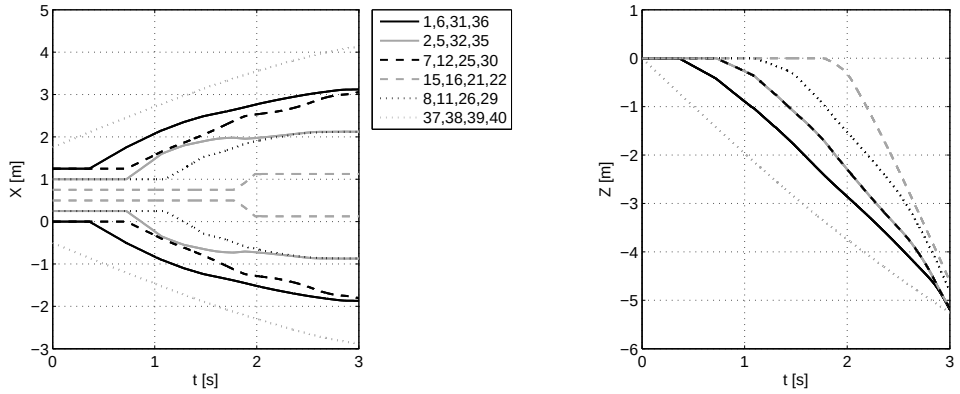

(a) (b)

FIGURE 2.4: x- and z-coordinates of some groups of nodes, in simulation of deployment.

It is observed that the model predicts snap loads: the threads are stretched and subject to fairly high loads for small periods of time only. However, this is a modeling artifact; tension magnitudes are expected to decrease and become smoother as the number of nodes used to model a thread increases. The relevant effect of the observed abrupt changes in tension is that they make it computationally expensive to simulate the deployment dynamics, especially due to the fact that the computational cost increases rapidly with the increase in the number of nodes, i.e., for larger nets. From this figure it is also evident that tension is propagated from outer to inner nodes of the net. Node 37 is a corner mass, which is subject to non-zero initial velocity in the simulation. As node 37 moves, the thread that links it to the rest of the net straightens and eventually stretches, creating a tension force as per equation (2.3): as a consequence of this, a peak in tension can be observed at $t = 0.36$ s on nodes 37 and 1. As time passes, tension propagates in the net: a second peak is visible for node 1, and corresponds to the onset of tension in the threads number 1 and 2. The delay between the peaks can be explained by the time it takes for the next innermost thread to straighten and for its end nodes to reach a distance equal to the nominal length of the thread. Also, it can be observed that nodes 8 and 15 are subject to a force arising from tension at sequentially later instants.

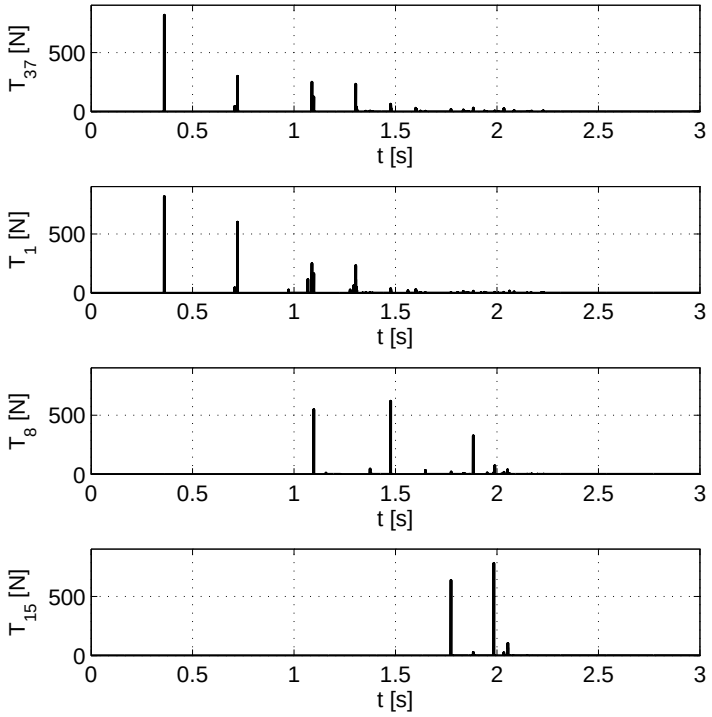

FIGURE 2.5: Tension force on different nodes, in simulation of deployment.

2.4.4 Verification of the simulators

Apart from the symmetry check exemplified in the previous Section, further verification activities were performed and are addressed in this Section.

2.4.4.1 Work-energy and linear momentum balance

First verification of the numerical tool for simulation of the net deployment dynamics in $0g$ and vacuum environment is achieved by evaluating the work-energy and the linear momentum balances.

Since no external forces are applied to the net and corner masses during the deployment phase under consideration, the linear momentum of the system is conserved. The linear momentum conservation and the work-energy balance can be written for each time t as:

$$\mathbf{p}(t) = \mathbf{p}_0 \tag{2.24}$$

$$T(t) = E_0 + W(t) \tag{2.25}$$

where $\mathbf{p}$ and E are the linear momentum and the total mechanical energy of the system, and subscript 0 indicates the time of net ejection $t = 0$. The kinetic energy T and work

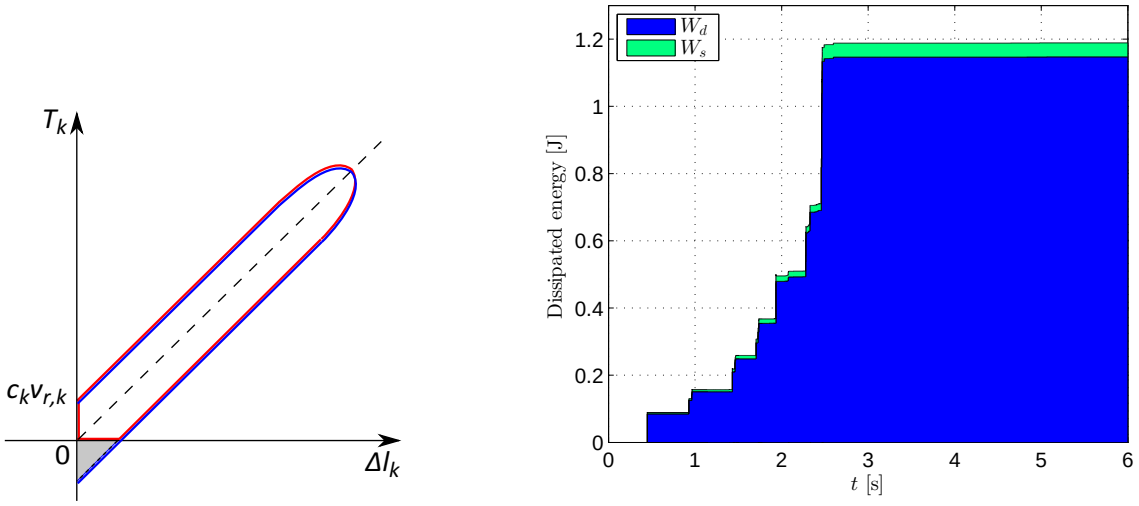

(a) (b)

FIGURE 2.6: a) Hysteresis loops for Kelvin-Voigt model with damping. Blue line: for structure able to withstand compression; red line: for structure unable to withstand compression. b) Energy dissipated due to the elastic and dissipative components of the tension in the threads.

W components in equation (2.25) can be evaluated using:

$$T(t) = \sum_{j=1}^{N_s^2} \frac{1}{2} m_j v_j^2(t) + \sum_{i=N_s^2+1}^{N} \frac{1}{2} m_i v_i^2(t) \tag{2.26}$$

$$W(t) = \int_0^t \sum_{k=1}^{N_T} \mathbf{T}_k(\tau) \cdot \left[\mathbf{v}_{1,k}(\tau) - \mathbf{v}_{2,k}(\tau)\right] d\tau \tag{2.27}$$

where, in the work of the tensile forces in the threads, the indices 1 and 2 denote the two end nodes of the k-th thread, as defined by the previously mentioned connectivity table (see Table 2.1 and equation (2.1)).

The reason for including the work of elastic forces in the work term (2.27) instead of the elastic potential energy is that the use of potential energy to account for the work done by the elastic component of the tension forces does not provide the correct formulation of the work-energy balance when damping is modeled in the threads. This occurs because the definition of elastic potential energy is not consistent with the non-linearized Kelvin-Voigt model of tension (i.e., equation (2.3)). Figure 2.6(a) illustrates how as a result of the non-linearization incurred when tension becomes compressive but the thread is elongated, as can happen for $k_k(l_k - l_{k,0}) < c_k v_{r,k}$, some energy stored in the spring (shown in grey) is lost during recovery of the unstretched length and therefore appears as dissipated through the elastic component of tension. This amount of energy is small compared to the dissipation of the dampers, but not negligible, as shown in Figure 2.6(b). The two work terms illustrated in Figure 2.6(b) are computed by separating the work

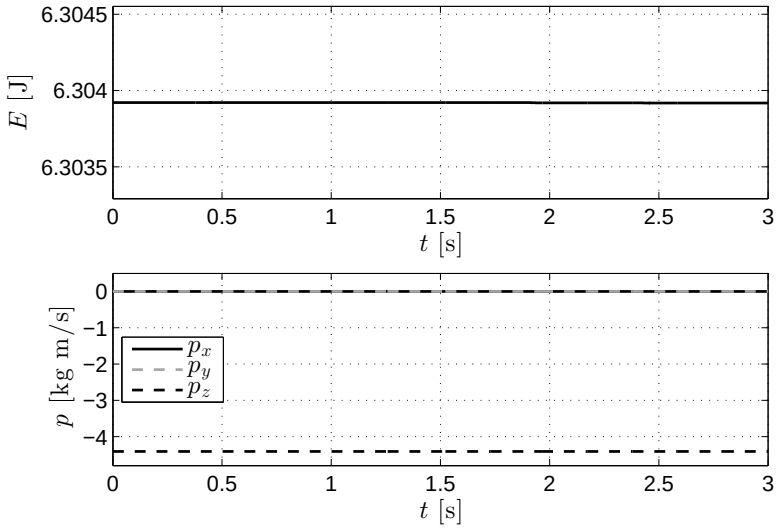

FIGURE 2.7: Work-energy and linear momentum balances.

definition into two components:

$$W_s(t) = \int_0^t \sum_{k=1}^{N_T} k_k\big(l_k(\tau) - l_{k,0}\big)\mathbf{e}_k(\tau) \cdot \big[\mathbf{v}_{1,k}(\tau) - \mathbf{v}_{2,k}(\tau)\big]\, d\tau \tag{2.28}$$

$$W_d(t) = \int_0^t \sum_{k=1}^{N_T} c_k v_{r,k}(\tau)\mathbf{e}_k(\tau) \cdot \big[\mathbf{v}_{1,k}(\tau) - \mathbf{v}_{2,k}(\tau)\big]\, d\tau \tag{2.29}$$

each evaluated consistently with the model of tension as per equation (2.3), i.e., corresponding work is incurred when the tension force is positive and the thread is elongated.

Post-processing of the same numerical integration results shown in Section 2.4.3 allowed verifying the work-energy and the linear momentum balances, apart from small drifts due to the numerical integration (see Figure 2.7): for 6 s of simulation with the Runge-Kutta 4-th/5-th order predictor/corrector method and a tolerance $\epsilon = 10^{-6}$, the relative error for $E(t)$ was of 4×10^{-7}, and the absolute error for the different components of the linear momentum was on the order of 10^{-15} kg·m/s.

2.4.4.2 Cross-verification of the two standard lumped-parameter modeling implementations

Another verification activity consisted in the comparison of deployment results obtained with the two simulators, which is the subject of the present Section. The results presented here are obtained with the same data collected in Table 2.2, apart from the simulation time (here $t_f = 3$ s) and the mesh and corner thread lengths (respectively, $l_{net,0} = 0.5$ m and $l_{CT,0} = 0.707$ m). The simulation in Vortex Dynamics was performed with a small

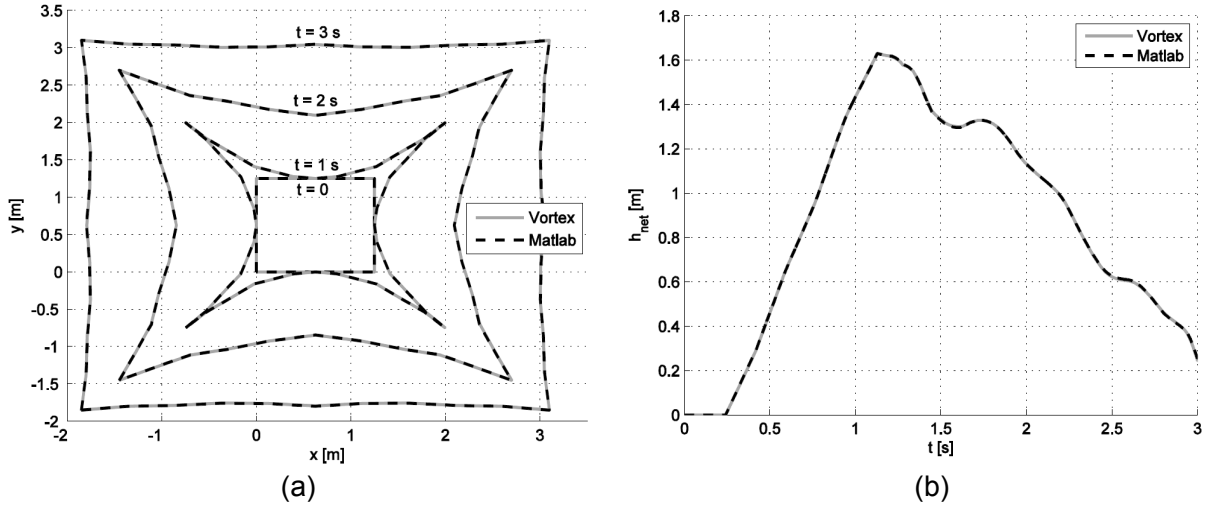

FIGURE 2.8: Comparison of results of deployment simulation with Vortex Dynamics and MATLAB simulators. (a): net's mouth shape; (b): net's height in time.

Quantity	**Maximum**	**Average**
$RMSE_{pos}$ (m)	0.00684	0.00294
$RMSE_{vel}$ (m/s)	0.0979	0.0515

TABLE 2.3: RMSE at position and velocity levels between the results of deployment simulations with Matlab and Vortex Dynamics simulators without bending stiffness.

time step of 5×10^{-5} s and took around 44 min on a laptop with Intel Core i7-4712HQ CPU @ 2.30 GHz processor and GeForce GT 750M graphics card.

The outcomes of the simulations in Vortex Dynamics and in MATLAB were found to agree very well. Plots of quantities for individual nodes appeared hardly distinguishable; Figure 2.8 provides tools to assess the agreement of meaningful overall geometrical characteristics of the net. In Figure 2.8(a) the projection of the nodes of the mouth section on the x-y plane is plotted for a few instants of the simulation; Figure 2.8(b) exhibits the height of the net, defined as per equation (2.9). None of these quantities alone is sufficient to prove perfect agreement between the two sets of data, but the study of these indexes provides good confidence in the verification.

Table 2.3 contains information on the maximum and average values of position and velocity RMSEs among the nodes of the net, for the two sets of positions and velocities at hand. Accuracy at the position level is on the order of millimeters, which is very good since it is three orders of magnitude smaller than the displacements of the nodes; at the velocity level, a certain accuracy degradation is expected: it appears to be on the order of centimeters per second, which is still satisfactory.

The variation along time of the position and velocity RMSEs averaged over the N nodes (see equation (2.12)) is represented in Figure 2.9. It was observed that discrepancies start

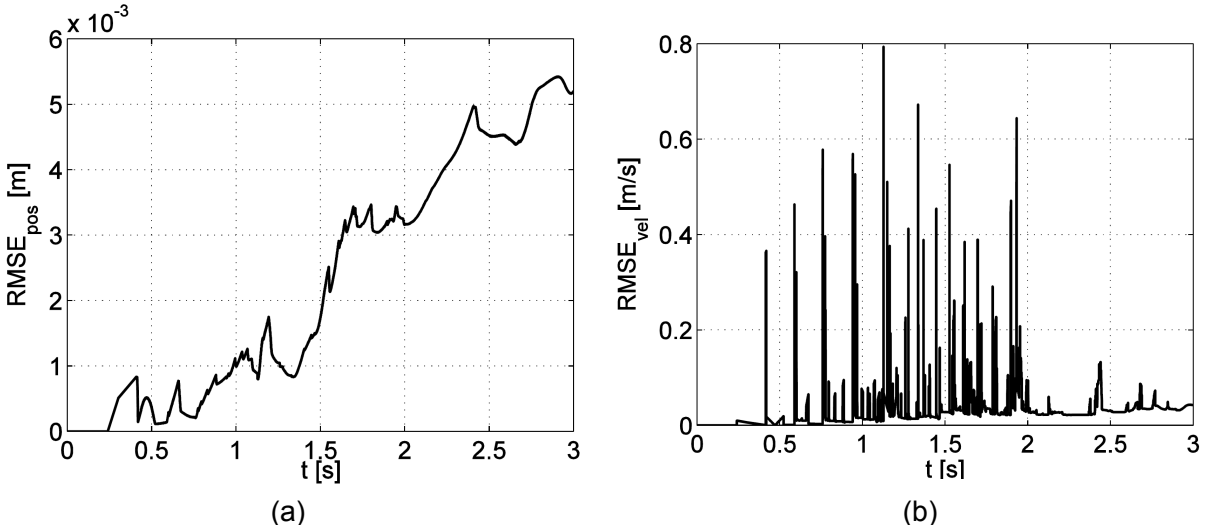

FIGURE 2.9: Average RMSEs among the nodes of the net in time between the results of deployment simulations with MATLAB and Vortex Dynamics simulators. (a): at position level; (b): at velocity level.

appearing soon after tension onset in the net in the form of snap loads (i.e., after about 0.25 s). Position RMSE increases in the course of the simulation but remains always very small. Velocity RMSE is usually small, except for multiple sharp peaks, which were found to correspond to instances in which some threads pass from a slack to a taut configuration. It should be noted that these plots appear discontinuous at some points because a selection on times had to be made: the MATLAB-based simulator uses a variable time step integration scheme, whereas the Vortex-Dynamics-based simulator employs a fixed step integrator; in the computation of RMSEs, only quantities at corresponding times were retained.

From the presented analysis, it is verified that the results of the two simulations match very well when a small time step is employed in Vortex Dynamics. With a time step of 1/60 s, which is set for real-time simulation, the computation time of the 3 s deployment maneuver is as low as 9 s. Although accuracy is reduced in this case (especially as far as reproducing snap loads), it was verified that Vortex Dynamics reproduces meaningful results, as far as positions and velocities are concerned: this makes it a powerful tool for the simulation of such complex systems as nets for ADR, well-suited for obtaining the motion response of the system in a reasonable amount of time.

Notwithstanding the differences intrinsic in the integration schemes employed in MATLAB and in Vortex Dynamics, it is safe to state that the simulations of net deployment with the standard lumped-parameter models implemented in the two simulators are in agreement. This also verifies that the differences in the two simulators (i.e., inertia of the nodes and slightly different definitions of tension) do not have appreciable effects on the deployment dynamics.

2.4.4.3 Validation against experiments on deployment

A laboratory-based test-bed was created at McGill university in parallel to the present research and is described in reference [23]. This test-bed allows to drop a net under gravity by releasing its four corners simultaneously from a square frame. This provided an opportunity to validate the Vortex-Dynamics-based simulator, by comparing the response of the experimental net and that predicted in simulation.

The net used in the experiments was a 2.25×2.25 m^2 (89 in. $\times$ 89 in.) net with 19.1 mm (0.75 in.) mesh size and made of nylon threads of 1.59 mm (1/16 in.) diameter; its mass was 0.792 kg. In simulation, a net characterized by the same mass and side length but with a coarser mesh (of 11.25 cm length) was used for computational and memory allocation reasons.

Comparison of four snapshots of the experimental recording and of the corresponding simulated response at matching time instances are shown in Figure 2.10. In Figure 2.10(a), the net corners appear to be dropping faster than the rest of the net. This could only be reproduced in simulation by prescribing an initial velocity to the corner nodes of the net. The snapshots in Figure 2.10(b) were obtained by prescribing initial velocities of $[\pm 1, \pm 1, -2.34]$ m/s to the four corner nodes, respectively.

In Figure 2.11 are plotted the vertical positions of two corners of the net over the duration of the fall, for the experiment (in black) and the simulation (in blue). Experimental data for the vertical positions of the two front corners of the net were reconstructed using the recorded video of the experiment and knowing the initial height of the net (i.e., the height of the frame). The vertical component of the initial velocity of the corners in the simulation (-2.34 m/s) was estimated from the initial slope of the experimental profiles of corner heights; the horizontal components were selected arbitrarily, but similar quantitative behavior was obtained with other values of the same order of magnitude. It should also be noted that the simulated responses of the two corners are not identical because of a small asymmetry in the initial shape/position of the net: it was not possible to have the net start exactly from its equilibrium position under gravity in simulation. Figure 2.11 shows very good agreement in the time of flight, which is approximately 0.68 s. Experimental and simulated results were also compared to the free-fall response of the net corners; differences increasing in time were observed and are explained by the effect of tension in the threads and of aerodynamic drag, that cause both the simulated and experimental responses to lag with respect to the free-fall motion.

Notwithstanding the difficulties in the comparison of simulations to experiments, due to imperfections in the initial conditions (it was not possible to specify the initial sagged configuration exactly) and in the net geometry (the mesh of the simulated net was coarser,

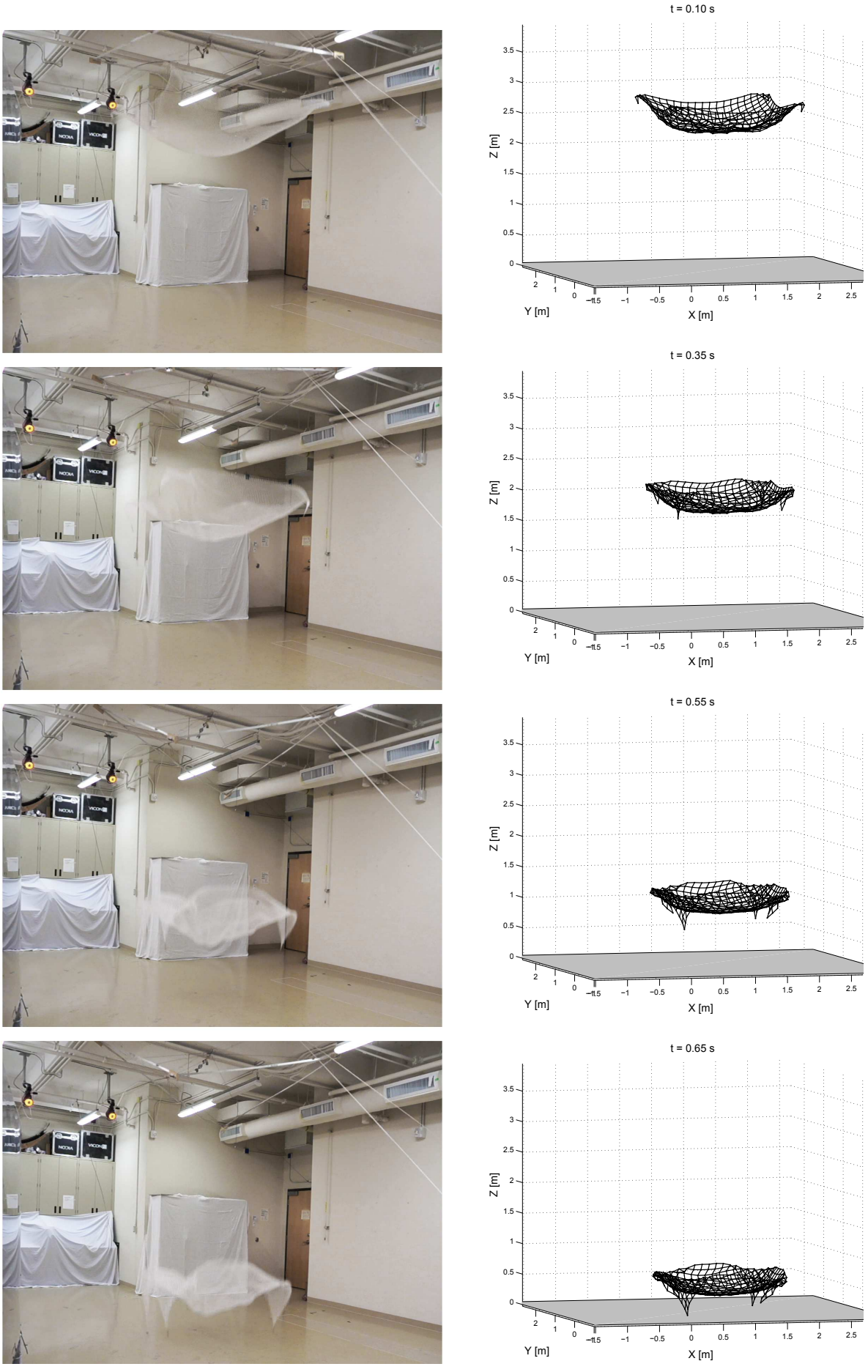

(a) Experiment.

(b) Simulation.

FIGURE 2.10: Snapshots from net drop experiment and simulation.

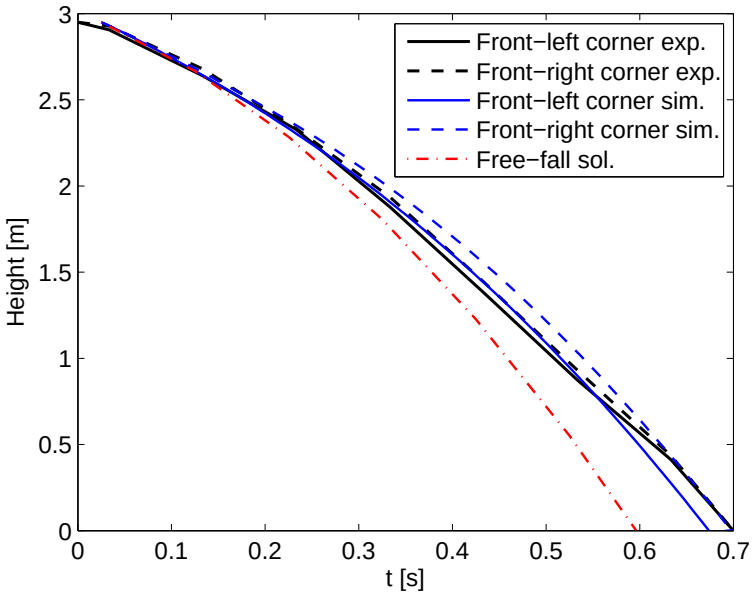

FIGURE 2.11: Vertical positions of two corners of the net: reconstructed from experiments (black), simulated (blue), and predicted with free-fall solution (red).

for computational reasons), these results show very good correspondence and provide further confidence in the developed modeling and simulation tools.

Chapter 3

Analysis of deployment dynamics

With the model of the system presented and the numerical tools demonstrated and validated in Chapter 2, multiple studies on the deployment phase were carried out and are the topic of this Chapter. Section 3.1 focuses on understanding what influence the stiffness modeling choices have on the deployment dynamics. In Section 3.2, an analysis based on the work-energy and linear momentum balances is proposed and provides insight into the key parameters leading the deployment dynamics; numerical simulations are employed to validate the analytical observations. Further interpretation is achieved through several numerical simulations in Section 3.3. Finally, Section 3.4 investigates the effect of tension in the main tether linking the net to the chaser on the deployment dynamics.

3.1 Effect of bending stiffness of net threads on deployment

One of the open issues in the simulation of the dynamics of nets in space is whether the bending stiffness of the threads of the net needs to be represented in the modeling and simulation. Notwithstanding the debate about the importance of modeling bending stiffness in tether-net dynamics simulation, only a few works in this research domain have provided some remarks on the subject (more detail is given in Section 3.1.1). The intent of this Section is to evaluate the importance of including bending stiffness in the modeling of nets for ADR in space. This is achieved by proposing an augmented lumped-parameter model of the net (in Section 3.1.2) and comparing the results of deployment simulations with and without representation of bending stiffness (in Sections 3.1.3 and 3.1.4).

3.1.1 Treatment of bending stiffness of nets and tethers in the literature

As was discussed in Section 1.2, among the existing simulators for the dynamics of tether-nets in space, the majority take a standard lumped-parameter approach, in which bending stiffness of the threads is not accounted for. Yu et al., in their work on space webs, neglected bending after commenting that it had been demonstrated that energy variation for shearing and bending is negligible with respect to energy variation for tensile force [61]. In his thesis on a tether-net simulation tool, Salvi discarded bending effects arguing that the value of bending stiffness per unit length is orders of magnitude lower than the value of axial stiffness per unit length, which makes the first irrelevant [21]. On the other hand, Golebiowski et al. used a Cosserat rod model, which enables reproducing stretching, bending and torsion behaviors; however, they did not comment on the values of bending stiffness, and on the reasons why they expected bending dynamics to be important [29, 30].

Researchers working on tether-nets for ADR have argued that the standard lumped-parameter approach proved sufficient for fishing nets; however, few comments on the role of bending stiffness were found in literature related to underwater nets. Lee et al. affirmed that the results of their simulation with lumped-parameter models and of experiments matched well in a qualitative comparison of the shape of the net and in a quantitative comparison of some geometrical properties of the net (e.g., depth of net center, width and height of net mouth) [62]. With the aim of simulating fishing nets, Takagi et al. [63] also employed lumped-parameter models with no discussion of bending effect and found qualitative agreement between experimental and theoretical net shape configurations; for quantitative analysis, they compared the overall horizontal and vertical dimensions of the net, and found slightly larger values in the numerical simulations. These discrepancies were attributed to reading error and parallax in the video image [63]. LeBris and Marichal and Bessonneau and Marichal modeled the threads as rigid bars constrained by rotational joints, subdividing each thread in two in order to describe its shape [58, 64]; they only accounted for tension, neglecting bending. By comparing experimental and calculated net shapes, LeBris and Marichal observed that, in still water, the effect of twine bending stiffness is not negligible on geometry, especially in the slack zones of the net. Buckham et al. addressed the dynamics of underwater tethers and affirmed that, if the motion of slack marine cables is to be simulated accurately, the effects of bending and torsional stiffness of the cable must be captured [65]. In his Ph.D. thesis, Buckham observed that when the tether is in high tension, the magnitude of the tensile forces dominates the tether dynamics, and bending and torsional effects are negligible; on the other hand, he showed that it is important to include a bending stiffness model for simulating the dynamics of slack tethers [66]. In any case, it is difficult to forecast the

effect of bending on the dynamics of nets in space on the basis of studies on underwater systems: neutrally buoyant tethers are in similar conditions to tethers in space, but the presence of hydrodynamic drag, when the tether moves in the water, creates very different external forcing conditions: for example, it is much more likely for threads subject to drag to be taut. Therefore, it is expected that in vacuum conditions, the effect of bending is going to be more significant than in underwater environment.

3.1.2 Lumped-parameter model augmented with bending stiffness

In order to have a tool that allows investigating the effect of the bending stiffness of the threads of the net on the deployment dynamics, a second model of the net was implemented in Vortex Dynamics using a combination of two types of joints: the same *distance joint* introduced in Section 2.4.2, and a position-based constraint equivalent to a prismatic joint. The first constraint allows proper modeling of the axial dynamics, whereas the second allows the model to account for the bending stiffness of the threads. In fact, the prismatic joint in Vortex Dynamics imposes constraint equations in the directions perpendicular to its primary axis and on the angular degrees of freedom, and these constraint equations can be relaxed by the user to allow for finite stiffness in these directions.

The distance joints were set up in the same way as described in Section 2.4.2: the attachment points of the constraints were set at the adjacent nodes, and the same relaxation parameters were set to model the axial stiffness and damping properties of the threads. The primary axes of the prismatic joints were set to be the same as the directions of the distance joints. Angular and translation constraints related to bending, pertaining to the prismatic joints, were relaxed with stiffness coefficients, which were estimated by approximating a thread to a cantilever beam subject to pure bending moment and to pure shear force, respectively. The corresponding angular stiffness related to bending, $k_{b,k}$, and transverse stiffness related to bending, $k_{t,k}$, in the k-th thread of the net are defined with:

$$k_{b,k} = \frac{E_{net} I_k}{l_{k,0}} \tag{3.1}$$

$$k_{t,k} = \frac{3 E_{net} I_k}{l_{k,0}^3} \tag{3.2}$$

where $I_k = \pi r_k^4/4$ is the area moment of inertia about the in-plane axis of a circular section of radius r_k. The corresponding damping coefficients for the k-th thread are approximated with $c_{b,k} = 2\xi_b k_{b,k}/\omega_{n1,b}$ and $c_{t,k} = 2\xi_b k_{t,k}/\omega_{n1,t}$, where ξ_b is the chosen

bending damping ratio and $\omega_{n1,b}$ and $\omega_{n1,t}$ are the first natural frequencies related to bending of a single cantilevered inner thread of the net (related to rotation and translation, respectively); some approximation is already underlying in the damping ratio, therefore, this approximation is expected to produce negligible error. With these stiffness and damping coefficients, Vortex Dynamics generates spring and damper reaction forces according to the Kelvin-Voigt model, both for the angular and transverse degrees of freedom associated with bending deformation.

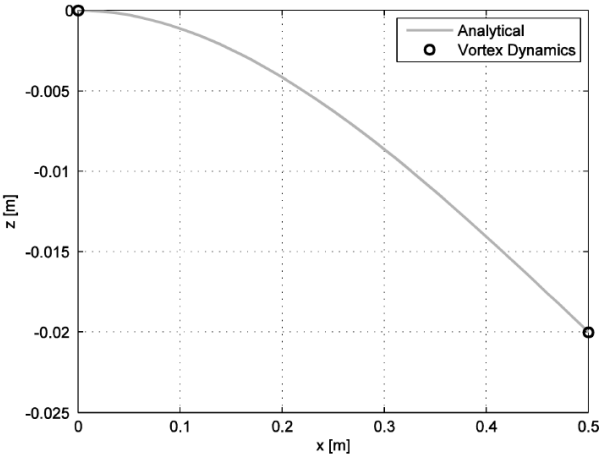

FIGURE 3.1: Static deflection of a cantilever beam; comparison of analytical and simulation results. The latter are obtained with a lumped-parameter model employing two masses and one prismatic joint in Vortex Dynamics.

The bending stiffness component of this model was validated by simulating the dynamics of a cantilever beam subject to its own weight and to a transverse tip load until steady state condition is reached, and by checking that the deflection at the tip is equal to the theoretical static deflection. In Figure 3.1 the comparison of the two results is shown for a 0.5 m long Aluminum beam, with circular section of 1 cm radius, subject to its own weight and to a tip load of 262 N. Vortex Dynamics results were obtained by modeling the beam with two lumped masses linked by one prismatic joint with bending and transverse stiffnesses defined in equations (3.1) and (3.2). As can be seen in Figure 3.1, the tip displacements are in agreement to 10^{-5} m.

It is also important to ensure that the results of simulations with completely relaxed bending-related joints match the results of simulations without bending stiffness representation in Vortex Dynamics. This was accomplished by setting all the $k_{b,k}$, $k_{t,k}$, $c_{b,k}$, and $c_{t,k}$ coefficients to zero and comparing the results with those obtained with the Vortex Dynamics implementation of the standard lumped-parameter model. In Table 3.1 are reported the RMSE values of this check for the same deployment scenario as specified in Table 2.2: it can be observed that all values are negligible; therefore, we can state that the combined joints setup was validated. The very small discrepancy between the two

Quantity	**Maximum**	**Average**
$RMSE_{pos}$ (m)	4.08×10^{-12}	3.27×10^{-14}
$RMSE_{vel}$ (m/s)	4.08×10^{-8}	8.88×10^{-10}

TABLE 3.1: RMSE at position and velocity levels between the results of deployment simulations in Vortex Dynamics employing the standard and the augmented lumped-parameter models, and setting bending stiffness and damping coefficients to zero.

data sets is likely due to the fact that the two systems are characterized by different sets of equations and the corresponding propagation of numerical errors.

3.1.3 Comparison of deployment simulations with and without bending stiffness

In this Section are compared the results of a deployment simulation with the two models implemented in Vortex Dynamics: the model without bending stiffness, as validated in Section 2.4.4.2, and the model presented in Section 3.1.2, which allows to account for bending stiffness. The net and deployment scenario considered here are the same as in Table 2.2, apart from the simulation time (here $t_f = 3$ s) and the mesh and corner thread lengths (respectively, $l_{net,0} = 0.5$ m and $l_{CT,0} = 0.707$ m); also, the bending damping ratio $\xi_b = 0.014$ was added, as estimated for Technora from tests in reference [21]. The aim of this study is to assess the importance of including bending stiffness in the simulation of the deployment of nets for ADR.

Simulation of the model with bending stiffness was performed with a time step of 5×10^{-5} s, and took 1 hr, 25 min of computation time with an Intel®Core™ i7-4712HQ CPU @ 2.30 GHz processor: a 92% increase compared to the simulation in Vortex Dynamics without bending stiffness. When bending stiffness is taken into account, both the area and shape of the mouth are remarkably affected (see Figure 3.2): the area increases more quickly, such that 90% of full deployment is obtained just after 2 seconds, compared to 3 seconds when bending stiffness is not represented; at $t = 1$ s, the corner nodes of the net are in almost the same position in the two simulations; however, for most of the deployment, the mouth shape is concave in simulations without bending stiffness and it is convex with bending stiffness, such that the surface covered by the net is much wider in the latter. For example, at $t = 1.5$ s, the mouth area obtained with the model with bending stiffness is approximately 2.5 times larger than for the model without bending stiffness.

The height profiles for the net are also dissimilar, as visible in Figure 3.3(a): it appears that inclusion of bending stiffness has an appreciable effect on the dynamics in the z-direction as well. On the other hand, the mouth diagonal profiles are similar, as shown in

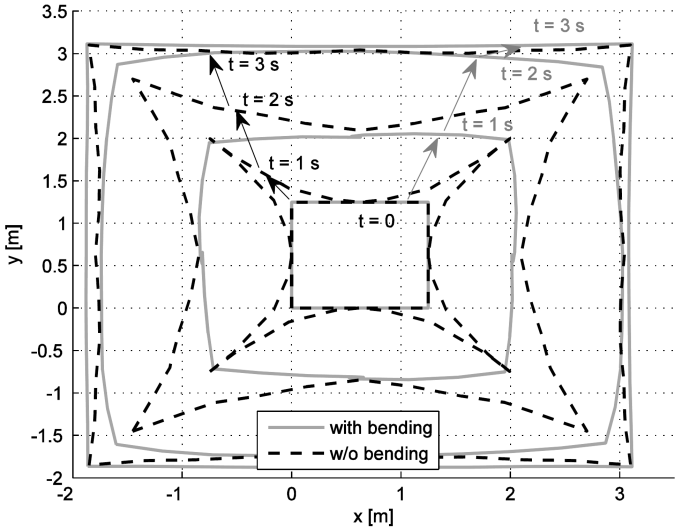

FIGURE 3.2: Comparison of the mouth shape of the net in time, in deployment simulation with Vortex Dynamics, without and with bending stiffness representation.

Figure 3.3(b). These results can be explained by interpreting the stiffness as the resistance to deformation in response to an applied force: the net with bending stiffness resists more the changes in its shape which are being forced by the motion of the corner masses, both in the $x-y$ plane and along the z-direction. Therefore, the mouth shape for the net with bending stiffness representation is always closer to a square (i.e., the initial mouth shape) with respect to that for the net without bending stiffness representation; similarly, the height of the net is lower for most of the deployment time in the first case.

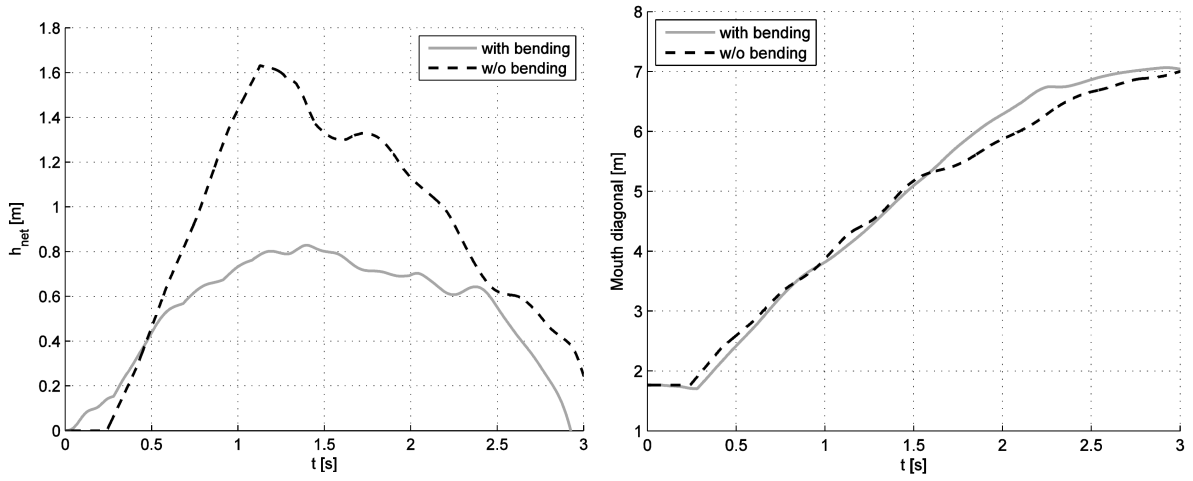

(a) (b)

FIGURE 3.3: Comparison of results of deployment simulation with Vortex Dynamics, without and with bending stiffness representation. (a): height of the net in time; (b): mouth diagonal in time.

RMSE values on positions and velocities averaged over time are collected in Table 3.2. The discrepancies between the two simulations are also apparent from these quantities: RMSEs are of the same order of magnitude as the positions and velocities themselves.

Quantity	**Maximum**	**Average**
$RMSE_{pos}$ (m)	0.760	0.516
$RMSE_{vel}$ (m/s)	1.47	1.02

TABLE 3.2: RMSE at position and velocity levels between the results of deployment simulations with Vortex Dynamics, without and with bending stiffness representation.

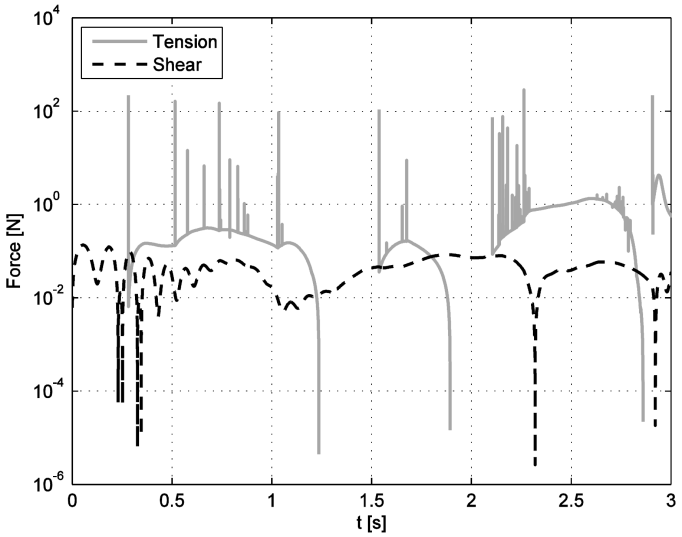

FIGURE 3.4: Tension and shear force in a corner thread, in deployment simulation with bending stiffness representation.

On the other hand, the evolutions of position and velocity of the center of mass of the net were checked, and were found to match between the two simulations. This is expected since the linear momentum of the system, which is prescribed by the initial velocities and the mass properties of the system, is conserved during the simulations (see Figure 2.7 and Section 3.2.2), and it is the same in the two cases.

It is interesting to analyze the impact of bending stiffness when the threads are slack and taut. In order to do this, the tension and shear forces in the threads are compared: in fact, as per equation (2.3), tension is nonzero when a thread is taut, and equal to zero when the thread is slack. In Figure 3.4, tension and shear forces in a corner thread are plotted against time. The logarithmic scale is used on the force axis because the two quantities can differ by orders of magnitude at the same instant; therefore tension forces are not plotted when the cable is slack. It is clear that axial dynamics is characterized by tension loads which can be 4 orders of magnitude higher than shear forces. However, bending stiffness is important when the rope is not under tension.

3.1.4 Sensitivity study on the effect of bending stiffness

The results of the previous Section have brought to light substantial differences between the overall geometrical and dynamical properties of the net in the deployment phase, when the bending stiffness of the threads of the net is considered and when it is neglected. However, the modeling of the bending stiffness presented in Section 3.1.2 is based on the approximation of the threads of the net with cantilever beams, which might lead to an overestimation of their bending stiffness properties. In order to achieve more complete understanding of the effect of bending stiffness on the deployment dynamics, this Section proposes a sensitivity analysis on quantities that are expected to influence the bending stiffness of the net threads.

According to McKenna et al. [67], two limiting cases for the mechanics of a rope can be defined to evaluate extreme values of its bending stiffness per unit length, EI. Here, in order to have corresponding evaluations of its axial stiffness per unit length, EA, the reasoning is extended to the axial direction. The limiting cases (illustrated by Figure 3.5) are:

1. a strong interaction among fibers, causing the rope to act as a solid rod (see Figure 3.5(a)), for which:

$$(EI)_{max} = E_f \pi \frac{r_{net}^4}{4} \tag{3.3}$$

$$(EA)_{max} = E_f \pi r_{net}^2 \tag{3.4}$$

2. freedom of each fiber to bend independently (see Figure 3.5(b)), for which:

$$(EI)_{min} = N_f E_f \pi \frac{r_f^4}{4} \tag{3.5}$$

$$(EA)_{min} = N_f E_f \pi r_f^2 \tag{3.6}$$

where E_f and r_f are the Young's modulus and the radius of the fiber, and N_f is the number of fibers in a rope of radius r_{net}. If a rope is fully packed, then $\pi r_{net}^2 = N_f \pi r_f^2$, from which $N_f = (r_{net}/r_f)^2$; in general, we can define the number of fibers in a thread as $N_f = \beta(r_{net}/r_f)^2$, where $0 < \beta \leq 1$ is called *packing coefficient*. Using this expression in equations (3.5) and (3.6), it can be shown that the limiting values for EA and EI of a rope can be found as expressed in Table 3.3.

It has already been shown in this Thesis that the axial and bending stiffness coefficients $k_{a,k}$, $k_{b,k}$, and $k_{t,k}$ depend on EA, EI, and the length of the threads. Considering the expressions collected in Table 3.3 and assuming that E_f and r_f are fixed once the material of the threads is selected, the parameters relevant to this sensitivity study are the mesh

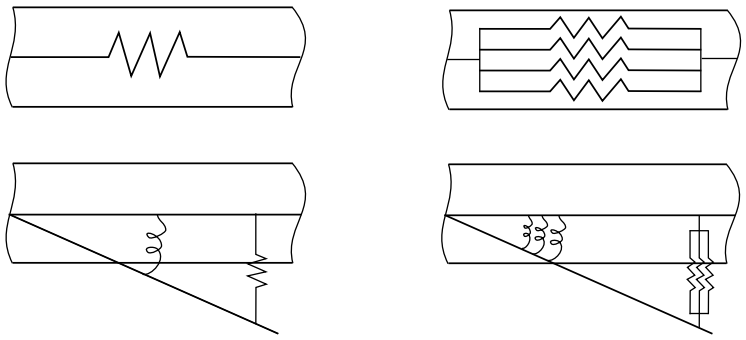

(a) (b)

FIGURE 3.5: Illustration of axial (top) and bending (bottom) stiffness properties of a thread: (a): with strong interaction among fibers; (b): where fibers are independent.

Solid rod	**Independent fibers**
$(EA)_{max} = E_f \pi r_{net}^2$	$(EA)_{min} = \beta E_f \pi r_{net}^2$
$(EI)_{max} = E_f \pi r_{net}^4/4$	$(EI)_{min} = \beta E_f \pi r_{net}^2 r_f^2/4$

TABLE 3.3: Limiting values for EA and EI of a rope.

length $l_{net,0}$, the thread radius r_{net} and the packing coefficient β. A first sensitivity study showed that r_{net} does not have a significant impact on the importance of bending stiffness, apart for long threads (of length approximately equal to one fifth the side length of the net); for the sake of conciseness, that sensitivity study is omitted in this Thesis.

On-ground tests for characterizing the stiffness properties of Technora braids were performed by Benvenuto et al. [68] and Salvi [21]; concurrently to our sensitivity study, we investigated how their experimental stiffness properties compare with the two limiting models. The following data on the tested braids were provided in references [68] and [21]:

$$\rho_{l,net} = 547 \text{ tex}^1 = 547 \times 10^{-6} \text{ kg/m} \qquad E_{net} = 25 \text{ GPa} \qquad EA = 9838.1 \times 10^3 \text{ N}$$
$$\rho_f = 1390 \text{ kg/m}^3 \qquad E_f = 73 \text{ GPa} \qquad EI = 1.34 \times 10^{-6} \text{ Nm}^2$$

from which the value of the tested braid radius was estimated as: $r_{net} = 3.54 \times 10^{-4}$ m $=$ 0.354 mm. The limiting values for EI and EA as per Table 3.3 are plotted together with the experimental EI and EA in Figure 3.6; notice that the graph for EA is linear, but the graph for EI is semi-logarithmic. An intersection between EA and $(EA)_{min}$ is observed and corresponds to $\beta = 0.3425$: the packing coefficient for the tested braid, therefore, can only be smaller or equal to 0.3425; higher values are grayed out in the plot. No further limitations are found from EI, but it can be observed that, when EA is minimum (i.e., for $\beta = 0.3425$), EI is higher than the minimum.

[1]The tex is a widely accepted unit of measure for the linear density of fibers and ropes, defined as the mass in grams per kilometer: 1 tex $=$ 1 g/km $= 10^{-6}$ kg/m.

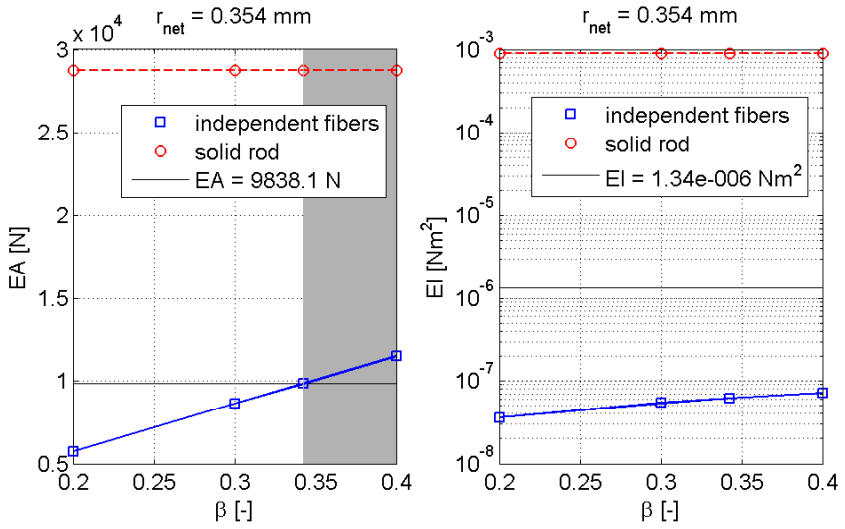

FIGURE 3.6: Experimental and limiting values of EI and EA for $r_{net} = 0.000354$ m, data from references [68] and [21], and different packing coefficients.

A sensitivity study was performed fixing r_{net} and varying the mesh length and the packing coefficient (considering only $0.2 \leq \beta \leq 0.4$). The ranges for the maximum position RMSE (obtained by comparing the deployment dynamics for a net without bending stiffness and a net with bending stiffness modeled with the two limiting cases), together with the values obtained from simulation with the experimental EA and EI from references [68] and [21], are reported in Figure 3.7. Circles represent the solid rod model, which is independent of β, squares represent the independent fibers model, and stars represent the experimental data. It is observed that the solid rod modeling produces the largest differences (on the order of 10^{-1} m), which increase when the mesh length decreases; as expected, these RMSEs do not depend on the packing coefficient. The independent fibers modeling is not very sensitive to the packing coefficient and produces much smaller differences from the case without bending (on orders of magnitude from 10^{-3} m to 10^{-2} m). It is also noticed that the results with the experimental data are very close to those for the independent fibers model when $l_{mesh} = 0.25$ m, but orders of magnitude higher for $l_{mesh} = 1$ m. In any case, the value of the RMSEs is on the order of centimeters, which is probably not negligible.

It should also be noted that, even though characterization of a Technora braid was performed on ground in [68] and [21], uncertainties exist on how braids behave in space: for example, due to the vacuum environment, braids could exhibit a higher stiffness in space than on ground. Experiments in vacuum would be necessary to evaluate the stiffness properties of braids before employing nets in space. The presented sensitivity study merely provides evidence of the fact that bending stiffness has non-negligible effects on the deployment dynamics even when realistic braids are considered for the threads of the net. However, in the light of this sensitivity results, the effect of bending stiffness in the

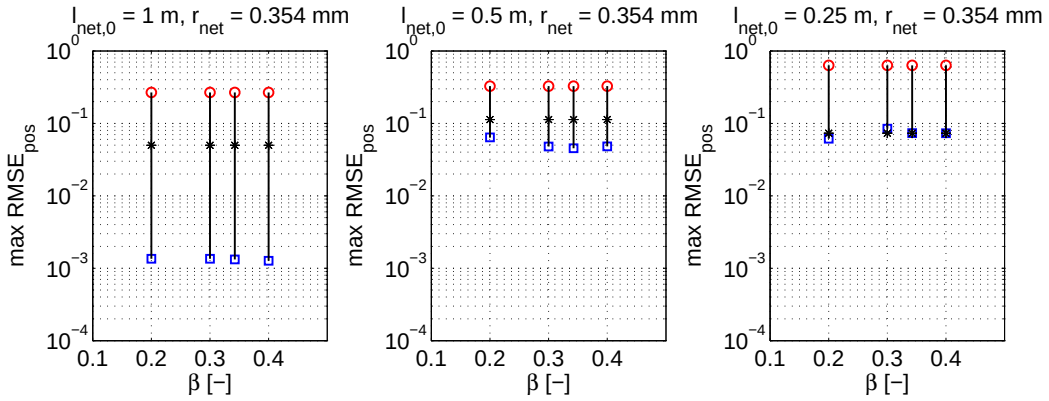

FIGURE 3.7: Spans of maximum position RMSE for $r_{net} = 3.54 \times 10^{-4}$ m and different mesh lengths, compared with the maximum position RMSE obtained with $EA = 9838.1$ N and $EI = 1.34 \times 10^{-6}$ Nm^2 (semi-logarithmic scale). Circles: solid rod model; squares: independent fibers model; asterisks: experimental EA and EI.

results in Section 3.1.3, which were based on a solid rod model of the threads, is expected to be exaggerated with respect to reality.

3.2 Energy and momentum analysis of deployment dynamics

Energy and momentum distribution in the net are recognized to be the driving factors for a correct deployment. In Section 2.4.3 it was noticed that the deployment dynamics of nets in space is driven by tension loads in the threads, which propagate from the corner masses to the innermost parts of the net. Taking this perspective, the conceptual partitioning of the net into the system of corner masses and the net proper is employed (see Section 3.2.1). Then, the work-energy and linear momentum principles are formulated in terms of velocities of the corresponding centers of mass of these two subsystems (in Section 3.2.2) and used to obtain novel analytical results characterizing the response of the net during deployment (in Section 3.2.3). This allows to determine in a formal way what configuration and ejection parameters govern the deployment dynamics, as well as to gain additional insight into the process. The analysis is carried out for an ejection where initial velocity is imparted to both the corner masses and the net proper; the results for the case in which the corner masses alone cause the net deployment (which is the condition most often simulated) can be derived as a special case. The analytical work is supplemented with numerical simulation, that contributes to the validation of the findings (in Section 3.2.4).

3.2.1 Assumptions and definitions

The proposed analysis is valid under some assumptions on the system and on the initial conditions of its deployment:

1. The shape of the net is symmetrical.
2. The inertia properties of the net system are modeled according to a lumped mass approach.
3. The ejection of the net and of the corner masses is symmetrical (i.e., the initial conditions are symmetrical).
4. The net is initially slack.

Let us call M_c the total mass of the corner masses and M_{net} the total mass of the net proper, defined as:

$$M_c = \sum_{i=N_s^2+1}^{N} m_i \tag{3.7}$$

$$M_{net} = \sum_{j=1}^{N_s^2} m_j \tag{3.8}$$

The total mass of the system is $M = M_c + M_{net}$. Finally, let $\bar{v}_c$ denote the velocity of the center of mass of the corner masses and $\bar{v}_{net}$ the velocity of the center of mass of the net proper. These definitions will be employed extensively in the rest of this Section.

3.2.2 Work-energy and linear momentum principles

Let us define $\mathbf{p}(t)$ as the linear momentum of the system composed of the net proper and corner masses at time t and $\mathbf{p}_0$ its value at the time of net ejection $t = 0$. Let us also call $E(t)$ the total mechanical energy of the system at time t and E_0 its initial value. As was observed in Section 2.4.4.1, no external forces are applied to the net and corner masses during the deployment phase under consideration; therefore, the linear momentum of the net is conserved and the work of non-conservative forces is the work done on the system by the dampers from $t = 0$ to time t, indicated with $W_{d,0-t}$. Then, at every instant t the linear momentum balance and the work-energy balance read as:

$$\mathbf{p}(t) = \mathbf{p}_0 \tag{3.9}$$

$$E(t) = E_0 + W_{d,0-t} \tag{3.10}$$

The total mechanical energy can be decomposed into kinetic energy T and elastic potential energy V: $E(t) = T(t) + V(t)$. Because of the symmetrical configuration of the system

(i.e., assumption 1) and symmetrical initial conditions (i.e., assumption 3), symmetry is expected to be preserved during the whole deployment phase. Hence, the only non-zero component of the velocity of the centers of mass of the net proper and of the corner masses will be that in the direction of the axis of symmetry, the so-called *direction of deployment*, parallel to the z-axis. As a consequence, the linear momentum equation (3.9) of the system reduces to a scalar equation in the direction of deployment. Using the definitions in Section 3.2.1, the scalar equation for the conservation of linear momentum at time t can be written as:

$$M_c \bar{v}_c(t) + M_{net} \bar{v}_{net}(t) = p_0 \tag{3.11}$$

where p_0 is the initial momentum in the direction of deployment. Similarly, equation (3.10) can be reformulated as:

$$\frac{1}{2} M_c \bar{v}_c^2(t) + \frac{1}{2} M_{net} \bar{v}_{net}^2(t) + \varepsilon(t) = E_0 \tag{3.12}$$

The term $\varepsilon(t)$ collects the contributions due to the kinetic energy of each of the corner masses *relative* to the center of mass of the corner masses, the kinetic energy of each of the net nodes *relative* to the center of mass of the net proper, the elastic potential energy of the net and of the corner threads $V(t)$, and the work done by the dampers $W_{d,0-t}$. By definition, $\varepsilon(t) \geq 0$. Collecting the elastic potential energy and the work of non-conservative forces in a unique work term, the energy term $\varepsilon(t)$ can be written as:

$$\varepsilon(t) = \frac{1}{2} \sum_{j=1}^{N_s^2} m_j \dot{\rho}_j^2(t) + \frac{1}{2} \sum_{i=N_s^2+1}^{N} m_i \dot{\rho}_i^2(t) - \int_0^t \sum_{k=1}^{N_T} \mathbf{T}_k(\tau) \cdot \left[\mathbf{v}_{1,k}(\tau) - \mathbf{v}_{2,k}(\tau) \right] d\tau \tag{3.13}$$

where $\dot{\rho}_j(t)$ is the magnitude of the velocity of the j-th node of the net proper relative to the velocity of the center of mass of the net proper, and $\dot{\rho}_i(t)$ is the same quantity for the corner masses.

At ejection, initial velocity is imparted to the corner masses with a certain inclination from the direction of deployment, in order to facilitate the net deployment. Additionally, a non-zero initial velocity can be given to the net proper parallel to the net ejection direction. If $\bar{v}_{c,0}$ and $\bar{v}_{net,0}$ are the velocities of the centers of mass of the corner masses and of the net proper at ejection, the expressions for the initial linear momentum and the initial total mechanical energy are:

$$p_0 = M_c \bar{v}_{c,0} + M_{net} \bar{v}_{net,0} \tag{3.14}$$

$$E_0 = \frac{1}{2} M_c \bar{v}_{c,0}^2 + \frac{1}{2} M_{net} \bar{v}_{net,0}^2 + \varepsilon_0 \tag{3.15}$$

with the initial value of $\varepsilon(t)$, ε_0, due only to the mass of the nodes and their initial motion relative to the centers of mass, in light of assumption 4.

3.2.3 Solution for centroidal velocities

The linear momentum conservation statement of equation (3.11) and the work-energy balance of equation (3.12) can be used to obtain a solution for the centroidal velocities at various milestones in the deployment process. In what follows, the main steps of the analysis are provided.

From equation (3.11), it is determined:

$$\bar{v}_{net}(t) = \frac{p_0 - M_c \bar{v}_c(t)}{M_{net}} \tag{3.16}$$

and, substituting this expression in equation (3.12), a quadratic equation in $\bar{v}_c(t)$ is obtained:

$$a\bar{v}_c^2(t) + b\bar{v}_c(t) + c(t) = 0 \tag{3.17}$$

where the coefficients are defined as:

$$a = \frac{1}{2} M_c \left(1 + \frac{M_c}{M_{net}}\right) \tag{3.18}$$

$$b = -\frac{M_c}{M_{net}} p_0 \tag{3.19}$$

$$c(t) = \frac{1}{2}\frac{p_0^2}{M_{net}} - E_0 + \varepsilon(t) \tag{3.20}$$

Making use of the total mass of the system M and with simple algebra it can be shown that:

$$\begin{aligned} \Delta(\varepsilon(t)) = b^2 - 4ac(t) = \\ = M_c^2 \left(\bar{v}_{c,0} - \bar{v}_{net,0}\right)^2 + \frac{2M_c M}{M_{net}} \left(\varepsilon_0 - \varepsilon(t)\right) \end{aligned} \tag{3.21}$$

For equation (3.17) to have physical solutions, the discriminant $\Delta(\varepsilon(t))$ must be positive definite. This establishes an upper bound on the total amount of energy that can be dissipated by the dampers, stored in the springs, and transformed into kinetic energy relative to the centers of mass:

$$\varepsilon(t) \leq \frac{M_{net} M_c}{2M} \left(\bar{v}_{c,0} - \bar{v}_{net,0}\right)^2 + \varepsilon_0 = \varepsilon_{max} \tag{3.22}$$

$\varepsilon(t)$	$\bar{v}_c(t)$	$\bar{v}_{net}(t)$
0	$\frac{p_0}{M} \pm \frac{M_{net}}{M}\sqrt{(\bar{v}_{c,0}-\bar{v}_{net,0})^2 + \frac{2M}{M_c M_{net}}\varepsilon_0}$	$\frac{p_0}{M} \mp \frac{M_c}{M}\sqrt{(\bar{v}_{c,0}-\bar{v}_{net,0})^2 + \frac{2M}{M_c M_{net}}\varepsilon_0}$
ε_{min}	$\begin{cases}\bar{v}_{c,max} & \text{or}\\ \bar{v}_{c,min}\end{cases}$	$\begin{cases}\bar{v}_{net,min} & \text{or}\\ \bar{v}_{net,max}\end{cases}$
ε_0	$\begin{cases}\bar{v}_{c,0} & \text{or}\\ \frac{M_c}{M}\left[(1-\frac{M_{net}}{M_c})\bar{v}_{c,0} + 2\frac{M_{net}}{M_c}\bar{v}_{net,0}\right]\end{cases}$	$\begin{cases}\bar{v}_{net,0} & \text{or}\\ \frac{M_c}{M}\left[2\bar{v}_{c,0} - (1-\frac{M_{net}}{M_c})\bar{v}_{net,0}\right]\end{cases}$
ε_{max}	p_0/M	p_0/M

TABLE 3.4: Velocity of centers of mass of corner masses and of net proper, for noteworthy values of $\varepsilon(t)$.

which, it is noted, is a function of ejection conditions and mass parameters only. With condition (3.22) imposed, solutions for $\bar{v}_c(t)$ and $\bar{v}_{net}(t)$ are found from equations (3.17) and (3.16), and upon simple manipulation they can be stated as:

$$\bar{v}_c(t) = \frac{p_0}{M} \pm \frac{M_{net}}{M M_c}\sqrt{\Delta(\varepsilon(t))} \tag{3.23}$$

$$\bar{v}_{net}(t) = \frac{p_0}{M} \mp \frac{1}{M}\sqrt{\Delta(\varepsilon(t))} \tag{3.24}$$

Equations (3.23) and (3.24) make explicit the relationship between $\varepsilon(t)$ and the velocities of the centers of mass of the net proper $\bar{v}_{net}(t)$ and of the corner masses $\bar{v}_c(t)$.

Analysis of extremum conditions provides further insight into the limiting values that these quantities can take in time. By differentiating equations (3.11) and (3.12), one can obtain:

$$M_c\dot{\bar{v}}_c(t) + M_{net}\dot{\bar{v}}_{net}(t) = 0 \tag{3.25}$$

$$M_c\bar{v}_c(t)\dot{\bar{v}}_c(t) + M_{net}\bar{v}_{net}(t)\dot{\bar{v}}_{net}(t) + \dot{\varepsilon}(t) = 0 \tag{3.26}$$

At the extrema of $\varepsilon(t)$, $\dot{\varepsilon}(t) = 0$ and substituting $\dot{\bar{v}}_c(t)$ as per equation (3.25) in equation (3.26) yields:

$$M_{net}\dot{\bar{v}}_{net}(t)\big(\bar{v}_{net}(t) - \bar{v}_c(t)\big) = 0 \tag{3.27}$$

The first solution of the above, $\bar{v}_{net}(t) = \bar{v}_c(t)$, corresponds to a condition where $\Delta(\varepsilon(t)) = 0$, as evident from equations (3.23) and (3.24); remembering the derivation of inequality (3.22), it is noted that this also corresponds to $\varepsilon(t) = \varepsilon_{max}$. Hence, the second solution of equation (3.27), $\dot{\bar{v}}_{net}(t) = 0$, corresponds to the other extremum for $\varepsilon(t)$, i.e., $\varepsilon(t) = \varepsilon_{min}$, $\Delta(\varepsilon(t)) = \Delta_{max}$, and, according to equation (3.25), $\dot{\bar{v}}_c(t) = 0$: this means that, when $\varepsilon(t)$ is at its minimum, $\bar{v}_c(t)$ and $\bar{v}_{net}(t)$ are both at their extrema (if one is at its maximum, the other is at its minimum, and vice versa).

$\varepsilon(t)$	$\bar{v}_c(t) - \bar{v}_{net}(t)$
0	$\sqrt{(\bar{v}_{c,0} - \bar{v}_{net,0})^2 + \frac{2M}{M_c M_{net}}\varepsilon_0}$
ε_{min}	$\begin{cases} \bar{v}_{c,max} - \bar{v}_{net,min} \\ \bar{v}_{c,min} - \bar{v}_{net,max} \end{cases}$ or
ε_0	$\pm\left(\bar{v}_{c,0} - \bar{v}_{net,0}\right)$
ε_{max}	0

TABLE 3.5: Difference between velocity of centers of mass of corner masses and of net proper, for noteworthy values of $\varepsilon(t)$.

Expressions for $\bar{v}_c(t)$ and $\bar{v}_{net}(t)$ for some notable values of $\varepsilon(t)$ are collected in Table 3.4. The case $\varepsilon(t) = 0$ indicates a condition where all the available energy is in the kinetic energy of the centers of mass of the corner masses and of the net proper. This condition is very unlikely to be achieved, but it yields lower and upper bounds on the values of $\bar{v}_c(t)$ and $\bar{v}_{net}(t)$; notice that the signs of $\bar{v}_c(t)$ and $\bar{v}_{net}(t)$ solutions are inverted: when $\bar{v}_c(t)$ is maximum, $\bar{v}_{net}(t)$ is minimum, and conversely. The case $\varepsilon(t) = \varepsilon_{max}$ represents one of the extremum conditions discussed above, corresponding to $\Delta(\varepsilon(t)) = 0$: the center of mass of the corner masses and the center of mass of the net proper move at equal velocities $\bar{v}_c(t) = \bar{v}_{net}(t) = p_0/M$. The other extremum condition, $\varepsilon(t) = \varepsilon_{min}$ is also reported: it leads to extremum solutions for $\bar{v}_c(t)$ and $\bar{v}_{net}(t)$, as was also previously mentioned. For $\varepsilon(t) = \varepsilon_0$, two solutions can be obtained from (3.23) and (3.24): one corresponds to the initial condition; the other is the realistic solution for $\varepsilon(t) = \varepsilon_0$ at $t > 0$. Expressions for the difference $\bar{v}_c(t) - \bar{v}_{net}(t)$ for the noteworthy values of $\varepsilon(t)$ are reported in Table 3.5, which will come in handy in the discussion of numerical results. In the deployment situation where initial velocity is imparted just to the corner masses, corresponding analytical results can be derived as a particular case of those in Tables 3.4 and 3.5, by setting $\bar{v}_{net,0} = 0$.

By analyzing Tables 3.4 and 3.5, it can be observed that dependency on the initial momentum of the system p_0 and total mass M is found, as was foreseeable, for all conditions subsequent to the initial ejection; the ratio of the mass of the net proper to that of the corner masses M_{net}/M_c and other mass ratios also appear in multiple expressions; additionally, the bounds for $\bar{v}_c(t)$ and $\bar{v}_{net}(t)$ depend on ε_0, ultimately on the magnitude and direction of the initial velocity imparted to the system.[2] All these quantities can be used as design parameters for the system, in order to optimize its deployment and ease the capture of debris. Further reasoning on the design parameters will be provided in Section 3.3.2.

[2]It can be demonstrated that $\dot{\rho}_i(0)$ depends both on v_e and the cosine of the angle θ between the initial velocity vector and the direction of deployment. Proof of this is provided in Appendix A.1.

3.2.4 Numerical validation of analytical findings

The outcome of the analysis is verified through numerical simulation of deployment with the MATLAB-based simulator presented in Chapter 2. This is done in Figure 3.8 for a deployment described by the data in Table 2.2, apart from $v_{e,net} = 1$ m/s: the first plot presents the velocity profiles for the center of mass of the corner masses $\bar{v}_c(t)$ and of the net proper $\bar{v}_{net}(t)$; the upper and lower bounds for both quantities, computed as indicated in the first line of Table 3.4, are drawn with horizontal dashed lines. The difference $\bar{v}_c(t) - \bar{v}_{net}(t)$ is depicted in the second plot of Figure 3.8, whereas the third plot presents $\varepsilon(t)$ during the deployment, computed as per equation (3.13), together with its maximum value ε_{max}, computed as per equation (3.22), and its initial value ε_0.

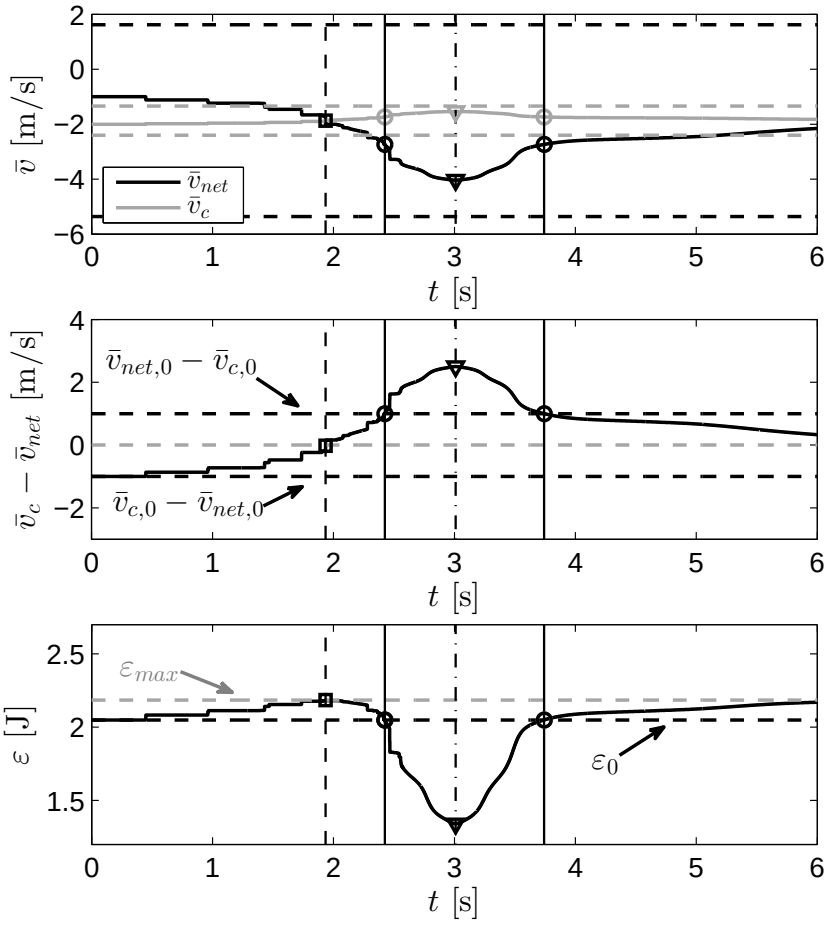

FIGURE 3.8: Numerical validation of analytical observations, for the general ejection scenario. Top: centroidal velocities (solid lines) and their analytical bounds (dashed horizontal lines). Middle: difference of centroidal velocities (solid line) and notable values (dashed lines). Bottom: $\varepsilon(t)$ (solid lines) and its notable values ε_0 and ε_{max} (dashed lines).

A few observations can be drawn from Figure 3.8 and allow validating the expressions collected in Tables 3.4 and 3.5. First, the limiting values for $\bar{v}_c(t)$ and $\bar{v}_{net}(t)$ are never

attained, and accordingly, $\varepsilon(t)$ is never zero. Second, it is clear that the situation when $\varepsilon(t) = \varepsilon_{min}$ corresponds to the instant when $\bar{v}_c(t)$ and $\bar{v}_{net}(t)$ are at their extrema, and the difference $\bar{v}_c(t) - \bar{v}_{net}(t)$ is maximum (see the vertical dash-dot line and the triangles). The times at which the centroidal velocities take values defined in Table 3.4 for $\varepsilon(t) = \varepsilon_0$ are identified and marked with circles and black vertical lines in the plots: this confirms the correspondence with the condition $\varepsilon(t) = \varepsilon_0$ at $t > 0$. Finally, $\varepsilon(t)$ is never higher than ε_{max}, which validates expression (3.22). The instant when $\varepsilon(t) = \varepsilon_{max}$ is indicated with a square and a black dashed vertical line in the plots and corresponds to the time when $\bar{v}_c(t) = \bar{v}_{net}(t) = p_0/M = -1.868$ m/s: observe that this value is exactly in the middle of the velocity bounds and whenever ε diminishes, the centroidal velocities approach their bounds (one its minimum, the other its maximum). It is also observed that after $\varepsilon(t)$ reaches its maximum, $\bar{v}_{net}/\bar{v}_c$ becomes larger than 1: therefore, the center of mass of the net proper may overtake the center of mass of the corner masses.

The analogous plots for the case in which only the corner masses are ejected also validated the analytical findings. In this case too, it was found that the center of mass of the net may overtake the center of mass of the corner masses during deployment.

Finally, a verification was performed for the deployment of a net with consideration of the bending stiffness of the threads, using the Vortex Dynamics implementation of the augmented lumped-parameter model introduced in Section 3.1.2 (see Figure 3.9). This confirmed the validity of the analysis for general modeling of the stiffness of the net threads as there is no dependence of $\varepsilon(t)$ on the specifics of the elastic potential energy.

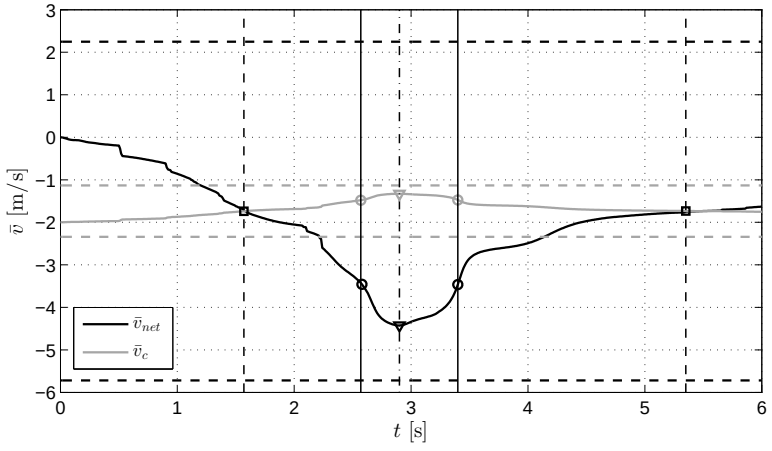

FIGURE 3.9: Numerical validation of analytical observations, for a net with representation of the bending stiffness of the threads and ejection of corner masses only ($v_{e,net} = 0$): centroidal velocities (solid lines) and their analytical bounds (dashed horizontal lines).

3.3 Results of deployment simulations

In Section 3.2, analytical findings on deployment dynamics were obtained and validated. Here, further interpretation of those findings is achieved by means of numerical simulations. The deployment sequence is visualized in Section 3.3.1 in two ejection scenarios and allows to study the effect of giving initial velocity to the net proper. The effect of the key parameters identified through analysis on the quality of deployment is investigated in Section 3.3.2.

3.3.1 Effect of giving initial velocity to net proper

In the following are reported results of net deployment simulations with initial velocity imparted to both the corner masses and the net proper, and to the corner masses alone, as per equations (2.8) and with $v_{e,net} = 1$ m/s or $v_{e,net} = 0$ respectively. Screenshots of the deployment phase shown in Figure 3.10 demonstrate different deployment dynamics for the two scenarios: in the first case, the net proper travels in the deployment direction from the start; in the second, it moves only after tensioning of the threads. One can notice that the net opens sooner in the second case, due to the higher relative velocity between the net and the corner masses. Notwithstanding the differences, in both simulations it is recognized that, after deployment is completed, the net overtakes the corner masses: this possibility was also suggested by the results of Section 3.2.4, and contradicts statements in the previous research [10].

The same observations are confirmed by Figure 3.11, which compares the distances traveled by the centers of mass of the net proper and of the corner masses in the two cases, as well as the evolution of the mouth area in time. Figure 3.11(a) demonstrates that in the first part of the simulation, approximately until the net reaches its maximum mouth area, the center of mass of the net proper is behind that of the corner masses; after that time the net overtakes the corner masses. Also, it is ascertained that, in the initial stage of the deployment, while the corner threads are slack, the motion of the center of mass of the corner masses is the same in both cases, whereas the center of mass of net proper moves in one case and remains still in the other. From Figure 3.11(b), it is seen that, if velocity is given to the net proper too, it takes more time for the net to start opening, and that the maximum value of mouth area is slightly lower, although it is reached somewhat earlier. The effective period (i.e., the time for which the mouth area is larger than 80% of its nominal value, as defined in Section 2.3) is of 0.9 s if velocity is given to both the corner masses and the net proper, as compared to 1.1 s for the case of velocity given to the corner masses alone. Although the specific values would vary depending on the ejection velocities, as well as on the net size, mass, and mesh properties, these results

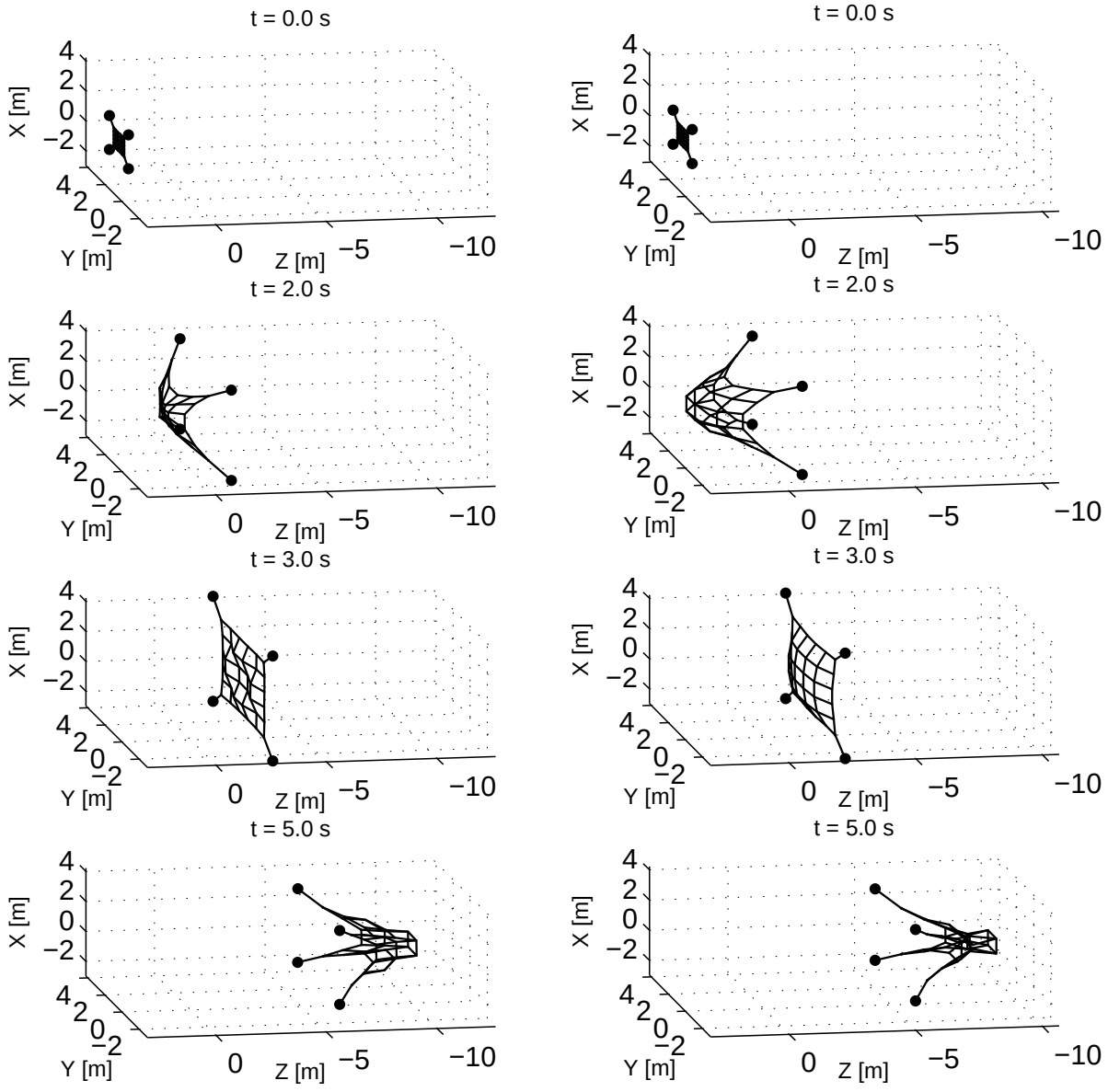

FIGURE 3.10: Screenshots of net deployment sequence. a) for initial velocity imparted to the net proper and to the corner masses; b) for initial velocity imparted only to the corner masses.

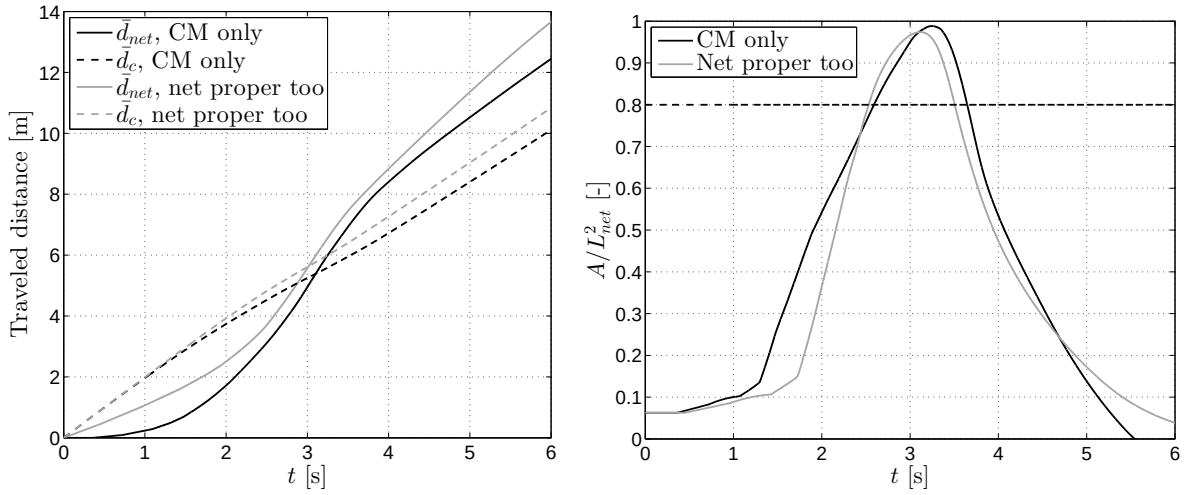

(a) (b)

FIGURE 3.11: Comparison of deployment simulation results when initial velocity is imparted only to the corner masses (CM), or also to the net proper. a) Distance traveled by the centers of mass of the net proper and of the corner masses. b) Mouth area.

suggest that ejection of the corner masses alone leads to a more complete and more lasting deployment.

3.3.2 Effect of key parameters on deployment and comparison to results in literature

From the expressions derived in Section 3.2.3, it is observed that the motion and configuration of the net during deployment depend on a few parameters that can be related to the mass properties of the system and to the initial conditions. For example, ε_{max} depends on ε_0, ultimately on the masses of the net and the corner masses, and on the magnitude and direction of the initial velocity. In Table 3.4, the dependence on the mass properties of the system appears in terms M_c/M, M_{net}/M, and M_{net}/M_c. However, it is likely that M_{net} will be determined by requirements on the configuration of the net and its material, that must guarantee envelopment of the target, withstand the capture loads, and contain pieces of debris possibly created during capture. This leaves M_c as the design parameter for the deployment. Also, the results in Section 3.3.1 indicate that ejection of the corner masses alone leads to a more complete and lasting deployment; therefore, the condition $\bar{v}_{e,net} = 0$ is preferred. The remaining parameters governing the deployment dynamics of nets in space can be reduced to:

- v_e the magnitude of the corner masses absolute ejection velocity;
- θ the shooting angle;
- M_c/M the ratio between the mass of the corner masses and the total mass.

	Investigated parameters				
Authors	v_e	θ	M_c/M (or m_{CM})	n	c
Present study	×	×	×		
Shan et al. [34]	×	×	×		
Salvi [21]	×	×	×	×	
Wormnes et al. [10]	×	×	×		
Lavagna et al. [9]	×	×	×		
Chen and Yang [31]		×			×

TABLE 3.6: Summary of existing studies on the effect of parameters on the quality of the deployment of nets in space.

Net and corner masses					
L_{net} (m)	$l_{net,0}$ (m)	r_{net} (m)	ρ_{net} (kg/m^3)	E_{net} (GPa)	ξ_a (-)
5	0.5	0.001	1390	70	0.106
l_{knot} (m)	$l_{CT,0}$ (m)	r_{CT} (m)	ρ_{CM} (kg/m^3)	m_{CM} (kg)	
0	0.7071	0.002	2700	parameter	
Initial conditions				**Simulation data**	
$v_{e,net}$	v_e (m/s)	θ (°)	α_{net} (-)	t_f (s)	Δt (s)
0	parameter	parameter	0.25	6	10^{-3}

TABLE 3.7: Data for the sensitivity study of a net deployment in space.

This Section summarizes the results of a sensitivity study showing how these parameters impact on the deployment dynamics, and gives a comparison with similar works in the literature. The main attributes of existing studies on the subject are summarized in Table 3.6. From this table, it is clear that the analytical derivation in Section 3.2.3 justifies many of the studies presented in the literature: there is agreement on the importance of v_e, θ, and M_c/M (or m_{CM}) in the deployment dynamics. Some authors have also studied the influence of the axial damping in the net threads c, and of the mesh number n (i.e., the number of meshes in the net).

As discussed in Chapter 2, multiple criteria to describe the quality of deployment have been proposed in the literature, but can be collected in the three categories introduced in Section 2.3: (i) *Maximum achievable deployment*, (ii) *Distance traveled*, and (iii) *Effective period*. The specific definitions employed in this Thesis were also given in Section 2.3. The numerical results of the performed sensitivity study are collected in Figure 3.12, for the net described in Table 3.7 (chosen of dimensions similar to other studies) and with initial velocity imparted to the corner masses only. For computational efficiency reasons, the Vortex Dynamics simulator was used to obtain the results in this Section; Δt is the fixed time-step size employed. Performance criteria (ii) and (iii) are particularly interesting from the point of view of safe and reliable capture of debris. Numerical results

for performance criterion (i) are included to support the observations on the effect of the different deployment parameters on the maximum deployment.

Table 3.8 proposes a comparison of the findings of existing studies and of the current research. Whereas the conclusions of this research are derived from the sensitivity study supported by Figure 3.12, the remaining information was inferred from graphs and discussions from available literature. The comparison of the findings is not straightforward, not only because of the different net configurations considered, but also because diverse ranges for the parameters are chosen, and the employed performance criteria are computed in different ways. For example, the *deployment area* is computed as the area of a rectangle defined by the position of the four corner masses by Shan et al. [34], whereas in this Thesis it is computed as the area of the polygon created by projecting on the $x-y$ plane the nodes on the perimeter of the net. In some papers, the performance criteria combine information from more than one of the identified criteria: for example, Salvi employed a *capture distance tolerance* criterion, that combines information from both the traveled distance and the effective period [21]. Finally, some authors provided suggestions on preferred values for these parameters, but did not study specifically how these impact on the deployment: for example, Wormnes et al. proposed *as low as reasonable* v_e, mass ratios on the order of 0.2, and θ such that the net is at its maximum deployment just before capture [10].

Notwithstanding the difficulties in the comparison of the results, overall agreement on the following findings was found:

- The extent of the maximum deployment is positively affected by increasing M_c/M and using moderate θ (see Figure 3.12(a) and (b)). Figure 3.12 suggests there is a lower limit to the mass ratio M_c/M for a successful deployment (i.e., reaching $A_{max}/L^2 > 0.8$ and non-zero effective period); however, it is also noticed that increasing M_c/M over a certain limit does not improve the quality of deployment. Differently, Shan et al. saw an increase in the maximum deployment area as θ is increased [34]. All studies considering variation of v_e found that this parameter barely has any effect on the maximum deployment; this is confirmed in Figure 3.12(a) and (b).

- The traveled distance decreases notably when θ is increased, whereas it does not depend sensibly on v_e nor on M_c/M (this is why the corresponding plot was omitted). The effects of θ and v_e are shown in Figure 3.12(e).

- The effective period decreases noticeably as v_e increases (see Figure 3.12(c) and (d)). It also decreases rapidly as M_c/M increases beyond 0.7 (as shown in Figure 3.12(c)) and depends strongly on θ, especially at low v_e (as shown in Figure 3.12(d)): in this

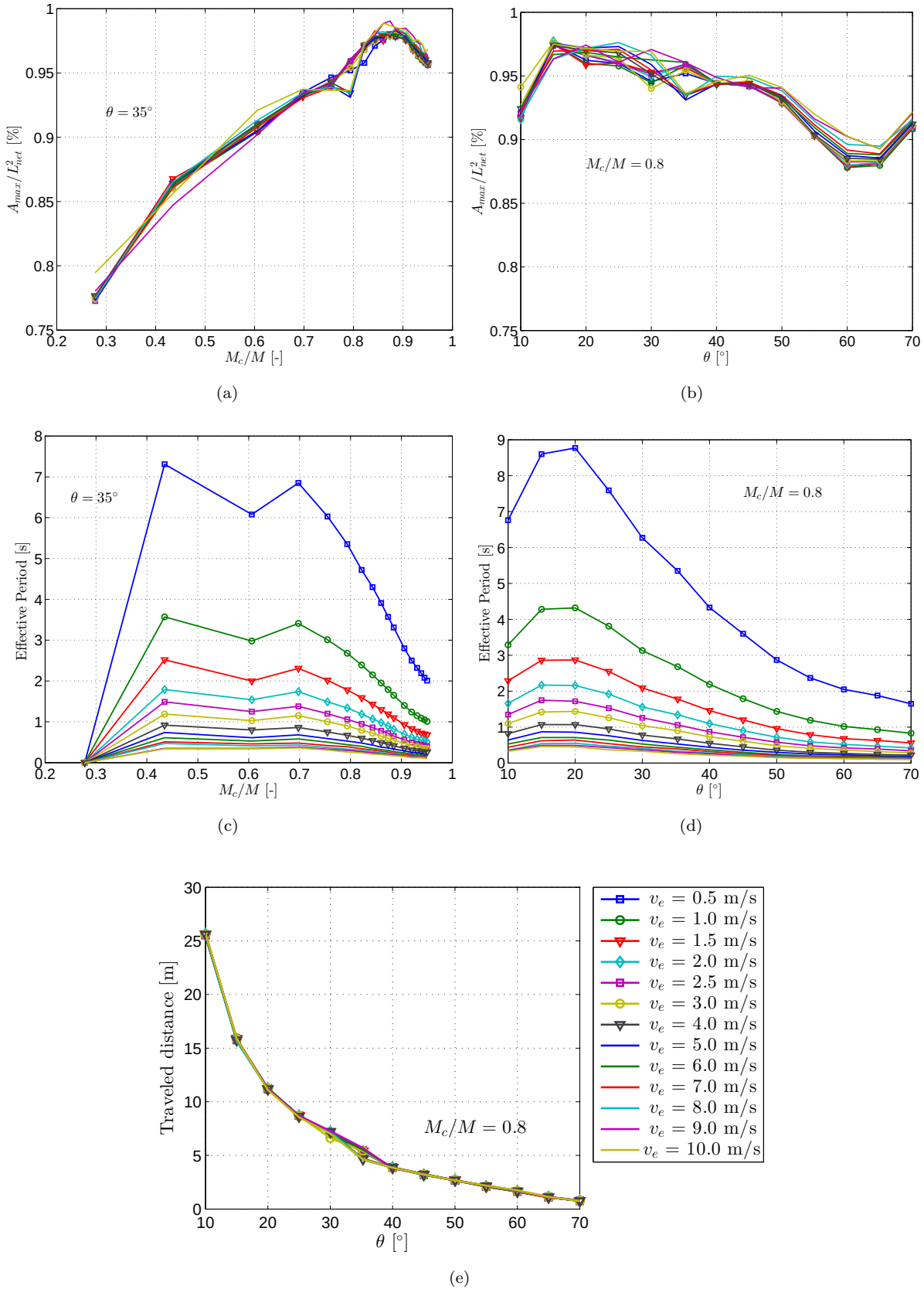

FIGURE 3.12: Results of sensitivity study on deployment of a 5×5 m^2 net. a) Maximum deployment varying v_e and M_c/M. b) Maximum deployment varying v_e and θ. c) Effective period varying v_e and M_c/M. d) Effective period varying v_e and θ. e) Traveled distance varying v_e and θ.

Authors	**Values**	**Max. deployment**	**Traveled distance**	**Effective period**
Effect of increasing v_e [m/s]				
Present study	0.5 - 10	Small effect	Small effect	Decreases (more at low M_c/M and θ)
Shan et al. [34]	10 - 28	Small effect	Small effect	Decreases
Salvi [21]	0.1 - 10	Small effect	Small effect on *capture distance tolerance*	
Lavagna et al. [9]	5 - 20	Optimum solution: 9 m/s	Not studied	
Effect of increasing θ [°]				
Present study	10 - 70	Increases till $\sim$ 20°, then decreases	Decreases	Increases till $\sim$ 20°, then decreases (more at low v_e)
Shan et al. [34]	35 - 70	Increases	Decreases	Small effect
Salvi [21]	5 - 50	Increases till $\sim$ 40°, then decreases	*Capture distance tolerance* increases till $\sim$ 40°, then decreases	
Lavagna et al. [9]	1 - 45	Optimum solution: 20°	Not studied	
Chen and Yang [31]	10 - 45	*Area when net has traveled 30 m* increases till $\sim$ 20°, then decreases		Not studied
Effect of increasing M_c/M [-]				
Present study	0.27 - 0.95	Increases till $\sim$ 0.9	Small effect	Decreases (more at low v_e)
Shan et al. [34]	0.89 - 0.98	Increases	Small effect	Increases or small effect
Salvi [21]	0.1 - 0.95	Increases	*Capture distance tolerance* increases till 0.6-0.95, then decreases	
Lavagna et al. [9]	0.75 - 0.98	Only found optimum solution (0.89)	Not studied	

TABLE 3.8: Summary of findings on the effect of the different parameters on the deployment dynamics.

study, it increases up to $\theta \approx 20°$, then decreases. The existence of optimal values of the shooting angle was also observed by other authors [9, 21]. Salvi concluded that the *capture distance tolerance* is higher for moderate values of M_c/M. On the other hand, the effect of M_c/M and θ could not be properly appreciated by Shan et al. because only a high value of ejection velocity ($v_e = 10$ m/s) was employed in their evaluations [34].

It should be noted that the same sensitivity analysis was performed for a larger net (20×20 m^2, with 0.5 m mesh length), and provided qualitatively the same results as those for the smaller net employed here.

Overall, considering that a long effective period increases the probability of successful capture, and that a large distance from the chaser to the target at capture is more desirable from the safety point of view, it seems preferable to use a moderate mass of the corner masses, a low initial velocity, and a low to moderate shooting angle. In the preliminary design of a net-based active debris removal mission, the results of the sensitivity studies suggest to select first the shooting angle, such that the distance traveled at the instant of maximum deployment is as desired, while maintaining a sufficient effective period; in fact, it was verified that the traveled distance does not depend on v_e or M_c/M. Then, the mass of the corner masses and the shooting velocity can be chosen to guarantee a sufficient effective period (of a few seconds). As far as the mass properties are concerned, these results suggest to use $0.4 < M_c/M < 0.7$. For example, for a 20×20 m^2 net with 0.5 m mesh length, assuming $15 - 50$ m as a reasonable distance for capture [8, 10], if $\theta = 20°$, $v_e = 2.5$ m/s and $M_c/M \approx 0.7$ are selected, then the obtained effective period is nearly 10 s and the traveled distance is around 42 m.

3.4 Effect of tension in the main tether on deployment dynamics

Up to this point in the Thesis, the net was considered isolated from the rest of the system; in reality, however, it must be attached to the chaser spacecraft via a main tether. The presence of a tether will always have an effect on the dynamics of the net, since tension is created in the tether and transmitted to the net when the latter moves and the mass of the tether is displaced. This Section examines the effect of the tensioning of the main tether on the deployment dynamics. To this end, Section 3.4.1 introduces the modeling of the chaser and of the tether implemented in the Vortex-Dynamics-based simulator. Section 3.4.2 discusses the effect observed in simulations of deployment with the chaser-tether-net system.

3.4.1 Modeling of chaser, tether and winch

The chaser is modeled as a simple cubic rigid body of side length L_{ch} and mass m_{ch}, free-floating without any thrust control. The tether linking the net to the chaser is modeled as a *flexible cable* in Vortex Dynamics, that is a series of multiple rigid bodies (capsules) constrained by means of relaxed prismatic constraints that allow to account for axial, bending, and torsional stiffness. The length of the tether is denoted with L_t, its cross-sectional radius r_t, and its density ρ_t. One end of the tether is attached to the central node of the net; the other end is attached to a winch on the chaser, that provides the

possibility to change the length of the cable in time (see a visualization of the system in Figure 3.13). The winch is modeled as a rigid body of cylindrical shape (with radius r_w and height h_w) and mass m_w. The spooling of the tether is controlled by means of a *hinge constraint* between the chaser part and the winch part. In the implemented simulator, it is possible to have a tether either locked, or free to spool out, or spooled in and out in a controlled way; combinations of these controls can also be achieved thanks to the flexibility of the simulator. The spooling velocity $\dot{L}_t(t)$ can be defined at every time step for which the hinge is motorized, and as the tether is winched in or out, parts are removed from or added to the cable.

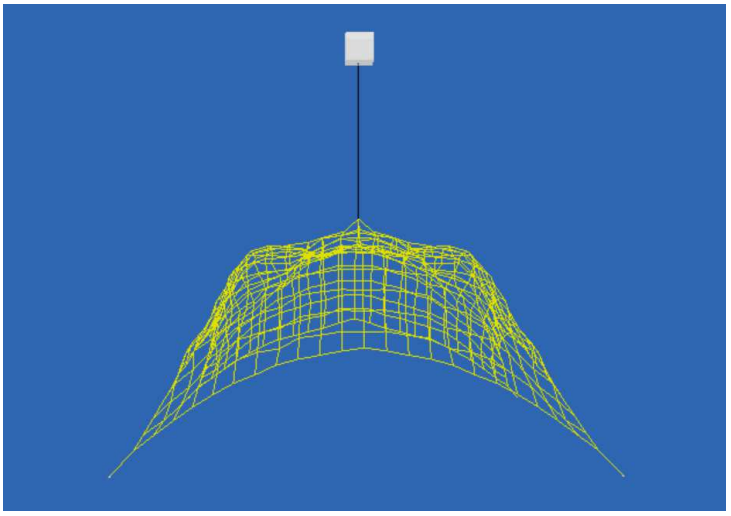

FIGURE 3.13: Visualization of the chaser-tether-net system.

A visualization of the model of flexible cables in Vortex Dynamics is proposed in Figure 3.14. Before introducing the tether in the simulator of the system at hand, the modeling of *cables* in Vortex Dynamics was tested separately, in simpler configurations and in the absence of the net, with and without the winch. Multiple benchmark tests were created for this purpose and allowed to reverse-engineer the cable model, by comparing the results of simulations to analytical solutions: the most relevant tests are included in Appendix B. Namely, it was observed that, for a cable made of n_{sec} parts (i.e., rigid bodies), $n_{sec} - 1$ prismatic joints are introduced, and therefore, the flexible length of the cable is $(n_{sec} - 1)/n_{sec}$ times the total length (i.e., the length depicted in red in Figure 3.14 is not flexible). The physical stiffness of the cable can be prescribed by specifying a modified value for the axial and bending stiffness of the cable:

$$(EA)_u = (EA)\frac{n_{sec} - 1}{n_{sec}} \tag{3.28}$$

$$(EI)_u = (EI)\frac{n_{sec} - 1}{n_{sec}} \tag{3.29}$$

In this Thesis, the tether is assumed to have negligible torsional stiffness.

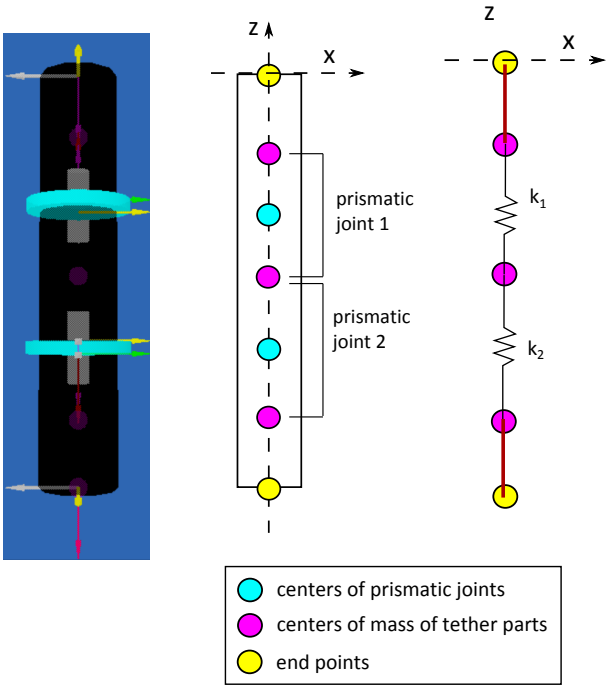

FIGURE 3.14: Visualization of a flexible cable in Vortex dynamics, and scheme of the composing parts and joints. Cable made of three parts and two prismatic joints. The segments in red are not flexible.

3.4.2 Deployment simulations in presence of main tether

The aim of this Section is to analyze the impact of the dynamics of the main tether on the deployment of the net. This is achieved by evaluating the identified deployment performance indices (maximum mouth area, effective period, traveled distance) under different *open loop* tether winching controls:

D1: the tether is free to spool out as it is tensioned by the net;
D2: the tether is free to spool out until t_w, then it is locked;
D3: the tether is free to spool out until t_w, then it is spooled in at a rate of 1.5 m/s;
D4: the tether is free to spool out until t_w, then it is spooled out at a rate of 2 m/s;
D5: the tether is free to spool out until t_w, then it is spooled out at a rate of 4 m/s;
D6: the tether is spooled out at a constant rate of 2 m/s.

In order to make the simulations more relevant and in preparation for the simulation of the overall ADR mission, a larger net is employed for the results in this Section, in particular of 22 m side length. Its parameters are collected in Table 3.9. The net is assumed to be stowed in a 1.1 m^2 square area, $d_{ch} = 0.1$ m below the lower part of the chaser, and its deployment is achieved by imparting initial velocity to the four corner masses alone. The tether material is assumed to be the same as that of the net (i.e., the Young's modulus and the density are the same).

Chaser spacecraft			**Winch**		
d_{ch} (m)	L_{ch} (m)	m_{ch} (kg)	r_w (m)	h_w (m)	m_w (kg)
0.1	1.5	1600	0.05	0.02	0.1
Tether					
	r_t (m)	ρ_t (kg/m^3)	E_t (GPa)	ξ_b (-)	
	0.002	1390	70	0.014	
Net and corner masses					
L_{net} (m)	$l_{net,0}$ (m)	r_{net} (m)	ρ_{net} (kg/m^3)	E_{net} (GPa)	ξ_a (-)
22	1	0.0005	1390	70	0.106
l_{knot} (m)	$l_{CT,0}$ (m)	r_{CT} (m)	ρ_{CM} (kg/m^3)	m_{CM} (kg)	
0	1.4142	0.0007	2700	0.5	
Initial conditions				**Simulation data**	
$v_{e,net}$	v_e (m/s)	θ (°)	α_{net} (-)	t_f (s)	Δt (s)
0	2.5	36.87	0.05	30	10^{-3}

TABLE 3.9: Data for the simulation of a deployment in space with the chaser-tether-net system.

With a free tether, the net reaches the threshold $A = 0.8L_{net}^2$ after almost 16 s of simulation. In order to see the effect of the tether controls on the deployment performance indices, the instant when the tether starts being winched was chosen as $t_w = 17$ s for controls D2–D5. With control D3, the effect of spooling the tether in is investigated: this is not expected to help the deployment, but the discussion of the spooling-in effect will pave the way for the study of possible capture mechanisms. For control D4, the magnitude of the spooling velocity was chosen lower than the spooling velocity observed in simulation with a free tether (see control D1 in Figure 3.15); for control D5, it is larger than the spooling velocity of a free tether. Finally, spooling out is prescribed since the beginning of the simulation for control D6, to study the impact of spooling out the tether earlier than the onset of movement of the center of the net (which happens at $t \approx 10.5$ s with a free tether).

In Figure 3.15, the prescribed rates of change of the tether length $\dot{L}_t(t)$ for the different controls and relevant time periods are plotted with black dashed lines; these are compared with the rates of change of the tether length obtained in the simulations, depicted with gray solid lines. It is observed that, whenever the winch is motorized, the rate of change of the tether length follows closely the imposed winching velocity; when the tether is free, the rate of change of the tether length varies in different ways, which are determined by the dynamics of the net at that instant.

In the following, results with these open loop controls are compared with each other and with respect to the case where no tether is provided: this condition is not realistic, but serves to compare the results to the existing literature. The profiles of net mouth area

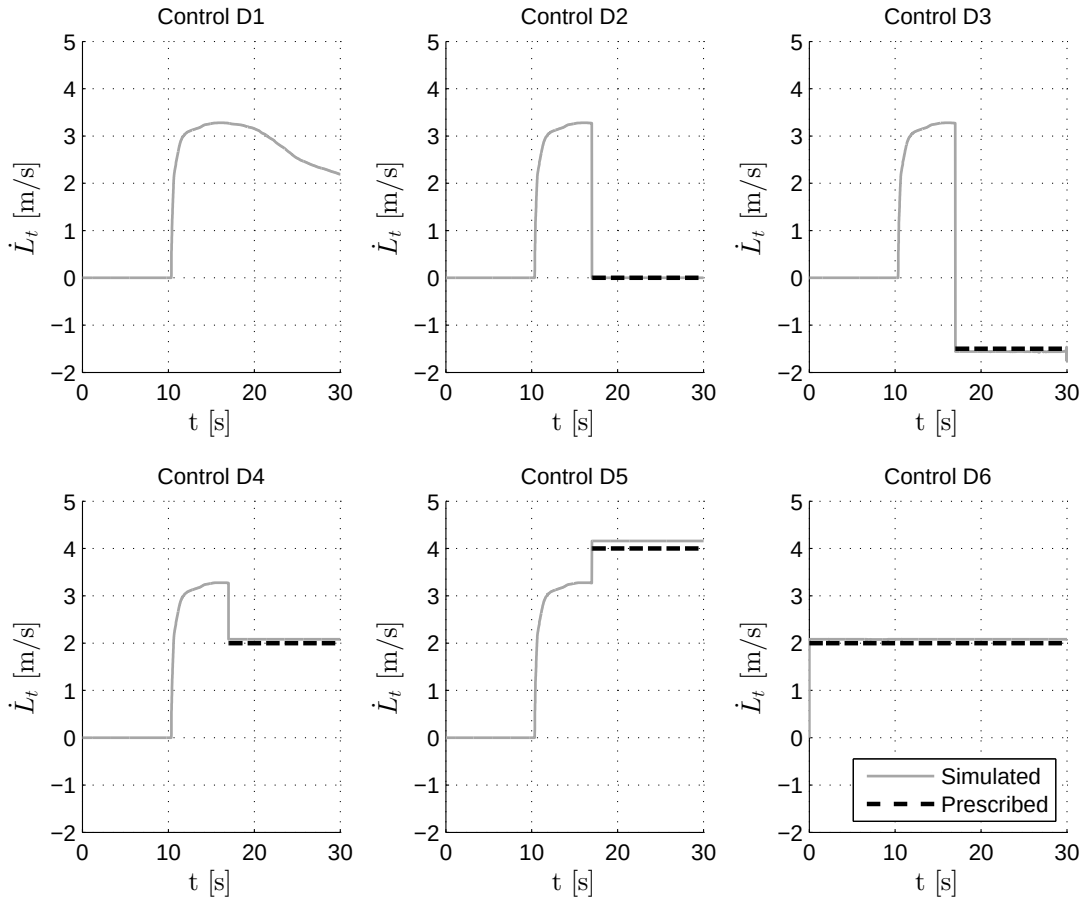

FIGURE 3.15: Prescribed open loop winching controls (black dashed lines) and obtained tether length rates (gray solid lines) in simulations of deployment.

as a function of the distance traveled by the center of mass of the net during deployment are depicted in Figure 3.16. The maximum mouth area is provided as a percentage of the nominal mouth area L_{net}^2. The threshold $A/L_{net}^2 = 0.8$ is shown with a dashed black line; although the effective period cannot be read directly from this graph, one can get some insight on the achievement of the condition for effective capture. Keeping in mind that larger values of maximum mouth area, of traveled distance, and of effective period are preferred for capture, one can observe that situations with no tether, free tether (i.e., control D1), and tether spooled out with control D4 are superior. In particular, it is noticed that spooling the tether out after the effective mouth area threshold is achieved is helpful for maintaining the net deployment: the effective period obtained with control D4 is 13% longer than that obtained with a free tether. The scenario where the tether is spooled out since the beginning of the deployment (i.e., control D6) grants higher traveled distances, but reduces the maximum mouth area and, especially, the effective period. In the case where the tether is free and then locked or spooled in (i.e., controls D2, D3), the mouth area undergoes a steep decrease as soon as the control is applied. Similar degradation of the performance indices is encountered in a situation where the tether is spooled out faster than it would with a free tether (i.e., control D5). Numerical values for

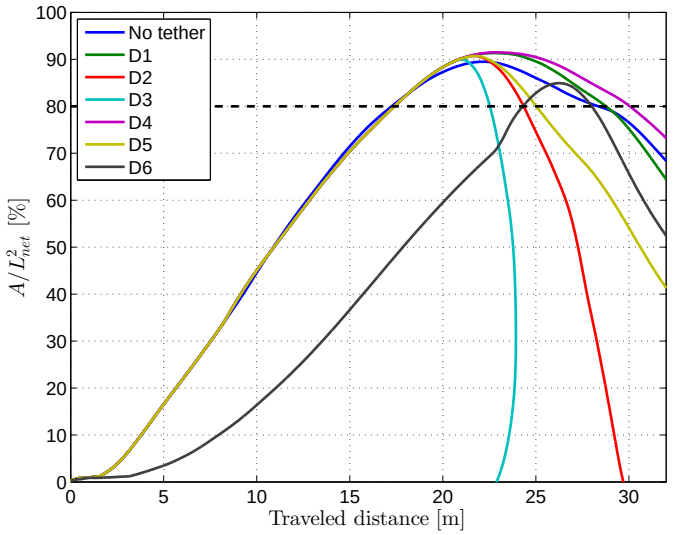

FIGURE 3.16: Mouth area versus distance traveled by the center of mass of the net during deployment.

TABLE 3.10: Results of deployment with different tether controls.

Performance index	**No tether**	**D1**	**D2**	**D3**	**D4**	**D5**	**D6**
A_{max}/L_{net}^2 (%)	89.5	91.3	90.7	90.0	91.5	90.7	84.9
Effective period (s)	4.9	5.4	3.5	2.7	6.1	3.5	1.4
Traveled distance (m)	22.1	22.8	21.7	21.0	22.8	21.8	26.3
Max tension (N)	n.a.	3.5	3.5	16.0	3.5	3.5	0.9

the maximum mouth area, the effective period, and the traveled distance obtained with the different controls are collected in Table 3.10. In this table additional information on the maximum tension experienced in the tether is included.

To complete the analysis of deployment, Figure 3.17 reports the maximum value of tension in the tether at each time, as retrieved with code during the simulation[3]. It is observed that a tension of around 3.5 N appears in the tether after the central mass of the net moves (i.e., at $t \approx 10.5$ s) for all simulations starting with a free tether (i.e., all but control D6); after this first peak, tension decreases quickly. It reappears at $t_w = 17$ s, especially in the locked tether and a tether that is spooled in; afterwards some visible tension persists in the tether.

Overall, the results of this analysis show that, almost any case in which a tether is included reduces the effective period, with respect to the deployment of the net alone; the only cases that prove slightly better are controls D1 and D4. From these results and for the sake of achieving a reliable capture of large space debris, it is recommended either to keep the tether free during the deployment of the net (which is simpler), or to spool it out

[3]As explained in Section 3.4.1, the flexibility of the tether is represented by a series of prismatic joints. The tension experienced in these joints can vary along the tether. Here, the maximum value of tension experienced along the tether at each instant is represented.

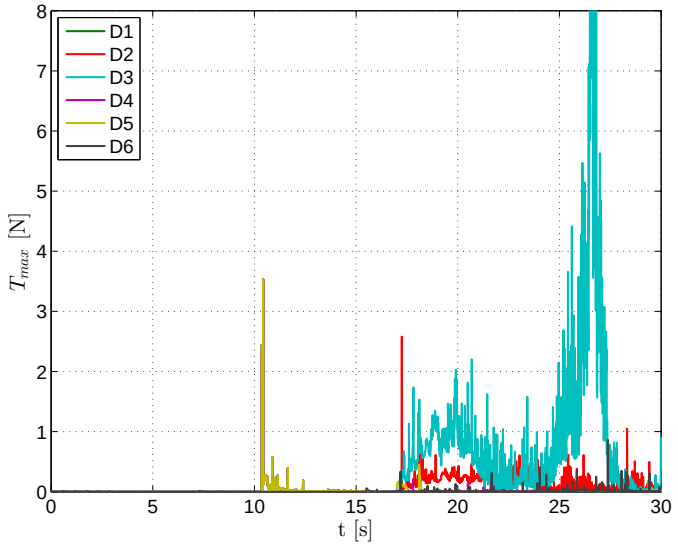

FIGURE 3.17: Maximum tension in the tether during simulation of deployment.

with a moderate velocity after the achievement of the effective mouth area (which gives better results). Spooling the tether out after the achievement of a desired deployment can help to maintain the net in the deployed configuration for a longer time. Based on the observation of the effect of tension during the deployment, it is conjectured that spooling in the tether after deployment – which generates significant tension in the tether – would be helpful in speeding up the capture dynamics, since the onset of significant tension in the tether brings the net to a closure.

3.5 Closing remarks on deployment dynamics

Chapters 2 and 3 dealt with the deployment dynamics of tether-nets for ADR. Simulators based on lumped-parameter models for the net were presented, validated against on-ground experiments and against each other, and employed to perform a number of analyses. A novel contribution is the evaluation of the effect of bending stiffness of the threads of the net on the deployment dynamics; although uncertainty exists on the stiffness properties of the threads in space, the impact of their bending stiffness on the configuration of the net during deployment may be important. Analytical derivations allowed to identify in a formal way (and for the first time, to the author's knowledge) bounds on centroidal velocities, as well as key parameters that govern the behavior of the net during deployment: the total mass of the system, the ratio between the mass of the corner masses and the total mass, the magnitude and direction of the initial velocities. A sensitivity study showed that more lasting deployment and safer capture can be obtained by employing moderately heavy corner masses, moderate shooting angles, and low shooting velocities. The possibility that the net may overtake the corner masses

upon deployment was confirmed. When the main tether was introduced, it was found that more complete and lasting deployment can be achieved either by keeping the tether free to spool out, or by spooling it out with a moderate velocity after the achievement of the effective mouth area. It was also verified that onset of moderate tension in the tether (obtained for example by spooling the tether in) brings the net to a closure.

Part III

Capture dynamics

Chapter 4

Capture Dynamics

Part II of this Thesis dealt with the deployment of tether-nets in space, whose success is tantamount to the effective capture of space debris. In the remainder of this Thesis, the actual net-based capture of space debris is addressed. As one can easily imagine, the simulation of capture of debris with a flexible system as complex as a tether-net is far from trivial. Multiple contact events are expected to occur, both among different parts of the net and between the net and the target debris. Therefore, the representation of the effect of contacts between the bodies in the system under consideration is key to the fidelity of the simulation to reality; at the same time, modeling and computational issues arise.

Evaluation of the success of capture is arduous *per se*: overall quantities describing the complex configuration of the net during capture have to be defined. The rotational motion of the target makes things even more complicated. The criteria devised for analyzing the results of capture in this Thesis are introduced in Section 4.1. A short literature review on the options for modeling contact dynamics is given in Section 4.2. The chosen approach is detailed in Section 4.3, together with its implementation in the MATLAB-based simulator; a simplified capture scenario is considered at this stage, to lighten the burden of collision detection. With this simplified scenario, the effect of contact modeling choices is investigated in Section 4.4. Modeling of contact dynamics in the Vortex-Dynamics-based simulator is presented in Section 4.5, and the simulation tool is employed in Section 4.6 to evaluate the effect of representing the bending stiffness of the threads of the net on the capture dynamics. Finally, the robustness of the net-based capture maneuver to inaccuracies in deployment is explored in Section 4.7.

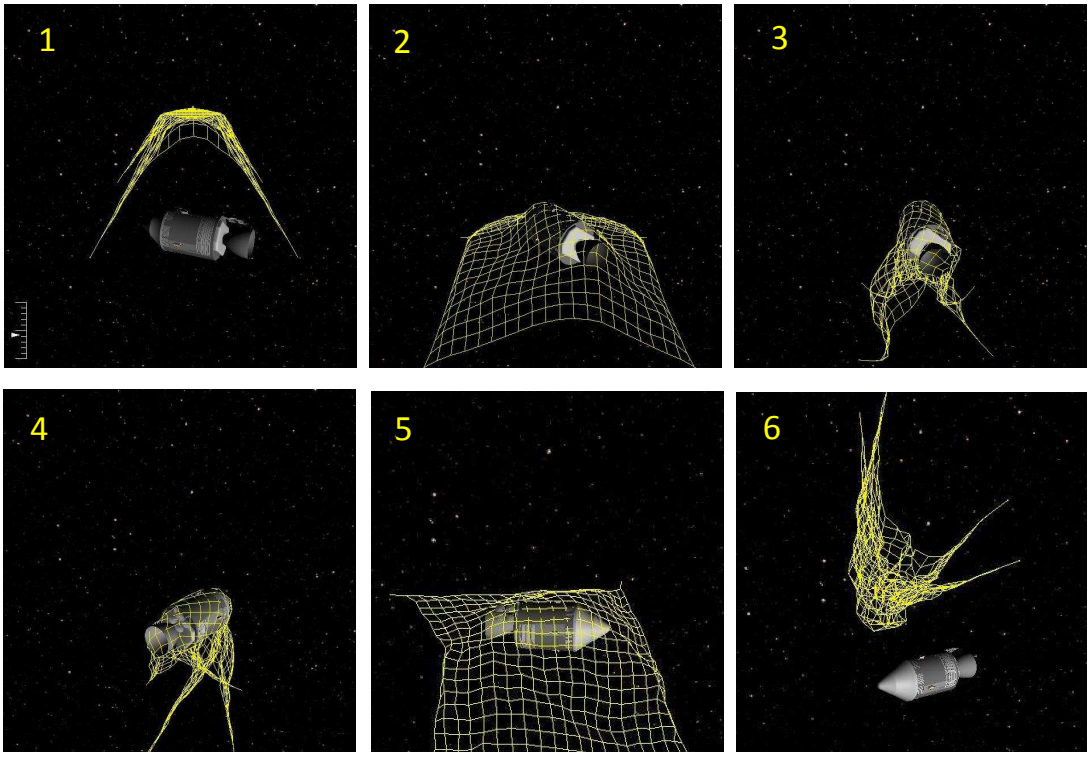

FIGURE 4.1: Illustration of net-based capture of rotating debris.

4.1 Criteria for successful capture

The evaluation of the effectiveness of capture of space debris with a tether-net is a difficult task, especially in the absence of a closing mechanism. For illustrative purposes, Figure 4.1 shows some screenshots of a simulation of capture of rotating debris. It is clear that the dynamics of the net after capture is complicated and hard to describe.

A few characteristic traits were identified to describe qualitatively the success of the maneuver:

1. Envelopment: said to occur whenever the net goes around the whole debris (see Figure 4.1, screenshot 3).
2. Envelopment sufficiently long for a closure mechanism to work successfully: if the mouth shape of the net remains entangled for more than 10 s[1].
3. Slip off: if, after envelopment, the mouth section is open and contact with the debris is lost (see Figure 4.1, screenshot 5).
4. Fly away: when the distance between net and debris increases after slip off (see Figure 4.1, screenshot 6).

The presence or absence of these features in the capture simulation results is evaluated thanks to their graphics visualization and by post-processing the simulation data (namely,

[1] 10 s is the time that was deemed sufficient for a closing mechanism to work in this study.

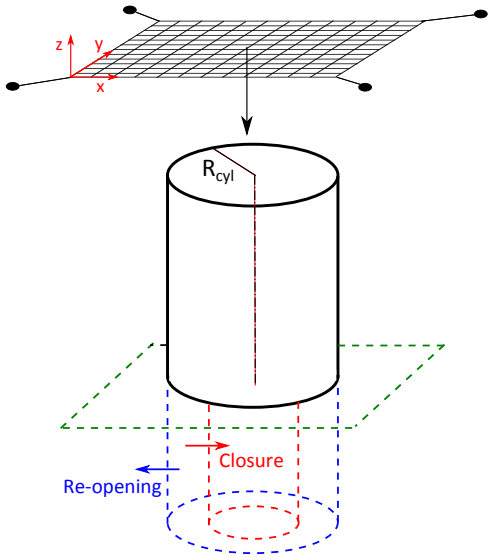

FIGURE 4.2: Illustration of criteria to describe the success of net-based capture of a cylindrical object.

the position of the nodes of the net in time). These criteria will prove useful in Sections 4.6 and 4.7.

A different set of criteria was defined for simpler capture scenarios, such as capture of non-rotating objects of more regular shape (such as cylinders). Three significant events in the capture maneuver were identified:

1. First impact between net and debris;
2. Closure of the net;
3. Re-opening of the net.

For the capture of a cylindrical object of radius R_{cyl} such as in the scenario illustrated in Figure 4.2, one can define *closure* as the instant when the four corner masses of the net enter a circle of radius $R_{cyl}/2$ (chosen arbitrarily and shown in red) beyond the distal surface of the target, and subsequent *re-opening* as the instant when the four corner masses exit a circle of radius R_{cyl} (shown in blue). These situations can be identified programmatically at run-time and will be used to evaluate quantitatively the effect of modeling choices on the success of capture in a simplified scenario in Section 4.4.

Finally, closing mechanisms that rely on tethers intertwined around the perimeter of the net or linking the four corner masses have been proposed in the literature to close the net around the target [10, 37]. For successful capture with closing mechanisms of this type, it is necessary that the closing maneuver is initiated when the corner masses are farther than the distal part of the target object (i.e., below the green plane in Figure 4.2), while the net is around it. To ease the process of closure, it is advantageous that the corner masses remain in this condition for as long as possible, so that more time is available for the closing mechanism to work. This criterion will be employed in Section 5.1.

4.2 Review of contact dynamics modeling

Many approaches are available for modeling contact dynamics: for a comprehensive literature review the reader may refer to the work by Gilardi and Sharf [69]. Two families of approaches to contact dynamics are *impulsive* models, and *continuous* models. Continuous models, as opposed to impulsive models, consider the contact phase to have finite duration and are well-suited to describe the evolution of multibody systems [69]. Within this class of methods, *compliant* and *complementarity* formulations can be distinguished [70].

In the *compliant* formulation the contact force normal to the surface of the colliding bodies is defined explicitly as a function of the local indentation (or penetration) and its rate. Multiple linear and non-linear expressions have been proposed: surveys have recently been published by Alves et al. [71] and Banerjee et al. [72], and more information will be provided in Section 4.3.2 of this Thesis. Any type of friction model can be used in the continuous compliant contact approach, both for sticking and slipping conditions. The basic model is Coulomb's dry friction law, which states that the magnitude of the friction force is proportional to the normal contact force in sliding conditions and undefined in sticking conditions; it can be improved by smoothing the transition from sticking to sliding conditions, which eliminates its typical discontinuity. Some alternatives are Stronge's expression for sticking contact, in which the tangential force is proportional to the tangential displacement of the contact point, and the *bristle* model, for which friction is proportional to a vector called bristle displacement (more detail on this can be found in Section 4.3.3). Whenever collisions occur, the Degree of Freedoms (DOFs) of the problem are separated into free and constrained: the dynamics equations for the free DOFs remain unchanged with respect to the unconstrained ones, while the others are modified by the contact dynamics through the addition of normal and tangential forces. Since both are already expressed in terms of the generalized coordinates, the system can be directly solved for those. The main drawback of any of the compliant contact force models is the need to evaluate the contact parameters [70].

In the *complementarity* formulation, no penetration is allowed and the contact is dealt with by enforcing the non-penetration constraints on all constrained DOFs. Additionally, sticking contact conditions are set for the DOFs subject to sticking contact; friction for slipping contact is expressed directly as a function of the normal contact force and the generalized coordinates. The resulting system of ODEs and constraints is cast in the form of a mathematical optimization problem, such as a Linear Complementarity Problem (LCP) or a Quadratic Programming (QP), for which solvers exist, and can be solved for the unknowns: the normal contact force vectors, the sticking friction force vectors, and the generalized coordinates. Unilateral constraints in terms of displacements can also

be differentiated once or twice in time to obtain a velocity-impulse or an acceleration-force formulation. Unfortunately, the solution of a complementarity problem is NP-hard, therefore computationally challenging.

Only few works in the literature on tether-nets for ADR available prior to this research gave details on how contact between the net and the target was treated. Bombelli modeled the geometry of the target as a 3D body, but its dynamics as that of a point mass; he assumed perfectly inelastic collisions between the knots of the net and the target: a node impacting the target acquired the same dynamics as the center of mass of the target [19]. A compliant approach, based on a linear normal contact force and Coulomb's friction force was implemented in a software upgrade by Benvenuto and Lavagna [36]. Wormnes et al. exploited the simulation capabilities of Bullet physics engine, in which the contact is dealt with by imposing linearized velocity constraints (that replace the non-penetration constraints); friction force is accounted for with an extremely simplified model, in which the tangential force does not depend on the normal force [10]. As recognized by the authors themselves, even though this approach is computationally affordable, this comes at a cost of lower physical relevance. Golebiowski et al. have also exploited the collision detection capabilities of Bullet physics engine and have modeled contacts with impulsive methods in the normal direction and with Coulomb's law in the tangential direction [30]. Yu et al. mentioned considering the problem of impact between a slack net and a rigid ball; however, no explanation of the implemented model for contact was provided [61].

4.3 Modeling of contact dynamics in MATLAB

It is foreseen that the contact scenario will be particularly complex for the problem under study. Since it is interesting to know how the system evolves during contact, and considering that the solution of a complementarity problem is NP-hard, a continuous compliant model was chosen for the implementation of contact dynamics for net-based debris capture. When the dynamics equations for the nodes of the net were stated, in equation (2.7), a term related to external forces was included. In the study of deployment dynamics in vacuum and in the absence of gravity, this term was irrelevant; however, external forces appear when contacts occur between the i-th mass and another body. The aim of this Section is to define these contact forces. Underlying the representation of contact forces are the detection of collisions and the description of contact geometry, which are addressed in Section 4.3.1. Once this information is available, normal contact forces and friction forces can be defined, as described in Sections 4.3.2 and 4.3.3.

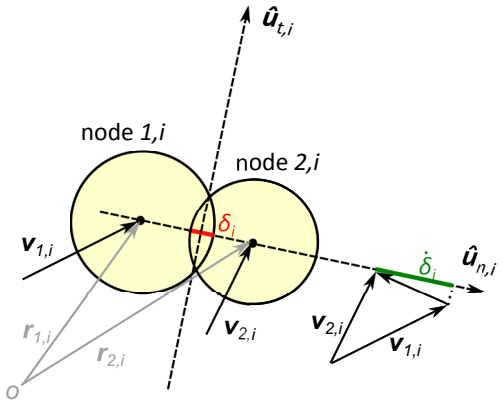

FIGURE 4.3: Collision detection and definition of penetration (in red) and rate of penetration (in green) for impact between two nodes in contact pair i.

4.3.1 Collision detection and contact geometry

In order to accurately represent collisions among the lumped masses composing the net, the corner masses, and the target of capture, collision detection must be performed at every time step of the simulation. This consists in checking if any of the net nodes and of the corner masses collide with each other and/or with the target; if this happens, a *contact pair* is created for each two colliding bodies, the geometry of contact is defined, and a contact force is applied to the bodies involved in the contact.

For collision detection and contact geometry purposes only, each node and corner mass is modeled as a sphere of radius proportional to its mass. Any of the impact events between two nodes of the net or corner masses can be seen as an impact between two spheres of generally different radii $R_{1,i}$ and $R_{2,i}$. The direction normal to the contact plane in impact pair i, $\hat{\mathbf{u}}_{n,i}$, can be defined with a unit vector in the direction linking the centers of mass of the two spheres, as shown in Figure 4.3 (in this figure, $\hat{\mathbf{u}}_{t,i}$ indicates a direction in the plane of contact). If $\mathbf{r}_{1,i}$ and $\mathbf{r}_{2,i}$ are the position vectors of the centers of mass of the two spheres in contact pair i with respect to the origin O of the inertial frame of reference, $\hat{\mathbf{u}}_{n,i}$ is defined as:

$$\hat{\mathbf{u}}_{n,i} = \frac{\mathbf{r}_{2,i} - \mathbf{r}_{1,i}}{||\mathbf{r}_{2,i} - \mathbf{r}_{1,i}||} \tag{4.1}$$

The two spheres are said to intersect when the distance between their centers of mass becomes smaller than the sum of their radii: $||\mathbf{r}_{2,i} - \mathbf{r}_{1,i}|| < R_{2,i} + R_{1,i}$. If this happens, the two spheres are colliding with velocities $\mathbf{v}_{1,i}$ and $\mathbf{v}_{2,i}$, and the penetration and rate of penetration (depicted in red and green in Figure 4.3) are found as:

$$\delta_i = R_{1,i} + R_{2,i} - ||\mathbf{r}_{2,i} - \mathbf{r}_{1,i}|| \tag{4.2}$$

$$\dot{\delta}_i = -(\mathbf{v}_{2,i} - \mathbf{v}_{1,i}) \cdot \hat{\mathbf{u}}_{n,i} \tag{4.3}$$

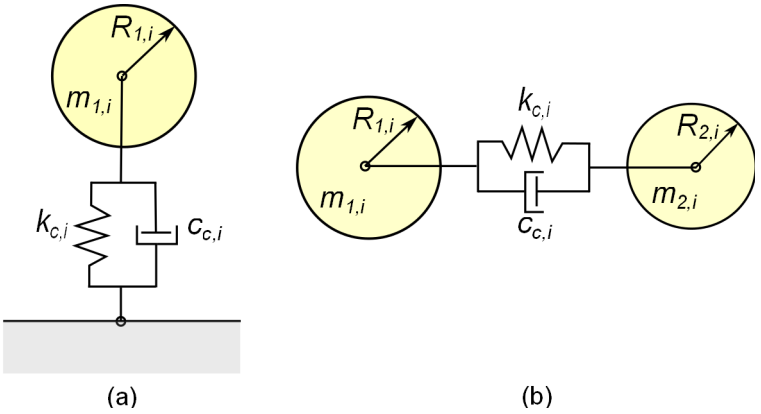

FIGURE 4.4: Continuous compliant normal contact force model for contact pair i. (a): sphere-plane. (b): sphere-sphere.

The detection of collisions between the nodes of the net and a target object depends on the geometry of the second. An example will be provided in Section 4.4.

Accurate collision detection is critical to the accuracy of the simulation of contact, for example to avoid unrealistically high contact forces due to artificially large penetrations. In order to accurately detect collisions in the numerical simulations, a 1×10^{-6} tolerance was selected for the employed Runge-Kutta integration scheme. It is anticipated that the need for such accuracy in the detection of collisions will considerably affect the computational efficiency of the simulation. It should also be noted that this modeling approach allows representing collisions only at the nodes of the net, and not along the threads; therefore, this method will only work for the detection of collisions with debris that does not have thin structural elements (this issue will be treated in Section 5.4 of this Thesis). This is expected to cause non-physical interpenetration among the threads of the net and between the threads of the net and the target, as well as underestimation of the energy lost due to contacts.

4.3.2 Normal force modeling

The normal contact force, by definition, acts in the direction normal to the contact plane: $\mathbf{F}_{n,i} = F_{n,i}\hat{\mathbf{u}}_{n,i}$. Note that, due to the definition given for $\hat{\mathbf{u}}_{n,i}$ in contact pair i between two spheres, the force vectors applied to the two masses, to be used in the $\mathbf{F}_{ext}$ term of equation (2.7), are $\mathbf{F}_{n,2,i} = F_{n,i}\hat{\mathbf{u}}_{n,i}$ and $\mathbf{F}_{n,1,i} = -F_{n,i}\hat{\mathbf{u}}_{n,i}$. The magnitude of the normal contact force $F_{n,i}$ remains to be determined and is the topic of the current Section.

Over the years, many continuous compliant models have been proposed for the contact force generated in the direction normal to the contact plane; interesting recent comparative studies can be found in references [71] and [72]. Typically, a spring simulates the elastic behavior, while a damper dissipates part of the energy during contact.

The linear model has been widely used because of its simplicity: the normal contact force is thought to arise from a linear spring and a linear damper placed in parallel between the two contacting bodies (see the conceptual representation in Figure 4.4 for contacts between (a) a sphere and a plane, and (b) two spheres). If, for the i-th contact, $k_{c,i}$ is the contact stiffness coefficient and $c_{c,i}$ is the contact damping coefficient (these coefficients being dependent on material and geometrical properties, in ways that will be shown later), the normal contact force can be simply computed as:

$$F_{n,i} = k_{c,i}\delta_i + c_{c,i}\dot{\delta}_i \tag{4.4}$$

A better representation of the normal contact force is the non-linear spring-damper model introduced by Hunt and Crossley [73], which overcomes the problems of the linear model, namely the discontinuity of the force at the beginning of impact and a non-physical "sticking" force keeping the bodies together at the end of impact [69]. In this formulation, the normal force arising at the i-th contact is found as:

$$F_{n,i} = \bar{k}_{c,i}\delta_i^n + \lambda_i\delta_i^n\dot{\delta}_i \tag{4.5}$$

where n is a constant dependent on the contact scenario, $\bar{k}_{c,i}$ the non-linear stiffness coefficient, and λ_i the non-linear damping coefficient.

In this Thesis, both the linear model (4.4) and a family of non-linear models (4.5) with different expressions for λ_i have been implemented. In order to define the stiffness and damping coefficients of the models, a few reasonable assumptions and considerations are made. First of all, all contacts are assumed to be elastic. Second, and for contact geometry purposes only, the nodes of the net are approximated to spheres of radii proportional to their mass, as already mentioned. Since target debris is characterized by dimensions much bigger than each node of the net, the first is approximated with a plane in the vicinity of each contact: impacts between a node of the net and the target, or between a corner mass and the target, are therefore modeled as impacts between a sphere and a plane. As a consequence, apart from some special cases (e.g., a node impacting an edge or vertex of the target), impact happens between two continuous and non-conforming surfaces, which make first contact at a point and for which the resulting stresses are highly concentrated. For computing contact stiffnesses, each contacting body can also be approximated to an elastic half-space loaded over a small elliptical region of its surface: in fact, the dimension of the contact area is expected to be much smaller than the characteristic dimensions of the bodies and than the radii of curvature of their surfaces at the impact point. Within these assumptions, Hertzian contact theory is valid and it is possible to use the well-known results summarized below; the reader is referred to Johnson's work for a detailed treatment of Hertzian theory [74].

For the reasons discussed above, the contact between the net and a debris target is studied as the result of the contact between the nodes of the net and a plane (see Figure 4.4(a)), ignoring singular cases such as contacts between a node of the net and an edge of the debris. According to Hertzian contact theory for this scenario, n appearing in equation (4.5) is 1.5 and the contact stiffness $\bar{k}_{c,i}$ relative to the impact of the i-th node with the debris can be computed with:

$$\bar{k}_{c,i} = \frac{4}{3}\sqrt{R_i}E_i^* \tag{4.6}$$

$$E_i^* = \frac{E_{1,i}}{1-\nu_{1,i}^2} + \frac{E_{2,i}}{1-\nu_{2,i}^2} \tag{4.7}$$

In these expressions, $E_{j,i}$ and $\nu_{j,i}$ for $j = 1, 2$ are the Young's modulus and the Poisson's ratio of the material of each body impacting at contact i, and R_i is the radius of the i-th sphere. For collisions between two nodes of radii $R_{1,i}$ and $R_{2,i}$ forming the i-th contact pair (see Figure 4.4(b)), the contact stiffness is found as:

$$\bar{k}_{c,i} = \frac{4}{3}\sqrt{R_{eq,i}}E_i^* \tag{4.8}$$

$$R_{eq,i} = \frac{R_{1,i}R_{2,i}}{R_{1,i}+R_{2,i}} \tag{4.9}$$

The contact stiffness employed in the linear normal contact force model is estimated as $k_{c,i} = \bar{k}_{c,i}(2\delta_{max}/3)^{n-1}$, with $\bar{k}_{c,i}$ from equation (4.6) or (4.8), once the order of magnitude of the penetration occurring between the bodies δ_{max} is assessed. This estimation is justified by the fact that, if damping is temporarily neglected, $F_{n,i} = k_{c,i}\delta_i$ should approximate linearly $F_{n,i} = \bar{k}_{c,i}\delta_i^n$ while passing through zero.

The damping coefficient in the linear model is computed as $c_{c,i} = 2\xi\sqrt{m_{c,i}k_{c,i}}$ with ξ as the chosen damping ratio and $m_{c,i}$ a mass that depends on the type of contact pair:

$$m_{c,i} = \begin{cases} m_i & \text{if sphere - plane} \\ \frac{m_{1,i}m_{2,i}}{m_{1,i}+m_{2,i}} & \text{if sphere - sphere.} \end{cases} \tag{4.10}$$

On the other hand, the damping coefficient in the non-linear models λ_i has attracted the attention of many researchers, who have proposed different expressions, among which are those reported in Table 4.1. These models make use of $v_{0,i}$, the relative velocity in the normal direction at the beginning of the contact event, and α_c, a coefficient that relates the coefficient of restitution e to the initial impact velocity as $e = 1 - \alpha_c v_0$ [73].[2] For the non-linear damping coefficients to be accurate, the energy dissipated during the contact process should be consistent with that defined as per the restitution coefficient. Alves et

[2]The coefficient of restitution e is a measure of the energy loss due to the motion in the direction normal to the contact plane. Multiple models exist for its definition.

Authors	**Expression**
Hunt-Crossley [73]	$\lambda_{HC,i} = \frac{3}{2}\alpha_c k_{c,i}$
Herbert-McWhannel [77]	$\lambda_{HM,i} = \frac{3}{2}\alpha_c \bar{k}_{c,i}\left(\frac{1}{1-\alpha_c v_{0,i}+\alpha_c^2 v_{0,i}^2}\right)$
Lee-Wang [78]	$\lambda_{LW,i} = \frac{3}{4}\alpha_c \bar{k}_{c,i}$
Lankarani-Nikravesh [79]	$\lambda_{LN,i} = \frac{3}{2}\alpha_c \bar{k}_{c,i}\left(1-\frac{\alpha_c v_{0,i}}{2}\right)$
Zhang-Sharf [76]	$\lambda_{ZS,i}$: $\bar{k}_{c,i}\ln\left[\frac{\lambda_i v_{0,i}+\bar{k}_{c,i}}{-\lambda_i(1-\alpha_c v_{0,i})v_{0,i}+\bar{k}_{c,i}}\right] - 2\lambda_i v_{0,i} + \alpha_c \lambda_i v_{0,i}^2 = 0$

TABLE 4.1: Different expressions for damping coefficient in non-linear models.

al. recommend employing Gonthier et al.'s model [75], or the equivalent model by Zhang and Sharf, because of their ability to correctly model the dissipation of energy for any value of the coefficient of restitution, including more plastic impacts [71]. For this work, it was chosen to implement the most traditional non-linear models as well as Zhang and Sharf's model, all of which were thoroughly discussed in reference [76]. Banerjee et al. suggest using two other models, one of which is linear, and the other is piecewise non linear [72]. Because of the non-physical "sticking" force issues related to linear models and the additional discontinuities that would be introduced by piecewise functions, it was decided not to include these two models in the simulator at hand. Only the traditional Kelvin-Voigt model – which was used in previous works on the simulation of net-based capture of debris, such as [27] – was included in order to highlight its problems. It is also worth mentioning that the non-linear models, relying on Hertz theory, can make use of the previously described relationships to evaluate the contact stiffness and damping coefficients; this makes them preferable with respect to the linear models. A drawback is the introduction of additional parameters, such as α_c, that are not always known nor easily evaluated.

4.3.3 Friction force modeling

Strictly speaking, Hertzian theory is valid only for frictionless contact. However, it is demonstrated that normal compression and tangential displacement can be treated separately [74]. In particular, tangential traction does not affect normal motion if the two materials are similar; in any case the effect is small and can reasonably be neglected (about 5% variation on the normal force) [74]. Therefore the normal force can always be found with Hertzian theory.

Since the nodes are modeled as point masses, friction force is expected to have a significant effect on their motion in case of continued contact only. This was found to happen only between the net and the debris; therefore, and for the sake of computational efficiency, contacts among nodes of the net and corner masses are assumed to be frictionless in the

MATLAB-based simulator. For contacts between the net nodes and the target, friction force is modeled; in this case, contact is complicated by different possible conditions: slipping and sticking. It is well-known that, in the slipping regime (i.e., when there exists relative velocity between the contacting bodies), the friction force is proportional to the normal contact force: $F_t = \mu_k F_n$, with μ_k the kinetic friction coefficient. Modeling of friction force in the sticking regime is more uncertain and has been the topic of multiple studies. In the traditional Coulomb's model, the value of friction force in sticking is not uniquely defined: $F_t \leq \mu_s F_n$, with μ_s the static friction coefficient. Multiple efforts to uniquely define this force, as well as to smoothen the transition from sticking to sliding friction have been made, for example in references [74, 80–85]. Among the various friction models available in the literature, Johnson's and bristle model are considered here because of their capability to explicitly and uniquely define the friction force both in sticking and slipping conditions.

4.3.3.1 Johnson's model

Jonhson studied the sticking regime as incipient sliding: while there is no sliding motion between the two contacting bodies as a whole, the friction force causes a small relative motion over a portion of the interface (this is called *micro-slip*) [74]. For two spheres in sticking contact, Johnson found that the relative tangential displacement $\delta_{t,i}$ can be related to the friction force with:

$$\delta_{t,i} = \frac{F_{t,i}}{8a_i}\left(\frac{2-\nu_{1,i}}{G_{1,i}} + \frac{2-\nu_{2,i}}{G_{2,i}}\right) \tag{4.11}$$

$$a_i = \left(\frac{3F_{n,i}R_{eq,i}}{4E_i^*}\right)^{1/3} \tag{4.12}$$

where $G_{j,i}$ for $j = 1, 2$ is the shear modulus of the materials of the contacting bodies, and E_i^* and $R_{eq,i}$ are defined in equations (4.7) and (4.9). Using the expression for the normal contact force by Hertz $F_{n,i} = \bar{k}_{c,i}\delta_i^n$ with $n = 1.5$, and extending the expression to 3D, the force of friction can be written as:

$$\mathbf{F}_{t,i} = k_{t,i}\boldsymbol{\delta}_{t,i} \tag{4.13}$$

$$k_{t,i} = 8\sqrt{R_{eq,i}}\delta_i^{1/2}G_i^* \tag{4.14}$$

$$G_i^* = \left[\frac{2-\nu_{1,i}}{G_{1,i}} + \frac{2-\nu_{2,i}}{G_{2,i}}\right]^{-1} \tag{4.15}$$

In these equations, $\boldsymbol{\delta}_{t,i}$ is the vector of relative tangential displacement and $k_{t,i}$ is the tangential stiffness for the i-th contact pair. Observe that the tangential stiffness varies during a contact, depending on the instantaneous penetration δ_i.

4.3.3.2 Bristle model

The bristle model imitates the presence of irregularities of the surfaces using bristles. In the original undamped model by Haessig and Friedland, the friction force is defined in 1D as $F_t = k_{br}s$, where k_{br} is the equivalent bristle stiffness and s is the bristle deflection [80]. This idea was extended to 3D by Ma et al. [84], and a damped version of the 3D model was proposed by Liang et al. in order to stabilize the oscillations during the transition between sliding and sticking regimes [81]. The undamped 3D model reads [81]:

$$\mathbf{F}_t = -k_{br}\mathbf{s} \tag{4.16}$$

$$\mathbf{s} = \begin{cases} \mathbf{s}_0 + \int_{t_0}^{t} \mathbf{v}_t d\tau & \text{if} \quad ||\mathbf{s}|| < s_{max} \\ s_{max}\hat{\mathbf{v}}_t & \text{if} \quad ||\mathbf{s}|| \geq s_{max} \end{cases} \tag{4.17}$$

$$s_{max} = \frac{\mu F_n}{k_{br}} \tag{4.18}$$

$$\mu = \begin{cases} \mu_k & \text{if} \quad v_t > v_d \\ \mu_s & \text{if} \quad v_t \leq v_d \end{cases} \tag{4.19}$$

In equation (4.17), $\mathbf{s}_0$ is the deflection at the starting time of contact t_0, $\mathbf{v}_t$ is the vector of relative tangential velocity between the two contact bodies at the contact point, $\hat{\mathbf{v}}_t$ its direction and v_t its magnitude. The maximum bristle deflection s_{max} is defined as per equation (4.18) and depends on the sticking or slipping regime as indicated by equation (4.19); the boundary between sticking and slipping conditions is dictated by a threshold magnitude of relative velocity v_d. It should be noted that, in the equations above, all the quantities but k_{br}, μ_k, μ_s, and v_d are functions of time; the dependence on time is omitted here and in the following to simplify the notation.

The damped bristle friction model reads [81]:

$$\mathbf{F}_t = -k_{br}\mathbf{s} - c_{br}\dot{\mathbf{s}} \tag{4.20}$$

with c_{br} the bristle damping coefficient (independent of time), and $\dot{\mathbf{s}}$ the derivative of the bristle deflection at time t. The related algorithm is not thoroughly explained in [81], but while implementing this model, it was found that the inclusion of the damping term undermines the physical consistency of the model, if equations (4.17) and (4.18) are not revised. In particular, any micro-slip friction model is expected to be consistent with Coulomb's model of friction, that is $||\mathbf{F}_t|| \leq \mu F_n$. In the context of bristle model (4.16), this is achieved through the appropriate definition of s_{max}. However, for the damped case (4.20), the conditions for switching between sticking and slipping (i.e., equations (4.17)-(4.19)) must be modified to ensure that $||-k_{br}\mathbf{s} - c_{br}\dot{\mathbf{s}}|| \leq \mu F_n$. This is achieved if it is observed that $\dot{\mathbf{s}} = \mathbf{v}_t$ if $||\mathbf{s}|| < s_{max}$ and it is declared that $\dot{\mathbf{s}} = \mathbf{0}$ when $||\mathbf{s}|| = s_{max}$. In

addition, as far as recovering the direction of the friction force in sliding, it is necessary to impose that the bristle deflection vector $\mathbf{s}$ is in the direction of $\mathbf{v}_t$. The modified definitions for the damped bristle friction model of equation (4.20) are proposed as:

$$\mathbf{s} = \begin{cases} \mathbf{s}_0 + \int_{t_0}^{t} \mathbf{v}_t d\tau & \text{if} \quad ||\mathbf{F}_t|| \leq \mu F_n \\ s_{max}\hat{\mathbf{v}}_t & \text{if} \quad ||\mathbf{F}_t|| > \mu F_n \end{cases} \tag{4.21}$$

$$\dot{\mathbf{s}} = \begin{cases} \mathbf{v}_t & \text{if} \quad ||\mathbf{F}_t|| \leq \mu F_n \\ \mathbf{0} & \text{if} \quad ||\mathbf{F}_t|| > \mu F_n \end{cases} \tag{4.22}$$

where s_{max} is defined with equation (4.18) and μ is selected with equation (4.19). For this model, initial conditions for both $\mathbf{s}(t_0)$ and $\dot{\mathbf{s}}(t_0)$ must be consistently set. In particular, initial conditions are computed as: $\mathbf{s}_0 = (\mu_k F_n / k_{br})\hat{\mathbf{v}}_t$ and $\dot{\mathbf{s}}_0 = \mathbf{0}$ if the contact point is sliding; $\mathbf{s}_0 = \mathbf{0}$ and $\dot{\mathbf{s}}_0 = \mathbf{v}_t$ if the contact point is sticking.

For the problem at hand, $\mathbf{v}_{t,i}$ for each contact pair is found at every time step by projecting the relative velocity vector on the tangent plane: remembering that friction is modeled only for contacts with the stationary target (see Section 4.3.3), $\mathbf{v}_{t,i} = (\mathbf{1} - \hat{\mathbf{u}}_{n,i}\hat{\mathbf{u}}_{n,i}^T)\mathbf{v}_i$, $\mathbf{1}$ being a 3-by-3 identity matrix. If contact begins for pair i, initial conditions are computed; otherwise, the bristle deflection $\mathbf{s}_i$ is found from its value at the previous step - if contact is sticking - or from its maximum - if slipping - as per equation (4.21). Similarly, $\dot{\mathbf{s}}_i$ is found with equation (4.22), and the friction force $\mathbf{F}_{t,i}$ is computed with equation (4.20), knowing $k_{br,i}$ and $c_{br,i}$.

The implementation of the damped bristle model in 3D was validated by simulating the dynamics of a block sliding on a slope following a curved trajectory, as was proposed by Liang et al. [81]: the results of this validation are collected in Appendix C.1. The implementations of Johnson's model and of the damped bristle model were also validated by simulating the dynamics of a point mass dragged on the ground with a linearly increasing force (see Appendix C.2). Upon comparison of the results and performance of simulations with the two models, it was noticed that the damped bristle friction model has a few advantages over Johnson's friction model: fewer transitions between sticking and slipping regimes, a more continuous friction force magnitude, and, consequently, a much lower computational time. For these reasons, the damped bristle friction model was chosen for simulation of the contact between the net and the debris target. Nonetheless, Johnson's model proved helpful in selecting the value for the bristle stiffness coefficient $k_{br,i}$ by making direct correspondence between equations (4.13) and (4.16). In particular, the constant k_{br} was estimated by fitting in the least squares sense the curve $k_t = k_t(\delta)$ for one contact pair with a polynomial of degree zero, from $\delta = 0$ to δ_{max}. The damping coefficient was then estimated as $c_{br} = 2\xi\sqrt{mk_{br}}$, with m the mass of an internal node

of the net. The coefficients of the bristle model are assumed to be independent of the contacting node ID.

4.4 Effect of contact dynamics modeling on capture dynamics

It is clear from the previous Section that a multitude of continuous compliant contact dynamics models exist in the literature, and there is no evident specific reason to select any one of these models. In this Section, the effect of choosing different models to represent the contact dynamics is investigated. The solution of the capture of an object with a net is challenging both from a computational point of view (because of contact detection issues, geometry considerations, and the inherent non-linearities) and from a description point of view. Section 4.4.1 describes a simplified capture scenario that allows to evaluate quantitatively the effect of contact modeling choices on the capture success; the implemented collision detection strategy is also presented. Section 4.4.2 collects the results and draws conclusions on the issue.

4.4.1 Simplified capture scenario

A reasonable scenario to be simulated in MATLAB is the capture of a stationary cylindrical target approximating the shape of launcher upper stages, which represent the majority of high priority targets for ADR missions [4]. The chosen geometry allows to simplify the contact detection phase and eases the evaluation of the capture success (allowing the use of the quantitative criteria introduced in Section 4.1).

Capture happens after a net deployment phase similar to that discussed in Part II: the net is initially in a stowed configuration on the inertial x-y plane, initial velocity is imparted to the four corner masses in a symmetrical way, and the net fully deploys in a few seconds. The cylindrical target is oriented so as to have its axis parallel to the inertial z-axis (see Figure 4.2); it is defined by specifying its radius R_{cyl}, its height H_{cyl}, and the position of its center in the inertial reference frame $(x_{cyl}, y_{cyl}, z_{cyl})$. The distance of the i-th mass, with position (x_i, y_i, z_i) in the inertial reference frame, from the axis of the cylinder is computed at every time step as:

$$d_i = \sqrt{(x_i - x_{cyl})^2 + (y_i - y_{cyl})^2} \tag{4.23}$$

Each of the three surfaces of the cylinder is assigned an index: 1 indicates the top circular area, 2 the lateral surface, and 3 the bottom circular area. Conditions for contact of a

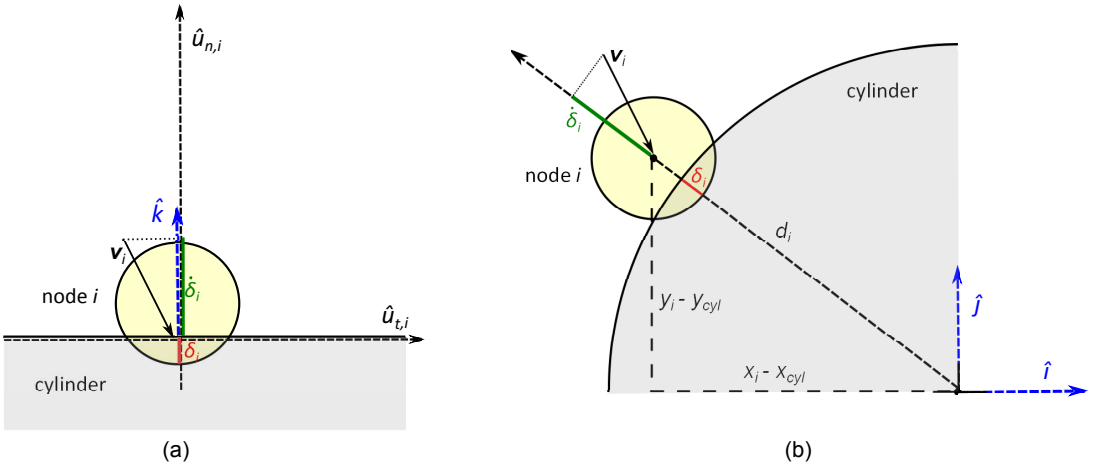

FIGURE 4.5: Collision detection and definition of penetration (in red) and rate of penetration (in green) for impact between node i and the cylinder. (a): face 1 and face 3. (b): face 2. Directions parallel to inertial axes indicated in blue.

Face #	Conditions for contact	Normal direction
1	$(d_i < R_{cyl}) \wedge (z_i \leq z_{cyl} + H_{cyl}/2 + R_i)$	$\hat{\mathbf{k}}$
2	$(z_{cyl} - H_{cyl}/2 < z_i < z_{cyl} + H_{cyl}/2) \wedge (d_i \leq R_{cyl} + R_i)$	$\hat{\mathbf{u}}_{n,i,2}$
3	$(d_i < R_{cyl}) \wedge (z_i \geq z_{cyl} - H_{cyl}/2 - R_i)$	$-\hat{\mathbf{k}}$

TABLE 4.2: Conditions for contact and definition of normal direction for each face of the cylinder.

node with each of the faces, as well as the direction normal to the plane of contact $\hat{\mathbf{u}}_{n,i}$, are collected in Table 4.2. In Figure 4.5 are reported the definitions of penetration and rate of penetration in the impacts between a node of the net and a face of the cylinder. The normal direction $\hat{\mathbf{u}}_{n,i,2}$ in case of contact with face 2 is defined as shown in Figure 4.5(b) and per the following equation:

$$\hat{\mathbf{u}}_{n,i,2} = [(x_i - x_{cyl})/d_i \quad (y_i - y_{cyl})/d_i \quad 0]^T \tag{4.24}$$

In Table 4.2, the second condition for contact determines whether penetration δ_i between a node or corner mass and a face of the cylinder occurs, i.e., whether $\delta_i > 0$. The penetration δ_i is therefore defined for each face as expressed in that condition; for example, for face 1, $\delta_i = R_i - (z_i - z_{cyl} - H_{cyl}/2)$. The rate of penetration is given by the derivative of δ_i, or by $\dot{\delta}_i = -\mathbf{v}_i \cdot \hat{\mathbf{u}}_{n,i}$ with $\mathbf{v}_i$ the velocity of the i-th mass in the inertial reference frame (since the target is stationary); for face 1, it is $\dot{\delta}_i = -\mathbf{v}_i \cdot \hat{\mathbf{k}} = -v_{z,i}$.

The target is assumed to be infinitely massive; this is justified by the ratio between the mass of a realistic debris (thousands of kilograms) and of a realistic net system (on the order of kilograms). As a result, forces and moments transmitted to the debris upon impact of the net have negligible effect on its motion.

4.4.2 Results of capture simulation with different contact force models

Simulation of capture of a stationary cylindrical debris with a net was performed with each of the models presented in Section 4.3.2, with and without friction. This allowed to evaluate the effect of employing different models on the overall capture dynamics. The parameters employed for these simulations are collected in Table 4.3. It should be noted that, for contact dynamics simulation purposes, several coefficients related to the materials of the contacting bodies need to be defined. In these simulations, the net is assumed to be made of Kevlar (a polymeric material having properties similar to Technora), and the corner masses and target are assumed to be made of aluminum; data on Kevlar was taken from references [86] and [87]. Although the density of Kevlar is slightly different from that of Technora, the conclusions of this study will not be affected. A search in the literature was performed to characterize the contact parameters, but some more assumptions were necessary. For the static friction coefficients μ_s, Kevlar-Kevlar pairs were assumed comparable to Nylon-Nylon pairs and Aluminum-Kevlar pairs were assumed comparable to Aluminum-Teflon pairs (data were obtained from reference [88]); the kinetic friction coefficients μ_k were estimated by dividing μ_s by 1.25. The threshold magnitude of the tangential relative velocity for sticking-slipping transition was set arbitrarily to $v_d = 0.001$ m/s. The α_c coefficients (formerly introduced in Table 4.1 to evaluate the non-linear damping coefficients λ_i) were estimated from experimental results on impact by Goldsmith [89][3]. As was mentioned at the end of Section 4.3.3, k_{br} and c_{br} coefficients were assumed independent of the contacting node ID.[4] Also, the contact stiffness coefficients, found as per equations (4.6) to (4.9), were divided by 10 in order to compensate the fact that the mass is lumped in the nodes.

The numerical simulation proved itself able to represent the contacts between the net and the debris, and among the nodes of the net. Figure 4.6 shows some snapshots of the system during capture, comparing the results obtained with the linear and Hunt and Crossley's non-linear normal contact force models. The net is deployed and contact with the cylinder is seen at $t = 2.0$ s. Due to contact with the cylinder, the net envelops it, and discrepancies in the positions of nodes and corner masses become appreciable between the two models (e.g., at $t = 4.0$ s). The corner masses impact each other below the target because of symmetry (at $t \approx 5$ s), and open again afterwards (e.g., at $t = 6.0$ s). In

[3] $\alpha_{c,al-al}$ was estimated by linearly interpolating an experimental plot of $e = e(v_0)$ for impact between spheres of the same size made of aluminum. In the absence of more relevant information, $\alpha_{c,al-net}$ and $\alpha_{c,net-net}$ were estimated by linearly interpolating an experimental plot of $e = e(v_0)$ for impact between a tennis ball and a stone slab.

[4] Bristle stiffness coefficient k_{br} was found by fitting in the least square sense $k_t(\delta)$ as per equation (4.14) from $\delta = 0$ to $\delta = \delta_{max} \approx 10^{-4}$ m (δ_{max} was estimated from a first run of the simulation). To evaluate k_t, in addition to the parameters in Table 4.3, $G_{al} = 25$ GPa and $G_{net} = 2.9$ GPa (from reference [87]) were employed.

Net and corner masses					
L_{net} (m)	$l_{net,0}$ (m)	r_{net} (m)	ρ_{net} (kg/m^3)	E_{net} (GPa)	ξ_a (-)
5	1	0.001	1440	70	0.106
l_{knot} (m)	$l_{CT,0}$ (m)	r_{CT} (m)	ρ_{CM} (kg/m^3)	m_{CM} (kg)	
0	1.4142	0.002	2700	0.5	
Target					
R_{cyl} (m)	H_{cyl} (m)	x_{cyl} (m)	y_{cyl} (m)	z_{cyl} (m)	
1	2	2.5	2.5	-2	
Contact parameters					
E_{al} (GPa)	ν_{al} (-)	ν_{net} (-)	$\alpha_{c,al-al}$ (s/m)	$\alpha_{c,al-net}$ (s/m)	$\alpha_{c,net-net}$ (s/m)
69	0.33	0.36	0.25	0.05	0.05
k_{br} (N/m)	c_{br} (Ns/m)	v_d (m/s)	$\mu_{s,al-al}$ (-)	$\mu_{s,al-net}$ (-)	μ_s/μ_k (-)
1.05×10^8	206	0.001	0.42	0.19	1.25
Initial conditions				**Simulation data**	
$v_{e,net}$	v_e (m/s)	θ (°)	α_{net} (-)	t_f (s)	ϵ (-)
0	2.5	36.87	0.5	8	10^{-6}

TABLE 4.3: Data for the simulation of net-based capture in a simplified scenario.

Figure 4.7 the responses with Hunt and Crossley's model with and without friction are compared. In this case, the discrepancies in the net configuration at corresponding times are less important, and become appreciable just after impact of the corner masses.

The times needed for integration with the five non-linear models with friction, of the linear model with friction, as well as Hunt and Crossley's model without friction, are compared in Figure 4.8(a); all simulations were performed on a laptop with Intel Core i7-4712HQ CPU @ 2.30 GHz. It is noticed that simulation with Lankarani and Nikravesh non-linear model took the longest time to integrate ($\approx$ 55 min), whereas simulation with Hunt and Crossley's and Lee and Wang's models took approximately half the time (between 24 and 26 min); as could be foreseen, a shorter integration time (of $\approx$ 11 min) was sufficient to perform a simulation without friction. In order to evaluate the effect of employing the different contact models on the overall dynamics, the three significant events in the capture maneuver that were identified in Section 4.1 are employed: (1) first impact with the debris, (2) closure defined as the instant when the four corner masses enter a circle of radius $R_{cyl}/2$, and (3) subsequent re-opening of the net defined as the instant when the four corner masses exit a circle of radius R_{cyl}. These noteworthy instants of time are compared in Figure 4.8(b). The time of first contact, as expected, is exactly the same ($t \approx 1.8$ s) in any simulation. Closure happens at $t \approx 4.7$ s in every simulation; the earliest closure is obtained at $t = 4.72$ s with Lee and Wang's model, the latest one is found at $t = 4.75$ s with the linear model. The simulated responses become more differentiated with time, as more contacts occur. Thus, re-opening of the corner masses

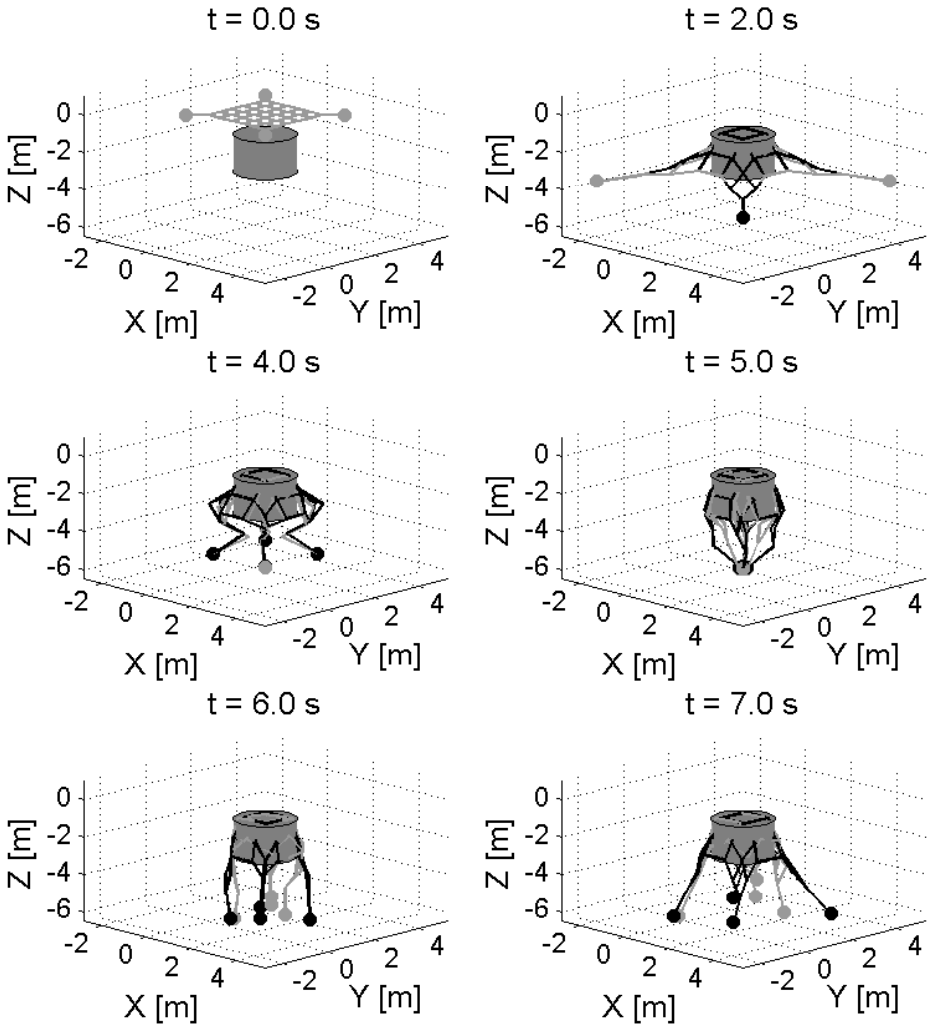

FIGURE 4.6: Capture sequence with linear model (grey net) and Hunt and Crossley's model (black net).

happens between $t = 6.0$ s with the model without friction and $t = 6.8$ s with Hunt and Crossley's model.

Overall, the effect of employing different normal contact force models or of neglecting friction is not fundamental to simulating the capture dynamics, especially until net closure. However, the choice of the contact force model does appear to influence substantially the computational time. It was observed that the non-linear models that express the damping coefficient in terms of the coefficient of restitution sometimes encounter numerical difficulties; considering the differences in computational efficiency and similarities in the overall dynamics, the more simple non-linear models (such as Hunt and Crossley's or Lee and Wang's) are recommended for simulating this particular dynamic scenario. In Section 4.3.2, it was observed that Alves et al. recommended models that are able to recover the restitution coefficient correctly for the whole span of its values (i.e., from 0 to 1); however,

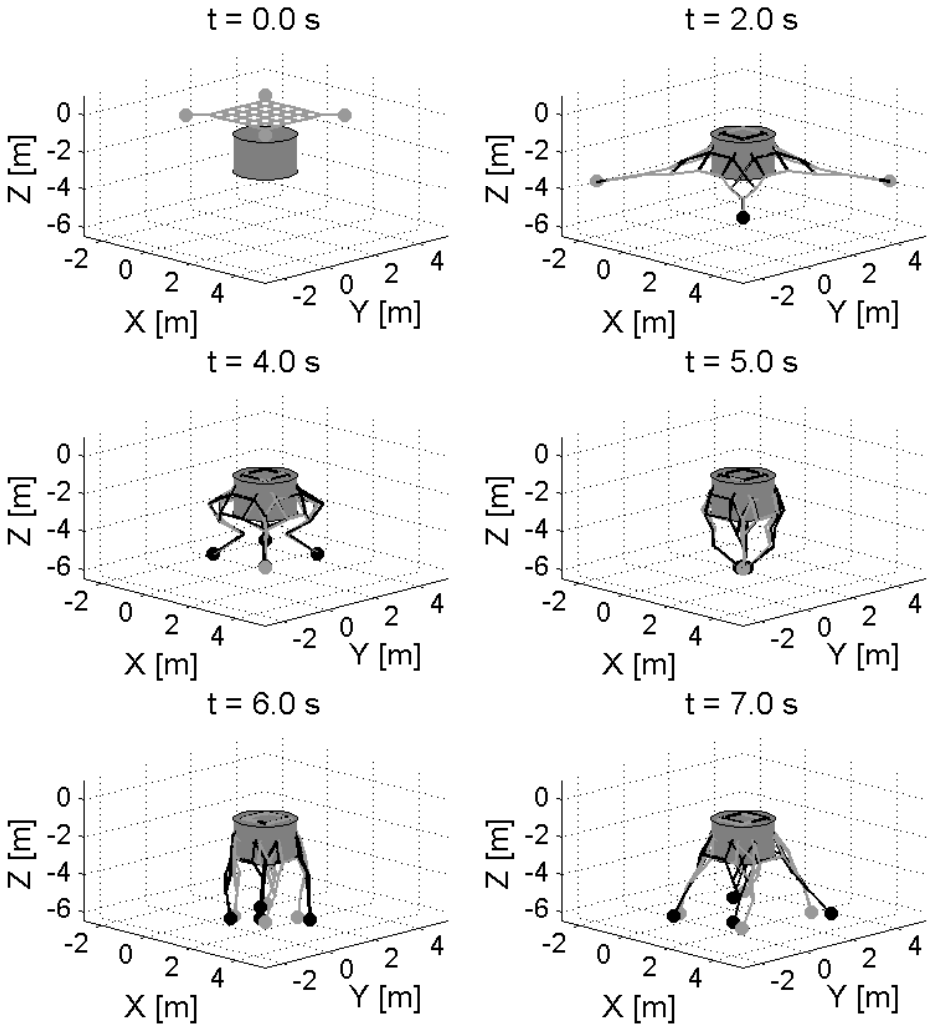

FIGURE 4.7: Capture sequence with Hunt and Crossley's model with friction (black net) and without friction (grey net).

they also noticed that all the proposed models provide similar damping factors when the restitution coefficient is higher than 0.7 [71]. From the results of simulation with Hunt and Crossley's model, it was found that the restitution coefficient e characterizing a new contact is lower than 0.7 in only approximately 4% of occurrences. This corroborates the finding that all the models employed in this work provide similar overall dynamics in this capture scenario. A model without friction is deemed to be sufficient for describing the overall dynamics of capture in this particular scenario: in fact, simulation of friction force did not have a significant effect on the response, but doubled the computational time. However, it is expected that friction will have a more important effect in scenarios where the rotation of the debris is modeled.

Figure 4.9 presents the contact force obtained with the linear model as well as with Hunt and Crossley's and Zhang and Sharf's non-linear models on two of the masses impacting

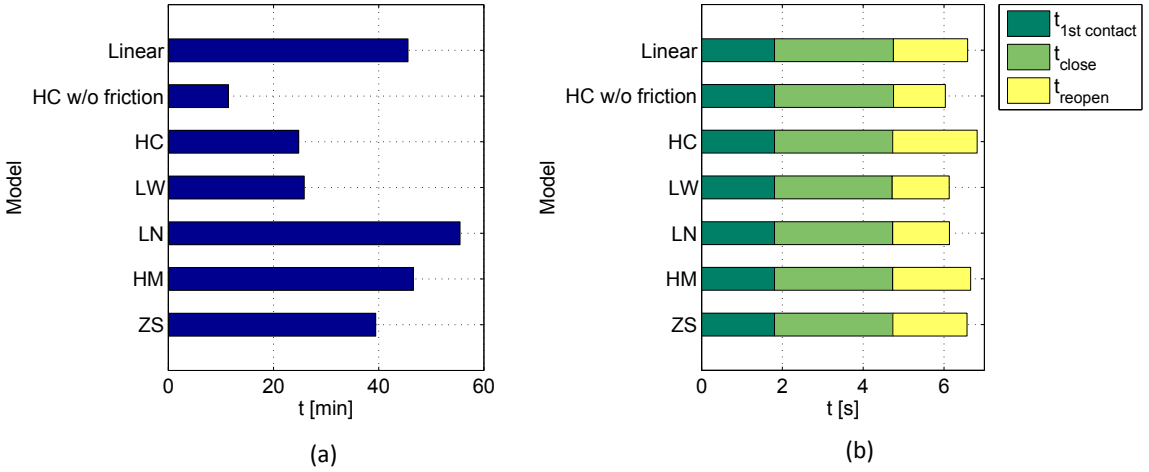

FIGURE 4.8: Comparison of (a) integration times and (b) events describing the overall capture dynamics, obtained with different contact dynamics models.

the cylinder: node 15, that impacts the top surface, and node 9, that impacts the lateral surface (the reader can refer to Figure 2.1 for the location of these nodes in the net). F_n is the normal contact force, whereas F_{t1} and F_{t2} indicate two orthogonal components of the friction force. For node 15, (F_{t1}, F_{t2}, F_n) are aligned with the inertial reference frame. For node 9, F_n depends instantaneously on the point of contact, F_{t1} is aligned with the inertial z-axis, and F_{t2} completes the orthogonal triad. Multiple peaks are observed; these correspond to multiple impact occurrences between the node and the cylinder, which are due both to the overall net dynamics and to the elasticity of impacts. Comparing the results of simulations with the three models, it can be noticed that the trends of the contact forces are similar, especially until around $t = 5$ s; however, it is clear that the normal contact force with the linear model can become unrealistically negative (i.e., a force that tends to keep the bodies together), whereas this does not happen with the non-linear model. Quantitatively, these results confirm that the orders of magnitude of the contact forces are consistent among the three models. However, the linear model yields normal contact forces noticeably lower than the non-linear models at the beginning of contact (e.g., approximately 25% decrease with respect to Hunt and Crossley's model at the first impact occurrence). From these figures, it is also evident that the forces of contact at first impact and during later sustained contact are characterized by different orders of magnitude: for node 15, the first impact force is $F_n \approx 1200$ N, whereas the contact forces experienced later are on the order of Newtons.

At a first glance, from Figure 4.9 it may seem that the contact forces are discontinuous, contrary to the nature of the continuous compliant model. A zoom on the first peak of the normal contact force experienced by node 15, in Figure 4.10(a), reveals that it does vary continuously during the very short impact period, of 0.1 ms duration. Figure 4.10(a) reports the results obtained with all the implemented models: it shows that the first

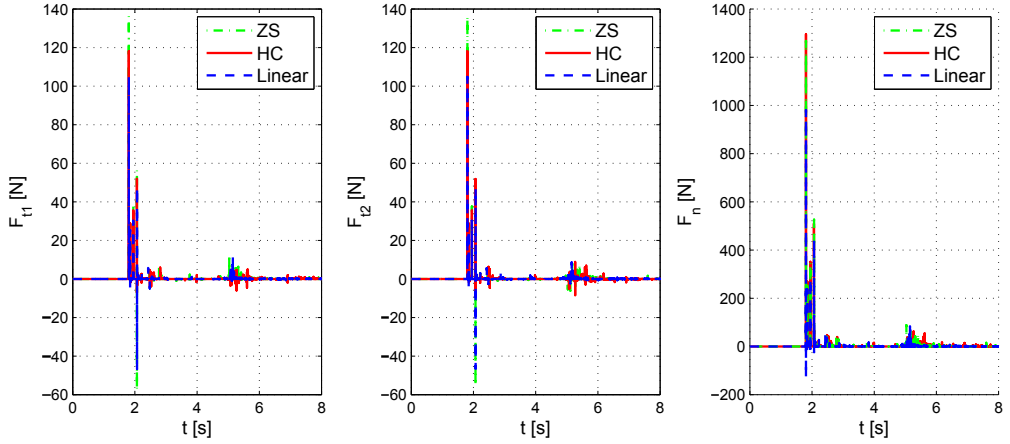

(a) Node 15.

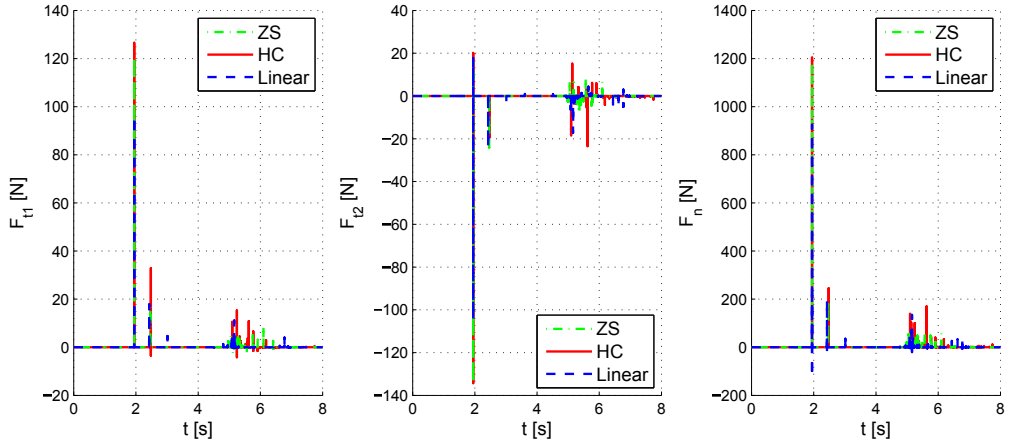

(b) Node 9.

FIGURE 4.9: Comparison of contact force on some nodes with Zhang and Sharf's model, Hunt and Crossley's model, and linear model.

impact happens at exactly the same instant with all the models, and that little variation in the normal contact force exists among the non-linear models. On the other hand, it makes the differences between the linear model and the non-linear models even more visible. It can be appreciated how, at the onset of contact, the linear model causes a contact force that becomes instantaneously different from zero (although at that instant the penetration is null): this is due to the linear damping term. Also, the non-physical "sticking" behavior as the objects are separating is clearly visible. In Figure 4.10(b), the normal contact force experienced by node 15 at three subsequent impact events is depicted. This highlights that the dynamics of node 15 is influenced by the small differences observed during its first impact with the debris: for example, the second peak is higher in magnitude and occurs later in simulations characterized by higher normal contact forces during the first impact (see Figure 4.10(a)).

The number of contacts experienced by the net during capture is represented in Figure

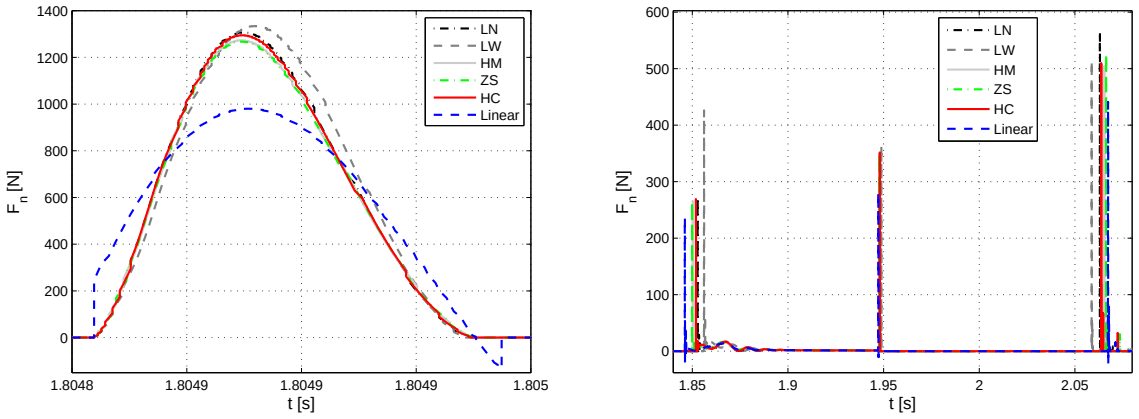

(a) (b)

FIGURE 4.10: Comparison of normal contact force on node 15 with all the implemented models. (a): zoom on first peak. (b): zoom on second, third, and fourth peaks.

4.11 for the simulation with Hunt and Crossley's model. Since the first impact with the top surface occurs, i.e., at $t \approx 1.8$ s, four contacts are observed. The four contacts are sustained for certain intervals, such as from 1.85 s to 1.95 s; this was also ascertained by verifying that F_n of node 15 oscillates after the second peak and settles at $F_n \approx 2$ N until the third peak (see Figure 4.10(b)). At around $t = 1.95$ s, 20 contacts are observed, which consist of the 4 nodes impacting the top and 16 new impacts of nodes with the lateral surface. At the corresponding time, the first impact force on node 9 is found in Figure 4.9(b). Additionally, from Figure 4.11 it is noticed that contact is often sustained and that multiple simultaneous contacts (often more than 8, and up to 20) occur later in the simulation. Considering that the net and debris in this set of simulations are much smaller than those envisaged for actual ADR missions, and that as a result many more simultaneous contacts are expected to occur in the real scenario, the continuous compliant modeling approach for the normal contact force seems well-suited to the problem. This formulation is also able to solve both impact and sustained contact situations, both of which were observed during net-based capture of debris.

In Figure 4.12 the friction force on node 15 and some related quantities are depicted for a short interval in order to validate the implemented friction model and highlight some of its features. The threshold velocity v_d determines the velocity at which transitions between sticking and slipping regimes occur; five transitions are visible in the top plot. At all transitions, a discontinuity in μF_n is observed in the second plot, due to the change in the coefficient of friction; also, from this diagram it is verified that $F_t \leq \mu F_n$ always, and that $F_t = \mu F_n$ during slipping. Finally, the third diagram compares the direction of the relative velocity and of the friction force, measured with θ from the x-axis: as expected, the two vectors are always aligned during this time span. This verifies the recovery of

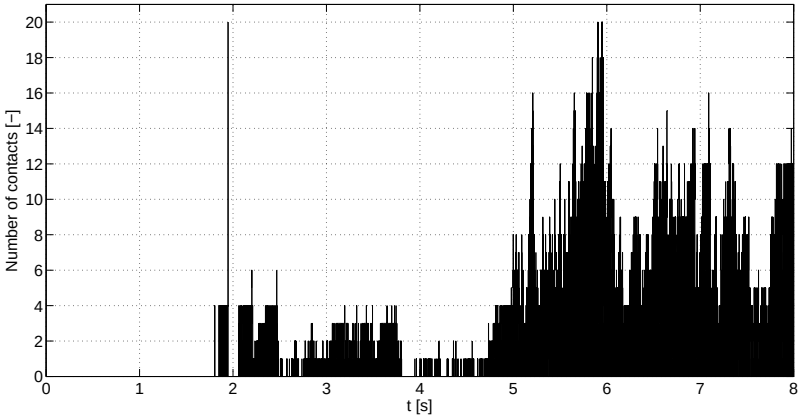

FIGURE 4.11: Number of simultaneous contacts in simulation of capture with Hunt and Crossley's model.

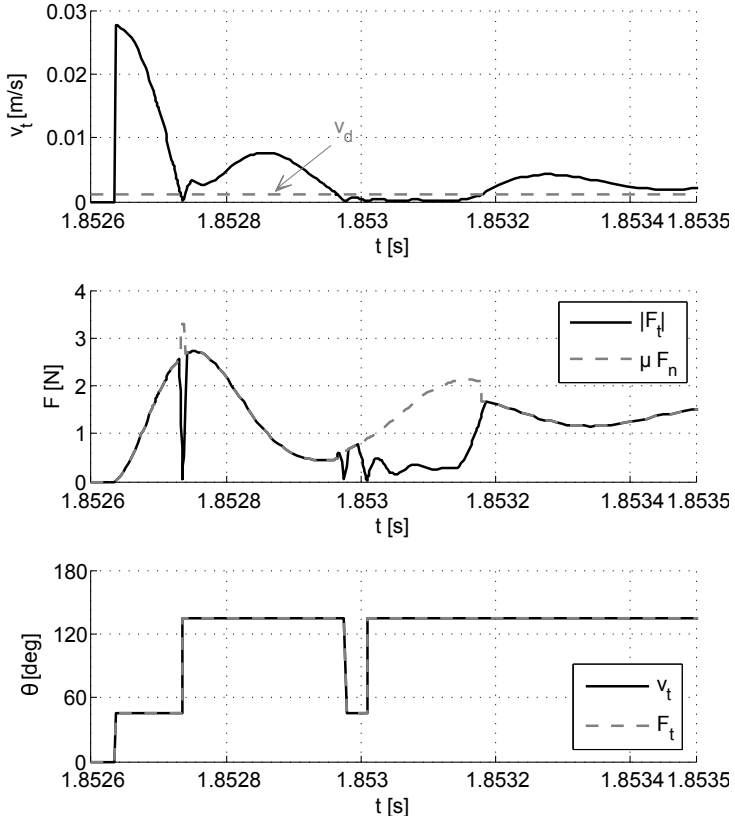

FIGURE 4.12: Friction force results on node 15 with Hunt and Crossley's model.

Coulomb's friction in slipping, demonstrates that the magnitude of the friction force is continuous, and confirms that transitions happen when they are expected to.

4.5 Modeling of contact dynamics in Vortex Dynamics

The rest of the studies on net-based capture dynamics contained in this Thesis were performed with the Vortex-Dynamics-based simulator, primarily because of its built-in collision detection features. Collision detection and contact geometry are the subjects of Section 4.5.1. Whenever a collision is detected, constraints due to contacts are added to the dynamics equations (which were stated in equation (2.21)) to account for normal and friction forces. The normal and friction force models employed are dealt with in Sections 4.5.2 and 4.5.3.

4.5.1 Collision detection and contact geometry

Each body in the multibody simulation tool is assigned a collision geometry. Several methods to define collision geometries are available in Vortex Dynamics, and have to be selected based on the need for computational efficiency versus accuracy of collision detection and response. For example, mesh-based collision geometries offer close identification with a graphics mesh, but introduce discontinuities in smooth surfaces; primitive geometries, such as spheres or cylinders, allow to construct smoother contact surfaces: simpler contact detection algorithms can be used, which improves the simulation performance. In this work, simple geometric primitives were selected to improve the computational efficiency: the nodes of the net and the corner masses were approximated to spheres of radii proportional to their mass; target objects were modeled with patched primitives (spheres and cylinders). Collision detection strategies for the simple geometries employed are well established and built-in in Vortex Dynamics (they consist of hierarchical, progressively more complex tests).

In Vortex Dynamics, each collision geometry is assigned a material, which consists of a set of collision-related properties (e.g., friction coefficient, contact stiffness). Each combination of materials results in a *contact material*, representative of the combined collision-related properties; in the simulator at hand, these properties were specified as the same contact stiffness and damping parameters discussed in Sections 4.3.2 and 4.3.3. These collections of properties are computed off-line and stored in a look-up table, which is used at run-time to determine the dynamic response between two objects with certain material properties.

4.5.2 Normal force modeling

In presence of contact constraints between the bodies in the simulation, the equations of motion and constraints in equation (2.21) become:

$$\begin{aligned} &\mathbf{M}\dot{\mathbf{v}} + \mathbf{c} - \mathbf{G}^T\boldsymbol{\lambda} - \mathbf{N}^T\boldsymbol{\nu} = \mathbf{f} \\ &\boldsymbol{\Phi}(\mathbf{q}) = \mathbf{0} \\ &\mathbf{0} \leq \boldsymbol{\nu} \perp \boldsymbol{\Phi}_c \geq \mathbf{0} \end{aligned} \tag{4.25}$$

where $\mathbf{N}$ is the Jacobian of the contact constraints, such that $\dot{\boldsymbol{\Phi}}_c = \mathbf{N}\mathbf{v}$, $\boldsymbol{\nu}$ is the array of normal contact forces, and $\boldsymbol{\Phi}_c$ is the array of distances. The third line in equation (4.25), to be read component-wise, states complementarity conditions, due to the unilateral nature of contact constraints: a force of contact can only be positive when the distance between two bodies is zero, and vice-versa.

Vortex Dynamics offers both impulsive and regularized models for contact forces in the direction normal to the contact plane: the impulsive model considers the contact phase to have infinitesimal duration and the impact to be rigid; the regularized model considers the contact to happen in a finite amount of time, during which a certain penetration is allowed. For this work, a regularized model was employed. The contact forces can be defined as:

$$\boldsymbol{\nu} = -\mathbf{K}_c\boldsymbol{\Phi}_c - \mathbf{B}_c\mathbf{N}\mathbf{v} \tag{4.26}$$

and the discretized equations can be written as:

$$\begin{bmatrix} \mathbf{1} & -h\boldsymbol{\Gamma} & \mathbf{0} & \mathbf{0} \\ \mathbf{0} & \mathbf{M} & -\mathbf{G}^T & -\mathbf{N}^T \\ \mathbf{0} & \mathbf{G} & \tilde{\mathbf{C}}_\Phi & \mathbf{0} \\ \mathbf{0} & \mathbf{N} & \mathbf{0} & \tilde{\mathbf{C}}_{\Phi_c} \end{bmatrix} \begin{bmatrix} \mathbf{q}_{n+1} \\ \mathbf{v}_{n+1} \\ h\boldsymbol{\lambda}_{n+1} \\ h\boldsymbol{\nu}_{n+1} \end{bmatrix} + \begin{bmatrix} -\mathbf{q}_n \\ -h\mathbf{M}\mathbf{v}_n - h(\mathbf{f}-\mathbf{c}) \\ \tilde{\mathbf{B}}_\Phi\boldsymbol{\Phi}_n \\ \tilde{\mathbf{B}}_{\Phi_c}\boldsymbol{\Phi}_{c,n} \end{bmatrix} = \begin{bmatrix} \mathbf{0} \\ \mathbf{0} \\ \mathbf{0} \\ \boldsymbol{\eta} \end{bmatrix} \tag{4.27}$$
$$\mathbf{0} \leq \boldsymbol{\nu} \perp \boldsymbol{\eta} \geq \mathbf{0}$$

where $\tilde{\mathbf{C}}_{\Phi_c} = \mathrm{diag}\{h^{-2}(1 + c_{c,k}/(hk_{c,k}))^{-1}/k_{c,k}\}$ and $\tilde{\mathbf{B}}_{\Phi_c} = \mathrm{diag}\{h^{-1}(1 + c_{c,k}/(hk_{c,k}))^{-1}\}$. The similarities between equations (2.22) and (4.26) and between the third and fourth lines in equation (4.27) is evident. However, the unilateral nature of the contact constraints causes the inclusion of term $\boldsymbol{\eta}$ to the right side of the fourth equation and of the complementarity conditions, to avoid that $\boldsymbol{\nu}$ becomes negative. The interested reader is referred to the paper by Lacoursière [60].

Notice that equation (4.26) corresponds in practice to a Kelvin-Voigt model similar to that described in equation (4.4), considering that the contact stiffness and damping matrices are composed of the coefficients $k_{c,i}$ and $c_{c,i}$. In order to estimate representative values

for the contact stiffness and damping coefficients, Hertzian contact theory was brought to assistance, as was done in the MATLAB simulator (see Section 4.3.2). However, in Vortex Dynamics, there exist default values of stiffness $\bar{k}$ and damping $\bar{c}$ for the sake of stability of simulation. For each contact, Vortex Dynamics chooses which pair to use between the user-defined $(k_{c,i}, c_{c,i})$ and the default $(\bar{k}, \bar{c})$, according to the perturbation made on the system, computed as $(1/h^2k)/(1 + c/(hk))$, with h the simulation time step: the chosen pair is that creating the highest perturbation. Moreover, the damping coefficient actually employed in the simulator depends on the time step and stiffness coefficient: $c_{c,i} + hk_{c,i}$ or $\bar{c} + h\bar{k}$.

4.5.3 Friction force modeling

The solution of problems with many contacts is not easy. The most accurate representation of friction forces offered by Vortex Dynamics at the time of writing is an approximation of the Coulomb's friction model, called *scaled box friction model*. As in Coulomb's model, the static friction force boundary is computed as proportional to the normal contact force; differently from it, this boundary is computed through several iterations in the same time step. Also, the friction force is computed component-wise along two orthogonal directions on the contact plane, which is expected to cause a small error.

If friction force is present and defined according to the scaled box friction model, the equations of motion are written as:

$$\begin{aligned}
&\mathbf{M}\dot{\mathbf{v}} + \mathbf{c} - \mathbf{G}^T\boldsymbol{\lambda} - \mathbf{N}^T\boldsymbol{\nu} - \mathbf{D}^T\boldsymbol{\beta} = \mathbf{f} \\
&\boldsymbol{\Phi}(\mathbf{q}) = \mathbf{0} \\
&\mathbf{0} \leq \boldsymbol{\nu} \perp \boldsymbol{\Phi}_c \geq \mathbf{0} \\
&\mathbf{D}(\mathbf{q})\mathbf{v} = \boldsymbol{\sigma} \\
&\mathbf{0} \leq (\boldsymbol{\beta} - \underline{\boldsymbol{\beta}}) \perp \boldsymbol{\sigma} \geq \mathbf{0}, \quad \mathbf{0} \leq (\bar{\boldsymbol{\beta}} - \boldsymbol{\beta}) \perp \boldsymbol{\sigma} \leq \mathbf{0}
\end{aligned} \tag{4.28}$$

The fourth line in equation (4.28) defines the relative tangential velocity $\boldsymbol{\sigma}$. The fifth line represents complementarity conditions on the friction constraint: either the magnitude of the tangential contact force $\boldsymbol{\beta}$ is between its lower bound $\underline{\boldsymbol{\beta}} = -\boldsymbol{\mu}\boldsymbol{\nu}$ and upper bound $\bar{\boldsymbol{\beta}} = \boldsymbol{\mu}\boldsymbol{\nu}$ (with $\boldsymbol{\mu}$ a matrix of friction coefficients of dimension $2N_c \times N_c$, with N_c the number of contacts) and the relative tangential velocity vanishes, or the bound on the friction force is reached and the relative tangential velocity takes the opposite sign.

Also, some regularization is introduced for the sake of stability of the simulation; therefore, actual sticking is not possible during contact. This modifies the equation $\mathbf{D}(\mathbf{q})\mathbf{v} = \boldsymbol{\sigma}$.

The discretized equations become:

$$\begin{bmatrix} \mathbf{1} & -h\boldsymbol{\Gamma} & \mathbf{0} & \mathbf{0} & \mathbf{0} \\ \mathbf{0} & \mathbf{M} & -\mathbf{G}^T & -\mathbf{N}^T & -\mathbf{D}^T \\ \mathbf{0} & \mathbf{G} & \tilde{\mathbf{C}}_\Phi & \mathbf{0} & \mathbf{0} \\ \mathbf{0} & \mathbf{N} & \mathbf{0} & \tilde{\mathbf{C}}_{\Phi_c} & \mathbf{0} \\ \mathbf{0} & \mathbf{D} & \mathbf{0} & \mathbf{0} & \tilde{\mathbf{C}}_D \end{bmatrix} \begin{bmatrix} \mathbf{q}_{n+1} \\ \mathbf{v}_{n+1} \\ h\boldsymbol{\lambda}_{n+1} \\ h\boldsymbol{\nu}_{n+1} \\ h\boldsymbol{\beta}_{n+1} \end{bmatrix} + \begin{bmatrix} -\mathbf{q}_n \\ -h\mathbf{M}\mathbf{v}_n - h(\mathbf{f}-\mathbf{c}) \\ \tilde{\mathbf{B}}_\Phi \boldsymbol{\Phi}_n \\ \tilde{\mathbf{B}}_{\Phi_c} \boldsymbol{\Phi}_{c,n} \\ \mathbf{0} \end{bmatrix} = \begin{bmatrix} \mathbf{0} \\ \mathbf{0} \\ \mathbf{0} \\ \boldsymbol{\eta} \\ \boldsymbol{\sigma} \end{bmatrix} \tag{4.29}$$

$$\mathbf{0} \leq \boldsymbol{\nu} \perp \boldsymbol{\eta} \geq \mathbf{0}$$

$$\mathbf{0} \leq (\boldsymbol{\beta} - \underline{\boldsymbol{\beta}}) \perp \boldsymbol{\sigma} \geq \mathbf{0}, \quad \mathbf{0} \leq (\bar{\boldsymbol{\beta}} - \boldsymbol{\beta}) \perp \boldsymbol{\sigma} \leq \mathbf{0}, \quad \underline{\boldsymbol{\beta}} \approx -\boldsymbol{\mu}\boldsymbol{\nu}_{n+1}, \quad \bar{\boldsymbol{\beta}} \approx \boldsymbol{\mu}\boldsymbol{\nu}_{n+1}$$

where $\tilde{\mathbf{C}}_D = \text{diag}\{1/(hb_i)\}$ and b_i is the viscous friction coefficient for the i-th contact. Again, for further details on this formulation, the interested reader is referred to the paper by Lacoursière [60].

4.6 Effect of bending stiffness on capture dynamics

Similarly to what was done in Section 3.1 for the deployment dynamics, the effect of representing the bending stiffness of the net threads on the capture dynamics is investigated in the next few pages. Simulations of capture of a tumbling target (which is modeled in Section 4.6.1) with and without representation of the bending stiffness of the net threads are compared in Section 4.6.2.

4.6.1 Model of tumbling debris

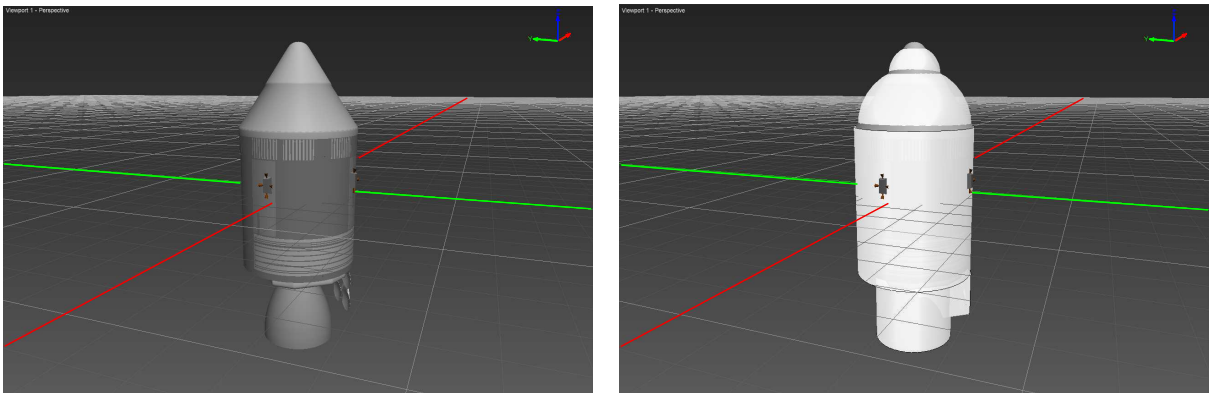

FIGURE 4.13: 3D model of debris (left), and model showing collision geometries (right) in Vortex Editor.

It was already mentioned that many of the debris objects that need to be removed from orbit are launcher upper stages [4]. The first target considered is modeled after Apollo spacecraft but is characterized by dimensions, mass, and shape similar to rocket upper

stages, which will be used as targets in Chapter 5. In Vortex Dynamics, the debris object is modeled as a *part*, which corresponds to a rigid body model. The model for the debris object used for this study was built in the Vortex Editor environment starting from a graphics 3D model[5], as shown in the left screenshot of Figure 4.13. To the part is automatically attached a reference frame, whose origin lies at the intersection of the red and green lines shown in Figure 4.13[6]. The positive directions of the unit vectors defining this reference frame are indicated at the top right corner of the screenshot. The collision geometry for the debris object used as target in this study was constructed by adding to the part multiple primitive geometries, as shown in the right screenshot of Figure 4.13. At run-time, the target part is imported into the C++ API to allow for interaction with the rest of the simulation.

The target under consideration has a length of $H_T = 11$ m, has a circular cross section of 3.9 m diameter (i.e., $R_T = 1.95$ m), and a mass of $m_T = 11900$ kg. The position of its center of mass relative to and expressed in the part reference frame is:

$$\mathbf{r}_{G,O'} = [-0.604 \quad -0.115 \quad -0.339]^T \text{m} \tag{4.30}$$

The inertia tensor in the part reference frame is:

$$\mathbf{I}_G = \begin{bmatrix} 63371.5 & 108.328 & 464.155 \\ 108.328 & 63384.9 & -825.275 \\ 464.155 & -825.275 & 16523.1 \end{bmatrix} \text{kg} \cdot \text{m}^2 \tag{4.31}$$

Since it is expected that debris be tumbling in the orbit, initial angular velocity $\boldsymbol{\omega}_T$ is given to the target object in simulations.

4.6.2 Capture simulation results

The parameters of the simulation are collected in Table 4.4. The initial configuration of the net was selected so as to be at $d_T = 10$ m distance and centered with respect to the geometrical center of the debris object. Upon consideration of the dimensions of the debris target, and taking into account the need to contain computational effort, the net was selected to be 20×20 m^2 wide and to have 1 m mesh length, which results in 445 rigid bodies and 844 threads (i.e, 844 *distance constraints* and 844 prismatic constraints). The target was oriented such that the direction of its maximum dimension was parallel

[5]The 3D model was found at the web page *The Apollo Connection - Apollo 3D ... Spacecraft Information and Models*: https://sites.google.com/site/theapolloconnection/, accessed on 3 June 2015.

[6]The origin of the part reference frame is positioned in the inertial reference frame at run-time according to the user-provided initial conditions.

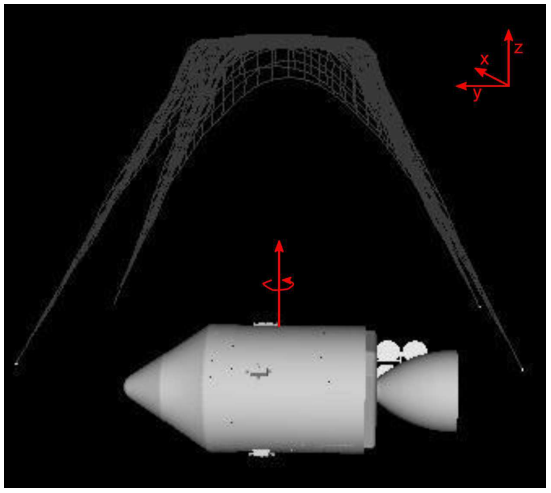

FIGURE 4.14: Scenario employed for evaluating the effect of representing the bending stiffness of the net threads on capture dynamics.

to the initial plane of the net, aligned with the y-direction of the global reference frame (see Figure 4.14). It was also made to spin at a rate of $\omega_T = 5°/\text{s}$ about an axis parallel to the z-axis at the initial instant of the simulation: $\boldsymbol{\omega}_T = \omega_T \hat{\mathbf{k}}$.

Net and corner masses					
L_{net} (m)	$l_{net,0}$ (m)	r_{net} (m)	ρ_{net} (kg/m^3)	E_{net} (GPa)	ξ_a (-)
20	1	0.0005	1390	70	0.106
l_{knot} (m)	$l_{CT,0}$ (m)	r_{CT} (m)	ρ_{CM} (kg/m^3)	m_{CM} (kg)	ξ_a (-)
0	1.4142	0.001	2700	0.5	0.014
Target					
R_T (m)	H_T (m)	m_T (kg)	E_T (GPa)	d_T (m)	ω_T (°/s)
1.95	11	11900	69	10	5
Initial conditions				**Simulation data**	
$v_{e,net}$	v_e (m/s)	θ (°)	α_{net} (-)	t_f (s)	Δt (s)
0	2.5	36.87	0.25	120	1/60

TABLE 4.4: Data for the simulation of net-based capture of debris to study the effect of bending stiffness and the robustness of capture.

The contact stiffness and damping parameters of the possible collision pairs are collected in Table 4.5. For computation of all these parameters, it was assumed that the Poisson's ratio is $\nu_{net} = 0.35$ for Technora [90], and $\nu_{al} = 0.33$ for Aluminum. The employed static friction coefficients were taken as $\mu_{s,al-al} = 0.45$ for Aluminum-Aluminum pairs [88], $\mu_{s,al-net} = 0.15$ for Aluminum-Technora pairs, and $\mu_{s,net-net} = 0.20$ for Technora-Technora pairs (for Technora, frictional properties of Nylon were used). For all the contact pairs, the kinetic friction coefficients μ_k were evaluated by dividing the corresponding static friction coefficients by 1.25, the viscous friction coefficient was set to 10^6 kg/s.

k_c ($\times 10^9$ N/m)	**T**	**CM**	**Corner node**	**Edge node**	**Inner node**
T	-	9.712	4.591	4.241	4.449
CM	sym.	6.867	4.161	3.895	4.055
Corner node	sym.	sym.	3.295	3.162	3.243
Edge node	sym.	sym.	sym.	3.044	3.116
Inner node	sym.	sym.	sym.	sym.	3.193

c_c (Ns/m)	**T**	**CM**	**Corner node**	**Edge node**	**Inner node**
T	-	1396	70	53	62
CM	sym.	830	66	50	59
Corner node	sym.	sym.	42	36	39
Edge node	sym.	sym.	sym.	32	34
Inner node	sym.	sym.	sym.	sym.	37

TABLE 4.5: Normal contact stiffness and damping coefficients for the possible collision pairs. T stands for target; CM stands for corner mass; corner node, edge node and inner node indicate generic nodes differently positioned in the net.

The net deployment and target capture maneuver was simulated for the duration of 120 s and using a time step of 1/60 s, with an Intel®Core™ i7-4712HQ CPU @ 2.30 GHz processor; without bending modeling, it took about 9 min to complete the simulation; with bending, it took approximately 1 hr, 20 min, for a nearly 8-fold increase in computation time. Animations of the maneuver revealed that in both simulations (with and without bending) the net wraps around the debris, but opens again and leaves the target after a certain time, because of the spin of the debris. The effect of including bending stiffness was found to be substantial from inspection of the simulation recordings.

The impact of including bending stiffness is also visible in Figure 4.15, where the mouth shape at different time instances with and without bending is compared; in each snapshot, the instantaneous direction of the debris is depicted in gray. It can be observed that, in both simulations, just before contact ($t = 9$ s) the net is almost deployed and the mouth shape is symmetric. Contact with the target happens at around $t = 9$ s for the simulation with bending, and at around $t = 13$ s for the simulation without bending: at $t = 14$ s, the effect of contact is visible in both plots and the net shape becomes asymmetric; the two shapes differ strongly from each other, with the net in the simulation without bending that is partially entangled, and the net in the simulation with bending not entangled at all. At subsequent times, the differences grow among the two simulations: a $t = 27$ s, for example, the net appears more entangled in the simulation with bending; at $t = 44$ s, both nets appear to have opened again, but the net with bending stiffness has a larger mouth area; finally, at $t = 82$ s, the net has left the target, traveling away from it in both cases, but the two section shapes and positions do not agree at all. Overall, the dynamics of the net during the capture phase appears to be very different in the two simulations. Due to the dissimilarities already appreciated in the deployment phase

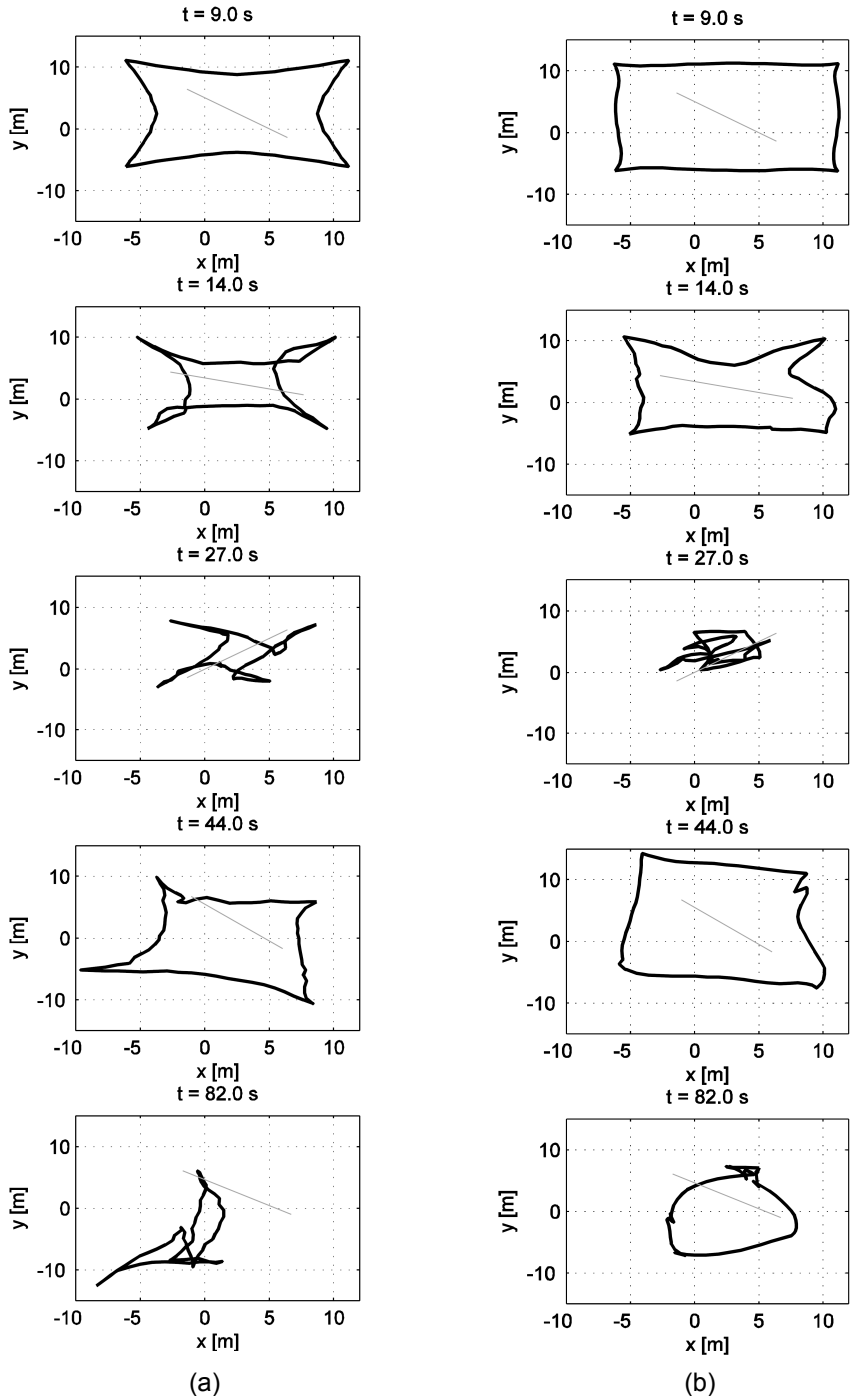

FIGURE 4.15: Mouth shape at different time instances in simulation of capture of rotating target. (a): without bending stiffness representation; (b): with bending stiffness representation.

(see Section 3.1), the net impacts the debris at different instants in the two simulations (about 9 s in simulation with bending stiffness representation, about 13 s in simulation without bending stiffness representation): therefore, the first impact between the net and debris occurs with the debris at different orientations, which has an important effect on the subsequent dynamics evolution.

The dynamics of the net was found to be more perceptibly influenced by the dynamics of the target spacecraft when bending stiffness representation is not included: the net takes less time to wrap around the target, and leaves it more quickly afterwards; the net with representation of bending stiffness takes more time to entangle the debris. This difference can once more be explained by the physical implication of bending stiffness, which causes resistance to changes in the shape of the net which are being imposed by the motion of the corner masses and the contacts with the debris. In spite of such large differences in the motion of the net during the capture maneuver, it was observed that the "global" results for the two simulations were comparable: in both cases the net wraps around the target but then opens up and leaves it after a few seconds. Also, the acquired rotation of the net about the positive z-axis, which corresponds to the initial condition given to the debris, can be recognized in both simulations, especially in the phase during which the net leaves the debris.

4.7 Robustness of net-based capture

One of the presumed advantages of using tether-nets over more traditional technologies in capture of debris is its robustness to inaccuracies in the capture process. In fact, uncertainties in the motion and inertia properties of the target are expected; a capture method proven to be robust to these uncertainties would be preferred. The deployment dynamics of the net itself, however, might be affected by inaccuracies – or worse, failures – in the ejection of the corner masses. The aim of this Section is to present a sensitivity study on the effectiveness of net capture in different mission scenarios. This is achieved by performing multiple simulations of the capture dynamics, and by inspecting the results.

In the nominal condition for the ejection of the net, it is assumed that its center is initially aligned with the origin of the debris part (which is close to the geometric center), and that the four corner masses are all ejected with the same initial velocity, symmetrically. The simulation parameters employed for investigating the robustness of capture are the same as in Table 4.4. Two nominal scenarios are considered: in scenario 1, the maximum dimension of the debris target is aligned parallel to the initial plane of the net; in scenario 2, it is perpendicular to the initial plane of the net (see Figure 4.16). In both cases, the target spins about its major axis of inertia. Simulations with the target spinning about

its minor axis of inertia were also performed but are omitted here because this condition is not likely to occur for realistic debris.

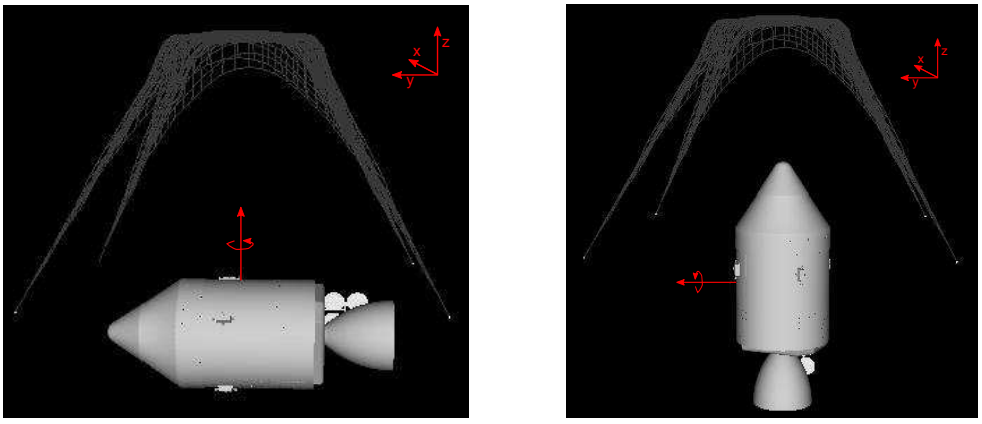

(a) Scenario 1 (b) Scenario 2

FIGURE 4.16: Nominal capture scenarios considered to study the robustness of net-based capture.

Let us indicate with $(\hat{\mathbf{i}}, \hat{\mathbf{j}}, \hat{\mathbf{k}})$ a reference frame oriented as the inertial reference frame but centered in the debris. Let us define with $(\hat{\mathbf{i}}_\mathbf{b}, \hat{\mathbf{j}}_\mathbf{b}, \hat{\mathbf{k}}_\mathbf{b})$ the debris body-fixed reference frame: $\hat{\mathbf{i}}_\mathbf{b}$ points through the nose of the debris and lies on a plane of symmetry; $\hat{\mathbf{j}}_\mathbf{b}$ and $\hat{\mathbf{k}}_\mathbf{b}$ lie on a plane perpendicular to this, and complete the orthogonal triad. The initial angular velocity vectors for the two nominal scenarios are:

$$\boldsymbol{\omega}_{T1} = \omega_T \hat{\mathbf{k}}_\mathbf{b} = \omega_T \hat{\mathbf{k}}$$
$$\boldsymbol{\omega}_{T2} = \omega_T \hat{\mathbf{k}}_\mathbf{b} = \omega_T \hat{\mathbf{j}}$$

The presence or absence of the characteristic features introduced in Section 4.1 in the simulated capture maneuver was evaluated thanks to their visualization, and by post-processing the simulation data (namely, the position of the net nodes in time). In nominal alignment and deployment conditions, the net envelops the target for a time sufficiently long for a closing mechanism to work (estimated as 10 s) in both scenarios. In this set of simulations, no closing mechanism was used and it was observed that the net, after enveloping the target, also slips off it in both scenarios. On the other hand, after slipping off the target, the net flies away from it only in scenario 1 (see the screenshots in Figure 4.1). In scenario 2, the rotation of the target helps the net to not fly away from it: after the net slips off the target, contact is recovered thanks to the spin motion of the latter, which collides with the open net and drags the net around itself. On the other hand, in scenario 1 the spinning motion of the debris is transferred to the net upon contact, and this is found to make the net open again and fly away.

4.7.1 Robustness of capture to inaccuracies

The success of capture may depend on the relative attitude between the target debris and the direction of the launch of the net, as well as on the magnitude and direction of the initial velocity imparted to the corner masses, and on the distance from the target at the time of launch (these two last parameters being related). On the other hand, net-based capture of debris is expected to be compliant to position and attitude misalignments, and robust to errors in the ejection of the corner masses. The flexibility of the simulator at hand, which is a characteristic anticipated in Chapter 1, allows to perform a sensitivity study on the robustness of capture by specifying simulations with different net ejection conditions, as well as target positions and orientations.

The effectiveness of capture in a certain number of non-nominal conditions is described in Table 4.6 for scenario 1 and in Table 4.7 for scenario 2. In these tables, the criteria identified in Section 4.1 to describe the success of capture are employed. The non-nominal scenarios simulated are defined in the first column of these tables; *partial CM failure* indicates a condition in which one of the corner masses is ejected with half the velocity with respect to the others; *Total CM failure* indicates an extreme condition in which one of the corner masses is not ejected at all (its initial velocity is null). Different misalignment conditions are taken into account, both associated with the relative position and the relative orientation between net and target. Relative position misalignment is considered in the inertial x- and y-directions separately; the magnitude of a realistic misalignment was chosen by assuming that the attachment between the net and the chaser spacecraft is provided by a 50 m long tether, and that ejection of the net takes place with an error in the shooting angle of approximately 5°. Relative orientation misalignment is examined only about the inertial x-axis in this set of simulations; in this case, the initial angular velocity of the target is defined as:

$$\boldsymbol{\omega}_{T1} = \omega_T \hat{\mathbf{k}}_\mathbf{b} = -\omega_T \sin(\theta_x)\hat{\mathbf{j}} + \omega_T \cos(\theta_x)\hat{\mathbf{k}}$$
$$\boldsymbol{\omega}_{T2} = \omega_T \hat{\mathbf{k}}_\mathbf{b} = \omega_T \cos(\theta_x)\hat{\mathbf{j}} + \omega_T \sin(\theta_x)\hat{\mathbf{k}}$$

with θ_x the relative orientation misalignment, depicted in Figure 4.17. A non-nominal situation regarding the relative distance between net and target at the time of ejection of the corner masses is also studied; in this case the error is 20% of the nominal distance. Finally, some of the misalignment and the corner mass failure conditions are combined. This set of twelve non-nominal scenarios, despite not being exhaustive with respect to all the possible non-nominal conditions, can be used to determine the robustness of the capture maneuver to possible failure modes of the net deployment, such as inaccuracies of the firing mechanism, or pointing errors.

	Envelopment	**Envelopment sufficiently long for closure**	**Slip off**	**Fly away**
Nominal capture	yes	yes	yes	no
Partial CM failure	yes	no	yes	yes
Total CM failure	no	no	yes	yes
2 m misalignment x-dir.	yes	no	yes	yes
4 m misalignment x-dir.	no	no	yes	yes
2 m misalignment y-dir.	yes	no	yes	yes
4 m misalignment y-dir.	yes	no	yes	yes
$\theta_x = 10°$ misalignment	yes	yes	yes	yes
$\theta_x = 20°$ misalignment	yes	yes	yes	yes
2 m distance error	yes	yes	yes	yes
2 m misalignment y-dir. + Partial CM failure	yes	no	yes	yes
4 m misalignment y-dir. + Partial CM failure	no	no	yes	yes
2 m misalignment y-dir. + $\theta_x = 20°$ misalignment	yes	no	yes	yes

TABLE 4.6: Comparison of effectiveness of net-based capture in nominal and non-nominal conditions for scenario 1.

	Envelopment	**Envelopment sufficiently long for closure**	**Slip off**	**Fly away**
Nominal capture	yes	yes	yes	yes
Partial CM failure	yes	yes	yes	no
Total CM failure	no	no	yes	yes
2 m misalignment x-dir.	yes	yes	yes	no
4 m misalignment x-dir.	yes	yes	yes	no
2 m misalignment y-dir.	yes	yes	yes	no
4 m misalignment y-dir.	no	no	yes	yes
$\theta_x = 10°$ misalignment	yes	yes	yes	no
$\theta_x = 20°$ misalignment	yes	yes	yes	no
2 m distance error	yes	yes	yes	no
2 m misalignment x-dir. + Partial CM failure	yes	yes	yes	no
4 m misalignment x-dir. + Partial CM failure	yes	yes	yes	no
2 m misalignment x-dir. + $\theta_x = 20°$ misalignment	yes	yes	yes	no

TABLE 4.7: Comparison of effectiveness of net-based capture in nominal and non-nominal conditions for scenario 2.

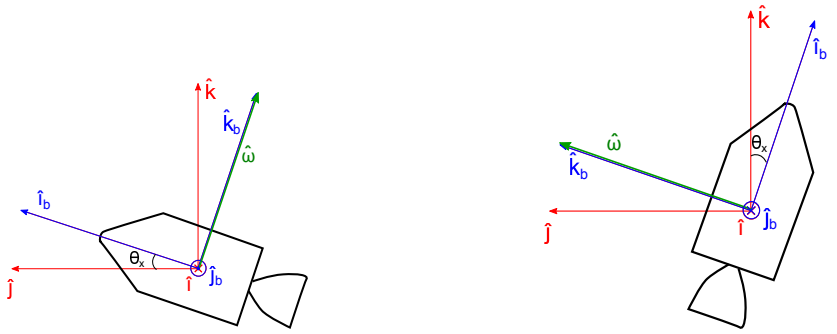

(a) Scenario 1 (b) Scenario 2

FIGURE 4.17: Reference frames and direction of initial angular velocity in tether-net capture scenarios 1 and 2, when non-nominal relative orientation is considered.

From Table 4.6, it can be verified that envelopment success in scenario 1 is robust especially to inaccuracies in attitude misalignments and to errors in the relative distance. All the other non-nominal conditions lead to insufficient envelopment time for closure, or to complete failures. From the results of simulations for scenario 2, it is observed that net capture success is robust to multiple inaccuracies and imperfections in the corner masses ejection and in the alignment between the initial configuration of the net and the target. In fact, in Table 4.7 it can be appreciated that only two situations lead to a capture failure: a total failure in the ejection of a corner mass, and a misalignment of 4 m in the y-direction; in all other cases, the net wraps around the target and remains entangled for an amount of time sufficient for successful capture, similarly to what happened in the nominal scenario.

For scenario 2, it is clear that the direction of the relative position misalignment matters. A misalignment in the inertial x-direction is mitigated by the rotational motion of the debris target, which results in the profile of the target presented to the net varying from 3.9 m (i.e., its diameter) to 11 m (i.e., its length) during the simulation. On the other hand, throughout the whole simulation the target spans only 3.9 m in the y-direction; therefore, misalignment in this direction is more critical.

Comparing the results of the two sets of simulations, for scenario 1 and scenario 2, it is apparent that the latter is more successful, both in nominal and non-nominal conditions of net deployment. The effectiveness of capture in scenario 2 seems to be less sensitive to inaccuracies: while 10 out of 12 non-nominal conditions led to a sufficiently long envelopment in this scenario, only 3 of them guaranteed successful capture in scenario 1. In scenario 1, the net also flies away from the debris target afterwards, which is not desirable. Overall, it can be stated that the more robust nominal net deployment condition to capture an object tumbling about its major axis of inertia appears to be when the spin axis of the debris is perpendicular to the net launch direction. However, a

certain level of robustness is observed in both scenarios: the net enveloped its target in most of the non-nominal ejection conditions.

4.7.2 Need for a closing mechanism

In the previous Section, it was ascertained that debris can be captured with a net even in presence of inaccuracies in the net ejection and of debris/net misalignments. However, in every single case the net was observed to slip off the target after capture, and in some cases even fly away. The slippage observed might not be present in case of debris with many protrusions, as was observed – for example – in parabolic flight experiments where Envisat mock-up was captured with a net. However, results of the presented simulations suggest that a closing mechanism needs to be included in the tether-net system, in order for the net to secure a target such as a launcher upper stage in it and grant its removal through a tugging action.

The absence of a closing mechanism and of the main tether in the previous sensitivity study does not allow to draw conclusions on preferred capture scenarios. In fact, the presence of tension in the main tether might cause unwanted transmission of loads to the chaser spacecraft. Although scenario 2 is preferable from a robustness point of view (i.e., capture can be achieved in more non-nominal ejection and misalignment conditions), scenario 1 could result in a safer capture (i.e., a capture in which chaser and target remain at a larger distance). This issue will be treated in Section 5.3.3, after possible closing mechanisms are introduced.

Chapter 5

Capture dynamics with closing mechanism

In Chapter 4, the fundamentals of the dynamics of net-based capture were investigated, and the robustness of capture to multiple net ejection inaccuracies was ascertained. However, it was observed that a closing mechanism needs to be provided in the tether-net system to maintain the net closed around its target during the removal phase of the mission. Several other researchers have reached the same conclusion and have proposed closing solutions to ensure that the net remains closed around the target in preparation for the towing phase of the mission. All the proposed mechanisms rely on a cinch-cord running between the corner masses or along the net perimeter; however, different solutions to activate closure have been suggested: spring-loaded reels placed in the net corners and actuated after contact with debris [10, 11, 19, 22], the action of corner masses initiated by breakage of tension links [18], and - more recently - the use of the winching of the main tether [23, 24]. The third solution for a net with the same geometry as considered in this Thesis was proposed by Sharf et al. [23] and is called *tether-actuated closing mechanism*. In the remainder of this Thesis, the alternative closing mechanism, independent of the winching of the main tether, is called *standard closing mechanism*.

In this Chapter, before introducing closing mechanisms in the tether-net system, an analysis of the effect that spooling the main tether has on the capture of a realistic target debris is presented (see Section 5.1). Then, in Section 5.2, modeling of the tether-actuated closing mechanism is proposed and results of capture with it are shown. Standard closing mechanisms are modeled and employed for capture simulations in Section 5.3. To overcome problems in simulation of capture of satellites with thin appendages, an alternative model of the threads of the net is proposed in Section 5.4. Capture of a small asteroid with a tether-net is the subject of Section 5.5. Finally, Section 5.6 concludes Part III with closing remarks on capture dynamics.

5.1 Effect of main tether on capture dynamics

In Section 3.4, it was suggested that modulation of the winching profile of the main tether could be exploited to ease the capture of the target spacecraft. The effect of tensioning of the main tether on capture dynamics is here evaluated by prescribing different open loop winching controls and by analyzing their effect on the performance criteria introduced in Section 4.1.

5.1.1 Model of Zenit-2 stage 2

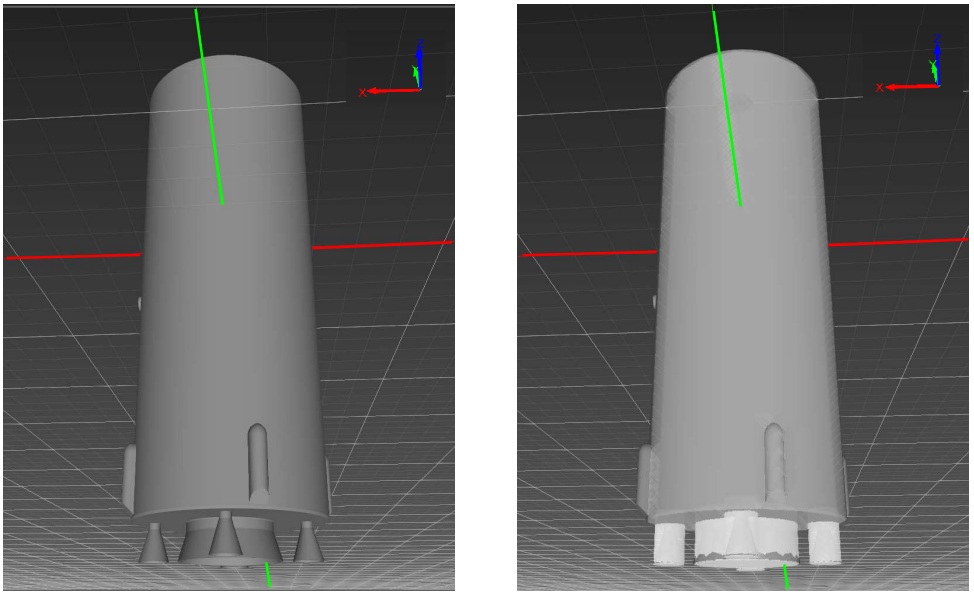

FIGURE 5.1: Stage 2 of Zenit-2 rocket. a) Graphics model. b) Collision geometry.

Existing research revealed that most of the high-risk objects in LEO are stage 2 of Zenit-2 rockets [4]. A model of this object was assembled in the Vortex Editor: its graphics model and collision geometries are shown in Figure 5.1. Stage 2 of Zenit-2 rockets is 11 m long, 3.9 m wide, and its mass is of 9000 kg; its inertia matrix was estimated by approximating the debris with a thick-walled cylindrical tube with open ends (10.2 m long, 3.9 m wide, with a 3 cm thick wall). The position of its center of mass in the part reference frame, whose origin lies at the intersection of the red and green lines shown in Figure 5.1 and whose orientation is indicated in the top right corner, is:

$$\mathbf{r}_{G,O'} = [0 \quad 0 \quad -1.183]^T \text{m} \tag{5.1}$$

The inertia tensor in the same reference frame is:

$$\mathbf{I}_G = \begin{bmatrix} 94880 & 0 & 0 \\ 0 & 94880 & 0 \\ 0 & 0 & 46295.5 \end{bmatrix} \text{kg} \cdot \text{m}^2 \tag{5.2}$$

5.1.2 Results of capture

The results presented here were obtained assuming that the target is non-rotating and oriented such that the axis of the main cylinder is parallel to the direction of net ejection. This makes the scenario similar to that depicted in Figure 4.2 and allows to use the quantitative capture performance criteria identified in Section 4.1; otherwise, the success of the capture maneuver in the absence of a closing mechanism remains ambiguous. The origin of the target part is initially centered with respect to the net, at a distance $d_T = 20$ m from the initial plane of the net, such that the top surface is at a distance of 15.9 m from it and the initial position of the center of mass of the target in the inertial reference frame is: $\mathbf{r}_G = [0.55 \quad 0.55 \quad -21.183]^T$ m. The simulation parameters are identical to those in Table 3.9; however, the dynamics is simulated for a longer time ($t_f = 60$ s).

Different open loop winching controls were prescribed to change the length of the main tether during the capture phase, similarly to what was done for the deployment phase in Section 3.4. The winching profiles are depicted in Figure 5.2, where meaningful capture events are also indicated: the times of first closure and reopening are shown with solid vertical lines, and the intervals for which the corner masses are farther than the distal part of the target are delimited by dashed vertical lines. With a free tether (see Figure 5.2, control C1), the net impacts the top surface of the target spacecraft at $t = 15.6$ s; the corner masses reach a distance from the chaser farther than the distal surface of the target spacecraft at $t = 24$ s and remain in that region until $t = 37.7$ s; closure and re-opening of the net as defined above happen at $t = 29.2$ s and at $t = 45.5$ s, respectively.

The open loop winching controls employed in the analysis of capture are:

C1: the tether is free to spool out as it is tensioned by the net;

C2: the tether is free to spool out, apart from the interval between $t = 18$ s and $t = 19$ s, when it is spooled in at a rate of 2 m/s;

C3: the tether is free to spool out, apart from the interval between $t = 29$ s and $t = 31$ s, when it is spooled in at a rate of 2 m/s;

C4: the tether is free to spool out, apart from the interval between $t = 24$ s and $t = 32$ s, when it is spooled in at a rate of 1 m/s;

C5: the tether is free to spool out, apart from the interval between $t = 17$ s and $t = 30$ s, when it is spooled out at a rate of 0.5 m/s;

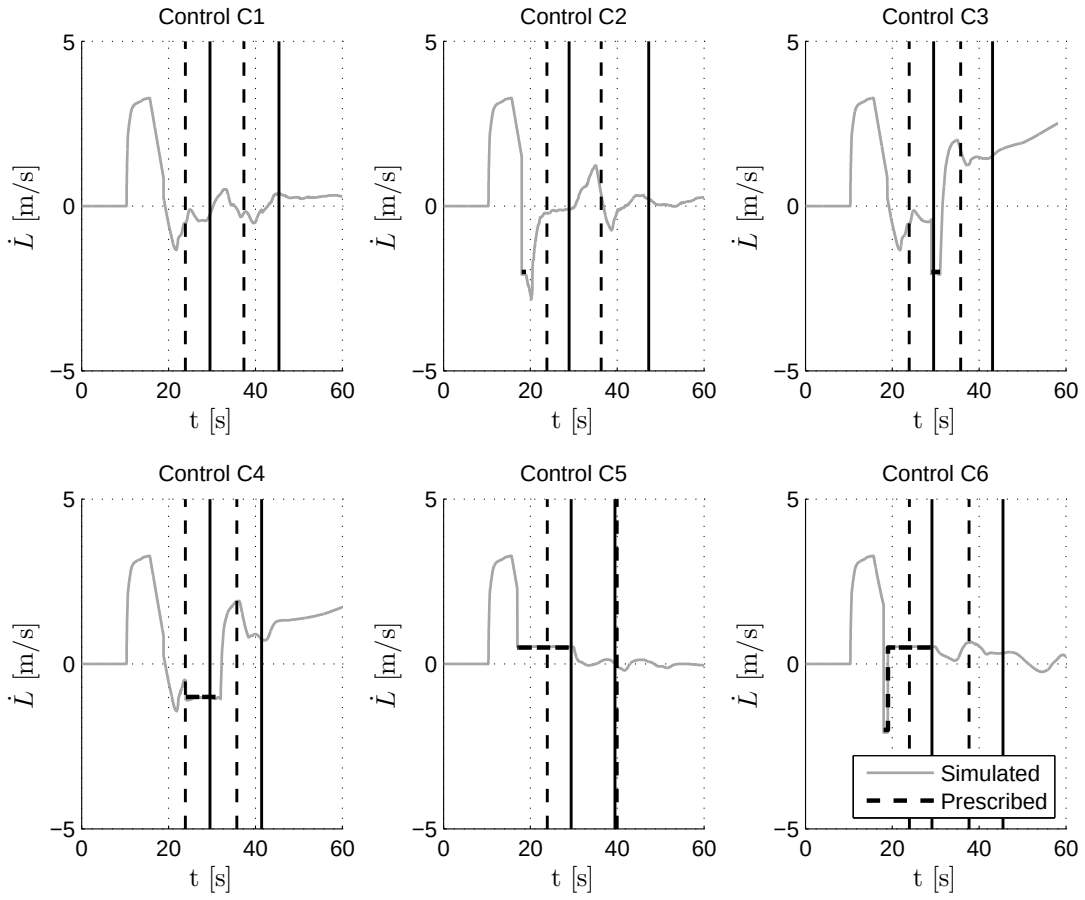

FIGURE 5.2: Prescribed open loop winching controls (black dashed lines) and obtained tether length rates (gray solid lines) in simulations of capture, with indication of meaningful capture events: times of first closure and reopening (solid vertical lines), and intervals for which the corner masses are farther than the distal part of the target (delimited by dashed vertical lines).

C6: the tether is free to spool out, apart from the interval between $t = 18$ s and $t = 19$ s, when it is spooled in at a rate of 2 m/s, and between $t = 19$ s and $t = 30$ s, when it is spooled out at a rate of 0.5 m/s.

These profiles were chosen such that the effect of different controls applied at different times relative to the capture events could be evaluated. With control C2, the tether is spooled in for a burst of time after impact but before beginning of closure; with control C3, the tether is spooled in for a burst of time during closure; spooling in for a longer time during closure is applied with control C4. The effect of spooling the tether out for a moderately long time is studied with control C5. Finally, control C6 provides a combination of spooling the tether in with a burst and then out for a moderately long time. Practical values were chosen for the magnitudes of the spooling velocities.

Since the time of contact with the top surface of the target is the same for each of the proposed simulations, it is not shown in Figure 5.2. From an analysis of the other closure-related events, it was found that spooling the tether in before closure only for a short

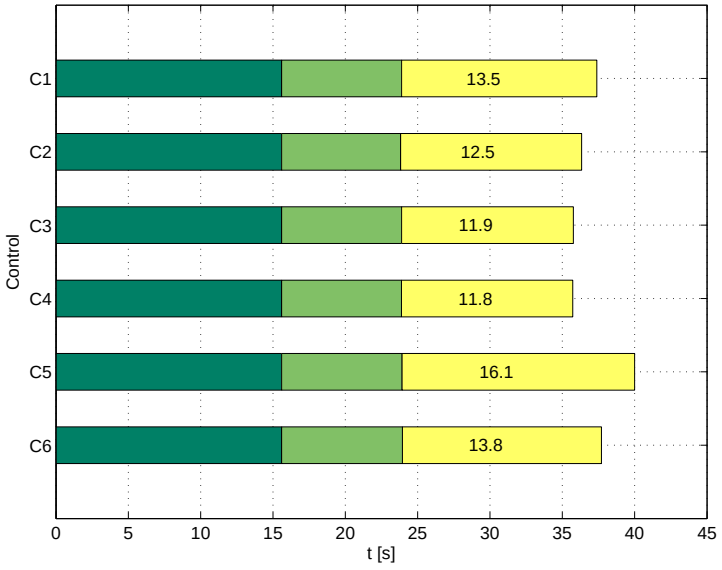

FIGURE 5.3: Comparison of capture-related events in simulations of capture with different tether controls. Dark green: interval from beginning of deployment to first contact between net and target; light green: interval from first contact to time when the corner masses are farther than the target; yellow: interval with corner masses farther than the target.

time (i.e., with control C2) makes the closure happen faster and the net remains closed around the target for a longer time with respect to the free case. On the other hand, spooling the tether in after closure (such as with controls C3 and C4) has a negative effect on the time the net stays around the target; also, the pulling force in the tether increases the risk that the net returns towards the servicing spacecraft after slipping off the target. Spooling the tether out after capture (i.e., with controls C5 and C6), does not seem to make the net stay closed around the debris for longer time. In all control scenarios, the net was seen to open again after "capture": this corroborates the idea that a closing mechanism is needed to secure the spacecraft in the net.

In Figure 5.3 a comparison of the intervals for which the corner masses remain farther than the distal part of the target is shown for the different winching controls. From the numerical values of the intervals for which the corner masses stay in the desired position, which are reported in the yellow bar (in seconds), the best winching profile appears to be the one in which the tether is simply spooled out for some time after the net impacts the target (i.e., control C5): the interval is increased by around 20% with respect to the case with a free cable. On the contrary, spooling the tether in at any time and for any duration (e.g., with controls C2, C3, C4, C6) shortens the time available for the actuation of a closing mechanism. Spooling in decreases this interval so much that even spooling the tether out for a long time afterwards (e.g., as per control C6) only recovers a situation similar to that obtained with the free tether case. Nonetheless, it can be noticed that the interval in question is higher than 10 s in any of the performed simulations: this time is deemed sufficient for a closing mechanism to work.

Overall, it was found that an actuated spooling out of the tether, initiated after the first contact between the net and debris, can be useful for the corner masses to remain on the distal side of the target for a longer period of time. This would be beneficial for a *standard* closing mechanism. A tether spooling out freely from the winch during the capture maneuver is also a good option. On the other hand, a *tether-actuated* closing mechanism requires tensioning of the main tether, and hence a spooling-in action; this is achievable, but would require accurate timing of winch actuation.

5.2 Capture of debris with tether-actuated closing mechanism

The *tether-actuated closing mechanism*, proposed by Sharf et al. in [23], consists in exploiting the winching capabilities of the main tether to close the perimeter of the net. The main tether is extended by making it pass through a ring at the center of the net (instead of attaching it there) and then through several rings along the net perimeter; the end of the tether is fixed at some point on the net perimeter. Upon actuation of the winch placed on the chaser, the length of the tether can be reduced, therefore causing closure of the perimeter of the net. In order to limit the spooling velocity of the winch required for closure, multiple tethers along different parts of the net perimeter can be provided instead of one; if n_t is the number of tethers forming the cinch cord, a winching velocity of $\dot{L}_t$ is sufficient to close the net perimeter at a rate $n_t\dot{L}_t$. An illustration of the proposed closing mechanism with two tethers forming the cinch cord is shown in Figure 5.4.

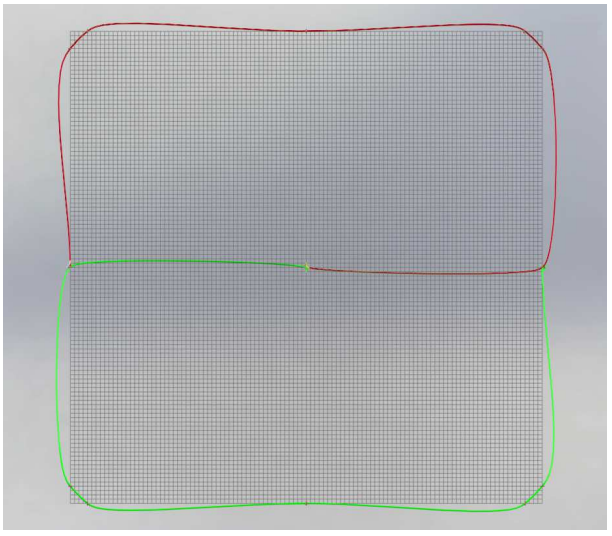

FIGURE 5.4: Illustration of the proposed tether-actuated closing mechanism with tethers forming the cinch cord [23].

5.2.1 Modeling of tether-actuated closing mechanism

To model this closing mechanism in the Vortex-Dynamics-based simulator, frictionless *ring* constraints were added between several nodes of the net (i.e., rigid bodies) and the tethers: these constraints keep the tether and the rigid body on the net in the same place (i.e., where the ring is placed), and maintain the sum of the lengths of the portions of tether on the sides of a ring constant (or varying at the prescribed rate).

The modeling of rings in Vortex Dynamics is based on the work by Servin and Lacoursière [91]. According to that work, one cable passing through $J+1$ rings attached to rigid bodies would increase the size of the constraint Jacobian by one row only, for maintaining the length constraint. The constraint for total length conservation says that the sum of the lengths of the J segments is always equal to the length of the cable $L_t(t)$ (considering that the length of the cable can vary because of a winch):

$$\phi_s = \sum_{j=1}^{J} l_j(t) - L_t(t) = 0 \tag{5.3}$$

In a velocity-level formulation, one can write:

$$\dot{\phi}_s = \sum_{j=1}^{J} \dot{l}_j(t) - \dot{L}_t(t) = 0 \tag{5.4}$$

where $\dot{L}_t(t)$ is the tether length rate at time t. Before introducing the net closing mechanism in the model, the modeling of the tethers with rings was tested separately, in simpler configurations and in the absence of the net: for a sample of the benchmark tests developed, the reader is referred to appendix B.

Due to limitations of the Vortex Dynamics engine at the time of writing, the cinch cord modeled in the simulator is somewhat different from what is envisaged and from the cinch cord employed in the experiments presented in [23], but it maintains the same principle of operation for achieving the net closure. It is composed of $n_t = 4$ separate tethers, all reeled on the same winch, and each passing through a ring at the central node of the net, then through a ring at a corner node on the net and a ring at the central node on a side of the net. Finally, each tether is attached to the next corner node, with respect to the corresponding "ringed" corner of the net. The topology of the four tethers, rings and attachments comprising the closing mechanism in the model is sketched in Figure 5.5. In this figure, the flow of the tethers is shown with arrows, for one of the tethers (in green).

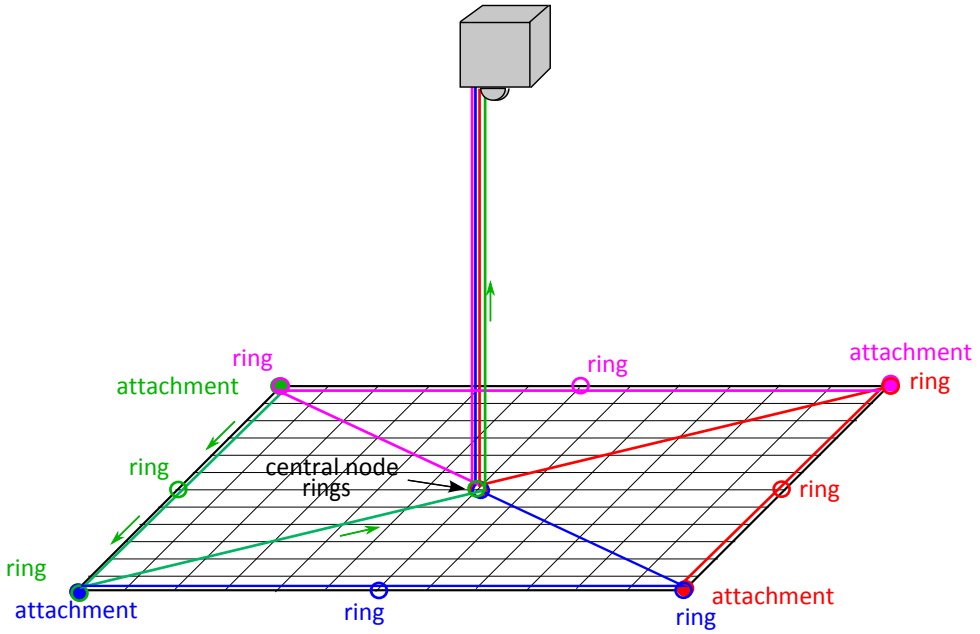

FIGURE 5.5: Sketch of topology of four tethers, rings and attachments of closing mechanism implemented for simulations. Green arrows indicate the flow of the green tether.

5.2.2 Results of capture

Simulation of capture of a realistic debris target with a tether-net system equipped with the proposed closing mechanism was performed to confirm its feasibility for ADR purposes. Stage 2 of Zenit-2 rockets was employed again; this time, in light of the considerations on the safety of capture in Section 4.7.2, the initial orientation of the target is set such that the axis of the main cylinder is parallel to the x-y plane (see Figure 5.6(a)) and the initial position of its center of mass is: $\mathbf{r}_G = [0.55 \quad 1.733 \quad -15]^T$ m. Most of the parameters collected in Table 3.9 are used for this simulation; exceptions are the simulation time $t_f = 120$ s (chosen to verify that capture is sustained) and the distance between the chaser and the net $d_{ch} = 7.25$ m. Although the choice for d_{ch} makes the system less realistic, it was dictated by issues due to limitations of the Vortex Dynamics engine at the time of writing.

During the deployment phase, the winch constraint is set to free, so that the tether can be spooled out freely as it is tensioned by the net. As was observed in Section 5.1, the tether-actuated closing mechanism requires good timing of the tether spool-in to initiate the net closure. Here, a closed loop PD control is used, such that the tether is reeled in slower and slower as the net closes around the target. Spooling in of the tether is initiated at $t = 15$ s, after the first contact between the net and the debris target, and is controlled according to: $\dot{L}_t = K_P d + K_D \dot{d}$, where $K_P = 0.1$ 1/s, $K_D = -0.01$, d is the length of the portion of a tether along the perimeter of the net, and $\dot{d}$ its derivative. In order to prevent high tensioning of the tethers, the winch constraint was modified as follows: if at any time the tension in any of the tethers exceeded a value of 1 N, the winch

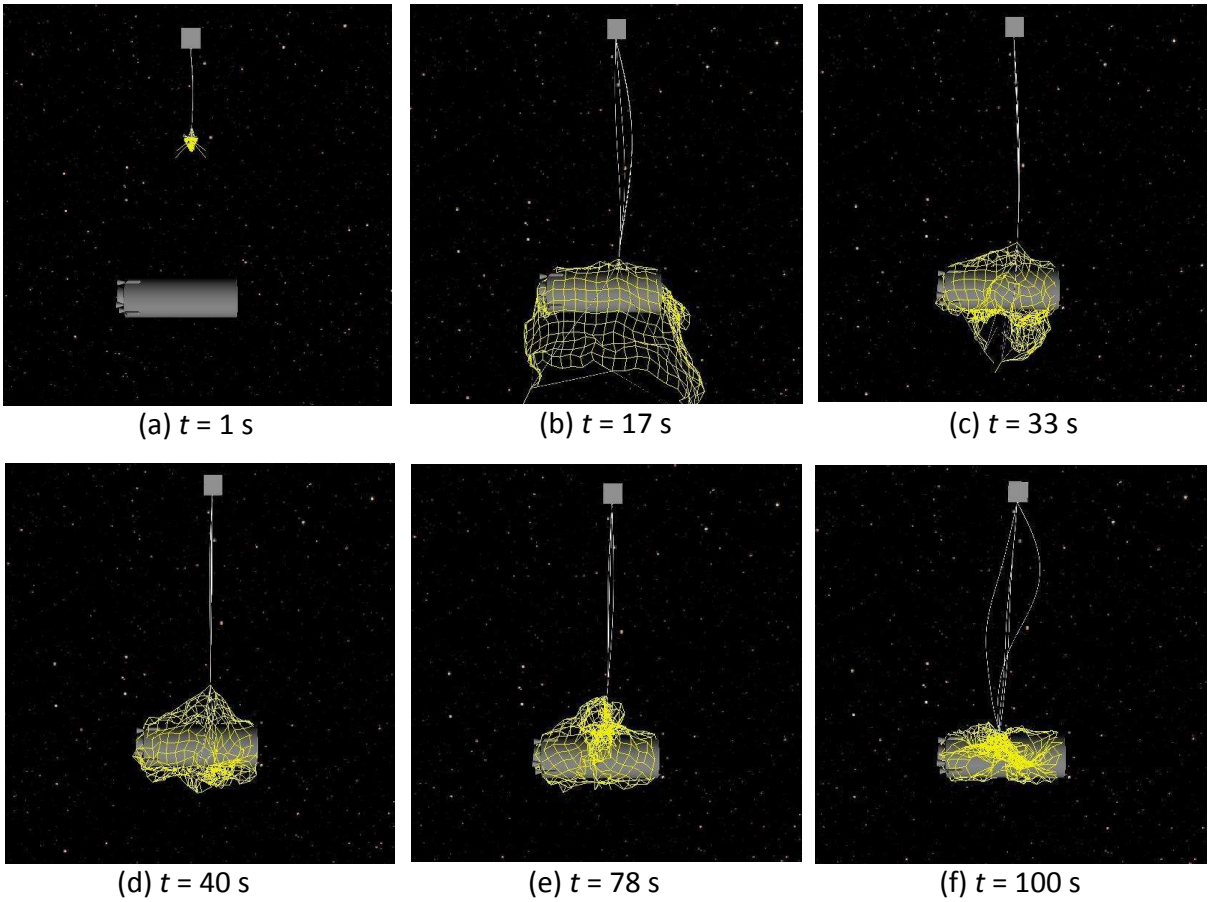

FIGURE 5.6: Simulation of net deployment, envelopment and containment of rotating debris: (a) net starts deploying, (b) net and debris are in contact, (c) closing mechanism is activated and tethers are shortened, (d) debris is captured, (e)-(f) capture is sustained.

was locked until tension returned to below the aforementioned limit. It is noted that the particular controller represents one of many possible control algorithms that could be employed to demonstrate the performance of the closing mechanism proposed. Further work on control strategies for this task is suggested to ensure optimal performance within practical hardware limitations and is beyond the scope of the present work.

Figure 5.6 displays several screenshots from a complete capture simulation starting with the folded configuration of the net, through deployment and to the closure of the net around the debris. It is confirmed that the tether-actuated closing mechanism behaves as expected, i.e., it shortens the tether around the net perimeter, herein keeping the net closed around the target spacecraft for more than 100 s. The same simulation was performed with different integration step sizes to ascertain the proper functioning of the closing mechanism and the time the net remains around the debris. After closure, the response is more sensitive to the step size, varying from the net remaining around the target for longer, to slipping off it. The latter occurs due to the modeling of a single ring only to constrain each side of the net to the cord of the closing mechanism. Ideally, more rings would be constraining the tether to the net perimeter, and the net would remain

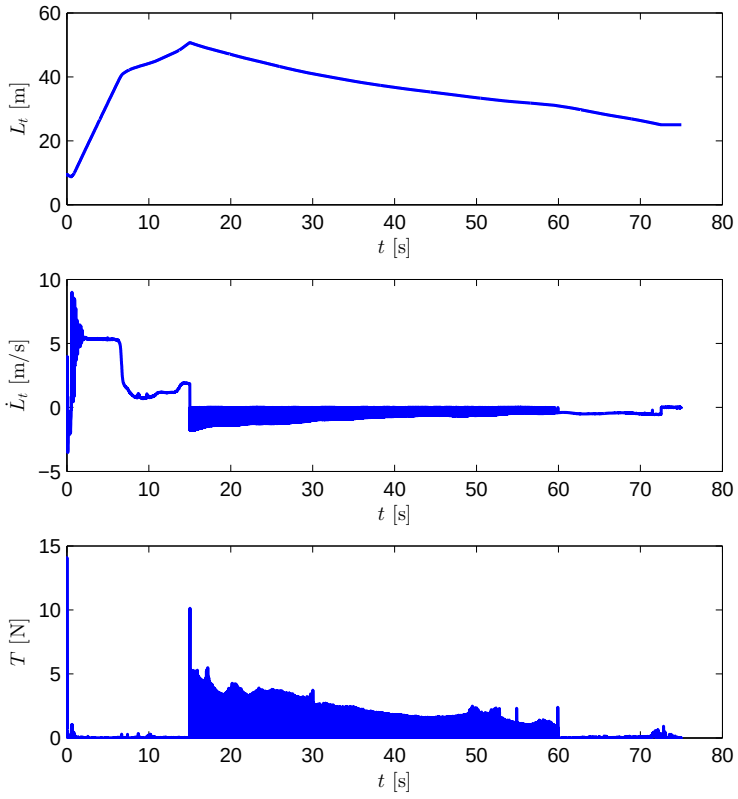

FIGURE 5.7: Length, length rate, and maximum tension of one of the tethers during simulation of capture with tether-actuated closing mechanism.

consistently closed around the target. As was previously mentioned, current limitations in Vortex Dynamics engine prevented a more accurate modeling of the closing mechanism.[1]

In Figure 5.7, the length, length rate, and maximum tension of one of the tethers during capture are plotted, to verify the correct winching. It is observed that the tether elongates under low tension during the deployment of the net, when it is free to spool out; afterwards, as the tether is winched in, its length decreases and the tension rises. The highest peak in tension occurs at the initiation of closure, at $t = 15$ s. For the whole simulation, tension remains within reasonable limits, although it exhibits high-frequency fluctuations. In the phase of spooling-in, the tether length rate remains under 2 m/s, which is within the working range indicated by Lanzani [92] for reel mechanisms. Control law design to optimize the response of the system during the closing of the net should be explored further.

Although these results were obtained with the standard lumped-parameter model of the net, corresponding simulations with inclusion of the bending stiffness of the threads of the net were performed: notwithstanding some differences in the dynamics of the net,

[1]Following notice of these issues to the marketing company, capabilities of the Vortex Dynamics engine are being extended.

the results of capture showed similar success and confirmed the working principle of the closing mechanism.

5.3 Capture of debris with standard closing mechanisms

Because of the issues encountered in the simulation of capture with the tether-actuated closing mechanism, results in the remainder of this Thesis are obtained with an implementation of standard closing mechanisms. These consist in additional threads running between the corner masses or along the perimeter of the net, that are winched in independently from the main tether, thanks to winches placed in some of the corner masses (see, for example, reference [10]).

5.3.1 Modeling of standard closing mechanisms

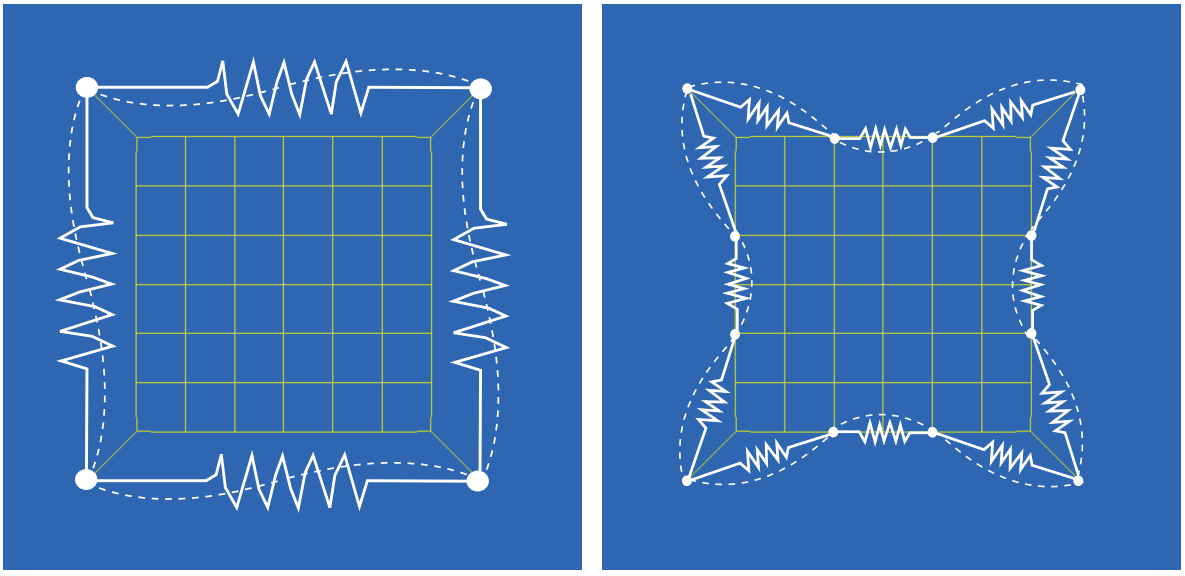

(a) (b)

FIGURE 5.8: Model of standard closing mechanism: (a) between corner masses; (b) around net perimeter.

Two versions of standard closing mechanisms were implemented in the simulator at hand: one made of tethers among the corner masses only (see Figure 5.8(a)), and one interlaced with the perimeter of the net (see Figure 5.8(b)). In the second type, two attachments are added on each side of the net so as to divide it in three parts of similar lengths; for example, on the side of the net on the x-axis, the attachments are placed at the nodes

of indices $i = \lfloor (N_s - 1)/3 \rfloor$ and $j = N_s - i$ (the reader can refer to Figure 2.1 for the numbering of nodes and the orientation of the x- and y-axes).

These closing mechanisms are modeled in a simplified way. Several distance joints between contiguous nodes along the closing mechanisms are created in the initialization phase (with maximum distance set to zero), but are left disabled during deployment of the net. From the time of activation of the closing mechanism (chosen by the user), constant forces are added between each couple of adjacent nodes along the closing mechanisms, that bring the nodes together. When the distance between two adjacent nodes on the closing mechanism decreases below 1 m, the abovementioned distance joints are enabled, so that the constrained rigid bodies are kept together for the rest of the capture maneuver. In Figure 5.8, these constraints are represented with white springs; the white dashed curves represent the tethers forming the closing mechanisms so modeled.

It is recognized that this modeling approach does not take into account real properties of the closing tether and of the winching of the closing mechanism; however, it allows to perform different assessments on the capture capabilities of tether-net systems, as will be shown in the following Sections. More realistic models could be implemented in Vortex Dynamics when the limitations on the number of rings are removed.

5.3.2 Capture of rotating debris

Simulations of capture of rotating stage 2 of Zenit-2 rocket were performed with both standard closing mechanisms. All the simulation parameters are the same as in Section 5.2, apart from $d_{ch} = 0.1$ m. The target is assumed to be rotating about its major axis of inertia at a rate of 5°/s. The main tether is simply attached to the winch on the chaser and to the central node of the net; it is left free to spool out during deployment, and it is locked at $t = 15$ s. The standard closing mechanism is also actuated at $t = 15$ s.

Figures 5.9 and 5.10 show some screenshots of the capture sequences obtained with the two versions of the standard closing mechanism, respectively. As a results of actuation of the closing mechanism, in Figure 5.10(b) it is seen that the corner masses and the attachment points on the sides of the net start approaching; although the effect of the closing mechanism is not visible in Figure 5.9(b), it is apparent from Figure 5.9(c) that the corner masses are brought together as desired. In both cases, debris appears to be successfully captured at $t = 24$ s. However, later in the simulation, debris remains contained in the case of the closing mechanism interlaced with the net only, as shown in Figures 5.10(d)-(e); the net slips off the debris for the closing mechanism between the corner masses, as shown in Figures 5.9(d)-(e).

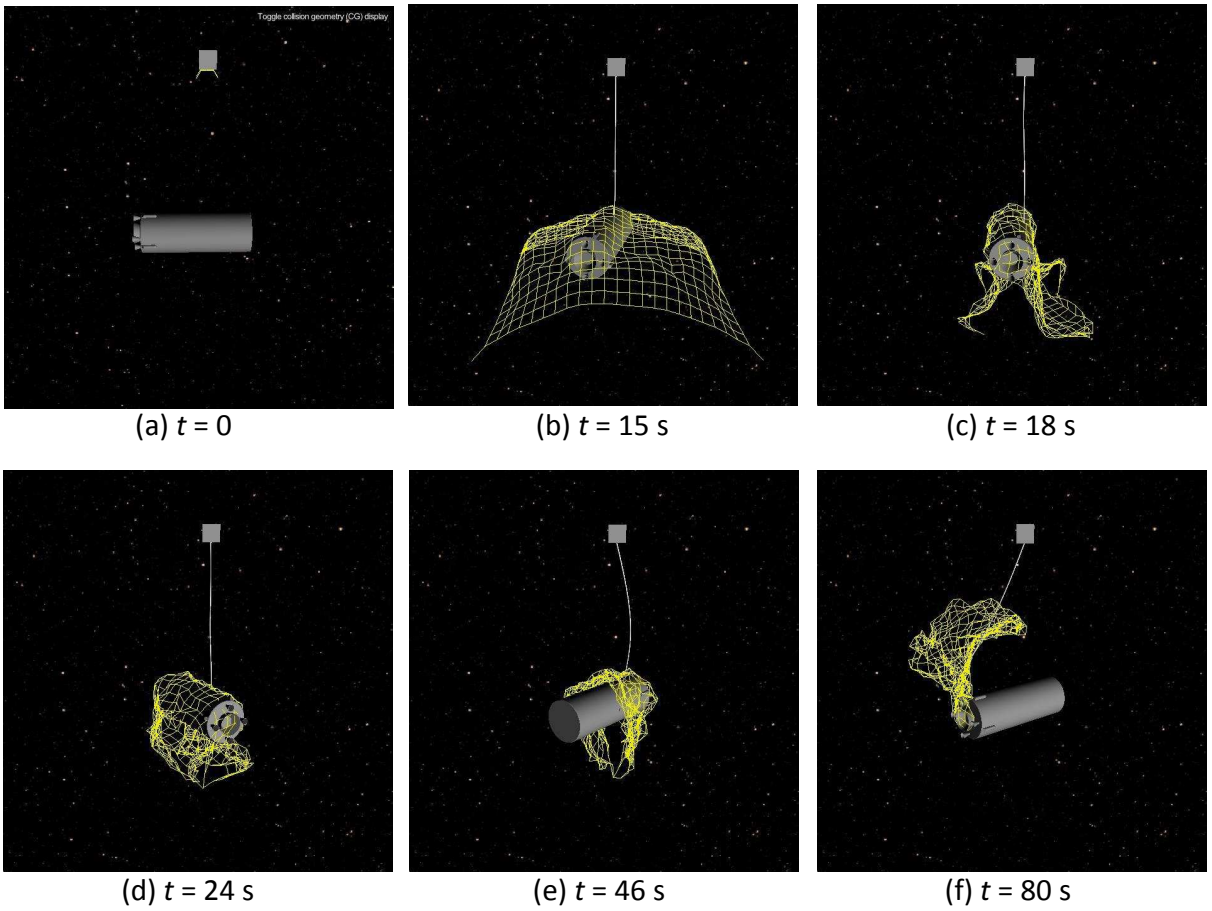

FIGURE 5.9: Simulation of capture with a standard closing mechanism among the corner masses: (a) net starts deploying, (b) net is fully open, (c) closing mechanism is active, (d) debris is captured, (e)-(f) net slips off.

From the outcome of these simulations, it was observed that a closing mechanism running simply among the four corner masses cannot guarantee containment of the considered debris after capture. In fact, the opening left by the part of the perimeter of the net between two corner masses is sufficiently large for the net to slip off the debris. On the other hand, inclusion of a closing mechanism with two attachments on each side of the net demonstrated successful capture of debris. For the net used in these simulations, the closing mechanism modeled as per Figure 5.8(b) has attachments at nodes of indices $i = 7$ and $j = 16$. It can be verified that the largest distance between two attachment points of this closing mechanism is 9 m; if one assumes that a circular space is created upon closure of this portion of the perimeter of the net, then the circle has a diameter of 2.9 m, smaller than the diameter of the target (i.e., 3.9 m), which guarantees containment of the latter.

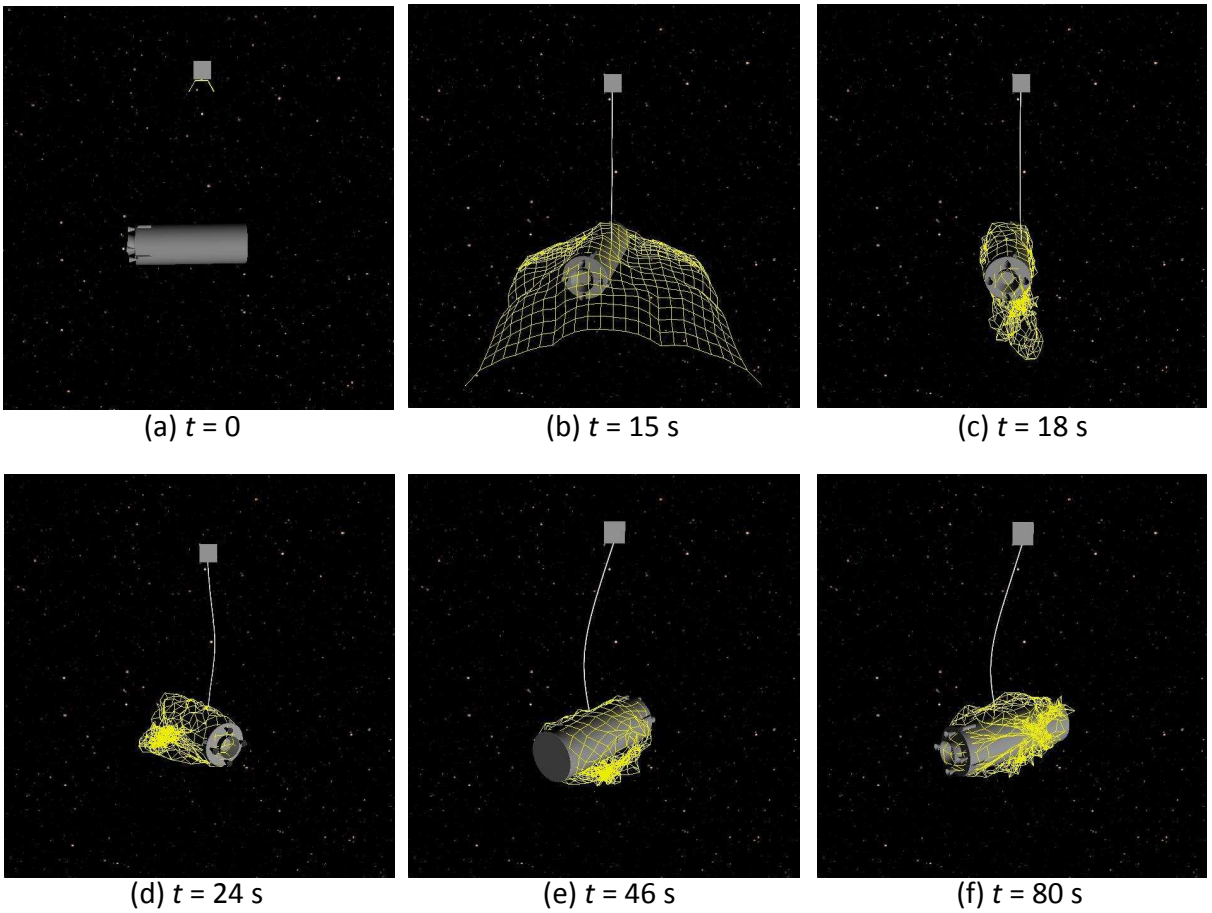

FIGURE 5.10: Simulation of capture with a standard closing mechanism around the perimeter of the net: (a) net starts deploying, (b) closing mechanism is activated, (c) closure is achieved, (d) debris is captured, (e)-(f) capture is sustained.

5.3.3 Preferred capture scenario

In Section 4.7.2, the issue of safety of the capture procedure was raised: it was observed that the presence of tension in the main tether when debris is successfully contained might cause unwanted transmission of loads to the chaser spacecraft. In order to identify safer capture scenarios, simulations of capture of rotating Zenit-2 stage 2 in different initial orientations relative to the direction of ejection of the net were compared. In the following, scenario 1 indicates a situation similar to that illustrated in Figure 4.16(a), and scenario 2 indicates a situation similar to that illustrated in Figure 4.16(b). In both cases, the net is equipped with a standard closing mechanism along the net perimeter. As in all previous studies, the chaser is free-floating and uncontrolled. Simulation results presented here were obtained with $t_f = 300$ s for scenario 1 and with $t_f = 60$ s for scenario 2.

Figure 5.11 compares the results of simulations in the two scenarios. The z-coordinates of notable points on the chaser and on the target during capture are shown in Figures 5.11(a) and (b): for the chaser, solely the center of mass is analyzed; for the rotating

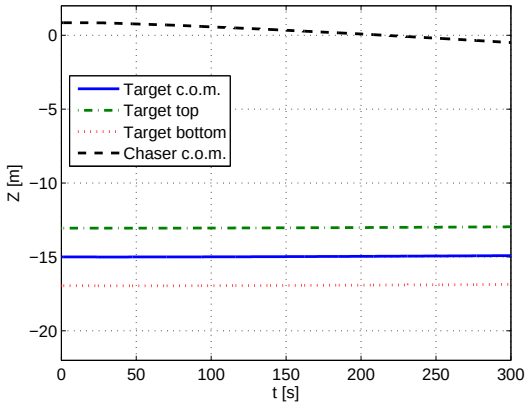

(a) Scenario 1.

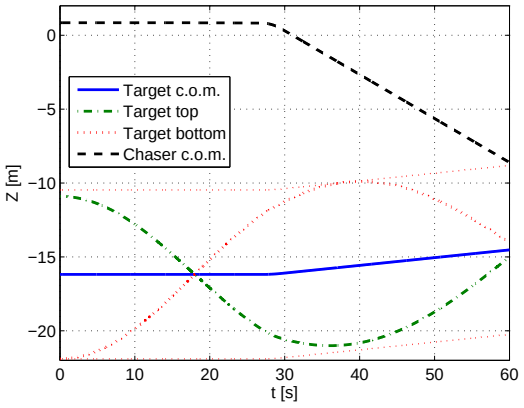

(b) Scenario 2.

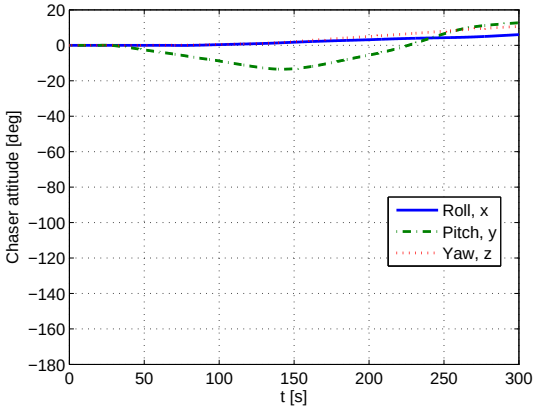

(c) Scenario 1.

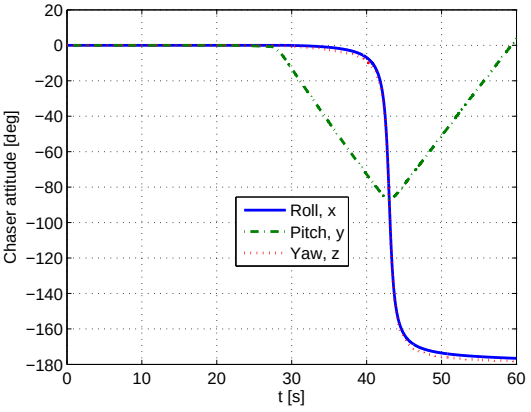

(d) Scenario 2.

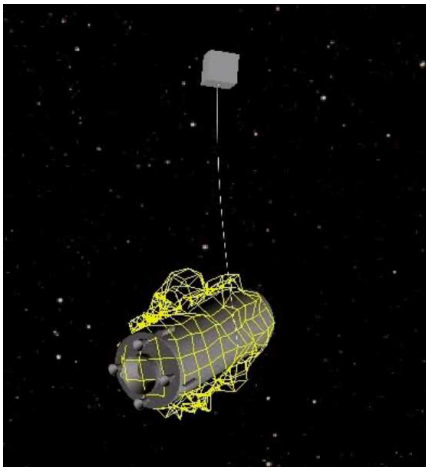

(e) Scenario 1 at $t = 300$ s.

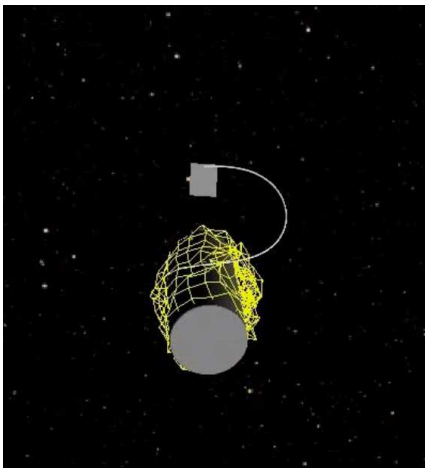

(f) Scenario 2 at $t = 60$ s.

FIGURE 5.11: Results of capture of rotating Zenit-2 stage 2 with standard closing mechanism interlaced with the net perimeter. (a)-(b): z-coordinates of chaser and target. (c)-(d): attitude of chaser. (e)-(f): Snapshots at end of simulation.

target, a point on the surfaces closer to and farther from the chaser (called *top* and *bottom* respectively) are also considered. It is clear at first sight that the dynamics in the two scenarios are very different. In scenario 2, the chaser is dragged towards the target by the tension in the main tether; just after one minute, the distance between the center of mass of the chaser and the center of mass of the target is of 5.77 m, that is the same as the distance between the center of mass and the *bottom* point of the target. At the end of the simulation time frame, in Figure 5.11(b) it is seen that the center of mass of the chaser (dashed black lines) and the envelop of the target (lightweight red dotted line) are very close, suggesting that an impact is imminent. Even in scenario 1, a free-floating chaser is dragged towards the target by the tension in the tether (see Figure 5.11(a)); however, this effect is much less pronounced, and chaser and target remain at a safe distance even after 5 minutes (e.g., a distance of more than 10 m between the center of mass of the chaser and the top of the target at $t = 300$ s).

The attitude of the chaser in the two scenarios is represented in Figures 5.11(c) and (d). Once again, it is evident that the orientation of the chaser is much less perturbed in scenario 1; the rotations happen slowly, and the maximum rotations are of around 10°. In scenario 2, instead, the chaser undergoes fast and large rotations. Although outside of the scope of the present work, the results on the attitude of the chaser in scenario 1 could serve to identify requirements for the design of the attitude control system of the chaser.

Snapshots of the system at the end of the simulations ease the visualization of the differences in the final configurations in scenarios 1 and 2 (see Figures 5.11(e) and (f)). All these results suggest that a safer capture scenario is one in which the target spin axis is aligned with the direction of ejection of the net, as was anticipated in Section 4.7.2.

5.4 Capture of Envisat

One of the most-wanted debris objects is Envisat spacecraft [4], a satellite for Earth-observation now decommissioned. Precisely because it is large and massive, orbiting in one of the highly populated Sun-Synchronous orbits, and it is owned by ESA, Envisat is the foreseen target for the first demonstration ADR mission [11]. Parabolic flight experiments to demonstrate that nets can capture Envisat have been performed recently [30, 38]. The topic of this Section is the simulation of capture of a target modeled after Envisat.

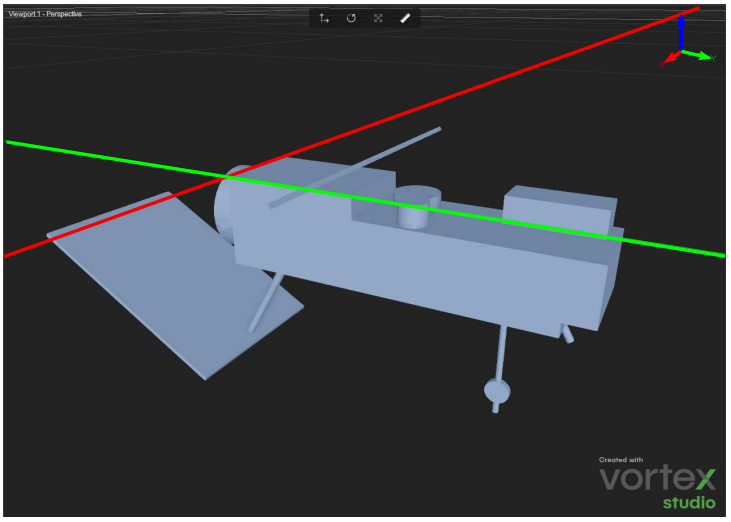

FIGURE 5.12: Model of Envisat. Notice the antenna (the thin element on the top of the spacecraft) and a solar array (the thin large element at its bottom).

5.4.1 Model of Envisat

A graphics model of Envisat spacecraft was created by scaling up the specification of a mock-up used for validation on a parabolic flight by Golebiowski et al. [30]. The model for Envisat is shown in Vortex Editor in Figure 5.12. The dimensions of its main body are of approximately 10 m × 2.5 m × 2.5 m; moreover, Envisat is equipped with thin structural members, such as an antenna and a solar array. The dynamics model of Envisat was implemented by assuming a uniformly distributed mass of $m_T = 8000$ kg and by using patched primitive collision geometries. The position vector of the center of mass in the body-fixed reference frame (i.e., the part reference frame) shown in Figure 5.12 (with origin at the intersection of the green and red lines, and orientation of the axes as indicated by the vectors at the top right corner) is:

$$\mathbf{r}_{G,O'} = [-1.220 \quad 3.509 - 1.464]^T \text{m} \tag{5.5}$$

The inertia tensor in the same reference frame is:

$$\mathbf{I}_G = \begin{bmatrix} 96977.9 & 680.194 & 205.104 \\ 680.194 & 14015.2 & -7999.64 \\ 205.104 & -7999.64 & 94688.4 \end{bmatrix} \text{kg} \cdot \text{m}^2 \tag{5.6}$$

5.4.2 Capture of Envisat with lumped-parameter model of net

Simulation of capture of Envisat was performed with the lumped-parameter model of the net. The same parameters collected in Table 3.9 are used for this simulation, apart from

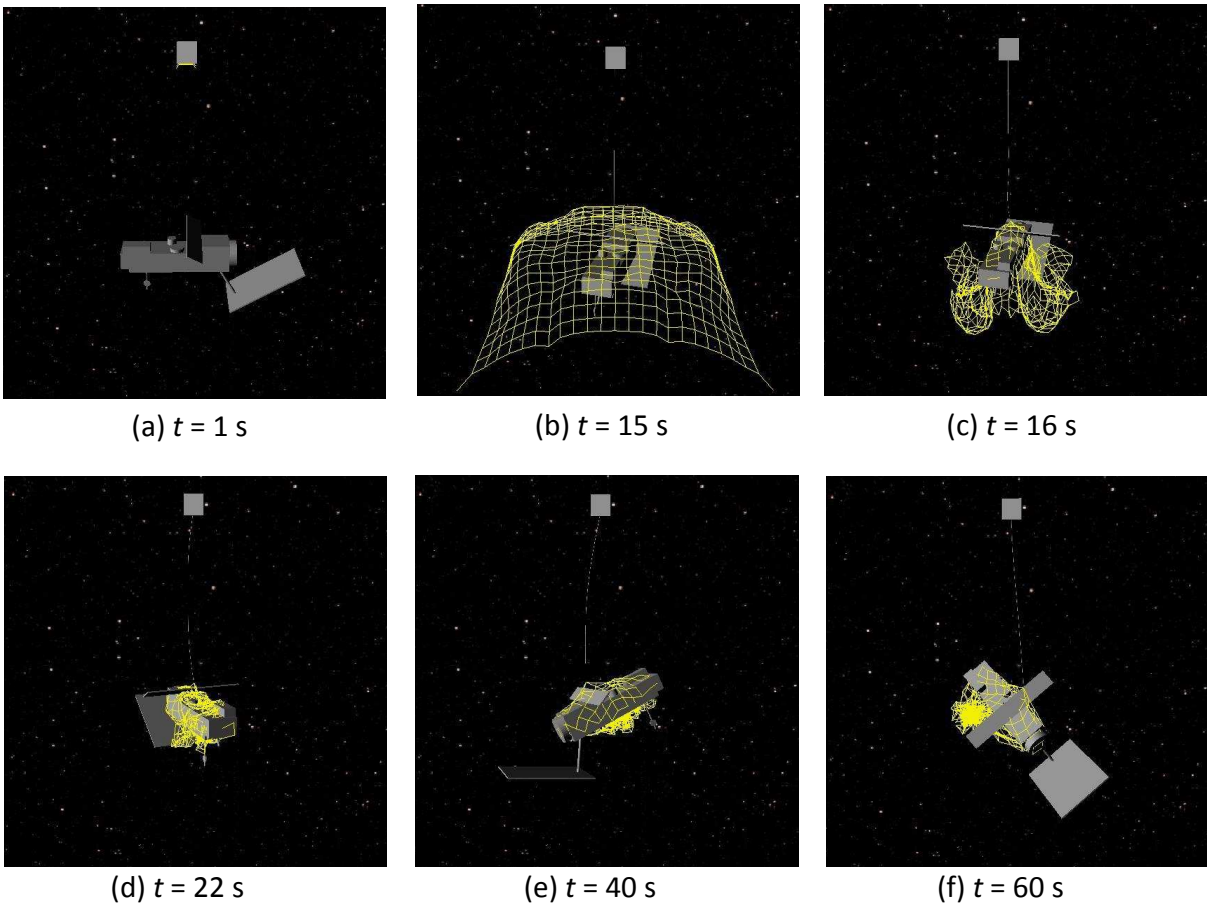

FIGURE 5.13: Capture of Envisat with net represented with the lumped-parameter model.

$t_f = 60$ s. Envisat is assumed to be rotating with $\omega_T = 5°/\text{s}$ about an axis parallel to the inertial z-axis and passing through its center of mass; this value of ω_T is almost the double of the best knowledge of the angular velocity of Envisat, which is of 2.67°/s [93]. The material of Envisat is assumed to be Aluminum. The net is equipped with a standard closing mechanism interlaced with the mouth of the net, to be actuated at $t = 15$ s.

Screenshots of the capture sequence are shown in Figure 5.13. The net is ejected at $t = 0$; at $t = 15$ s it is fully deployed and the closing mechanism is actuated (its effect on the mouth of the net is visible in Figure 5.13(b)); closure is achieved at $t = 16$ s. In the later screenshots, it is observed that, although capture of Envisat is sustained, the lumped-parameter model of the net fails to correctly detect collisions with certain parts of Envisat. For example, looking at the screenshot for $t = 15$ s, one would expect that the net will envelop the large and thin antenna placed at the top of Envisat; instead, such envelopment is not confirmed in the later screenshots (see also Figure 5.14 for a closeup view). The tumbling of Envisat, visible through the whole simulation, is due to its asymmetric inertia distribution.

The main drawback of the lumped-parameter net model presented in Section 2.1 is that

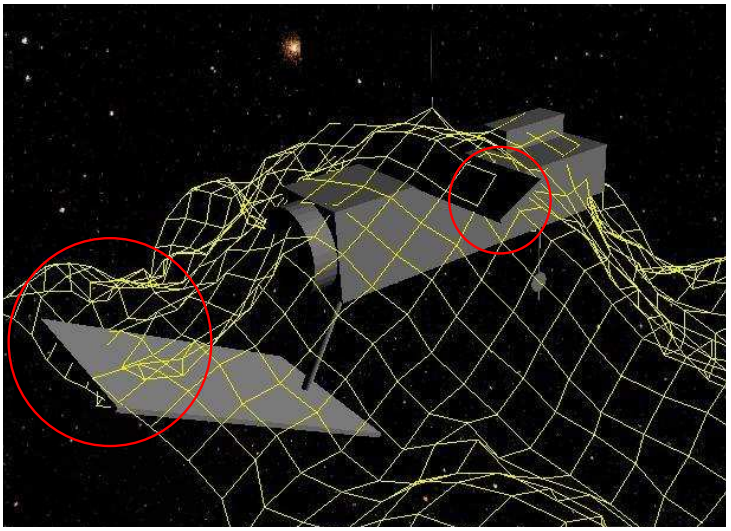

FIGURE 5.14: Illustration of inability of lumped-parameter model to correctly detect collisions with thin structural elements of Envisat.

it is not capable of detecting collisions along the threads of the net: in fact, only the small rigid bodies at the physical knots of the net possess mass properties and collision geometries. This causes two main issues:

1. only collisions with objects whose minimum dimensions are larger than the distance between two physical knots of the net can be correctly detected (e.g., see the problem in detecting collisions with the antenna and solar array of Envisat in Figure 5.14);
2. the physics of contact may be considerably different from what happens in reality, since the contact forces are lumped at the knots of the net, instead of being distributed along the threads of the net.

In order to remedy these issues, two options were considered: (i) adding multiple nodes along the threads of the net within the lumped-parameter approach, and (ii) modeling the threads as series of rigid bodies and constraints. The second solution, referred to as *cable-based model*, was implemented and is described and employed in the rest of this Section.

5.4.3 Cable-based model of net

In the cable-based model, each thread of the net is modeled with a flexible *cable* (i.e., a series of slender rigid bodies and prismatic constraints) in Vortex Dynamics. Each cable is attached to two of the physical knots of the net, or to a corner of the net and a corner mass. The physical knots of the net and the corner masses are modeled as small spherical rigid bodies, as in the lumped-parameter model. The mass of the knots of the net is m_{knot}, and the mass of the corner masses is simply m_{CM}; both these quantities were defined in Section 2.1.2. Contrarily to the lumped-parameter model, the mass of the threads of the

net and of the corner threads is not lumped at the adjacent knots and corner masses; instead, it is distributed along the slender rigid bodies (called *sections*) composing the cables (details on the modeling of cables in Vortex Dynamics were provided in Section 3.4.1).

In order to limit the number of rigid bodies, which is a bottleneck of the simulation, it was chosen to use four sections for each thread of the net ($n_{sec} = 4$). The initial configuration of each cable was selected such that the physical knots of the net are in the same positions as those defined by the stowing ratio α_{net} in the lumped-parameter model. This is done as sketched in Figure 5.15(a): each cable is defined to pass through three *way points* (shown in red) whose position vectors in the inertial reference frame $(\hat{\mathbf{i}}, \hat{\mathbf{j}}, \hat{\mathbf{k}})$ are

$$\begin{aligned} \mathbf{r}_{A,i} &= \mathbf{r}_{1,i} + a\hat{\mathbf{a}} + b\hat{\mathbf{b}} \\ \mathbf{r}_{B,i} &= \mathbf{r}_{1,i} + 2a\hat{\mathbf{a}} \\ \mathbf{r}_{C,i} &= \mathbf{r}_{1,i} + 3a\hat{\mathbf{a}} - b\hat{\mathbf{b}} \end{aligned} \tag{5.7}$$

where $\mathbf{r}_{1,i}$ is the position vector of one of the knots to which the i-th cable is attached, and the coefficients and the unit vectors in equations (5.7) are:

$$a = \frac{\alpha_{net} l_{net,0}}{n_{sec}} \qquad \hat{\mathbf{a}} = \frac{\mathbf{r}_{2,i} - \mathbf{r}_{1,i}}{||\mathbf{r}_{2,i} - \mathbf{r}_{1,i}||}$$

$$b = \sqrt{\left(\frac{l_{net,0}}{n_{sec}}\right)^2 - a^2} \qquad \hat{\mathbf{b}} = -\hat{\mathbf{a}} \times \hat{\mathbf{k}}$$

The resulting initial configuration of a net with $N_s = 6$ nodes on a side, compressed with $\alpha_{net} = 0.25$ is shown in Figure 5.15(b). It should be noted that, due to this packaging, the cables composing the net should not be allowed to collide at the start of the simulation: therefore, contacts among cables, that is the threads of the net, are not allowed at the time of writing. For collisions between cables and other bodies in the simulation, one can choose to model the cables with *capsule*-like collision geometries around each section, or with spheres of the same diameter as the cable placed at the same position as the center of mass of the section. The second approach is more convenient in terms of memory and computational effort, but very similar to the lumped-parameter method as far as collision detection is concerned. Therefore, the first approach was taken. The contacts between cables and the target, at the time of writing, are assumed to be inelastic.

The implementation of the cable-based model was validated by comparing the results of deployment simulations against those obtained with the lumped-parameter model, using the same data collected in Table 2.2, apart from the simulation time (here $t_f = 3$ s) and the mesh and corner thread lengths (respectively, $l_{net,0} = 0.5$ m and $l_{CT,0} = 0.707$ m); a small $l_{knot} = 0.005$ m was also considered, for the knot parts to have non-zero mass. In

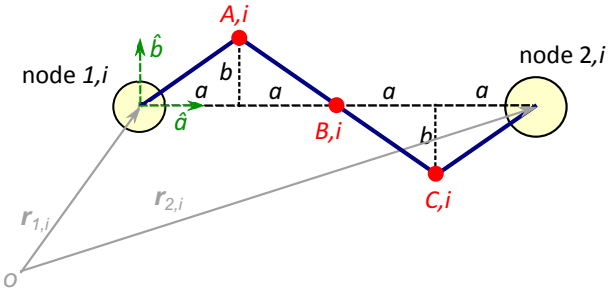

(a)

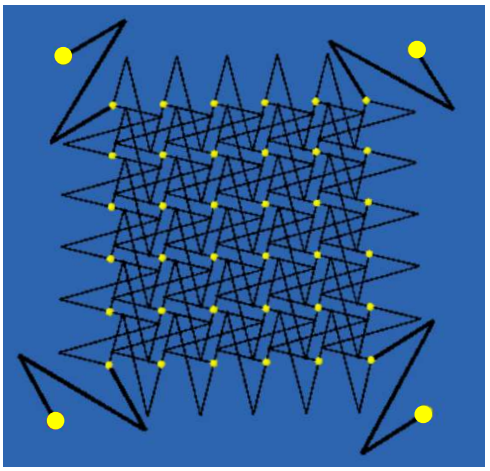

(b)

FIGURE 5.15: (a): Initial shape of the cable modeling a thread of the net (in blue), passing through way points (in red). (b): Initial configuration for a net with $N_s = 6$ (dimensions of the knots and threads not in scale).

Quantity	**Maximum**	**Average**
$RMSE_{pos}$ (m)	0.120	0.0837
$RMSE_{vel}$ (m/s)	0.957	0.648

TABLE 5.1: RMSE at position and velocity levels between the results of deployment simulations with the cable model and the standard lumped-parameter model of the net.

order to limit the complexity of the problem for the preliminary simulations presented in this Section, the bending stiffness of the cables was neglected and *ball and socket* joints were chosen to model the attachments between knot parts and cables. Simulation was performed with a time step of 5×10^{-5} s, and took about 17 min of computation time with an Intel®Core™ i7-4712HQ CPU @ 2.30 GHz processor (without showing the graphics at run-time). Comparison of the mouth shape of the net obtained in simulation of deployment with the cable model and the standard lumped-parameter model is shown in Figure 5.16. RMSEs at position and velocity levels between the knot parts are collected in Table 5.1. Results show very good agreement, in the absence of bending stiffness. Although the RMSEs are not negligible, they are commensurate with the discrepancies expected because of the inherent differences in the model (e.g., the mass distribution). The overall dynamics remains very similar, as Figure 5.16 clearly demonstrates. This agrees with recent results by Shan et al., who found very similar deployment results with the standard lumped-parameter model and with an ANCF cable element model without bending stiffness; both these works suggest that the actual shape of the threads of the net is not important in the deployment phase, when bending stiffness is negligible [94].

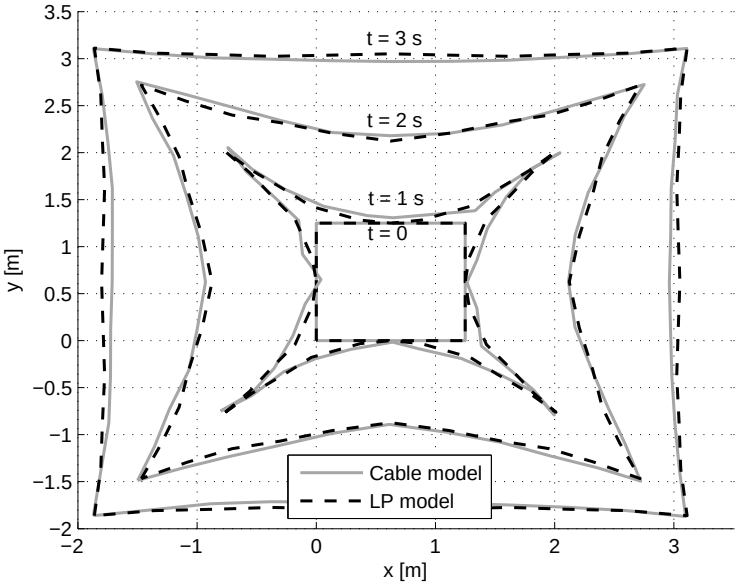

FIGURE 5.16: Comparison of the mouth shape of the net in time, in deployment simulation with the cable model and the standard lumped-parameter (LP) model.

5.4.4 Envelopment of thin structure with cable-based model of net

The aim of this Section is to demonstrate the capability of the cable-based model of the net to properly detect collisions with structures with the smallest dimension less than the mesh size of the net. Unfortunately, the number of cables that can be added in the simulation is very limited at this time, especially when *capsule* collision geometries are specified, so that the full capture of Envisat with a cable-based model could not be simulated. Instead, a simplified target object is considered, in particular, a thin structure with the same geometry as the solar array of Envisat spacecraft (4.9 m $\times$ 7.2 m $\times$ 0.12 m) and fixed on a plane parallel to the x-y plane. A 9×9 m^2 net characterized by $N_s = 5$ starts in a fully deployed configuration on the x-y plane and falls under gravity onto the target. A standard closing mechanism running among the corner masses is actuated after 1.5 s.

Figure 5.17 presents selected snapshots of the simulation. From inspection, it is confirmed that collisions between the net and the thin structure are correctly detected. Contact with the target is seen at $t = 1.5$ s; the effect of the closing mechanism is visible at $t = 2$ s; closure around the solar array is verified at $t = 3$ s (in Figure 5.17(d), a zoom on a corner of the thin structure is also included). Differently from what was observed in Section 5.4.2 for collisions between the net and the thin structures on Envisat spacecraft, the threads remain around the panel as expected and the net properly envelops the structure. This

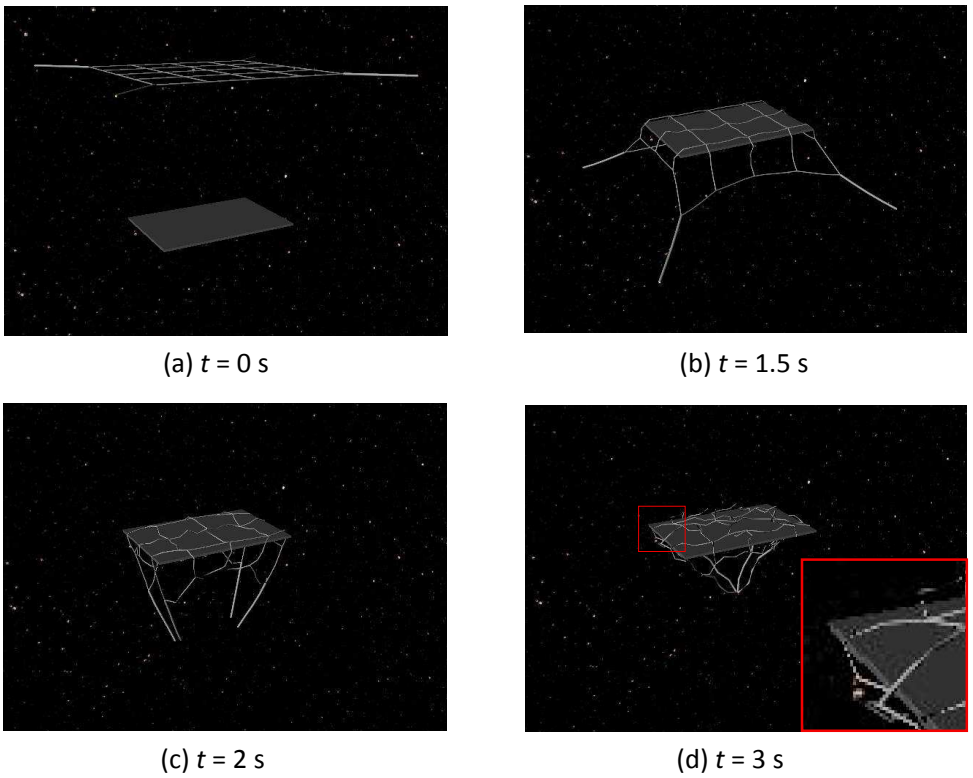

FIGURE 5.17: Capture of Envisat solar array with net represented with the lcable-based model.

confirms the suitability of the cable-based model to simulate net-based capture of debris with thin structural elements.

5.5 Application of net-based capture to asteroids

The aim of this Section is to demonstrate another possible application of tether-nets in space. In fact, in addition to their ADR applications, tether-nets could be used to capture small asteroids, for example for scientific examination or planetary defense [95]. In this Section, simulation results for capture of a small asteroid modeled after Bennu asteroid are presented. The inertia properties of the modeled asteroid are assumed to be those of an ellipsoid with semi-axes 12.5 m $\times$ 10 m $\times$ 10 m and with uniform density[2] of 1300 kg/m^3. The resulting mass is $m_T \approx 5.45 \times 10^7$ kg and the resulting inertia tensor in a body-fixed reference frame $(\hat{\mathbf{i}}_\mathbf{b}, \hat{\mathbf{j}}_\mathbf{b}, \hat{\mathbf{k}}_\mathbf{b})$ where $\hat{\mathbf{i}}_\mathbf{b}$ is in the direction of the semi-major axis of the ellipsoid is:

$$\mathbf{I}_G = \begin{bmatrix} 8.71 & 0 & 0 \\ 0 & 11.16 & 0 \\ 0 & 0 & 11.16 \end{bmatrix} \times 10^9 \text{ kg} \cdot \text{m}^2 \tag{5.8}$$

[2]Density was assumed similar to the bulk density of Bennu.

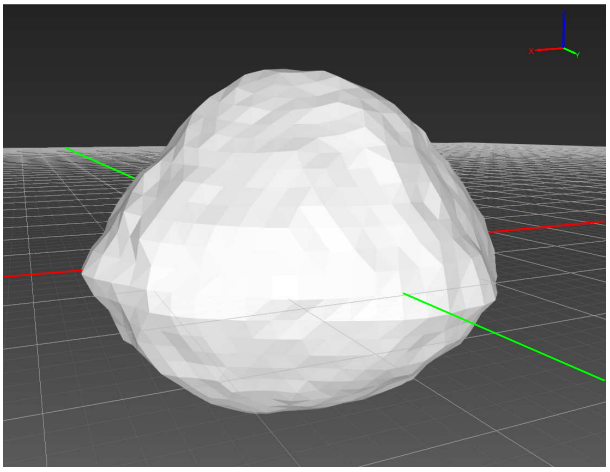

FIGURE 5.18: 3D model and collision geometry of asteroid.

Asteroids are expected to be rotating slowly. For the hypothetical asteroid considered in this Thesis, an angular velocity[3] of $\omega_T = 0.0004$ rad/s was assumed about the major moment of inertia axis: $\boldsymbol{\omega}_T = \omega_T \hat{\mathbf{k}}_\mathbf{b}$.

A 3D graphics model of Bennu[4] was scaled down to the chosen dimensions, and a convex mesh collision geometry was added based on this 3D model (see Figure 5.18, where the $\hat{\mathbf{i}}_\mathbf{b}$ and $\hat{\mathbf{j}}_\mathbf{b}$ axes of the body-fixed reference frame are also shown in red and green, respectively). This type of collision geometry was chosen because patched primitives (used for Zenit and Envisat) are not well-suited to represent the shape of the asteroid; however, deterioration of computational efficiency is expected as a result of this choice.

Asteroids being larger and more massive than space debris, the tether-net system was scaled-up compared to those used previously in this Thesis: the net has a side length of 40 m and a total mass of 23 kg. The parameters for the simulation of asteroid capture are collected in Table 5.2. The same materials for the net and tether as in the rest of the simulations in this Thesis are used. A search in the literature was performed to identify parameters for contact between the net and the asteroid material; ranges for the Young's modulus of rocks reported in [96] are large and a value of $E_{rock} = 50$ GPa was chosen in the upper range of carbonaceous materials, since many asteroids are made of carbon silicates. The other parameters for contact were chosen arbitrarily in reasonable ranges: $\nu_{rock} = 0.25$, and $\mu_{rock-net} = \mu_{rock-al} = 0.2$. The net is ejected from the chaser at a distance of 25 m from the target. A standard closing mechanism among the corner masses only was actuated at $t = 22$ s to close the net around the asteroid; the main tether is free to spool out during deployment of the net, and is locked at the same time.

[3]Estimated from the rotation period of Bennu, available at nssdc.gsfc.nasa.gov/planetary/factsheet/asteroidfact.html, last accessed on June 24, 2017.

[4]Available on NASA 3D Resources website nasa3d.arc.nasa.gov/detail/bennu, last accessed on June 15, 2017.

Chaser spacecraft			**Winch**		
d_{ch} (m)	L_{ch} (m)	m_{ch} (kg)	r_w (m)	h_w (m)	m_w (kg)
0.1	2.0	1600	0.1	0.02	0.1
Tether					
	r_t (m)	ρ_t (kg/m^3)	E_t (GPa)	ξ_b (-)	
	0.003	1390	70	0.014	
Net and corner masses					
L_{net} (m)	$l_{net,0}$ (m)	r_{net} (m)	ρ_{net} (kg/m^3)	E_{net} (GPa)	ξ_a (-)
40	2	0.001	1390	70	0.106
l_{knot} (m)	$l_{CT,0}$ (m)	r_{CT} (m)	ρ_{CM} (kg/m^3)	m_{CM} (kg)	
0	2.8284	0.001	2700	4.0	
Initial conditions				**Simulation data**	
$v_{e,net}$	v_e (m/s)	θ (°)	α_{net} (-)	t_f (s)	Δt (s)
0	2.5	36.87	0.05	60	10^{-3}

TABLE 5.2: Data for simulation of capture of a small asteroid.

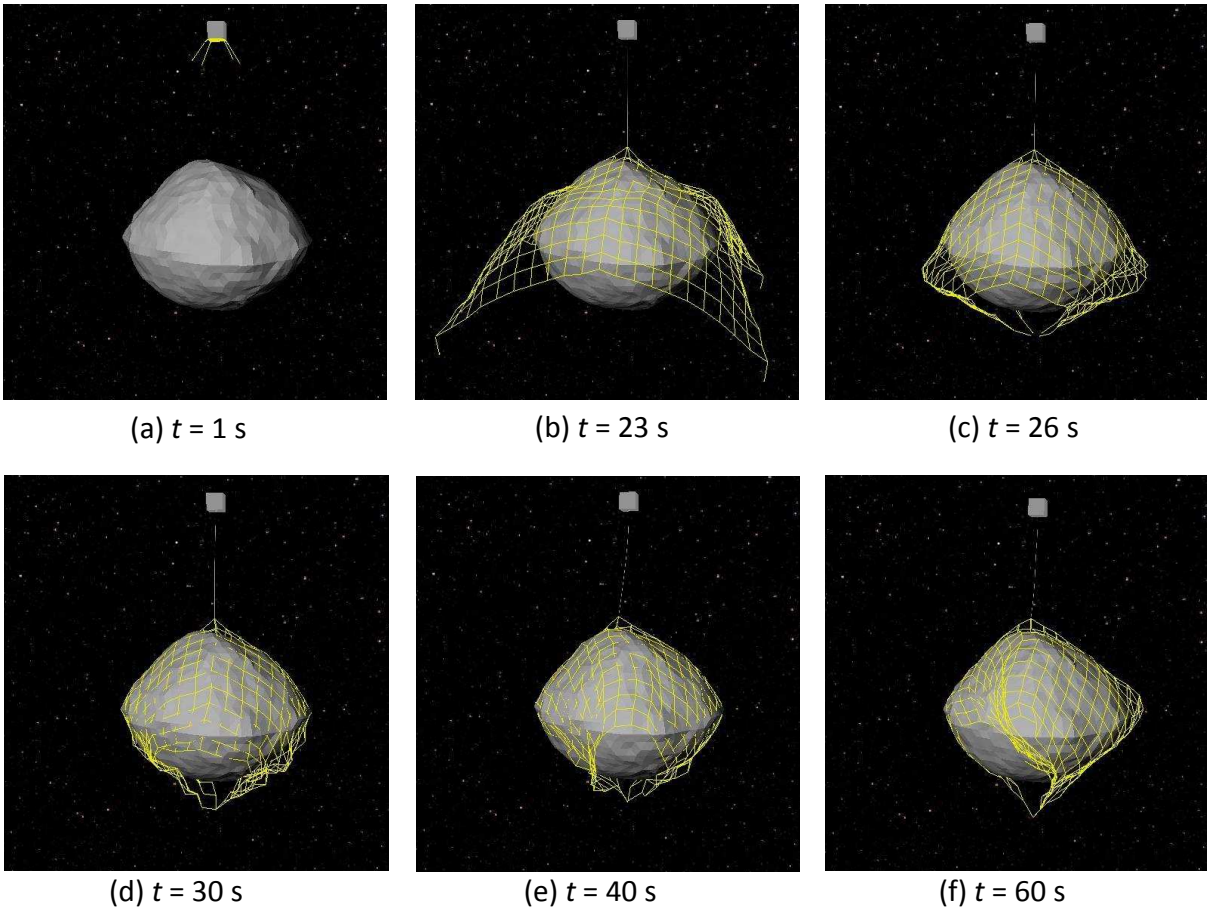

FIGURE 5.19: Capture of a small asteroid with net represented with the lumped-parameter model.

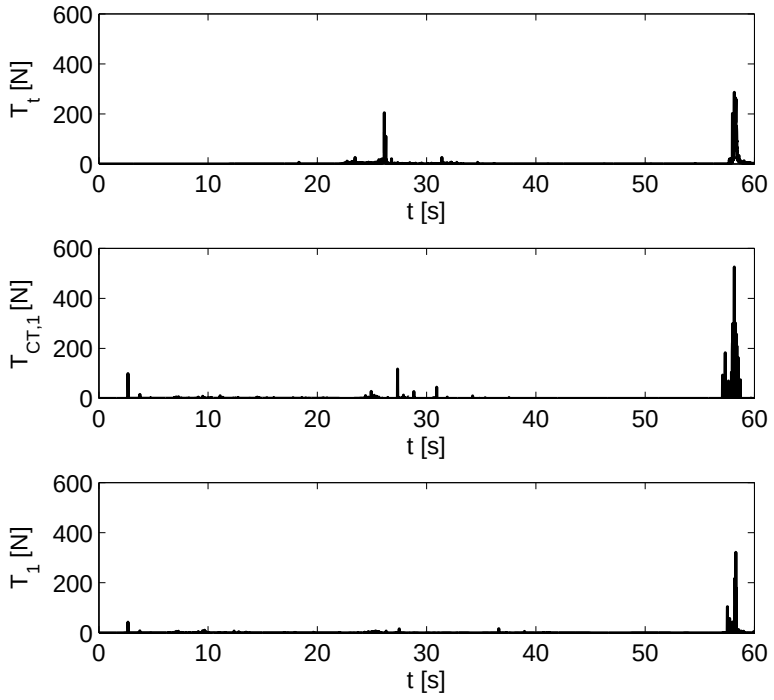

FIGURE 5.20: Tension developed during capture of a small asteroid: in the main tether T_t, in a corner thread $T_{CT,1}$, and in one of the tethers of the net T_1.

Simulation with an Intel®Core™ i7-4712HQ CPU @ 2.30 GHz processor (showing the graphics at run-time) took around 3 hours, 12 min. Figure 5.19 reports snapshots for the capture sequence. It is clear that, although the angular velocity of the asteroid was accounted for, its effect is negligible in the time frame of capture. At $t = 23$ s, it is seen that the main tether is locked, the net is around the asteroid, and the closing mechanism is functional. Closure is almost achieved at $t = 26$ s and is confirmed at $t = 30$ s. For the remainder of the simulation, capture of the asteroid is sustained. It is observed that the chosen closing mechanism was sufficient to guarantee containment of the asteroid during capture, differently from what was observed for capture of Zenit-2 stage 2 in Section 5.3.2.

These simulation results suggest that tether-nets could indeed be used to capture not only large debris, but also small asteroids. However, for the design of the ejection mechanism, it must be considered that the mass of the net and corner masses will be substantially higher in this application, due to its larger size. Attention should also be paid to the tensions developed in the main tether and in the threads of the net during capture; the results for the presented simulation are collected in Figure 5.20 and show peaks soon after closure is achieved (i.e., at $t \approx 26$ s) and towards the end of the simulation (i.e., at $t \approx 58$ s), especially in the main tether and in the corner threads. Onset and distribution of tension in the system, however, would depend on several features of the system and of its control. Issues such as the control of the main tether and the set-up and control of the

closing mechanism need further investigation to ensure that tensions remain reasonable and that the load distribution is balanced in the system.

5.6 Closing remarks on capture dynamics

This Section brings Part III to an end. In the last two Chapters, the dynamics of capture was studied to different degrees of detail. A large part of Chapter 4 focused on the fundamentals of capture dynamics and its implementation for the application at hand. Several continuous compliant contact force models and micro-slip friction models were presented and implemented; the effect of choices on the modeling of contact dynamics between the net and debris was evaluated in a simplified capture scenario. The effect of taking into account the bending stiffness of the threads of the net on capture of realistic rotating debris was later investigated; it was found that - notwithstanding differences in the dynamics - the success of capture was similar. Finally, the robustness of capture to multiple non-nominal ejection conditions was confirmed, while the need for a closing mechanism was suggested.

Subject of Chapter 5 was the capture of realistic debris with a net equipped with a closing mechanism. Two types of solutions to close the net were considered: a tether-actuated closing mechanism and a standard mechanism actuated thanks to winches in the corner masses. Tensioning of the main tether is necessary to actuate the first closing mechanism; instead, an actuated spooling out of the main tether could help capture with a standard mechanism. A model for the tether-actuated closing mechanism was implemented and allowed to confirm the feasibility of this solution for ADR missions; current limitations in the simulation framework, however, prevented a realistic simulation of this set-up. Simulations with a standard closing mechanism of two types showed that capture is more reliable if the closing tethers are interlaced with the mouth of the net, and that capture is safer if the spin axis of the target is aligned with the direction of ejection of the net. Simulation of capture of Envisat spacecraft manifested that the lumped-parameter model of the net is unable to detect collisions with thin structural components of the target. In order to overcome this issue, a cable-based model of the net was proposed; although simulation of capture of Envisat could not be performed with this model due to memory limitations of Vortex Dynamics, its potential was demonstrated. Finally, simulations suggested that tether-nets could provide a viable solution for capture of small asteroids.

Part IV

Conclusion

Chapter 6

Conclusions

6.1 Summary of results and discussion of contributions

Tether-nets have only recently been proposed as capture mechanisms for Active Debris Removal (ADR). Although some simulators existed before the research presented in this Thesis, the technology readiness of this capture solution was low, and many aspects of tether-net ADR missions remained overlooked. Through this research, new knowledge, results and insights on the deployment and capture phases of a tether-net ADR mission were produced.

One of the main contributions of this Thesis is the implementation of a simulator for the deployment and capture phases of a tether-net ADR mission. This simulator includes the chaser, the main tether with the winch to spool it in and out, the net, closing mechanisms, and multiple realistic debris. Throughout this Thesis, the functioning of the different elements of the simulator, its ability to represent various scenarios, and the possibility to use it to perform diverse studies on the dynamics of tether-net systems and planning for tether-net ADR were demonstrated.

A standard lumped-parameter modeling of the net was implemented in the simulation tool (based on the commercial Vortex Dynamics multibody dynamics simulation framework). The implementation of this model was verified with energy and linear momentum principles, as well as by comparing deployment results with the same model created in a MATLAB environment, and against experimental results.

Although multiple works published previously and concurrently to this research have studied the deployment dynamics of nets in space, none have considered the effect of inertia properties and tensioning of the main tether on the quality of deployment. Indeed,

to the author's knowledge, no other simulator of tether-net systems for ADR can simulate the winching of the main tether to date. In this Thesis, it was demonstrated that the spooling of the main tether – and the consequent modulation of tension in it – can be exploited to improve the quality of deployment, as well as to speed up the capture dynamics, or to keep the net around its target for a longer time. For the sake of achieving a reliable capture, it was recommended to keep the tether free to spool out, or to actively spool it out with moderate velocity, during deployment. It was also observed that, if a standard closing mechanism is to be used, spooling the tether out during capture would be beneficial; on the other hand, if a tether-actuated closing mechanism is to be employed, accurate timing of the actuation to winch the tether in is needed.

Novel to the body of literature on nets for ADR is also an analytical study of the deployment dynamics, based on the work-energy and the linear momentum principles. Expressions for the centroidal velocities at several milestones in the deployment process (defined by an energy quantity for the system), as well as limits for these, were found; it was confirmed that these findings are valid notwithstanding the stiffness modeling choices. Moreover, the analysis allowed to determine in a formal way the key parameters that govern the deployment dynamics: the total mass of the system, the ratio between the mass of the corner masses and the net proper (or the total mass), the magnitude and direction of the initial velocities. A numerical sensitivity study showed that these parameters impact the quality of the deployment variably; it also allowed to suggest ranges of their values that should be used to achieve a more lasting deployment and safer capture.

Simulation of contact dynamics for tether-net ADR applications was basic before this research. The first effort to evaluate the effect of employing different continuous compliant contact force models on the capture dynamics was performed for this Thesis, using a simplified scenario: the effect was found to be moderate from the time of first contact of the net with the debris to net closure, and important after closure; however, the overall performance of the capture maneuver was not significantly affected by the contact force modeling choice. With a view to achieving reliable but efficient simulation of capture of debris with a realistically sized net, simple non-linear models were recommended. It should be noted that, following this work, other researchers have adopted non-linear continuous compliant contact force models. However, to date, this work is the only one to consider micro-slip friction modeling for tether-net ADR applications.

The first analysis of the importance of taking into account the bending stiffness of the threads of the net was performed in this Thesis; this was enabled by implementations of lumped-parameter models for the net with and without representation of the bending stiffness of the threads. It was found that, notwithstanding significant differences in the dynamics of the net, the success of capture in the two scenarios remained similar.

In all simulations without closing mechanisms, the net was observed to slip off the target after the envelopment phase. In order to overcome this issue, a novel tether-actuated closing mechanism for a net was modeled and simulated. Despite the limitations of the modeling – dictated by limitations of the underlying simulation framework at the time of writing –, it was demonstrated that a tether-actuated closing mechanism could be used to secure debris in the net after capture.

A standard closing mechanism was also implemented in the simulation tool. The current modeling approach does not allow to account for the inertia and stiffness properties of the closing tether, nor to simulate realistic winching profiles; however, it allowed to perform different assessments on the capture capabilities of tether-net systems. It was shown that a closing mechanism interconnecting the four corner masses only does not ensure that debris such as spent rocket stages remain contained in the net after capture. Simulations also allowed to conclude that a scenario where the net is ejected in a direction parallel to the axis of rotation of the target is safest; however, it was also found in this Thesis that capture in this scenario is less robust to inaccuracies in the ejection of the net.

It was demonstrated in this Thesis that lumped-parameter models, albeit widely used for nets for ADR, are inherently deficient in representing collisions between the threads of the net and thin structural elements on the debris target, such as solar arrays. Solutions to this problem were considered and an alternative model, based on cables in Vortex Dynamics, was proposed. The capability of this model to represent collisions with thin elements was verified in simulations of capture, with the solar array of Envisat spacecraft as a target.

Overall, simulations of capture of launcher upper stages, of Envisat, and of a small asteroid with representation of the main components of the system were presented and confirmed that it is feasible to capture large and massive debris of different shapes and under rotation by using a tether-net system.

6.2 Suggestions for future work

Although novel and useful insight into the dynamics of deployment and capture of debris was achieved with this Thesis, some issues remain open, and new interesting directions for research are discussed in the following.

Tools to evaluate the effect of bending stiffness on the deployment and capture dynamics were provided in this Thesis. However, uncertainty on the actual stiffness properties of braids in the environment of space exist; therefore, before clear conclusions on the need to take into account the bending stiffness of the threads of the net can be drawn,

experimental characterization of these properties in microgravity and vacuum conditions is needed.

The modeling and implementation of the tether-actuated closing mechanism needs further development to match that proposed for the actual mission scenario: more rings have to be added around the net perimeter, and a lower number of main tethers (ideally just one) should be used. In this Thesis, it was demonstrated that timing of the actuation of such closing mechanism is critical to the success of the capture maneuver; therefore, optimization studies on the tether control law could be considered. The standard closing mechanism could also be implemented more accurately, including actual winches and tethers. More realistic models of both closing mechanisms could be implemented in Vortex Dynamics as soon as the limitations on the number of rings along a cable are overcome.

Although some experimental validation of the simulation tool was included in this Thesis, the need for more extensive and quantitative validation is acknowledged. One foreseen validation activity is the comparison of simulation results with the parabolic flight experiments on net-based capture of a mock-up of Envisat. This will be possible once developments in the multibody dynamics simulation framework allow to simulate the realistic capture of Envisat with the proposed cable-based model of the net; room for improvement in the modeling of contact parameters for the threads of the net exists.

It would be interesting to perform a sensitivity study on the robustness of capture in non-nominal ejections of the net, similarly to what was presented in Section 4.7 of this Thesis, but in the presence of closing mechanisms. It is foreseen that the timing of actuation of the closing mechanism would be key to the success of capture in this case.

One topic of great interest is the capability of tether-net systems to dampen the rotational motion of the target in the post-capture phase. Some studies in the literature have approached this problem by modeling the effect of the net with a few fixed attachments of the tether to the target. The simulation tool at hand could enable such studies at a higher degree of fidelity, by veritably considering the action of the threads of the net on the target; however, more attention would need to be paid to the modeling of friction and of torsional stiffness and damping in the main tether. Control to stabilize the post-capture dynamics of the chaser should also be introduced. Finally, orbital dynamics was neglected in this study, in light of the short duration of the deployment and capture phases of a tether-net ADR mission; for longer simulations, involving the post-capture dynamics, the effect of orbital dynamics and of perturbations (such as those due to the gravity gradient) should also be considered.

After stabilization of the system, the disposal of the target should also be investigated. A first option is to tug the target to its disposal orbit; alternatively, the target can be

retrieved by shortening the main tether. In both cases, the final disposal is achieved by maneuvering the chaser. The dynamics of the system composed of chaser, main tether, net and target should be controlled attentively to avoid collisions.

Part V

Appendices

Appendix A

Analytical derivations

In Section 3.2, an analysis of the deployment dynamics based on the work-energy and linear momentum balance was proposed. In those derivations, it was suggested that $\dot{\rho}_i(0)$, i.e., the magnitude of the relative velocity of the i-th node with respect to the center of mass, depends on the magnitude and direction of the ejection velocity. Here, proof of this statement is provided.

A.1 Proof that $\dot{\rho}_i(0)$ depends on the magnitude and direction of the ejection velocity

By definition:

$$\begin{aligned}\dot{\rho}_i(0) &= ||\dot{\rho}_i(0)|| = ||\mathbf{v}_i(0) - \bar{\mathbf{v}}_c(0)|| = \\ &= \sqrt{(v_{i,x}(0) - \bar{v}_{c,x}(0))^2 + (v_{i,y}(0) - \bar{v}_{c,y}(0))^2 + (v_{i,z}(0) - \bar{v}_{c,z}(0))^2}\end{aligned}$$

Due to symmetry:

$$\begin{aligned}v_{i,x}(0) &= v_{i,y}(0) \\ \bar{v}_{c,x}(0) &= \bar{v}_{c,y}(0) = 0\end{aligned}$$

Therefore:

$$\dot{\rho}_i(0) = \sqrt{2(v_{i,x}(0))^2 + (v_{i,z}(0) - \bar{v}_{c,z}(0))^2}$$

Remembering that $v_x = v_y = v_e \sin\theta/\sqrt{2}$ and $v_z = v_e \cos\theta$ as defined in Section 2.2:

$$\begin{aligned}\dot{\rho}_i(0) &= \sqrt{v_e^2 \sin^2\theta + (v_e \cos\theta - \bar{v}_{c,z}(0))^2} = \\ &= \sqrt{v_e^2 \sin^2\theta + v_e^2 \cos^2\theta + \bar{v}_{c,z}^2(0) - 2v_e \cos\theta \bar{v}_{c,z}(0)} = \\ &= \sqrt{v_e^2 + \bar{v}_{c,z}^2(0) - 2v_e \cos\theta \bar{v}_{c,z}(0)}\end{aligned}$$

This shows that $\dot{\rho}_i(0)$ depends on the magnitude of the ejection velocity v_e and the cosine of its angle relative to the direction of deployment θ.

Appendix B

Benchmark tests for cables in Vortex Dynamics

Here are presented the most relevant benchmark tests devised to validate the behavior of cables in Vortex Dynamics. The results presented here were obtained with a *flexible* tether, with distributed mass and stiffness properties.

B.1 Simple tethered mass under gravity

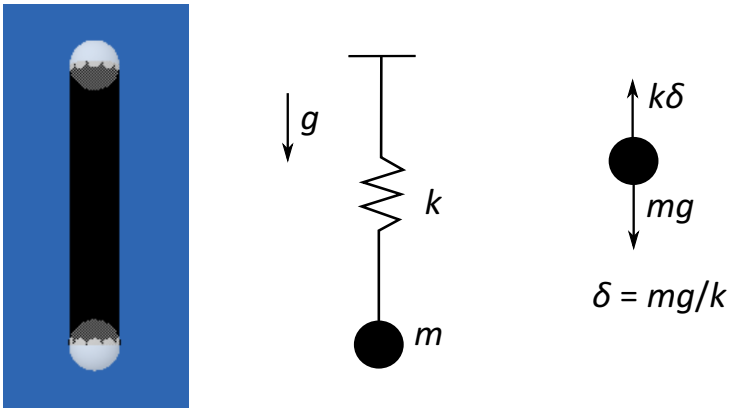

FIGURE B.1: Tethered mass under gravity. (a): system in Vortex Dynamics; (b): analytical approximate model; (c): equilibrium.

In this scenario, a mass m is attached to a fixed part through an elastic tether of length L_0 and stiffness per unit length (EA); the tether elongates under the effect of the Earth's gravity. The cable is assumed to have negligible mass[1]. The system is represented in

[1]In Vortex Dynamics, a very small density is specified for the cable, because a flexible cable always has mass.

Figure B.1(a), where parts are shown in white and the cable is shown in black. For this problem, the analytical approximate model of the system is shown in Figure B.1(b), and the deflection at equilibrium can be easily found as shown in Figure B.1(c). For $m = 1$ kg, $(EA) = 100$ N, and $L_0 = 1$ m, the stiffness of the cable is $k = 100$ N/m, and the static deflection is $\delta = mg/k = 0.0981$ m.

In a first simulation, the default number of sections in the cable $n_{sec} = 3$ was employed, and a noticeably smaller deflection ($\delta = 0.065$ m) was found. This made it apparent that the stiffness of the cable is higher than the theoretical $(EA)/L_0$. This is due to the fact that for n_{sec} sections, only $n_{sec} - 1$ prismatic joints are introduced; as a consequence, the total length of the cable accounted for as elastic is smaller than the total cable length L_0 (see Figure 3.14). In fact, if one assumes that a prismatic joint models the extension of a section of the cable of length $L_i = L_0/n_{sec}$, then the axial stiffness of each prismatic joint is found as: $k_i = (EA)/L_i$, for $i = 1, ..., n_{sec} - 1$. The equivalent stiffness k_e is the stiffness of $n_{sec} - 1$ springs in series. For the problem at hand and $n_{sec} = 3$, this would result in a static deflection of $\delta = mg/k_e = 0.065$ m, which corresponds to the value found in simulation. The analytical solution would be recovered with the same process but considering n_{sec} springs of stiffness k_i in parallel.

In practice, the correct stiffness for a flexible cable in Vortex Dynamics can be recovered by employing a modified value for (EA), dependent on the physical (EA) and on the number of sections n_{sec} as per equation (3.28). For $n_{sec} = 3$, one should use $(EA)(n_{sec} - 1)/n_{sec} = 2(EA)/3$; then, the correct tension force and deflection at equilibrium are retrieved, as can be seen in Figure B.2. The first plot shows the length of the cable, which goes from 1 m to 1.0981 m at equilibrium, after an overshoot; the second plot shows the elongation, which starts at zero and settles at 0.0981 m, after an overshoot; the third plot shows the maximum tension in the cable (maximum because in general different joints can be subject to different tensions), which at equilibrium is 9.81 N, equal to mg.

The same results were obtained after replacing the fixed part at the top with a winch part, and locking the hinge constraint.

B.2 Simple tethered mass under gravity - with locked winch and massive tether

The same simulation as in Section B.1 was performed with a massive cable. The axial force $T(x)$ and deflection $u(x)$ at the coordinate x in a beam under concentrated tip load

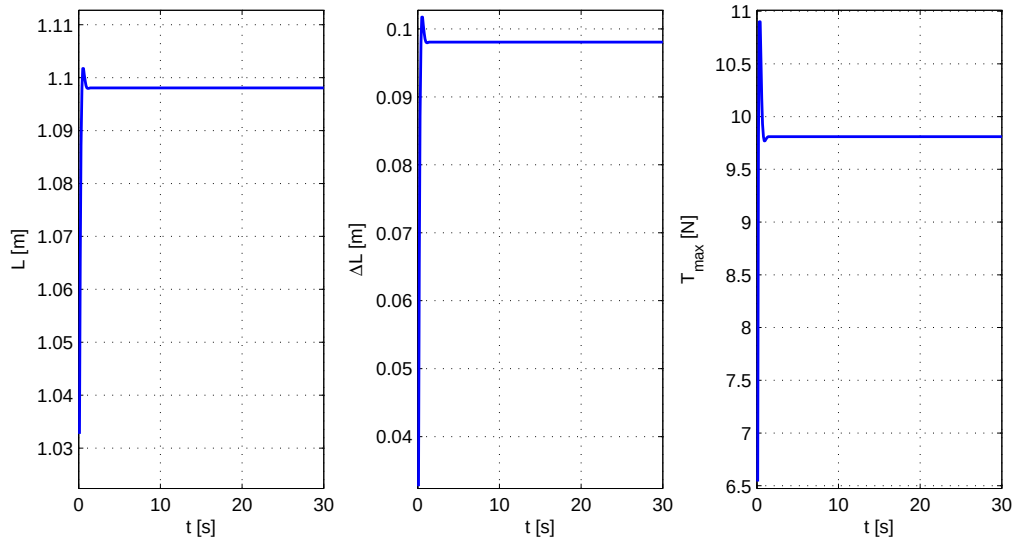

FIGURE B.2: Results of simulation of tethered mass under gravity till equilibrium, with flexible cable model and $(EA)\frac{n_{sec}-1}{n_{sec}}$.

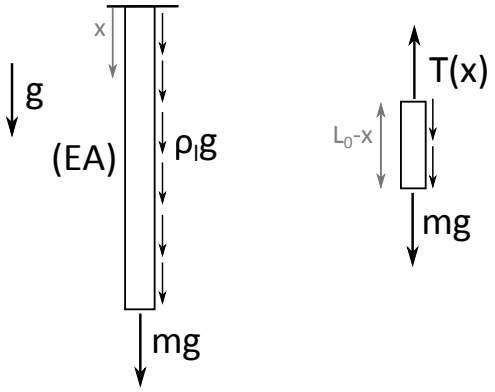

FIGURE B.3: Analytical equilibrium solution for massive beam with tip load under gravity.

mg and distributed load $\rho_l g$ (see Figure B.3) are:

$$T(x) = mg + \rho_l g(L_0 - x) \tag{B.1}$$

$$u(x) = \int_0^x \frac{T(\tau)}{(EA)} d\tau + u_0 = \ldots = \frac{1}{(EA)}(mgx + \rho_l g L_0 x - \rho_l g L_0^2/2) \tag{B.2}$$

With the data defined in Section B.1 and with a linear density set at $\rho_l = 1.0$ kg/m, the maximum tension in the cable T_{max} and the static deflection at the tip δ are:

$$T_{max} = T(x = 0) = (m + \rho_l L_0)g = (1 + 1) \cdot 9.81 = 19.62 \text{ N} \tag{B.3}$$

$$\delta = u(x = L_0) = \frac{1}{(EA)}(mgL_0 + \rho_l g L_0^2/2) = 0.1472 \text{ m}. \tag{B.4}$$

In simulation, if the linear density is set to $\rho_l = 1.0$ kg/m, the correct deflection is recovered, but the maximum value of the tension in the cable is lower than 19.62 N. The

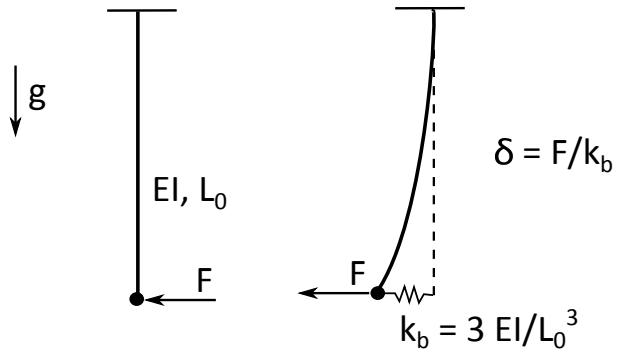

FIGURE B.4: Analytical equilibrium solution for a beam with tip load, valid for small displacements.

correct maximum tension (i.e., 19.62 N) can be recovered for any number of sections by specifying a linear density modified according to: $\rho_l n_{sec}/(n_{sec}-1)$; however, the elongation predicted in this case is higher than the expected value. The difference found with ρ_l is due to the fact that in Vortex Dynamics cable modeling, the mass of cable in the section above the first prismatic joint (see red portion in Figure 3.14) does not have an effect on tension since it is fixed to the top; for this Thesis, it was decided to use ρ_l, acknowledging the existence of this error.

B.3 Simple tether with transverse force at its tip

In order to verify the correct value of the bending stiffness to be input, a simulation was performed with an elastic but almost massless tether with bending stiffness (EI) attached to a fixed part and with a tip mass subject to a constant transverse force F; in this case, gravity was neglected. For this problem, the tip displacement at equilibrium can be found modeling the cable as a beam, as in Figure B.4. For $L_0 = 1$ m, $F = 10$ N, and $(EI) = 50$ Nm^2, the equivalent transverse spring constant is $k_b = 3(EI)/L_0^3 = 150$ N/m, and the static tip displacement is $\delta = F/k_b = 0.0\bar{6}$ m.

Similarly to what was found in Section B.1, it was observed that the tip deflection obtained in simulation is far from the analytical solution, when (EI) is used as an input. The best agreement in the static tip deflection was found for $(EI)(n_{sec}-1)/n_{sec}$. Unfortunately, the dependence on n_{sec} is reduced, but not avoided, unlike the case of axial stiffness. The results obtained with different parameters are reported in Table B.1, where it can be observed that the relative error is of around 10% for a cable composed of 5 sections, and 0.3–1.5 % for a cable composed of 20 sections, in all cases where the deflection of the cable is small. Even for a scenario involving large deflections (i.e., the first line in the table), the relative error remains under 10 %.

L_0	F	(EI)	δ			**Rel. error**	
			($n_s = 5$)	**($n_s = 20$)**	**(theory)**	**($n_{sec} = 5$)**	**($n_{sec} = 20$)**
[m]	[N]	[Nm^2]	[m]	[m]	[m]	[%]	[%]
1	30	50	0.194717	0.215068	0.2	-2.64	7.53
1	10	50	0.0605499	0.066153	0.066666667	-9.18	-0.77
0.8	10	50	0.0309304	0.034122	0.034133333	-9.38	-0.03
0.8	4	50	0.0123009	0.01358	0.013653333	-9.91	-0.54
1	4	50	0.0240345	0.0262627	0.026666667	-9.87	-1.51

TABLE B.1: Static deflections of the cable tip under transverse load, in different scenarios, and comparison with theoretical results.

B.4 Simple tether with motorized winch and rings

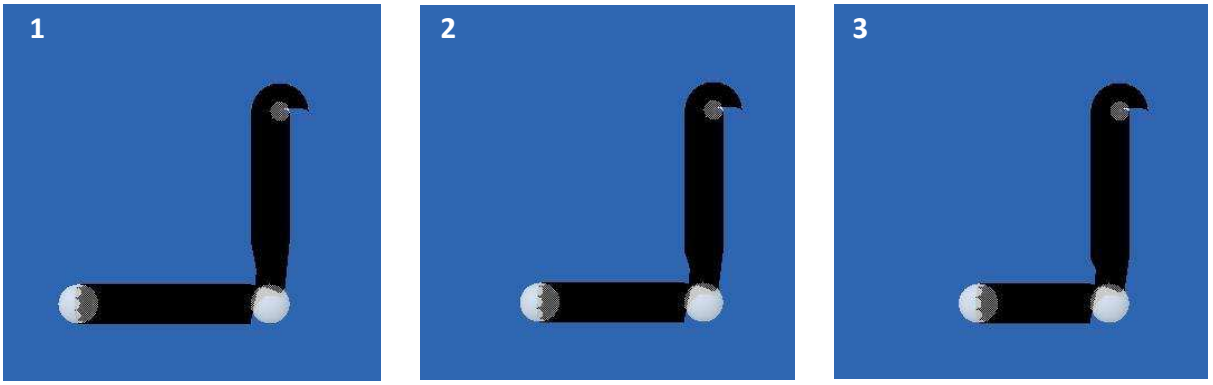

FIGURE B.5: Screenshots of simulation of motorized tether with rings, spooling in without gravity, and flexible cable model.

This section presents a scenario with a simple tethered system with a motorized winch and rings (see Figure B.5), in order to validate the correct functioning of these elements. Three parts (shown in white) are set: the part at the top of Figure B.5 is fixed and has a winch; the second, where the cable (which is shown in black) bends, is equipped with two rings (with their axes parallel to each of the segments of the cable); the third is free to move, and the tether is attached to its center. In this scenario, the winch spools the tether in at a rate of $\dot{L} = 0.1$ m/s. Three screenshots of the simulation are collected in Figure B.5: it can be seen that the cable length diminishes in time. Moreover, the two segments remain vertical and horizontal as they were at the beginning of the simulation. The profile of the tether length during the simulation is collected in Figure B.6. One can notice that the expected cable length is recovered, apart from some initial oscillations and a small constant offset.

From these simulations, it appears that the motorized winch and rings work as expected. However, simulations were observed to fail when more than three rings are added, at the time of writing.

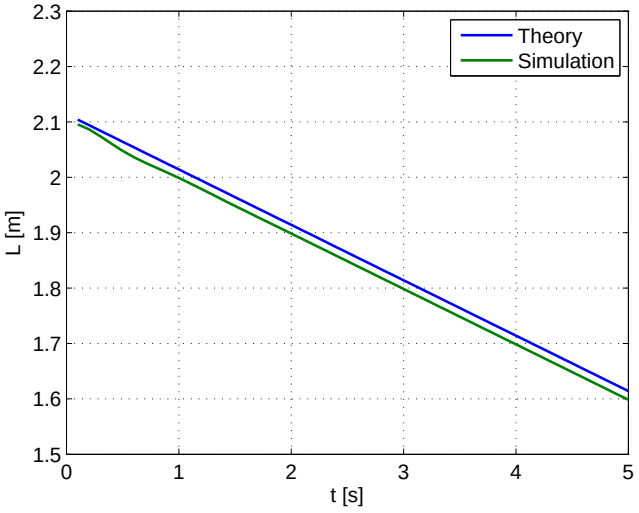

FIGURE B.6: Results of simulation of motorized tether with ring, spooling in without gravity, and flexible cable model.

Appendix C

Validation of friction force models

In Section 4.3, the modeling of contact dynamics was presented. Here are collected the results of validation activities on the implementation of friction force models.

C.1 Validation of bristle friction model

The scenario used for validation is described in Section 3.2 of the paper by Liang et al. [81]. A point mass m slides on a plane inclined with an angle θ from the horizontal plane, starting with an initial velocity $\mathbf{v}_0 = 0.4\hat{\mathbf{j}}$ m/s, where $\hat{\mathbf{j}}$ is directed as shown in Figure C.1. Due to the gravity, the point mass also slides along the $\hat{\mathbf{i}}$ axis. The situation is depicted in Figure C.1, and the parameters used in the simulation are collected in Table C.1.

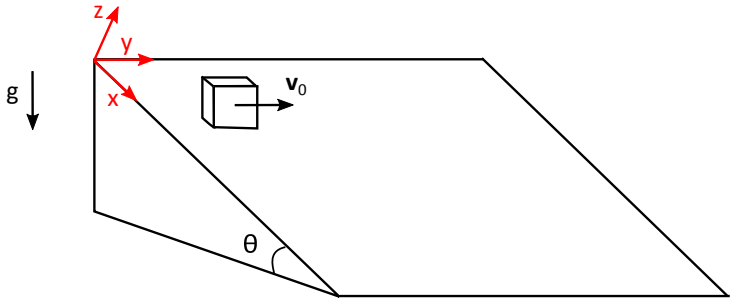

FIGURE C.1: Inclined plane simulation scenario (the same as in [81]).

In the following plots, unless otherwise specified, blue lines represent the results published by Liang et al. [81] (digitized from the paper), black lines represent the results obtained with the implemented code for the undamped formulation (i.e., equations (4.16)–(4.19)), and red lines represent the results obtained with the implemented code for the damped formulation (i.e., equations (4.20)–(4.22)); continuous lines refer to quantities in the y-direction, whereas dashed lines refer to quantities in the x-direction.

Parameter	**Symbol**	**Value**
Mass	m	1 kg
Bristle stiffness	k_{br}	50000 N/m
Bristle damping	c_{br}	80 Ns/m
Threshold velocity	v_d	0.001 m/s
Inclination angle	θ	15°
Static friction coefficient	μ_s	0.6
Kinetic friction coefficient	μ_k	0.5

TABLE C.1: Material parameters used in Liang et al's simulation.

Results in terms of positions, velocities, friction force and bristle deflection are collected in Figure C.2. It can be noticed that important oscillations characterize the undamped model results. The amplitude of oscillations obtained with the damped model for quantities in y-direction are similar to those that characterize Liang et al.'s results (that also consider damping). Overall, there is quite good agreement between the results of the two simulations, but some discrepancies can be seen; some differences may be due to imprecise digitization of the paper's data (e.g., the offset visible in Figure C.2(a)), but the directions of friction force and bristle deflection in the second part of the time frame (see Figure C.2(c) and (d)) are actual differences.

It was confirmed that the correct modulus of the friction force is recovered in sliding. An analysis was performed on the directions of friction, bristle deflection and relative tangential velocity vectors (see Figure C.3). Directions were found as:

$$\theta_F = acos\left(-F_{tx}/\sqrt{F_{tx}^2 + F_{ty}^2}\right) \tag{C.1}$$

$$\theta_v = acos\left(v_{tx}/\sqrt{v_{tx}^2 + v_{ty}^2}\right) \tag{C.2}$$

$$\theta_s = acos\left(s_{tx}/\sqrt{s_{tx}^2 + s_{ty}^2}\right) \tag{C.3}$$

It was found that, in sliding, the model used in this Thesis recovers the direction of the friction force as prescribed by Coulomb's model (see Figure C.3(a)); Liang et al's results seem to indicate that their model did not recover this direction (see Figure C.3(b), that shows data coming from digitization of plots and spline interpolation with Matlab).

As part of the validation efforts, a simulation was performed with an implementation corresponding to the model in [81]. The results are reported in Figure C.4. Better agreement to Liang et al.'s results is found, especially as far as the directions of the bristle deflection and the friction force are concerned. Small differences still exist in the sticking regime.

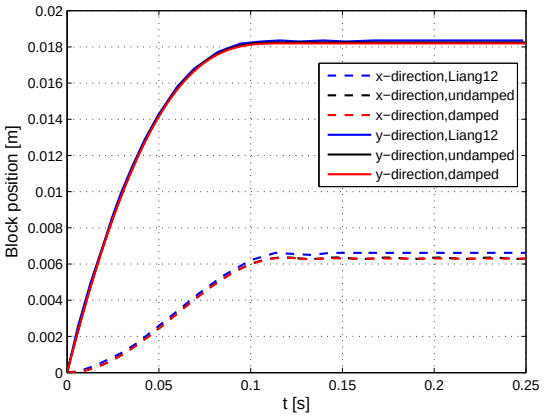

(a) Position

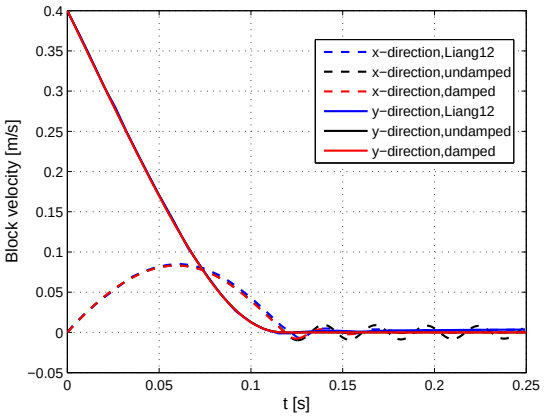

(b) Velocity

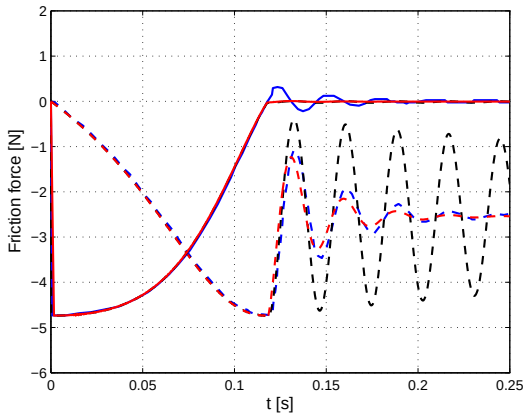

(c) Friction force

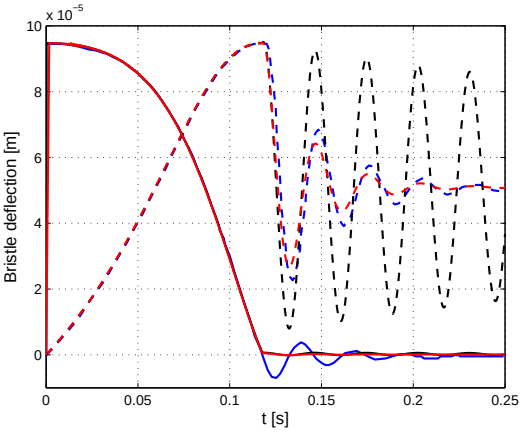

(d) Bristle deflection

FIGURE C.2: Comparison of results with undamped bristle model (black lines), damped bristle model (red lines), and results in reference [81] (blue lines).

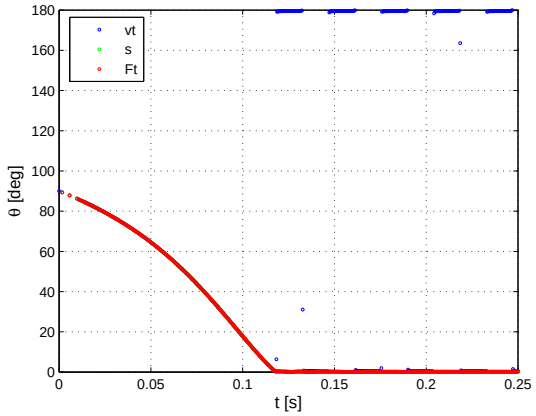

(a) Damped bristle model.

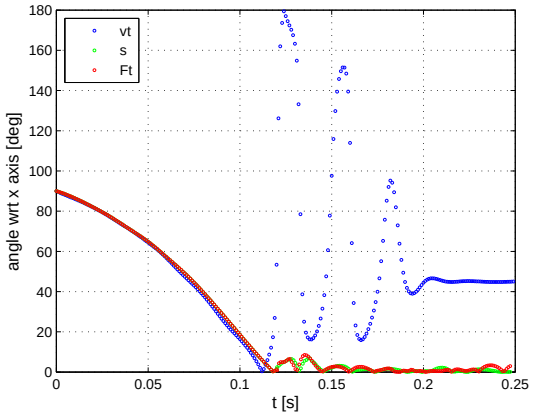

(b) Results in reference [81].

FIGURE C.3: Directions of friction, bristle deflection and relative tangential velocity vectors.

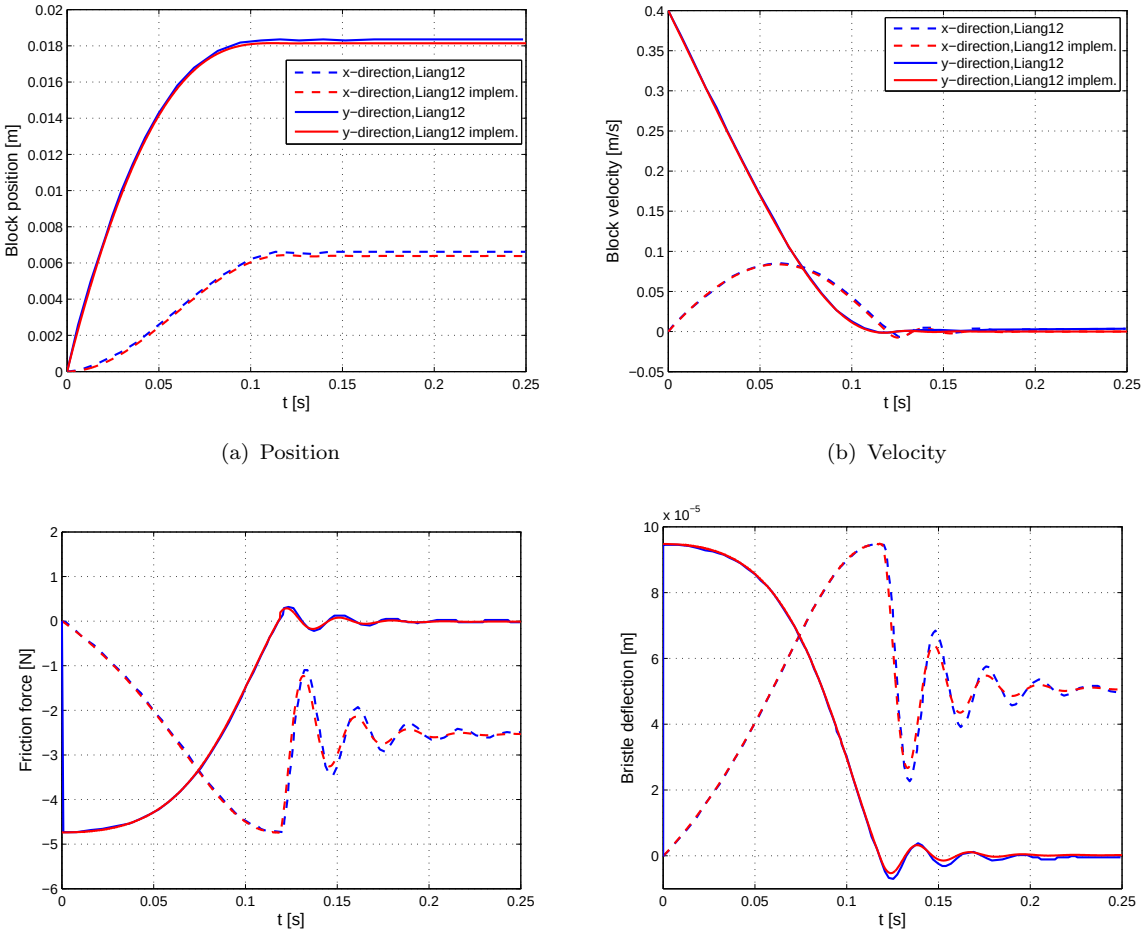

(a) Position

(b) Velocity

(c) Friction force

(d) Bristle deflection

FIGURE C.4: Comparison of results reconstructed from reference [81] (blue lines) and obtained implementing the model by Liang et al. (red lines).

C.2 Comparison of simulations with bristle and Johnson's friction models

In this section are reported the results of a simulation in which a point mass is dragged on a horizontal plane by applying a force linearly increasing with time along the x-direction: $F_x(t) = at$. The parameters used in the simulation are collected in Table C.2. According to the chosen parameters, the mass is expected to start moving at around $t = 0.25\,s$. The integration was performed for a time horizon of 0.5 s.

With the bristle friction model, integration took about 0.7 s. The results are collected in Figure C.5. It is observed that, indeed, the mass starts moving after about 0.25 s, in the x-direction (see Figure C.5(a)); no movement is observed in the y-direction, as expected, while the z-coordinate is subject to numerical oscillations about its initial value (computed so that the normal contact force equilibrates the weight of the body). Similar trends are found for velocities. Friction force magnitude versus time is illustrated

Parameter	**Symbol**	**Value**
Mass	m	2 kg
Multiplicative coefficient for F_x	a	39.24 N/s
Bristle stiffness	k_{br}	500000 N/m
Bristle damping	c_{br}	80 Ns/m
Threshold velocity	v_d	0.001 m/s
Static friction coefficient	μ_s	0.5
Kinetic friction coefficient	μ_k	0.4

TABLE C.2: Material parameters used in the simulation of one mass dragged on the ground.

in Figure C.5(b), together with the magnitude of the applied force and the magnitude of μF_n, the limiting magnitude of the friction force: it can be noticed that before $t = 0.25\,s$ (i.e., in the sticking regime), the magnitude of the friction force is lower than μF_n and such as to equilibrate the applied force. At $t = 0.25\,s$, $F_t = \mu_s F_n$ and remains constant for a few time steps, as long as the relative tangential velocity is lower than the threshold value v_d. As soon as the magnitude of the relative tangential velocity is higher than the threshold, the body slips, and a jump to a lower value of the friction force, which is equal to $\mu_k f_n$, is seen. In Figure C.5(c) and C.5(d) the trend for v_t can be appreciated; in particular, the second is a plot of v_t and of the threshold value in the first instants of the simulation, and shows oscillations that are soon damped thanks to the damping coefficient c_{br}. If a lower value of c_{br} or of v_d was used, these oscillations would exceed v_d and a few initial stick-slip transitions (of negligible effect on the overall dynamics) would occur.

The same scenario was simulated with Johnson's friction model. For comparison to the results obtained with the bristle model, Figure C.6 reports the x-coordinate, the friction force and the tangential relative velocity obtained in this case. It was found that the simulation results are more sensitive to changes in the value of the stiffness coefficient k_t, that discontinuities are created, and that it takes much longer to integrate (about 32 s, compared to 0.7 s with the bristle friction model). In particular, many more transitions between stick and slip are observed; each of these transitions causes a discontinuity in the dynamics.

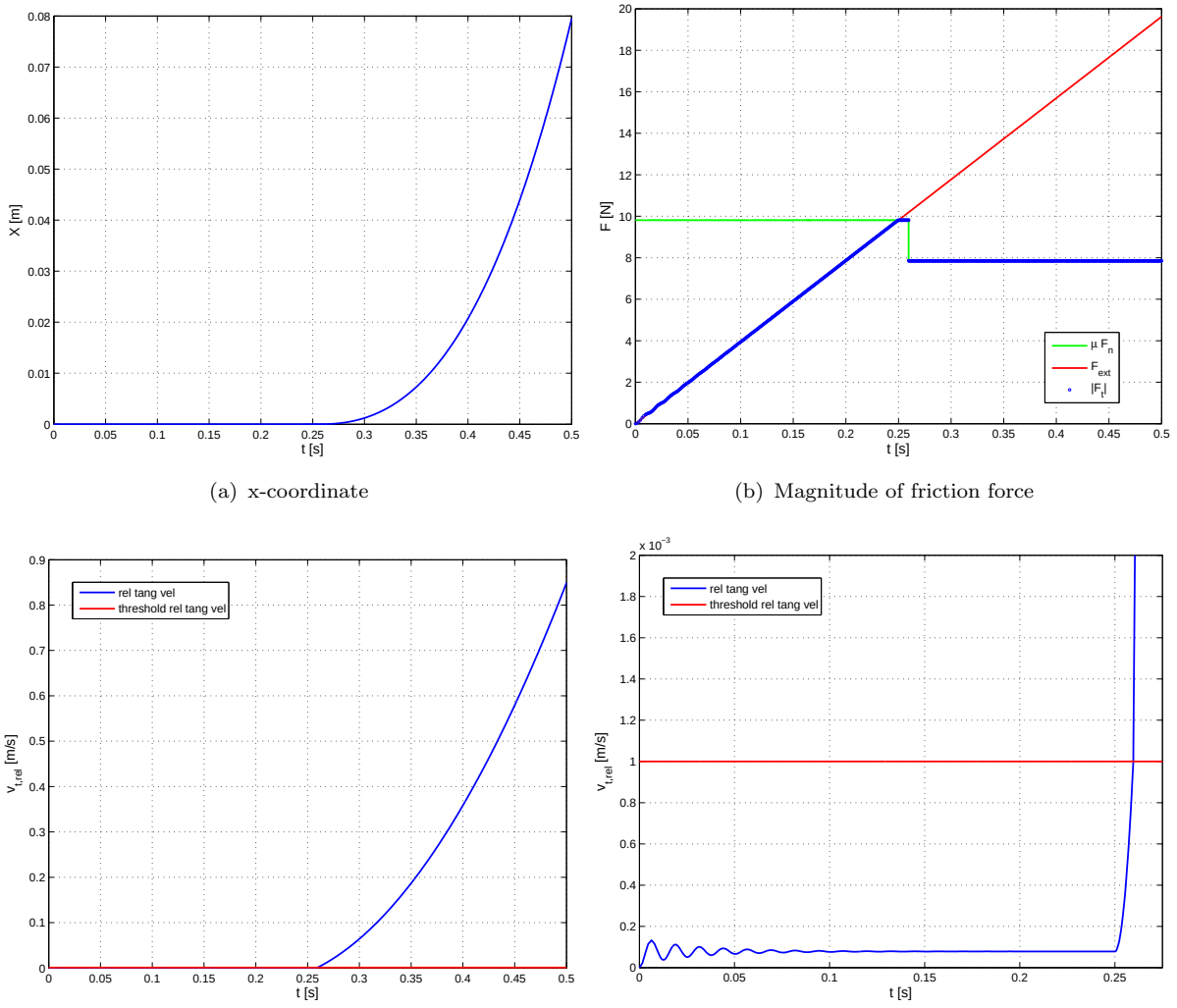

(a) x-coordinate

(b) Magnitude of friction force

(c) Relative velocity

(d) Relative velocity - zoom on beginning of simulation

FIGURE C.5: Results of simulation of one mass dragged on the ground, with bristle friction model.

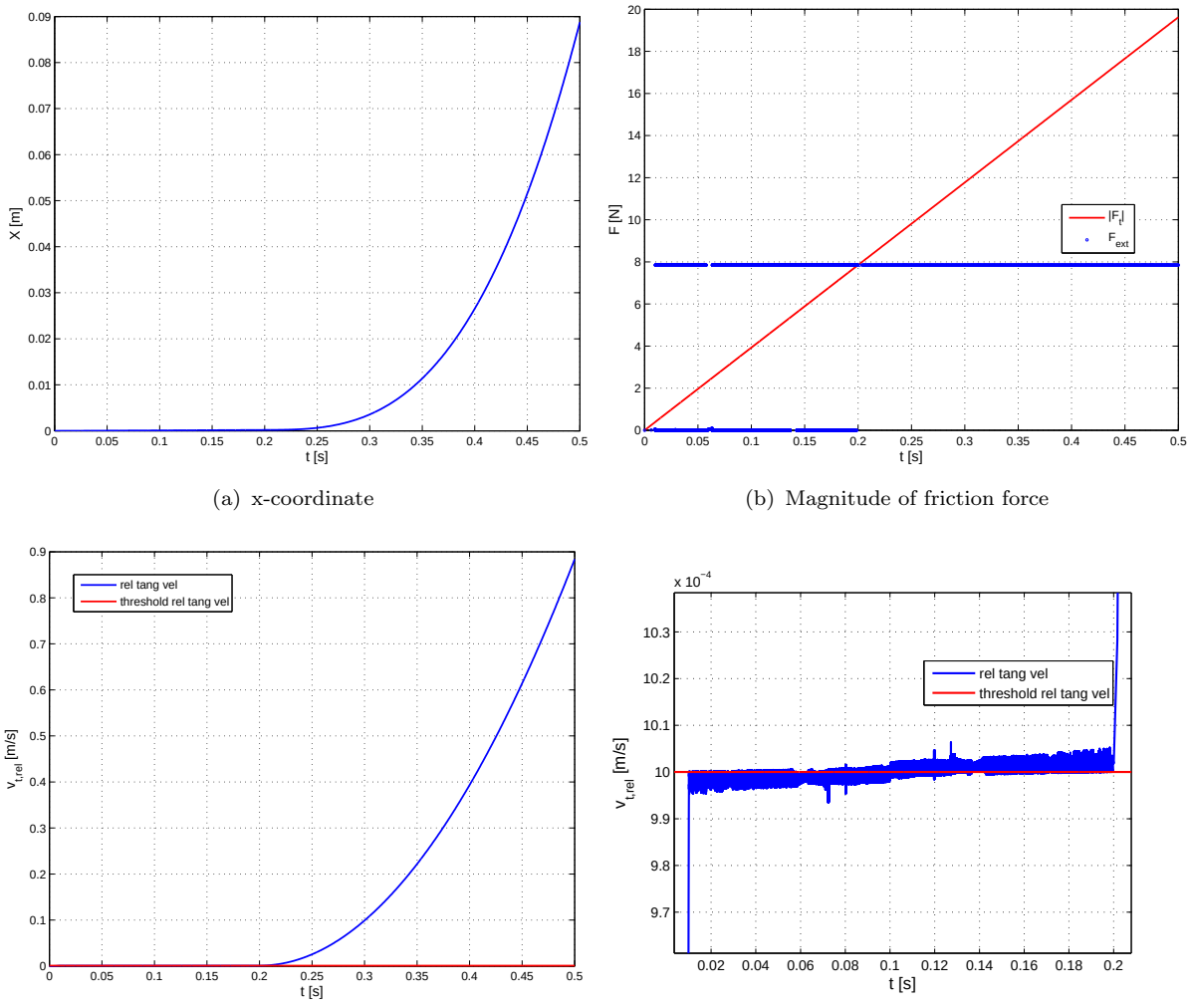

(a) x-coordinate

(b) Magnitude of friction force

(c) Relative velocity

(d) Relative velocity - zoom on beginning of simulation

FIGURE C.6: Results of simulation of one mass dragged on the ground, with Johnson's friction model.

Bibliography

[1] Donald J. Kessler. Collisional cascading: the limits of population growth in low earth orbit. *Advances in Space Research*, 11(12):63–66, 1991. ISSN 0273-1177.

[2] Jer Chyi (J.-C.) Liou. An active debris removal parametric study for leo environment remediation. *Advances in Space Research*, 47(11):1865–1876, 2011. ISSN 0273-1177. doi: 10.1016/j.asr.2011.02.003.

[3] Heiner H. Klinkrad and Nicholas L. Johnson. Space debris environment remediation concepts. In *Fifth European Conference on Space Debris (ESA SP-672, July 2009)*, Darmstadt, Germany, 2009.

[4] Carsten Wiedemann, Sven Flegel, Marek Möckel, Johannes Gelhaus, Vitali Braun, Cristopher Kebschull, Jörg Kreisel, Manuel Metz, and Peter Vörsmann. Cost estimation of active debris removal. In *63rd International Astronautical Congress, IAC 2012*, Naples, Italy, October 2012. International Astronautical Federation. IAC-12-A6.5.3.

[5] Shin-Ichiro Nishida, Satomi Kawamoto, Yasushi Okawa, Fuyuto Terui, and Shoji Kitamura. Space debris removal system using a small satellite. *Acta Astronautica*, 65(1-2):95–102, 2009. ISSN 00945765. doi: 10.1016/j.actaastro.2009.01.041.

[6] Suril V Shah, Inna Sharf, and Arun K Misra. Reactionless Path Planning Strategies for Capture of Tumbling Objects in Space Using a Dual-Arm Robotic System. In *AIAA Guidance, Navigation and Control Conference*, Boston, MA, 2013.

[7] Inna Sharf, Pamela Woo, Thai-Chau Nguyen-Huynh, and Arun Misra. System rigidization and control for post-capture maneuvering of large space debris. In *Aerospace Conference, 2016 IEEE*, pages 1–12, Big Sky, MT, 2016. IEEE. ISBN 1467376760.

[8] Bernd Bischof, Lothar Kerstein, Juergen Starke, H. Guenther, and Wolf-Peter Foth. ROGER - Robotic Geostationary Orbit Restorer. *Science and Technology Series*, 109:183–193, 2004. ISSN 0278-4017.

[9] Michèle R. Lavagna, Roberto Armellin, Alessandro Bombelli, Riccardo Benvenuto, and Riccardo Carta. Debris removal mechanism based on tethered nets. In *Proceedings of the 11th International Symposium on Artificial Intelligence, Robotics and Automation in Space, i-SAIRAS 2012*, Turin, Italy, September 2012.

[10] Kjetil Wormnes, Jan Hein de Jong, Holger Krag, and Gianfranco Visentin. Thrownets and Tethers for Robust Space Debris Capture. In *Proceedings of the 64th International Astronautical Congress, IAC 2013*, Beijing, China, 2013. International Astronautical Federation. IAC-13, A6.5, 2x16445.

[11] Robin Biesbroek, Luisa Innocenti, Stéphane Estable, Michael Oswald, Richard Haarmann, Gerrit Hausmann, Carole Billot, and Simona Ferraris. The e.Deorbit Mission: Results of ESA's Phase A Studies for an Active Debris Removal Mission. In *66th International Astronautical Congress (IAC 2015)*, Jerusalem, Israel, 12-16 October 2015. International Astronautical Federation. IAC-15-A6.6.5.

[12] Joshua J. Loughman. Overview and analysis of the soldier satellite concept for removal of space debris. In *AIAA Space 2010 Conference and Exposition*, Anaheim, CA, 2010.

[13] Claude R Phipps. A laser-optical system to re-enter or lower low earth orbit space debris. *Acta Astronautica*, 93:418–429, 2014. ISSN 0094-5765.

[14] Claudio Bombardelli and Jesus Pelaez. Ion beam shepherd for contactless space debris removal. *Journal of Guidance, Control, and Dynamics*, 34(3):916–920, 2011. ISSN 0731-5090 1533-3884. doi: 10.2514/1.51832.

[15] Minghe Shan, Jian Guo, and Eberhard Gill. Review and comparison of active space debris capturing and removal methods. *Progress in Aerospace Sciences*, 80:18–32, 2016. ISSN 03760421. doi: 10.1016/j.paerosci.2015.11.001.

[16] Joseph A. Carroll. Space transport development using orbital debris. Report, Tether Applications, Inc., 2 December 2002. URL http://images.spaceref.com/docs/spaceelevator/800Carroll.pdf.

[17] Robin Biesbroek, Tiago Soares, Jakob Hüsing, Kjetil Wormnes, and Luisa Innocenti. The e.Deorbit CDF Study: A Design Study for the Safe Removal of a Large Space Debris. In *64th International Astronautical Congress, IAC 2013*, Beijing, China, 2013. International Astronautical Federation, IAF.

[18] Guang Zhai and Jing-Rui Zhang. Space Tether Net System for Debris Capture and Removal. In *4th International Conference on Intelligent Human-Machine Systems and Cybernetics (IHMSC 2012)*, volume 1, pages 257–261, Nanchang, China, 2012. IEEE. ISBN 1467319023.

[19] Alessandro Bombelli. *Multidisciplinary design of a net-based device for space debris active removal*. Master's thesis, 2012. Politecnico di Milano.

[20] Vaios J. Lappas, Jason L. Forshaw, Lourens Visagie, Aurélien Pisseloup, Thierry Salmon, Eric Joffre, Thomas Chabot, Ingo Retat, Robert Axthelm, Simon Barraclough, Andrew Ratcliffe, Andy Bradford, Haval Kadhem, Nimal Navarathinam, Jeroen Rotteveel, Cesar Bernal, Franois Chaumette, Alexandre Pollini, and Willem H. Steyn. REMOVEDEBRIS: an EU Low Cost Demonstration Mission to Test ADR Technologies. In *65th International Astronautical Congress (IAC 2014)*, Toronto, ON, 2014. IAC-14-A6.6-10x27091.

[21] Samuele Salvi. *Flexible devices for active space debris removal: the net simulation tool*. Master's thesis, 2014. Politecnico di Milano.

[22] Riccardo Benvenuto and Riccardo Carta. *Implementation of a net device test bed for space debris active removal feasibility demonstration*. Thesis, 2012. Politecnico di Milano.

[23] Inna Sharf, Benjamin Thomsen, Eleonora M. Botta, and Arun K. Misra. Experiments and Simulation of a Net Closing Mechanism for Tether-Net Capture of Space Debris. *Acta Astronautica*, 2017. Revised version submitted.

[24] William J. O'Connor and Deborah J. Hayden. Detumbling of Space Debris by a Net and Elastic Tether. *Journal of Guidance, Control, and Dynamics*, pages 1–8, 2017. ISSN 0731-5090 1533-3884. doi: 10.2514/1.g001838.

[25] Panfeng Huang, Fan Zhang, Jun Ma, Zhongjie Meng, and Zhengxiong Liu. Dynamics and configuration control of the Maneuvering-Net Space Robot System. *Advances in Space Research*, 55(4):1004–1014, 2015. ISSN 02731177. doi: 10.1016/j.asr.2014.11.009.

[26] Zhongjie Meng, Panfeng Huang, and Jian Guo. Approach Modeling and Control of an Autonomous Maneuverable Space Net. *IEEE Transactions on Aerospace and Electronic Systems*, pages 1–1, 2017. ISSN 0018-9251. doi: 10.1109/taes.2017.2709794.

[27] Riccardo Benvenuto, Samuele Salvi, and Michèle Lavagna. Dynamics analysis and GNC design of flexible systems for space debris active removal. *Acta Astronautica*, 110:247–265, 2015. ISSN 0094-5765. doi: 10.1016/j.actaastro.2015.01.014.

[28] Lorenzo Cercós, Raluca Stefanescu, Alberto Medina, Riccardo Benvenuto, Michèle Lavagna, I. Gonzàlez, N. Rodrguez, and Kjetil Wormnes. Validation of a Net Active Debris Removal Simulator within Parabolic Flight Experiment. In *Proceedings of the 12th International Symposium on Artificial Intelligence, Robotics and Automation in Space, i-SAIRAS 2014*, Montreal, Canada, 2014.

[29] Wojciech Golebiowski, Rafal Michalczyk, Michal Dyrek, Umberto Battista, and Kjetil Wormnes. Validated Simulator for Space Debris Removal with Nets and Other Flexible Tethers Applications. In *66th International Astronautical Congress, IAC 2015*, Jerusalem, Israel, 12-16 October 2015. International Astronautical Federation. IAC-15,D1,1,6,x30579.

[30] Wojciech Golebiowski, Rafal Michalczyk, Michal Dyrek, Umberto Battista, and Kjetil Wormnes. Validated simulator for space debris removal with nets and other flexible tethers applications. *Acta Astronautica*, 129:229–240, 2016. ISSN 00945765. doi: 10.1016/j.actaastro.2016.08.037.

[31] Q. Chen and L. Yang. On dynamics of casting a net structure of flexible cables on orbit. In *Proceedings of the 60th International Astronautical Congress, IAC 2009*, Daejeon, Korea, 2009. IAC-09-C1.8.8.

[32] Haitao Liu, QingBin Zhang, Leping Yang, and Yanwei Zhu. Modeling and Simulation of Deployment Dynamics of Space Webs. In *Proceedings of the 64th International Astronautical Congress, IAC 2013*, Beijing, China, 2013. International Astronautical Federation, IAF. IAC-13-A6,P,35.p1x19691.

[33] Likun Liu, Jinjun Shan, Yuan Ren, and Zhicheng Zhou. Deployment Dynamics of Throw-Net for Active Debris Removal. In *65th International Astronautical Congress, IAC 2014*, Toronto, Canada, September - October 2014. IAC-14-A6.5.4.

[34] Minghe Shan, Jian Guo, and Eberhard Gill. Deployment dynamics of tethered-net for space debris removal. *Acta Astronautica*, 132:293–302, 2017. ISSN 00945765. doi: 10.1016/j.actaastro.2017.01.001.

[35] Johannes Gerstmayr and Ahmed A. Shabana. Analysis of thin beams and cables using the absolute nodal co-ordinate formulation. *Nonlinear Dynamics*, 45(1-2):109–130, 2006. ISSN 0924-090X 1573-269X. doi: 10.1007/s11071-006-1856-1.

[36] Riccardo Benvenuto and Michèle R. Lavagna. Flexible capture devices for medium to large debris active removal: Simulations results to drive experiments. In *12th Symposium on Advanced Space Technologies in Automation and Robotics (ASTRA 2013)*, ESA/ESTEC, Noordwijk, the Netherlands, May 15-17 2013.

[37] Riccardo Benvenuto, Michèle Lavagna, and Samuele Salvi. Multibody dynamics driving gnc and system design in tethered nets for active debris removal. *Advances in Space Research*, 58(1):45–63, 2016. ISSN 0273-1177. doi: 10.1016/j.asr.2016.04.015.

[38] Alberto Medina, Lorenzo Cercós, Raluca M. Stefanescu, Riccardo Benvenuto, Vincenzo Pesce, Marco Marcon, Michèle Lavagna, Iván González, Nuria Rodrguez López, and Kjetil Wormnes. Validation results of satellite mock-up capturing

experiment using nets. *Acta Astronautica*, 134:314–332, 2017. ISSN 00945765. doi: 10.1016/j.actaastro.2017.02.019.

[39] Guang Zhai, Jing-Rui Zhang, and Zhang Yao. Circular orbit target capture using space tether-net system. *Mathematical Problems in Engineering*, 2013. ISSN 1024-123X.

[40] Kalyan K. Mankala and Sunil K. Agrawal. Dynamic modeling and simulation of impact in tether net/gripper systems. *Multibody System Dynamics*, 11(3):235–250, 2004. ISSN 1384-5640.

[41] Arun K. Misra and Vinod J. Modi. A survey on the dynamics and control of tethered satellite systems. In *International Conference on Tethers in Space*, Arlington, VA, 1986.

[42] Vladimir V. Beletsky and Evgeny M. Levin. Dynamics of space tether systems. *Advances in the Astronautical Sciences*, 83, 1993.

[43] Arun K. Misra. Dynamics and control of tethered satellite systems. *Acta Astronautica*, 63(11-12):1169–1177, 2008. ISSN 00945765. doi: 10.1016/j.actaastro.2008.06.020.

[44] Vladimir S. Aslanov and Alexander S. Ledkov. *Dynamics of tethered satellite systems*. Woodhead Publishing, Cambridge, U.K., 2012. ISBN 0857096001.

[45] Vladimir S. Aslanov and Vadim V. Yudintsev. Dynamics of large space debris removal using tethered space tug. *Acta Astronautica*, 91:149–156, 2013. ISSN 0094-5765. doi: 10.1016/j.actaastro.2013.05.020.

[46] Vladimir S. Aslanov and Vadim V. Yudintsev. Dynamics of Large Debris Connected to Space Tug by a Tether. *Journal of Guidance, Control, and Dynamics*, 36(6):1654–1660, 2013. ISSN 0731-5090. doi: 10.2514/1.60976.

[47] Vladimir S. Aslanov. Chaos Behavior of Space Debris During Tethered Tow. *Journal of Guidance, Control, and Dynamics*, pages 1–7, 2015. ISSN 0731-5090 1533-3884. doi: 10.2514/1.g001460. Published online on September 15, 2015.

[48] Lee Jasper and Hanspeter Schaub. Tethered towing using open-loop input-shaping and discrete thrust levels. *Acta Astronautica*, 105(1):373–384, 2014. ISSN 00945765. doi: 10.1016/j.actaastro.2014.10.001.

[49] Marco Sabatini, Paolo Gasbarri, and Giovanni B. Palmerini. Elastic issues and vibration reduction in a tethered deorbiting mission. *Advances in Space Research*, 57(9):1951–1964, 2016. ISSN 02731177. doi: 10.1016/j.asr.2016.02.010.

[50] H.T.K. Linskens and Erwin Mooij. Tether Dynamics Analysis and Guidance and Control Design for Active Space-Debris Removal. *Journal of Guidance, Control, and Dynamics*, 39(6):1232–1243, 2016. ISSN 0731-5090 1533-3884. doi: 10.2514/1.g001651.

[51] Sean Cleary and William J. O'Connor. Control of space debris using an elastic tether and wave-based control. *Journal of Guidance, Control, and Dynamics*, 39(6): 1392–1406, 2016. ISSN 0731-5090 1533-3884. doi: 10.2514/1.g001624.

[52] Andrea Bellanca, Vincenzo Pesce, Paolo Lunghi, and Michèle Lavagna. Wave based control analysis and experimental validation for reliable space transportation applications. In *GNC 2017: 10th International ESA Conference on Guidance, Navigation, and Control Systems*, Salzburg, Austria, 29 May - 2 June 2017.

[53] Kirk Hovell and Steve Ulrich. Attitude Stabilization of an Uncooperative Spacecraft in an Orbital Environment using Visco-Elastic Tethers. In *AIAA SciTech, Guidance, Navigation, and Control Conference*, San Diego, CA, 4-8 January 2016.

[54] Riccardo Benvenuto, Samuele Salvi, and Michèle Lavagna. Net capturing of tumbling space debris: contact modelling effects on the evolution of the disposal dynamics. In *13th Symposium on Advanced Space Technologies in Automation and Robotics (ASTRA 2013)*, ESA/ESTEC, Noordwijk, the Netherlands, May 11-13 2015.

[55] Rui Qi, Arun K. Misra, and Zongyu Zuo. Active Debris Removal Using Double-Tethered Space-Tug System. *Journal of Guidance, Control, and Dynamics*, 40(3): 722–730, 2017. ISSN 0731-5090 1533-3884. doi: 10.2514/1.g000699.

[56] Jason L. Forshaw, Guglielmo S. Aglietti, Nimal Navarathinam, Haval Kadhem, Thierry Salmon, Aurélien Pisseloup, Eric Joffre, Thomas Chabot, Ingo Retat, Robert Axthelm, Simon Barraclough, Andrew Ratcliffe, Cesar Bernal, Franois Chaumette, Alexandre Pollini, and Willem H. Steyn. RemoveDEBRIS: An in-orbit active debris removal demonstration mission. *Acta Astronautica*, 127:448–463, 2016. ISSN 00945765. doi: 10.1016/j.actaastro.2016.06.018.

[57] Camille Pirat, Muriel Richard-Noca, Christophe Paccolat, Federico Belloni, Reto Wiesendanger, Daniel Courtney, Roger Walker, and Volker Gass. Mission Design and GNC for In-Orbit Demonstration of Active Debris Removal Technologies with Cubesats. In *66th International Astronautical Congress (IAC 2015)*, Jerusalem, Israel, 12-16 October 2015. International Astronautical Federation. IAC-15-A6.6.2.

[58] Jean S. Bessonneau and Dominique Marichal. Study of the Dynamics of Submerged Supple Nets (Applications to Trawls). *Ocean Engineering*, 25(7):563–583, 1998. ISSN 00298018. doi: 10.1016/s0029-8018(97)00035-8.

[59] Chai-Cheng Huang, Hung-Jie Tang, and Jin-Yuan Liu. Dynamical Analysis of Net Cage Structures for Marine Aquaculture: Numerical Simulation and Model Testing. *Aquacultural Engineering*, 35(3):258–270, 2006. ISSN 01448609. doi: 10.1016/j.aquaeng.2006.03.003.

[60] Claude Lacoursière. *A Regularized Time Stepper for Multibody Systems*. Department of Computing Science, Umea University, 2006.

[61] Yang Yu, HeXi Baoyin, and JunFeng Li. Dynamic modelling and analysis of space webs. *Science China Physics, Mechanics and Astronomy*, 54(4):783–791, 2011. ISSN 1674-7348.

[62] Chun-Woo Lee, Ju-Hee Lee, Bong-Jin Cha, Hyun-Young Kim, and Ji-Hoon Lee. Physical modeling for underwater flexible systems dynamic simulation. *Ocean Engineering*, 32(3-4):331–347, 2005.

[63] Tsutomu Takagi, Takashi Shimizu, Katsuya Suzuki, Tomonori Hiraishi, and Katsutaro Yamamoto. Validity and layout of NaLA: a net configuration and loading analysis system. *Fisheries Research*, 66(2-3):235–243, 2004.

[64] Fabien LeBris and Dominique Marichal. Numerical and experimental study of submerged supple nets: applications to fish farms. *Journal of Marine Science and Technology*, 3(4):161–170, 1998.

[65] Brad Buckham, Frederick R. Driscoll, and Meyer Nahon. Development of a finite element cable model for use in low-tension dynamics simulation. *Journal of Applied Mechanics*, 71(4):476–485, 2004. ISSN 0021-8936.

[66] Bradley J Buckham. *Dynamics Modelling of Low-Tension Tethers for Submerged Remotely Operated Vehicles*. Ph.D. thesis, 2003. University of Victoria.

[67] Henry A. McKenna, John W.S. Hearle, and Nick O'Hear. *Handbook of fibre rope technology*. Elsevier, 2004. ISBN 1855739933.

[68] Riccardo Benvenuto and Michèle Lavagna. Tether design for space debris towing. In *ASTRA 2015*, Noordwijk, The Netherlands, 2015. Poster.

[69] Gabriele Gilardi and Inna Sharf. Literature Survey of Contact Dynamics Modelling. *Mechanism and Machine Theory*, 37(10):1213–1239, 2002. ISSN 0094-114X. doi: 10.1016/S0094-114x(02)00045-9.

[70] Inna Sharf and Yuning Zhang. A Contact Force Solution for Non-Colliding Contact Dynamics Simulation. *Multibody System Dynamics*, 16(3):263–290, 2006. ISSN 1384-5640. doi: 10.1007/s11044-006-9026-2.

[71] Janete Alves, Nuno Peixinho, Miguel Tavares da Silva, Paulo Flores, and Hamid M Lankarani. A comparative study of the viscoelastic constitutive models for frictionless contact interfaces in solids. *Mechanism and Machine Theory*, 85:172–188, 2015. doi: 10.1016/j.mechmachtheory.2014.11.020.

[72] Arnab Banerjee, Avishek Chanda, and Raj Das. Historical origin and recent development on normal directional impact models for rigid body contact simulation: a critical review. *Archives of Computational Methods in Engineering*, pages 1–26, 2016. ISSN 1134-3060. doi: 10.1007/s11831-016-9164-5.

[73] Kenneth H. Hunt and Frank R. Erskine Crossley. Coefficient of Restitution Interpreted as Damping in Vibroimpact. *Journal of Applied Mechanics-Transactions of the ASME*, 42(2):440–445, 1975. ISSN 0021-8936.

[74] Kenneth Langstreth Johnson. *Contact Mechanics*, book section 1-5, 11. Cambridge University Press, United Kingdom, 1987. ISBN 0521347963.

[75] Yves Gonthier, John McPhee, Christian Lange, and Jean-Claude Piedboeuf. A regularized contact model with asymmetric damping and dwell-time dependent friction. *Multibody System Dynamics*, 11(3):209–233, 2004. ISSN 1384-5640. doi: 10.1023/B:MUBO.0000029392.21648.bc.

[76] Yuning Zhang and Inna Sharf. Compliant Force Modelling for Impact Analysis. In *International Design Engineering Technical Conferences and Computers and Information in Engineering Conference, ASME 2004*, pages 595–601, Salt Lake City, Utah, September 28-October 2 2004. American Society of Mechanical Engineers.

[77] R.G. Herbert and D.C. McWhannell. Shape and Frequency Composition of Pulses from an Impact Pair. *Journal of Manufacturing Science and Engineering*, 99(3): 513–518, 1977. ISSN 1087-1357.

[78] Ting W. Lee and A.C. Wang. On the dynamics of intermittent-motion mechanisms. part 1: Dynamic model and response. *Journal of Mechanical Design*, 105(3):534–540, 1983. ISSN 1050-0472.

[79] Hamid M. Lankarani and Parviz E. Nikravesh. Continuous contact force models for impact analysis in multibody systems. *Nonlinear Dynamics*, 5(2):193–207, 1994. ISSN 0924-090X.

[80] David A. Haessig and Bernard Friedland. On the modeling and simulation of friction. *Journal of Dynamic Systems, Measurement, and Control*, 113(3):354–362, 1991. ISSN 0022-0434.

[81] Jianxun Liang, Steven Fillmore, and Ou Ma. An extended bristle friction force model with experimental validation. *Mechanism and Machine Theory*, 56:123–137, 2012. ISSN 0094-114X. doi: 10.1016/j.mechmachtheory.2012.06.002.

[82] Dean Karnopp. Computer simulation of stick-slip friction in mechanical dynamic systems. *Journal of Dynamic Systems Measurement and Control-Transactions of the ASME*, 107(1):100–103, 1985. ISSN 0022-0434.

[83] Brian Armstrong-Hélouvry, Pierre Dupont, and Carlos Canudas De Wit. A survey of models, analysis tools and compensation methods for the control of machines with friction. *Automatica*, 30(7):1083–1138, 1994. ISSN 0005-1098.

[84] Ou Ma, Kerman Buhariwala, Neil Roger, John MacLean, and Robert Carr. MDSF – A Generic Development and Simulation Facility for Flexible, Complex Robotic Systems. *Robotica*, 15(01):49–62, 1997. ISSN 0263-5747. doi: 10.1017/S0263574797000076. Published online: 08 September 2000.

[85] J. Tinsley Oden and E.B. Pires. Nonlocal and nonlinear friction laws and variational principles for contact problems in elasticity. *Journal of Applied Mechanics*, 50(1): 67–76, 1983. ISSN 0021-8936.

[86] DuPont. Kevlar aramid fiber technical guide. www.dupont.com/content/dam/dupont/products-and-services/fabrics-fibers-and-nonwovens/fibers/documents/Kevlar_Technical_Guide.pdf. USA, [retrieved 28 April 2016].

[87] John Pilling. Properties of selected fibres. www.mse.mtu.edu/~drjohn/my4150/compositesdesign/props.html, 2006. Composite Materials Design course online material, Department of Materials Science and Engineering, Michigan Technological University, [retrieved 27 April 2016].

[88] Joseph R. Davis. *Concise Metals Engineering Data Book*, book section 14, pages 189–199. ASM International, The Netherlands, 1997. ISBN 161503983X.

[89] Werner Goldsmith. *Impact: The theory and physical behavior of colliding solids*, pages 258–262. Arnold, first edition, 1960.

[90] David A. Hensher. *Fiber-Reinforced-Plastic (FRP) Reinforcement for Concrete Structures: Properties and Applications*. Elsevier, 2013. ISBN 148329143X.

[91] Martin Servin and Claude Lacoursière. Massless cable for real-time simulation. *Computer Graphics Forum*, 26(2):172–184, 2007. ISSN 1467-8659.

[92] Mattia Lanzani. *Reel Mechanism Design for Active Debris Removal*. Master's thesis, 2014.

[93] Daniel Kucharski, Georg Kirchner, Franz Koidl, Fan Cunbo, Randall Carman, Christopher Moore, Andriy Dmytrotsa, Martin Ploner, Giuseppe Bianco, Mikhailo Medvedskij, Andriy Makeyev, Graham Appleby, Michihiro Suzuki, Jean-Marie Torre, Zhongping Zhang, Ludwig Grunwaldt, and Feng Qu. Attitude and Spin Period of Space Debris Envisat Measured by Satellite Laser Ranging. *IEEE Transactions on Geoscience and Remote Sensing*, 52(12):7651–7657, 2014. doi: 10.1109/tgrs.2014.2316138.

[94] Minghe Shan, Jian Guo, Eberhard Gill, and Wojciech Golebiowski. Validation of space net deployment modeling methods using parabolic flight experiment. *Journal of Guidance, Control, and Dynamics*, 2017. To appear.

[95] Havard Fjaer Grip, Masahiro Ono, J Balaram, Jonathan Cameron, Abhinandan Jain, Calvin Kuo, Steven Myint, and Marco Quadrelli. Modeling and simulation of asteroid retrieval using a flexible capture mechanism. In *Aerospace Conference, 2014 IEEE*, pages 1–14. IEEE, 2014. ISBN 1479916226.

[96] Frederic Gladstone Bell. Chapter 11 - Engineering properties of rock. In Frederic Gladstone Bell, editor, *Engineering Properties of Soils and Rocks*, pages 256 – 295. Butterworth-Heinemann, third edition, 1992. ISBN 978-0-7506-0489-5. doi: https://doi.org/10.1016/B978-0-7506-0489-5.50014-7.